



HAL
open science

Thermodynamic optimization of solar receivers : analysis of entropy generation rates in anisothermal flows subjected to asymmetric thermal boundary conditions

Jean-Marc Avellaneda

► To cite this version:

Jean-Marc Avellaneda. Thermodynamic optimization of solar receivers : analysis of entropy generation rates in anisothermal flows subjected to asymmetric thermal boundary conditions. Thermics [physics.class-ph]. Université de Perpignan, 2019. English. NNT : 2019PERP0035 . tel-02502538

HAL Id: tel-02502538

<https://theses.hal.science/tel-02502538>

Submitted on 9 Mar 2020

HAL is a multi-disciplinary open access archive for the deposit and dissemination of scientific research documents, whether they are published or not. The documents may come from teaching and research institutions in France or abroad, or from public or private research centers.

L'archive ouverte pluridisciplinaire **HAL**, est destinée au dépôt et à la diffusion de documents scientifiques de niveau recherche, publiés ou non, émanant des établissements d'enseignement et de recherche français ou étrangers, des laboratoires publics ou privés.

THÈSE

Pour obtenir le grade de
Docteur

Délivré par
UNIVERSITE DE PERPIGNAN VIA DOMITIA

Préparée au sein de l'école doctorale 305 :
Énergie et Environnement
Et de l'unité de recherche PROMES-CNRS (UPR 8521)

Spécialité : **Physique**

Présentée par **Jean-Marc Avellaneda**

**THERMODYNAMIC OPTIMIZATION OF SOLAR RECEIVERS:
ANALYSIS OF ENTROPY GENERATION RATES IN
ANISOTHERMAL FLOWS SUBJECTED TO ASYMMETRIC
THERMAL BOUNDARY CONDITIONS**

Soutenue le 20 décembre 2019 devant le jury composé de :

M. Jérôme BELLETTRE, PR, LTeN
M. Jean CASTAING-LASVIGNOTTES, MCF, PIMENT
M. Jocelyn BONJOUR, PR, CETHIL
M. Michel PONS, DR, LIMSI
M. Gilles FLAMANT, DR, PROMES
M. Pierre NEVEU, PR, PROMES
Mme Françoise BATAILLE, PR, PROMES

Rapporteur
Rapporteur
Examineur
Examineur
Examineur
Directeur de thèse
Directeur de thèse

Thermodynamic optimization of solar receivers:
analysis of entropy generation rates in anisothermal
flows subjected to asymmetric thermal boundary
conditions

Optimisation thermodynamique des récepteurs
solaires : analyse de la puissance entropique générée
dans des écoulements anisothermes soumis à des
conditions aux limites thermiques asymétriques

Résumé en français

1 Introduction

La consommation sans cesse croissante d'énergie et les effets délétères dus aux rejets de substances polluantes ou à effet de serre dans l'environnement ainsi qu'à l'exploitation de ressources non renouvelables, impose de rechercher des solutions techniques plus durables. Les centrales solaires et particulièrement les centrales thermodynamiques à tour peuvent contribuer à relever ce défi. Dans ce type de centrale, un champ de miroirs, nommés héliostats, concentre le rayonnement solaire sur un récepteur placé au sommet d'une tour. Un fluide caloporteur y est porté à haute température avant d'alimenter une turbine afin de produire de l'électricité. Ces centrales offrent en particulier l'avantage d'être connectables à un système de stockage [218] permettant de faire face à la variabilité de la ressource solaire (nuits et passages nuageux) afin de maintenir une production constante d'électricité et mieux s'intégrer au réseau de distribution électrique existant. Afin d'assurer leur développement sur un marché concurrentiel, il est nécessaire d'améliorer leur efficacité et de réduire leur coût (mesuré par le coût actualisé de l'électricité produite ou LCOE [214] [169]).

Un moyen d'accroître le rendement consiste à augmenter la température du fluide de travail en entrée du cycle thermodynamique (c'est-à-dire en sortie du récepteur solaire), l'efficacité théorique étant normalement améliorée car le rendement de Carnot augmente. Il est toutefois nécessaire de veiller à plusieurs contraintes. Premièrement, le fluide de transfert doit pouvoir supporter de hautes températures (de l'ordre de 1000 °C), ce qui n'est pas le cas de la technologie actuellement la plus répandue qui utilise des sels fondus [140]. De nombreuses recherches portent aujourd'hui sur l'utilisation de fluides solaires adaptés, comme les lits fluidisés ou les suspensions denses de particules solides [81] ainsi que sur l'emploi de gaz, dont l'air [91] qui constitue une ressource abondante et non polluante pouvant accepter des températures élevées. Deuxièmement, les parois constituant le récepteur doivent pouvoir résister aux hautes températures exigées sans vieillissement accéléré du fait des contraintes chimiques et thermomécaniques générées [162]. Enfin, la course aux hautes températures trouve une limite dans les pertes par rayonnement thermique qui augmentent rapidement avec la température de surface et impliquent un point de fonctionnement au-delà duquel un accroissement de température de paroi aboutit à une dégradation du rendement du récepteur [130]. Un autre domaine d'application de l'énergie solaire concentrée est la chaleur de procédé : dans le cas des systèmes réactifs, il s'agit de thermochimie solaire et il est question de récepteurs-réacteurs solaires si le récepteur est le siège de la réaction chimique. Dans ce type d'applications, la problématique de l'optimisation des transferts de chaleur est similaire à celle des récepteurs mettant en oeuvre un fluide non réactif. Par contre, d'autres contraintes apparaissent telles que les transferts de

matière et la cinétique chimique.

Améliorer la performance des récepteurs solaires consiste en particulier à intensifier les échanges thermiques tout en évitant une trop grande chute de pression qui correspond à une perte parasite d'énergie. Or, l'amélioration du premier critère s'accompagne généralement d'une dégradation du second. Pour rechercher le meilleur compromis entre ces deux effets opposés, une façon de procéder consiste à utiliser une mesure commune regroupant toutes les puissances utiles perdues au sein du canal d'écoulement : la puissance entropique générée permet de réaliser cette agrégation et est le fondement des méthodes de minimisation de la génération d'entropie (EGM) [26]. Ainsi, le présent travail de thèse se concentre sur l'estimation, l'analyse et la minimisation de la puissance entropique générée dans l'écoulement, en prenant en compte deux caractéristiques essentielles des récepteurs solaires : l'existence de gradients thermiques (pouvant être élevés) et la présence de conditions aux limites thermiques asymétriques (puisque'un côté du récepteur est éclairé par le rayonnement solaire concentré et l'autre pas).

La physique des écoulements fluides dans les récepteurs solaires réels est complexe, du fait de leurs géométries, des caractéristiques thermiques qui viennent d'être citées, mais également du fait que les écoulements sont turbulents [8] [9] [230] [211] [68] [69]. Trois approches différentes sont décrites dans la suite de ce document, apportant chacune un éclairage complémentaire à la compréhension des taux de génération d'entropie dans les écoulements anisothermes soumis à des conditions aux limites asymétriques et portant chacune des simplifications par rapport aux récepteurs réels. Dans la première approche, publiée dans le *Journal of Thermophysics and Heat Transfer* [12], la couche limite laminaire externe d'un fluide s'écoulant au-dessus d'une plaque plane chauffante est utilisée comme plateforme d'essais pour étudier l'influence de plusieurs paramètres sur les taux de génération d'entropie locaux et intégrés. L'effet du type de condition aux limites thermiques (température imposée vs densité de flux de chaleur imposée) et de son intensité (écart de température paroi / fluide) sont étudiés. Dans la seconde approche, qui a fait l'objet d'une communication à l'International Heat Transfer Conference IHTC16 [10], un écoulement en canal plan, chauffé sur une partie d'une de ses parois, fait l'objet d'une optimisation variationnelle visant à trouver des champs de vitesse minimisant une fonctionnelle objectif directement liée à la puissance entropique générée dans le canal. Les champs de vitesse et de température résultants sont étudiés, l'amélioration en terme de génération d'entropie économisée est évaluée et l'influence des conditions aux limites est décrite. La même approche d'optimisation est applicable à d'autres processus d'advection-diffusion comme la diffusion massique d'une espèce minoritaire dans un écoulement convectif : une comparaison est faite avec les résultats qualitatifs obtenus dans le cas du transfert de chaleur. Le troisième axe d'analyse consiste à étudier l'écoulement turbulent quasi-compressible en canal plan d'un gaz dont les propriétés physiques dépendent de la température. Les parois sont à des températures différentes avec un ratio de 2. Les statistiques de l'écoulement sont décrites et l'influence du type de condition aux limites thermique est étudiée, ce qui a donné lieu à une publication dans l'International Journal of Heat and Fluid Flow [11]. La puissance entropique générée localement est ensuite analysée en termes moyens et fluctuants. L'effet du ratio de température entre les deux parois, du type de conditions aux limites thermiques et du nombre de Reynolds de friction moyen est décrit. Ainsi, plusieurs explorations et cartographies de la génération d'entropie sont effectuées : elles sont présentées successivement dans la suite de ce résumé.

2 Puissance entropique générée dans une couche limite laminaire

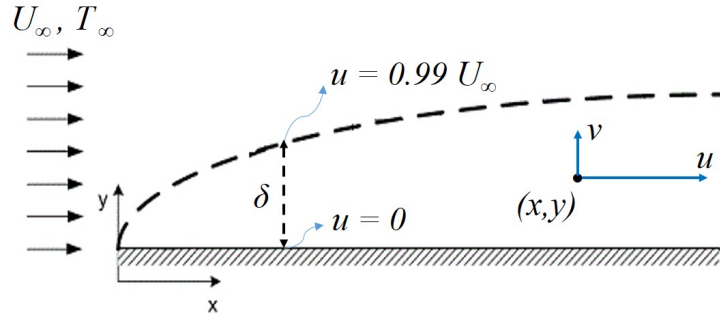


FIGURE 1 : Couche limite au dessus d'une plaque plane

On considère l'écoulement bidimensionnel stationnaire d'un fluide Newtonien incompressible et à propriétés constantes au-dessus d'une plaque plane semi-infinie. Le fluide arrive avec une vitesse et une température constantes et uniformes et est à la fois chauffé et cisailé par la plaque (figure 1). Les échanges radiatifs, les effets de la gravité et les échauffements visqueux sont négligés. Dans le cadre de ces hypothèses, un raisonnement sur les ordres de grandeurs des différents termes permet de simplifier les équations des Navier-Stokes dans la couche limite laminaire [208] et d'exprimer la conservation de la masse, de la quantité de mouvement et de l'énergie sous la forme suivante :

$$\frac{\partial u}{\partial x} + \frac{\partial v}{\partial y} = 0 \quad (1)$$

$$u \frac{\partial u}{\partial x} + v \frac{\partial u}{\partial y} = \nu \frac{\partial^2 u}{\partial y^2} \quad (2)$$

$$u \frac{\partial T}{\partial x} + v \frac{\partial T}{\partial y} = \alpha \frac{\partial^2 T}{\partial y^2} \quad (3)$$

Dans ces équations, x et y sont l'abscisse et l'ordonnée, respectivement et $u(x, y)$ et $v(x, y)$ les composantes longitudinale et normale à la paroi de la vitesse, ρ est la masse volumique du fluide, ν sa viscosité cinématique, $T(x, y)$ sa température et α sa diffusivité thermique. A ces trois équations, il convient d'adjoindre les conditions aux limites suivantes pour la vitesse (Eq. 4) et pour la température, cette dernière dépendant du type de condition aux limites thermique : (Eq. 5) pour une plaque à température fixée (isotherme) et (Eq. 6) dans le cas où la densité de flux thermique y est imposée (isoflux) :

$$u(x, 0) = 0, \quad v(x, 0) = 0, \quad \lim_{y \rightarrow \infty} u(x, y) = U_\infty \quad (4)$$

$$T(x, 0) = T_w, \quad \lim_{y \rightarrow \infty} T(x, y) = T_\infty \quad (5)$$

$$-k \frac{\partial T}{\partial y} \Big|_{y=0} = q'', \quad \lim_{y \rightarrow \infty} T(x, y) = T_\infty \quad (6)$$

où U_∞ et T_∞ sont respectivement la vitesse et la température du fluide en entrée et dans l'écoulement libre. T_w et q'' sont respectivement la température et la densité de flux thermique à la paroi. La solution de similarité (des profils $u(y)$ et $T(y)$ au long de la plaque) consiste à introduire plusieurs variables adimensionnelles [116] : l'ordonnée η , la fonction f (liée à la fonction courant Ψ) et l'écart de température avec la paroi θ :

$$\eta = y \sqrt{\frac{U_\infty}{\nu x}} \quad (7)$$

$$\psi = \sqrt{U_\infty \nu x} f(\eta) \quad (8)$$

$$u = \partial \psi / \partial y, \quad v = -\partial \psi / \partial x \quad (9)$$

$$\theta(\eta) = \frac{T_w - T}{T_w - T_\infty} \quad (10)$$

Ce changement de variables permet d'aboutir à des équations différentielles ordinaires, plus faciles à résoudre numériquement, portant sur la vitesse (Eq. 11, qui est l'équation de Blasius [37] [170]) et la température (Eq. 12 pour une plaque isotherme et Eq. 13 pour une plaque isoflux) ainsi qu'aux conditions aux limites associées (Eqs. 14 et 15) :

$$f''' + \frac{1}{2} f f'' = 0 \quad (11)$$

$$\theta'' + \frac{1}{2} Pr f \theta' = 0 \quad (12)$$

$$\theta'' + \frac{1}{2} Pr f \theta' + \frac{1}{2} Pr f' (1 - \theta) = 0 \quad (13)$$

$$f(0) = 0, \quad f'(0) = 0, \quad \lim_{\eta \rightarrow \infty} f(\eta) = 1 \quad (14)$$

$$\theta(0) = 0, \quad \lim_{\eta \rightarrow \infty} \theta(\eta) = 1 \quad (15)$$

La puissance entropique générée localement (en $W.K^{-1}.m^{-3}$) s'exprime de la façon suivante [26], où ϕ est le terme de dissipation visqueuse dans l'équation de l'énergie (également nommé : fonction de dissipation visqueuse) explicité ci-dessous pour un écoulement incompressible bidimensionnel :

$$\dot{S}_{gen}''' = \frac{k(\nabla T)^2}{T^2} + \frac{\phi}{T} \quad (16)$$

$$\phi = \mu \left\{ 2 \left[\left(\frac{\partial u}{\partial x} \right)^2 + \left(\frac{\partial v}{\partial y} \right)^2 \right] + \left(\frac{\partial u}{\partial y} + \frac{\partial v}{\partial x} \right)^2 \right\} \quad (17)$$

Dans le cas d'une plaque isotherme et en retenant de la fonction de dissipation visqueuse uniquement le terme majoritaire $(\partial u/\partial y)^2$, l' equation 16 exprim ee  a l'aide des fonctions f et θ permet d'obtenir la puissance entropique g en er e localement sous forme adimensionnelle S_3 (Eq. 18), l'adimensionnalisation  etant faite par r ef erence  a la quantit e kU_∞^2/ν^2 . Elle d epend du nombre de Reynolds local $Re_x = U_\infty x/\nu$, du nombre de Prandtl $Pr = \nu/\alpha$, du nombre d'Eckert $Ec = U_\infty^2/(C_p(T_w - T_\infty))$ ainsi que du rapport thermique adimensionnel $\tau = T_w/(T_w - T_\infty)$ et elle est la somme de trois contributions correspondant respectivement  a la g en eration d'entropie par conduction horizontale de la chaleur, par conduction verticale de la chaleur et enfin par frottement visqueux, identifi ees respectivement par les indices $(.)_{ch}$, $(.)_{cv}$ et $(.)_f$ (Eqs. 19).

$$S_3 = \frac{\theta'^2}{Re_x(\tau - \theta)^2} \left(\frac{\eta^2}{4Re_x} + 1 \right) + \frac{PrEc}{Re_x(\tau - \theta)} f''^2 \quad (18)$$

$$S_{3,ch} = \frac{\theta'^2}{Re_x(\tau - \theta)^2} \left(\frac{\eta^2}{4Re_x} \right), \quad S_{3,cv} = \frac{\theta'^2}{Re_x(\tau - \theta)^2}, \quad S_{3,f} = \frac{PrEc}{Re_x(\tau - \theta)} f''^2 \quad (19)$$

Par int egration  a abscisse fix ee, on obtient la puissance entropique surfacique g en er e S_2 (Eq. 20) et une seconde int egration, entre deux positions le long de la plaque (identifi ees par leurs nombre de Reynolds locaux Re_a et Re_b), aboutit  a la puissance entropique totale g en er e entre ces deux positions (Eq. 21). Les fonctions Ω sont des int egrales sur le domaine de variation de la variable η et ne d ependent que de τ et des fonctions f , θ et leurs d eriv ees.

$$S_2 = \left(\frac{\Omega_{ch}}{4Re_x} + \Omega_{cv} + PrEc \Omega_f \right) Re_x^{-\frac{1}{2}} \quad (20)$$

$$S_1 = \frac{1}{2} (Re_a^{-\frac{1}{2}} - Re_b^{-\frac{1}{2}}) \Omega_{ch} + 2 (Re_b^{\frac{1}{2}} - Re_a^{\frac{1}{2}}) (\Omega_{cv} + PrEc \Omega_f) \quad (21)$$

Dans le cas d'une plaque soumise  a une densit e de flux thermique uniforme et constante (cas isoflux), la puissance entropique adimensionnelle g en er e localement s' ecrit de la fa on suivante :

$$S_3 = \frac{\theta'^2}{Re_x(\tau - \theta)^2} \left(\left(\frac{\eta\theta' - \theta + 1}{\theta'} \right)^2 \frac{1}{4Re_x} + 1 \right) + \frac{PrEc}{Re_x(\tau - \theta)} f''^2 \quad (22)$$

La puissance entropique surfacique r epond  a la m eme forme math ematique que dans le cas isotherme (Eq. 20), sachant que la fonction θ y est diff erente et que le param etre τ ainsi que le nombre d'Eckert et les fonctions Ω d ependent d esormais de la distance

au bord d'attaque. La puissance entropique totale entre deux positions Re_a et Re_b est obtenue par intégration numérique.

Afin de comparer les simulations à température de paroi imposée avec celles à densité de flux fixée, un point de référence commun à toutes les simulations a été choisi et correspond à $Re_{x,ref} = 1000$. A ce point, la température est la même pour toutes les simulations qui partagent par ailleurs la même vitesse de l'écoulement libre U_∞ et le même nombre de Prandtl $Pr = 1$. Les équations de la couche limite laminaire ont été résolues numériquement via un schéma Runge-Kutta du quatrième ordre [121] et les fonctions f et θ ont été validées par rapport à la littérature [87] [53] [54]. Pour une large plage de valeurs du paramètre $\tau = T_w/(T_w - T_\infty)$ au point de référence (τ_{ref}) et pour les deux types de conditions aux limites thermiques, les puissances entropiques générées localement en fonction de η ont été calculées, ainsi que l'évolution des puissances surfaciques en fonction de la position de long de la paroi. Enfin, le comportement de la puissance entropique totale est étudié dans le cas où on impose la puissance thermique échangée entre le fluide entrant et la plaque.

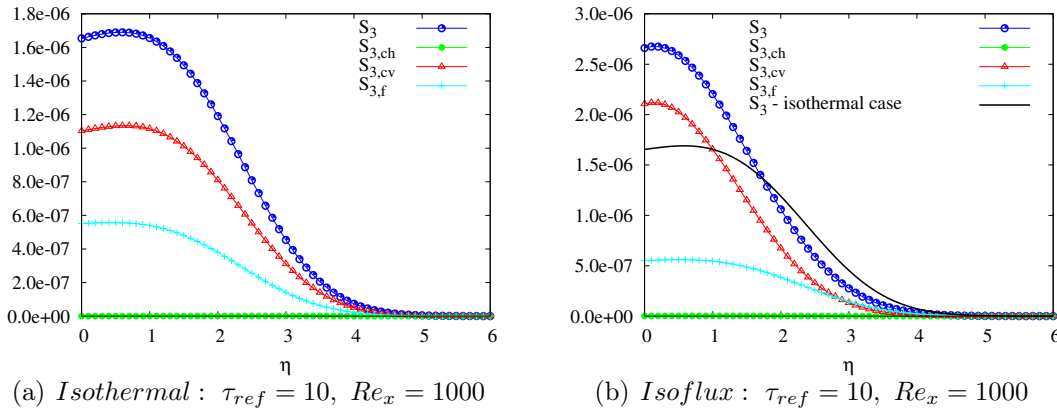


FIGURE 2 : Puissance entropique adimensionnelle générée localement (S_3). Plaque isotherme (à gauche) et isoflux (à droite). La courbe de S_3 pour le cas isotherme est également affichée pour servir de comparaison sur le graphique du cas isoflux (ligne noire en traits pleins).

La puissance entropique adimensionnelle générée localement en chaque point de la couche limite (S_3) présente un profil en fonction de la distance adimensionnée à la paroi (η) qui dépend du type de condition aux limites thermiques (isotherme ou isoflux), du paramètre τ et de la distance au bord d'attaque (exprimée sous forme adimensionnelle par Re_x). Il en est de même de la composition de cette puissance, c'est à dire des parts relatives correspondant aux conductions verticales et horizontales de la chaleur et à la part visqueuse. La part liée à la conduction horizontale (ainsi que les parts des termes qui ont été négligés dans la fonction de dissipation visqueuse) ne devient significative que près du bord d'attaque (par exemple pour $Re_x = 10$). Un exemple de comparaison isotherme / isoflux est présenté dans la figure 2, au point de référence $Re_x = 1000$ et pour un écart de température entre la plaque et l'écoulement libre égal à un dixième de la température de paroi, toujours au point de référence. La puissance entropique générée est strictement positive à la paroi et peut présenter un maximum local, avant de décroître vers zéro en atteignant l'écoulement libre isentropique. La position de ce maximum local dépend du type de condition aux limites thermiques (isotherme vs

isoflux) mais également de la valeur de τ au point de référence : il trouve sa source dans la compétition entre les évolutions de la température et de son gradient vertical en proche paroi. Les comparaisons entre les simulations à plaque isotherme et isoflux ont été effectuées en modifiant la valeur de τ au point de référence et en se déplaçant le long de la plaque : elles sont détaillées en section 2.5 du manuscrit de thèse.

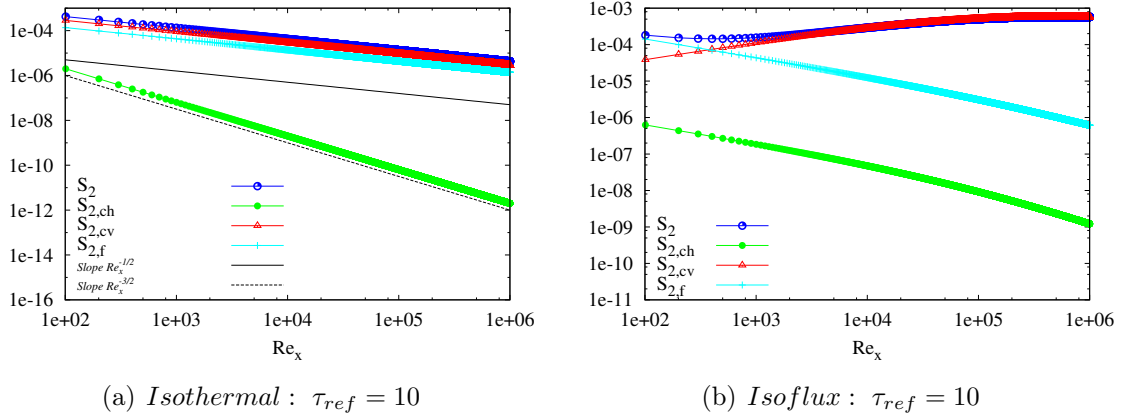


FIGURE 3 : Plaque isotherme (à gauche) et isoflux (à droite) : puissance entropique surfacique adimensionnelle pour $\tau_{ref} = 10$ et Re_x de 100 à 1000000

La puissance entropique surfacique adimensionnelle S_2 dépend également de la valeur de τ choisie au point de référence et de la position le long de la paroi. Pour une plaque isotherme, S_2 décroît quand le nombre de Reynolds local augmente (figure 3(a)). Dans le cas d'une plaque à densité de flux thermique imposée, S_2 est le résultat de la concurrence entre deux causes lorsque l'on s'éloigne du bord d'attaque : l'augmentation de l'écart de température relatif ($\tau(x)$ diminue) d'une part, et l'épaississement de la couche limite thermique, d'autre part. La courbe résultante présente en particulier un minimum dont la position dépend de la valeur de τ au point de référence (figure 3(b)).

La puissance entropique adimensionnelle totale générée entre deux positions fixées le long de la paroi (S_1) est une fonction décroissante de τ_{ref} . Par contre, si on impose une puissance thermique échangée par unité de largeur de plaque q' (notée q_1 sous forme adimensionnelle - cf. Eq. 23) entre la plaque et le fluide (à partir d'une position donnée exprimée par son nombre de Reynolds local Re_a), S_1 présente un minimum (cf. figure 4) pour une valeur optimale τ_{opt} qui dépend du type de condition aux limites thermiques. Dans le cas isoflux, il est possible de s'éloigner de façon significative de τ_{opt} (par exemple, en autorisant des écarts de températures relatifs plus élevés), sans modifier sensiblement la puissance entropique générée. Lorsque le point de fonctionnement est à τ_{ref} très petit et aux alentours de 2 par exemple (c'est le cas des récepteurs solaires dans lesquels les gradients de température sont élevés), réduire l'écart relatif de température peut apporter une réduction significative de la puissance entropique générée. Dans le cas d'une plaque isotherme, la valeur de τ_{opt} est indépendante du point de départ de l'intervalle d'intégration (Re_a) et de la puissance fixe échangée (q_1). Par contre, dans le cas isoflux, τ_{opt} est une fonction croissante de ces deux grandeurs.

$$q_1 = \frac{q'}{kT_{w,ref}} \quad (23)$$

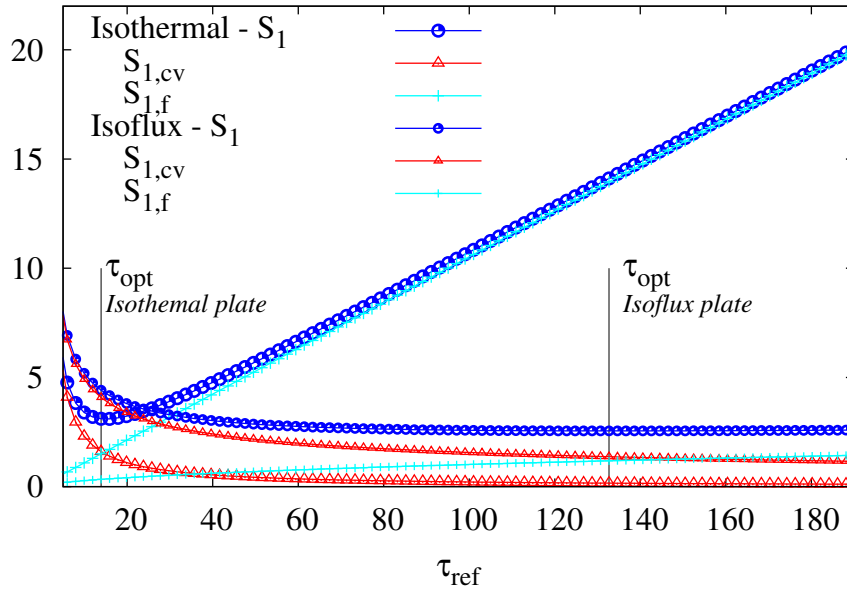


FIGURE 4 : Puissance entropique totale générée à partir de $Re_a = 1000$ avec $q_1 = 26.67$ (τ_{ref} allant de 5 à 190.)

En complément des travaux présentés ci-dessus, le développement d'une couche limite laminaire pour un fluide rencontrant une plaque chauffante est simulé avec le logiciel Fluent et la puissance entropique générée est calculée. Deux buts sont poursuivis : le premier est de vérifier qu'il peut y avoir un sens à négliger la fonction de dissipation visqueuse dans l'équation de l'énergie tout en la prenant en compte dans le calcul de l'entropie générée. Le second est de comparer les ordres de grandeurs obtenus en résolvant les équations de Navier-Stokes incompressibles avec ceux tirés des équations de la couche limite laminaire résolues par la méthode de similarité et l'équation de Blasius.

Une analyse théorique, fondée sur les équations adimensionnées (l'équation de l'énergie dans la couche limite laminaire et la formule de calcul de la puissance entropique générée), tend à démontrer que si le nombre de Brinkman $Br = PrEc$ est très petit devant l'unité, la fonction de dissipation visqueuse est négligeable devant le terme conductif dans l'équation de l'énergie. Par contre, pour pouvoir négliger le terme visqueux dans le calcul de la puissance entropique générée, il faut que $Br.\tau$ soit petit. Deux simulations ont été effectuées dans une situation où $Br = 0.01$ et $Br.\tau = 1$, l'une en résolvant l'équation de l'énergie en prenant en compte l'échauffement visqueux et l'autre en négligeant cette contribution. L'analyse de ces deux simulations montre que les profils de températures obtenus sont quasiment identiques et que la fonction de dissipation visqueuse peut effectivement être négligée dans l'équation de l'énergie pour un nombre de Brinkman petit. Par ailleurs, la part liée au frottement visqueux n'est pas négligeable dans le calcul de la puissance entropique générée (elle est du même ordre de grandeur que la part liée à la conduction de la chaleur) car le produit $Br.\tau = 1$ n'est pas négligeable devant l'unité.

Dans les deux simulations décrites ci-dessus, l'erreur sur le bilan d'entropie est inférieure à 1% du flux net d'entropie (que ce soit par transfert convectif de matière ou par conduction de la chaleur depuis les parois). Toutefois, dans la situation étudiée où

l'entropie générée est petite par rapport aux flux d'entropie (conductifs ou convectifs), l'ordre de grandeur de la puissance entropique générée est le même que celui de l'erreur numérique constatée sur le bilan d'entropie. Afin de s'assurer que cette erreur n'est pas concentrée sur le calcul de la puissance entropique générée, une analyse a été effectuée en calculant quatre écoulements : deux à flux imposés et deux à températures imposées, avec pour chaque cas les valeurs $\tau_{ref} = 2$ et $\tau_{ref} = 100$. Les résultats obtenus sont proches de ceux fondés sur l'équation de Blasius. Les écarts sont plus prononcés, tout en conservant les ordres de grandeurs, pour la puissance entropique d'origine visqueuse, du fait de la solution différente et plus réaliste obtenue en résolvant directement les équations de Navier-Stokes pour le champ de vitesse longitudinal [60]. En synthèse, les puissances entropiques calculées sont cohérentes avec celles obtenues précédemment dans le cadre simplifié de la méthode de similarité et des approximations de la couche limite laminaire.

3 Optimisation variationnelle d'un écoulement interne

Dans cette section, on considère à nouveau un écoulement bidimensionnel stationnaire d'un fluide Newtonien incompressible à propriétés constantes, cette fois à l'intérieur d'un canal plan (figure 5) dont un tiers d'une paroi transfère au fluide une densité de flux thermique uniforme et constante (les autres parois étant adiabatiques). Comme précédemment, les effets de la gravité sont négligés et il en est de même des échanges radiatifs et de l'échauffement visqueux. Le fluide entre dans le canal à vitesse et à température uniforme et constante. La pression relative en sortie est fixée à zéro.

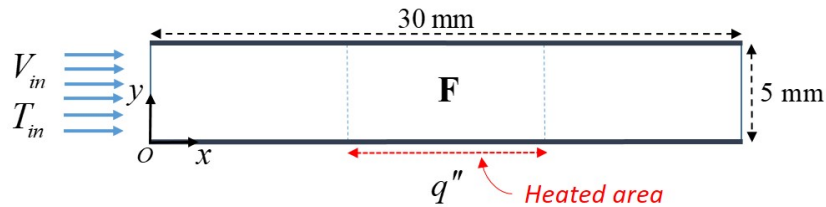


FIGURE 5 : Caractéristiques du domaine.

Les équations de l'écoulement sont indiquées ci-dessous et la puissance entropique locale générée est calculée comme précédemment (Eqs. 16 et 17).

$$\nabla \cdot \mathbf{V} = 0 \quad (24)$$

$$\rho \mathbf{V} \cdot \nabla \mathbf{V} = -\nabla P + \mu \nabla^2 \mathbf{V} + \mathbf{F} \quad (25)$$

$$\mathbf{V} \cdot \nabla T = \frac{k}{\rho C_p} \nabla^2 T \quad (26)$$

Dans ces équations, \mathbf{V} est le vecteur vitesse, P la pression, T la température, ρ la masse volumique du fluide, μ sa viscosité dynamique, k sa conductivité thermique et C_p sa capacité calorifique à pression constante. \mathbf{F} est un champ de force volumique qui est utilisé dans le processus d'optimisation décrit ci-après.

On se place dans le cas où le nombre de Bejan (Eq. 27) est proche de l'unité, c'est à dire que la puissance entropique générée par dissipation visqueuse est petite devant celle qui est générée du fait des transferts de chaleur à travers les différences finies de température.

$$Be = \frac{\dot{S}_{gen,c}}{\dot{S}_{gen,c} + \dot{S}_{gen,f}}, \quad (.)_c : \text{transfert de chaleur } (.)_f : \text{ frottement visqueux} \quad (27)$$

On cherche à minimiser la puissance entropique générée par ce terme majoritaire tout en prenant en compte la dissipation visqueuse à travers un facteur pondérateur, nommé W_{Φ} permettant de donner un poids relatif plus ou moins important à la chute de pression dans la procédure d'optimisation [141] [108]. La fonctionnelle objectif est une combinaison linéaire de la puissance entropique générée par conduction de la chaleur, d'une part, et de la fonction de dissipation visqueuse, d'autre part :

$$J = \iiint_{\Omega} \left(\frac{k}{T^2} (\nabla T)^2 + W_{\Phi} \Phi \right) .d\Omega \quad (28)$$

La conservation de la masse et de l'énergie sont prises en compte en utilisant deux multiplicateurs de Lagrange (respectivement λ_1 et λ_2 qui sont des fonctions de la position dans le canal) et le critère Lagrangien à minimiser est :

$$J^* = \iiint_{\Omega} \left\{ \frac{k}{T^2} (\nabla T)^2 + W_{\Phi} \Phi + \lambda_2 \left[\frac{k}{\rho C_p} \nabla^2 T - \mathbf{V} \cdot \nabla T \right] + \lambda_1 \nabla \cdot \mathbf{V} \right\} .d\Omega \quad (29)$$

L'expression du champ de force volumique est obtenue en annulant la première variation de J^* par rapport aux composantes u et v de la vitesse et en prenant en compte l'équation de conservation de la quantité de mouvement :

$$\mathbf{F} = \frac{\lambda_2}{2W_{\Phi}} \nabla T + \rho \mathbf{V} \cdot \nabla \mathbf{V} \quad (30)$$

Annuler la première variation de J^* par rapport à la température permet d'aboutir à une équation de type transport pour le second multiplicateur de Lagrange λ_2 , qui est nécessaire au calcul de la force volumique :

$$\nabla \cdot \left(\rho \mathbf{V} \lambda_2 - \frac{-k}{C_p} \nabla \lambda_2 \right) = \frac{2k\rho}{T} \nabla \cdot \left(\frac{\nabla T}{T} \right) \quad (31)$$

Les conditions aux limites applicables à l'équation 31 dépendent de celles de la température : si cette dernière est imposée, l'équation 32 s'applique. Si la densité de flux thermique est imposée, c'est l'équation 33 qui doit être appliquée ($\partial/\partial n$ étant la dérivée normale au bord du domaine) :

$$\lambda_2 = 0 \quad (32)$$

$$\frac{\partial \lambda_2}{\partial n} = \frac{2\rho C_p}{T^2} \frac{\partial T}{\partial n} \quad (33)$$

Une quarantaine de simulations ont été effectuées avec de l'air entrant à $T_{in} = 300\text{ K}$, en imposant une densité de flux thermique de 1000 W.m^{-2} à la plaque chauffante et pour trois valeurs du nombre de Reynolds ($Re = 20$, $Re = 30$ et $Re = 320$). Le champ de force \mathbf{F} est appliqué dans le tiers central du canal (au-dessus de la zone chauffée). Le facteur pondérateur W_{Φ} couvre un large spectre de valeurs (de $W_{\Phi} \approx 0.54\text{ K}^{-1}$ à $W_{\Phi} \approx 1.23 \times 10^5\text{ K}^{-1}$), de façon à aborder des situations allant du cas où la dissipation visqueuse a un poids relatif significatif dans l'optimisation à des simulations où elle est a priori négligeable.

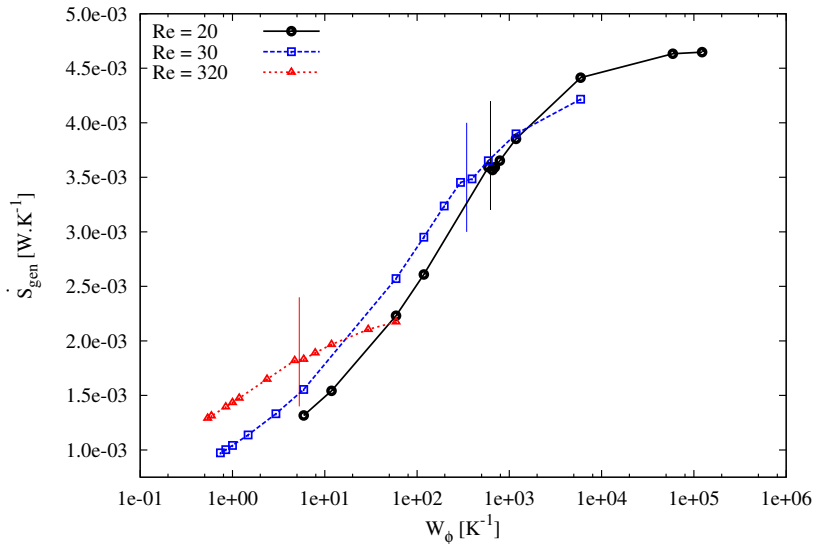


FIGURE 6 : Puissance entropique totale générée dans le canal \dot{S}_{gen} en fonction de W_{Φ}

La puissance entropique générée dans le canal dépend du nombre de Reynolds et est une fonction croissante de W_{Φ} (figure 6). Pour de petites valeurs de ce facteur (par exemple $W_{\Phi} = 1\text{ K}^{-1}$ à Reynolds 30), le gain relatif peut être élevé par rapport à une situation non optimisée (74% de réduction relative de la puissance entropique générée). Ce gain est obtenu au prix d'un accroissement de la puissance entropique générée par frottement visqueux, qui reste toutefois plusieurs ordres de grandeur inférieure à la génération d'entropie liée à la conduction de chaleur (figure 7).

Une irrégularité apparaît dans les courbes de génération d'entropie et est matérialisée dans la figure 6 par des lignes verticales. Cette irrégularité est également visible pour la puissance entropique générée par frottement visqueux (figure 7, surtout à $Re = 20$ et $Re = 30$) et une analyse des autres grandeurs dans le canal, comme les vitesses et températures maximales ou encore la dissipation visqueuse totale, fait également apparaître le même phénomène de rupture.

Cette irrégularité est concomitante à un changement de régime dans l'écoulement, correspondant à une transition entre des profils de vitesse (figure 8) allant de peu à très perturbés par rapport au cas où aucune optimisation n'est pratiquée (et aucun champ de force volumique appliqué). Les champs de vitesse très perturbés correspondent à de petites valeurs du facteur de pondération (par exemple, lorsque $W_{\Phi} = 296\text{ K}^{-1}$ à Reynolds 30) et il en est de même pour les champs de température et de puissance entropique générée par conduction de la chaleur ou par frottement visqueux. Pour de plus grandes valeurs (par exemple $W_{\Phi} = 394\text{ K}^{-1}$), les champs sont peu perturbés et

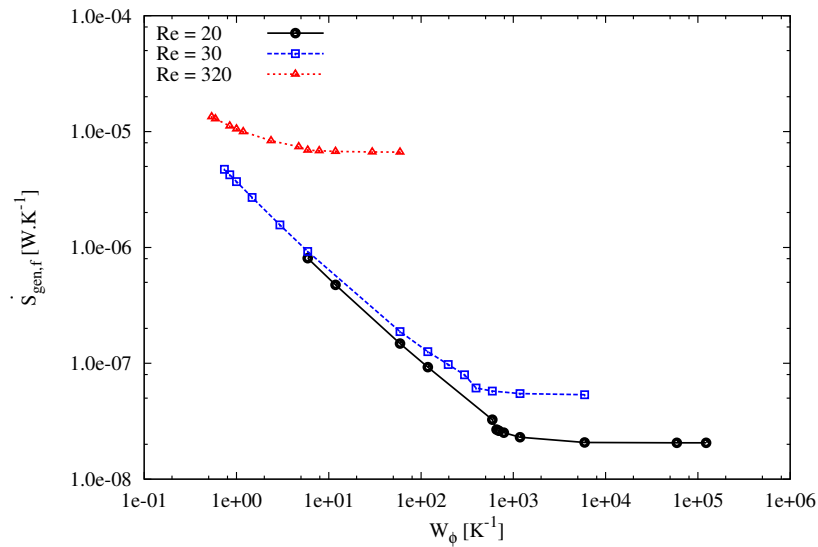


FIGURE 7 : Puissance entropique générée dans le canal du fait des frottements visqueux $\dot{S}_{gen,f}$ en fonction de W_Φ

lorsque W_Φ est très grand (par exemple au-delà de $10^5 K^{-1}$), les champs de vitesse et de température tendent vers ceux du cas non-optimisé.

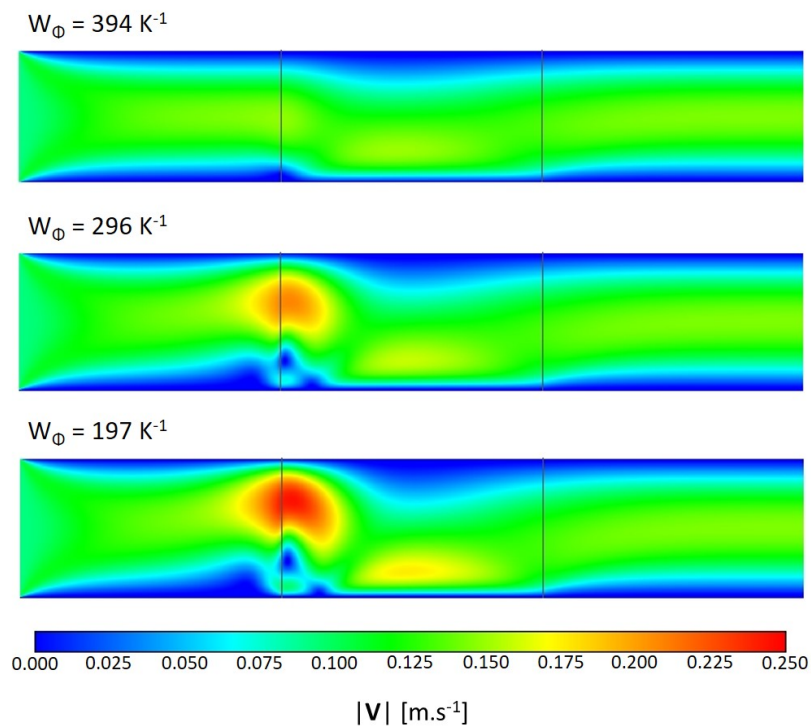


FIGURE 8 : Norme du vecteur vitesse pour $W_\Phi = 394 K^{-1}$, $296 K^{-1}$ et $197 K^{-1}$. $Re = 30$.

Les champs de vitesse obtenus par optimisation variationnelle tendent à plaquer l'écoulement vers la paroi chauffante. Par ailleurs, dès que le facteur de pondération W_Φ devient inférieur à la valeur critique qui déclenche la transition vers les régimes très

perturbés, un vortex apparaît, collectant le fluide en début de zone chauffée, avant de l'entraîner vers le centre du canal, de l'accélérer et enfin de le ramener vers le segment chauffant. Ce champ de vitesse induit un meilleur mélange dans le canal : la température maximale baisse dans le volume et son écart-type est réduit. Par ailleurs, la température de la paroi chaude (figure 9) ainsi que le profil de température en sortie du canal sont homogénéisés. Le fait que la température maximale de la plaque chauffante soit réduite constitue un avantage pour les récepteurs solaires où les matériaux constituant les parois sont soumis à rude épreuve.

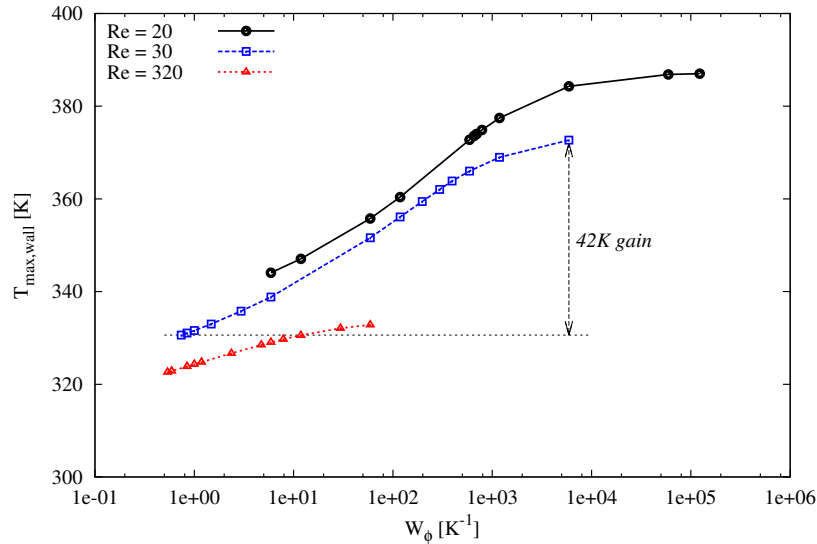


FIGURE 9 : Température maximale de la paroi chauffante [K].

Après avoir utilisé l'air comme fluide, une centaine de simulations ont été effectuées avec de l'eau (un fluide aux propriétés thermo-physiques très différentes) et ce pour deux types de processus d'advection-diffusion différents : en premier lieu, l'optimisation variationnelle a été appliquée au transfert de chaleur, exactement comme cela vient d'être décrit dans le cas de l'air (cette fois à Reynolds 10 et 20 et avec une densité de flux thermique à la paroi chauffante de 15000 W.m^{-2}). Les résultats obtenus sont qualitativement semblables à ceux présentés précédemment : la puissance entropique générée décroît quand W_ϕ diminue et les températures sont homogénéisées. Parallèlement, la dissipation visqueuse augmente et il existe une valeur critique W_ϕ induisant un changement de régime entre des champs peu et très perturbés par rapport à des situations sans optimisation. Une comparaison à même nombre de Reynolds montre que cette valeur critique n'est pas la même pour les simulations effectuées avec l'eau et avec l'air.

L'influence des conditions aux limites a également été investiguée. En particulier, la densité de flux thermique à la paroi chauffante a une influence sur la puissance entropique générée (en relation croissante) et sur la valeur critique de W_ϕ induisant la transition entre les régimes peu et très perturbés : plus la densité de flux de chaleur est élevée, plus cette valeur critique est élevée. Si on fixe la valeur du facteur pondérateur W_ϕ ainsi que le nombre de Reynolds et que la densité de flux thermique imposée varie, on constate (figure 10) que la puissance entropique générée (que ce soit par conduction ou par frottement visqueux) ainsi que les vitesses et températures maximales dans le

canal sont en relation croissante avec la densité de flux thermique. Par ailleurs il existe une valeur critique de cette dernière qui induit une transition de régimes peu perturbés (pour une densité de flux inférieure à la valeur critique) à très perturbés (dès que la densité de flux critique est dépassée). Le même type de comportement est constaté lorsque c'est la vitesse en entrée du canal que l'on fait varier, en maintenant constante la densité de flux de chaleur et la valeur de W_ϕ : il existe une valeur critique de cette vitesse d'entrée qui provoque la transition de régime.

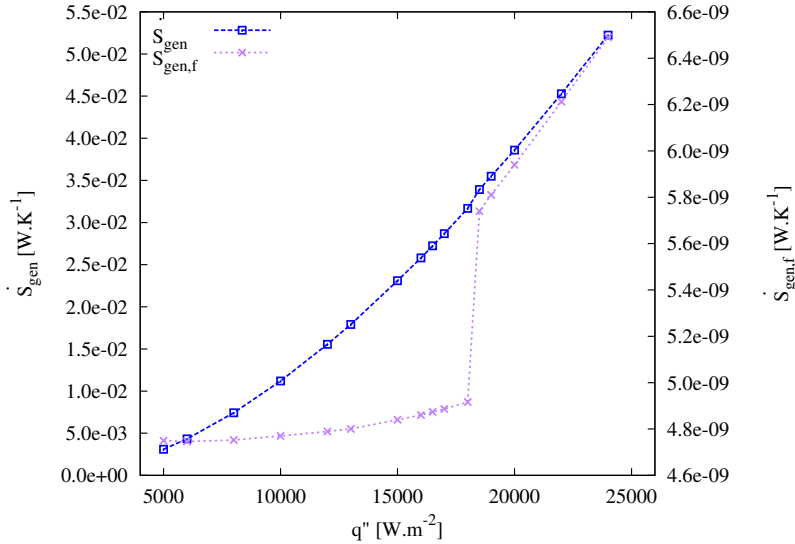


FIGURE 10 : Puissance entropique totale générée \dot{S}_{gen} ainsi que sa composante provenant du frottement visqueux $\dot{S}_{gen,f}$ en fonction de la densité de flux thermique à la paroi chauffante ($Re = 20$ et $W_\phi = 1.23 \times 10^5 K^{-1}$).

A titre de comparaison, la diffusion d'une espèce chimique minoritaire a été étudiée en conservant l'eau comme fluide majoritaire, la solution étant très diluée et considérée comme idéale. Cette fois, le tiers central de la plaque inférieure du canal est le siège de la production uniforme et constante d'une espèce minoritaire qui diffuse dans le canal tout en étant entraînée par l'écoulement. Le scalaire passif étudié n'est plus la température mais la fraction massique de l'espèce minoritaire. Le système différentiel à résoudre conserve la même forme pour l'équation de continuité et la conservation de la quantité de mouvement (Eqs. 24 et 25). Par contre, l'équation de l'énergie est remplacée par l'équation de diffusion de l'espèce minoritaire (Eq. 34) qui est similaire mathématiquement mais s'appuie sur un coefficient de diffusion dont la valeur et le processus physique sous-jacent sont différents. Par ailleurs la puissance entropique générée localement a une forme différente [48] (Eq. 35) et cela est répercuté sur la fonctionnelle objectif (Eq. 36) et le critère de Lagrange à minimiser (Eq. 37). Comme précédemment, l'application du calcul des variations permet d'obtenir l'expression du champ de force volumique (Eq. 38) ainsi que l'équation de transport du multiplicateur de Lagrange λ_2 (Eq. 39) et la condition aux limites correspondante (Eq. 40) pour les bords du domaine où une condition de von Neumann est utilisée.

$$\mathbf{V} \cdot \nabla w_1 = D \nabla^2 w_1 \quad (34)$$

$$\dot{S}_{gen}''' = \frac{\rho^2 \bar{R} D}{\bar{M}_1 \bar{M}_2 w_1 (1 - w_1) \bar{c}} (\nabla w_1)^2 + \frac{\Phi}{T} \quad (35)$$

$$J = \iiint_{\Omega} \left(\frac{\rho^2 \bar{R} D}{\bar{M}_1 \bar{M}_2 w_1 (1 - w_1) \bar{c}} (\nabla w_1)^2 + W_{\Phi} \Phi \right) d\Omega \quad (36)$$

$$J^* = \iiint_{\Omega} \left\{ \frac{\rho^2 \bar{R} D}{\bar{M}_1 \bar{M}_2 w_1 (1 - w_1) \bar{c}} (\nabla w_1)^2 + W_{\Phi} \Phi \right. \\ \left. + \lambda_2 \left[D \nabla^2 w_1 - \mathbf{V} \cdot \nabla w_1 \right] + \lambda_1 \nabla \cdot \mathbf{V} \right\} d\Omega \quad (37)$$

$$\mathbf{F} = \frac{\lambda_2}{2W_{\Phi}} \nabla w_1 + \rho \mathbf{V} \cdot \nabla \mathbf{V} \quad (38)$$

$$\nabla \cdot [\rho \mathbf{V} \lambda_2 - (-\rho D) \nabla \lambda_2] = \\ \frac{\rho^3 \bar{R} D}{\bar{M}_1 \bar{M}_2 w_1 (1 - w_1) \bar{c}} \left[\nabla \cdot \left(\frac{\nabla w_1}{w_1 (1 - w_1)} \right) + \frac{\nabla \cdot (\nabla w_1)}{w_1 (1 - w_1)} \right] \quad (39)$$

$$\frac{\partial \lambda_2}{\partial n} = \frac{\rho^2 \bar{R}}{\bar{M}_1 \bar{M}_2 \bar{c}} \frac{2}{w_1 (1 - w_1)} \frac{\partial w_1}{\partial n} \quad (40)$$

Dans ces équations, w_1 est la fraction massique de l'espèce minoritaire, D son coefficient de diffusion dans le solvant, \bar{R} est la constante (molaire) des gaz parfaits, \bar{M}_1 et \bar{M}_2 sont les masses molaires du soluté et du solvant respectivement et \bar{c} est la concentration molaire totale en [$mol.m^{-3}$], qui est supposée constante dans la solution très diluée.

Les résultats obtenus dans le cas de la diffusion d'une espèce minoritaire sont qualitativement similaires à ceux obtenus pour le transfert de chaleur. Ceci est également vrai quant à la dépendance des puissances entropiques générées en fonction de l'intensité de flux appliquée dans la zone d'échange en paroi inférieure (densité de flux thermique ou densité de flux massique suivant le type de diffusion étudié). En particulier, il existe une valeur critique de la densité de flux massique déclenchant le passage des profils de vitesse et de fraction massique du composé minoritaire de la configuration peu perturbée à la configuration très perturbée.

Ainsi, le comportement des grandeurs physiques dans l'écoulement est qualitativement semblable pour des fluides différents, des processus de diffusion différents (mais partageant des modèles mathématiques proches) et des conditions aux limites différentes (densités de flux, nombres de Reynolds). Il en est de même quant à l'existence de régimes d'écoulement plus ou moins perturbés et d'une valeur critique du facteur pondérateur de la dissipation visqueuse dans la fonctionnelle objectif. Cette valeur critique a fait l'objet de tests visant à vérifier sa stabilité au maillage (des maillages deux et trois fois plus fins ont été utilisés) ainsi que sa dépendance éventuelle aux conditions initiales : l'existence de cette valeur critique est confirmée ainsi que son ordre de grandeur qui semble par ailleurs relié à un passage d'une optimisation centrée sur la dissipation visqueuse (profils peu perturbés) à une optimisation centrée sur la puissance entropique générée par la conduction de la chaleur (profils très perturbés).

4 Puissance entropique générée dans un écoulement turbulent

On s'intéresse maintenant à un écoulement tridimensionnel en canal plan bi-périodique sur les directions longitudinale et transversale (figure 11), turbulent et statistiquement établi et stationnaire, pour un fluide dont les propriétés physiques (la masse volumique, la viscosité et la conductivité thermique) dépendent de la température qui agit désormais en scalaire actif et assure une connexion entre les équations de la quantité de mouvement et celle de l'énergie. Les plaques bordant le canal sont à des températures différentes avec un ratio mur chaud vs mur froid $T_2/T_1 = 2$ et le nombre de Reynolds de frottement moyen entre la paroi chaude et la paroi froide est $Re_{\tau m} = 180$. Le fluide est considéré comme un gaz parfait et l'approximation à bas nombre de Mach (approximation quasi-compressible) est utilisée [190] car elle correspond aux écoulements dans les récepteurs solaires où les vitesses du fluide sont petites par rapport à la vitesse du son.

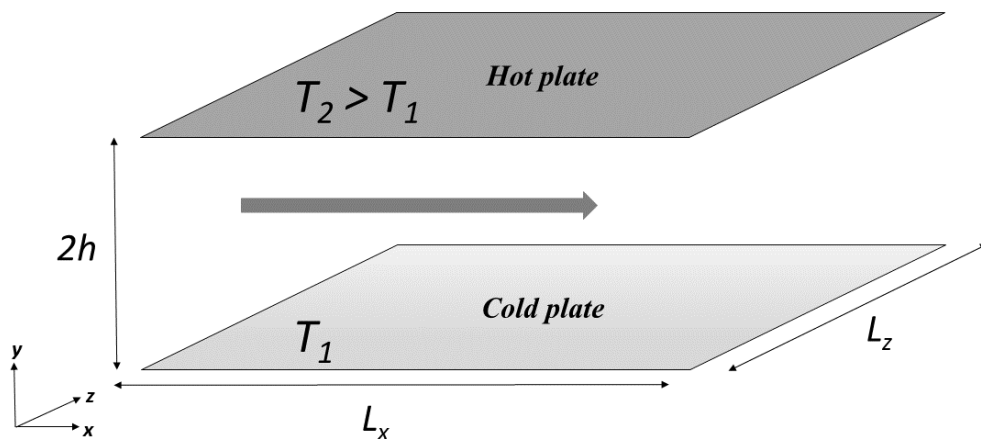


FIGURE 11 : Canal plan bi-périodique : les axes x et z sont des directions d'homogénéité

Sous ces hypothèses, les équations gouvernant l'écoulement sont les suivantes :

$$\frac{\partial \rho}{\partial t} + \frac{\partial(\rho U_j)}{\partial x_j} = 0 \quad (41)$$

$$\begin{aligned} \frac{\partial(\rho U_i)}{\partial t} + \frac{\partial(\rho U_i U_j)}{\partial x_j} &= -\frac{\partial P_{dyn}}{\partial x_i} \\ + \frac{\partial}{\partial x_j} \left[\mu \left(\frac{\partial U_i}{\partial x_j} + \frac{\partial U_j}{\partial x_i} \right) \right] &- \frac{2}{3} \frac{\partial}{\partial x_j} \left(\mu \frac{\partial U_k}{\partial x_k} \right) \end{aligned} \quad (42)$$

$$\rho C_p \left(\frac{\partial T}{\partial t} + U_j \frac{\partial T}{\partial x_j} \right) = \frac{\partial P_{th}}{\partial t} + \frac{\partial}{\partial x_j} \left(k \frac{\partial T}{\partial x_j} \right) \quad (43)$$

$$\frac{\partial P_{th}}{\partial x_i} = 0 \quad (44)$$

Dans ce système d'équations, les indices i et j obéissent à la convention de sommation d'Einstein et ρ est la masse volumique du fluide, U_i sont les composantes de sa vitesse, μ est sa viscosité dynamique, $C_p = 1005 \text{ J.kg}^{-1}\text{K}^{-1}$ sa capacité calorifique à pression constante, k sa conductivité thermique et T sa température. x_i sont les coordonnées cartésiennes et t est le temps. La pression est décomposée en deux termes : $P = P_{dyn} + P_{th}$ où P_{dyn} rend compte des variations de pression dues à la vitesse et P_{th} est une pression uniforme reliée à la masse volumique et à la température via l'équation d'état du fluide (où $r = 287 \text{ J.kg}^{-1}\text{K}^{-1}$ est la constante spécifique de l'air) :

$$P_{th} = \rho r T \quad (45)$$

La viscosité dynamique dépend de la température suivant la loi de Sutherland [221] et la conductivité thermique également car elle est dérivée de la viscosité en retenant un nombre de Prandtl constant $Pr = 0.76$:

$$\mu = 1.461 \times 10^{-6} \frac{T^{1.5}}{T + 111} \quad (46)$$

$$k = \frac{\mu C_p}{Pr} \quad (47)$$

Des simulations numériques directes de référence ont été effectuées pour deux types de conditions aux limites thermiques : dans un premier temps une simulation à températures imposées aux parois a été réalisée et les densités de flux thermiques obtenues aux parois ont été constatées. Ces densités ont ensuite été utilisées pour réaliser une simulation à densité de flux imposée aux parois afin de disposer de simulations comparables. La comparaison des statistiques de la turbulence pour ces deux simulations montre que les profils de vitesse longitudinale et normale aux parois, ainsi que les écarts-types des fluctuations des vitesses sont quasiment identiques et ne sont donc pas réellement influencés par le type de condition aux limites. Il en est de même pour la corrélation des fluctuations des vitesses longitudinales et normales aux parois. Le profil de la température est également très proche. D'autres statistiques sont plus impactées et en particulier les fluctuations de la température (figure 12) dont l'écart-type présente un profil différent suivant le type de conditions aux limites thermiques : à densités de flux imposées la variance de la température n'est plus nulle aux parois et sa valeur dimensionnelle est plus élevée du côté chaud du canal (en termes adimensionnés par la température de frottement, c'est à la paroi froide que les fluctuations sont les plus importantes).

Les deux simulations de référence ont été poursuivies, après une modification du code de thermo-hydraulique afin de calculer et de moyennner des grandeurs additionnelles comme la puissance entropique générée localement en tout point du canal, dont l'expression est la suivante :

$$\dot{S}_{gen}''' = \frac{k}{T^2} \left[\left(\frac{\partial T}{\partial x} \right)^2 + \left(\frac{\partial T}{\partial y} \right)^2 + \left(\frac{\partial T}{\partial z} \right)^2 \right] + \frac{\Phi}{T} \quad (48)$$

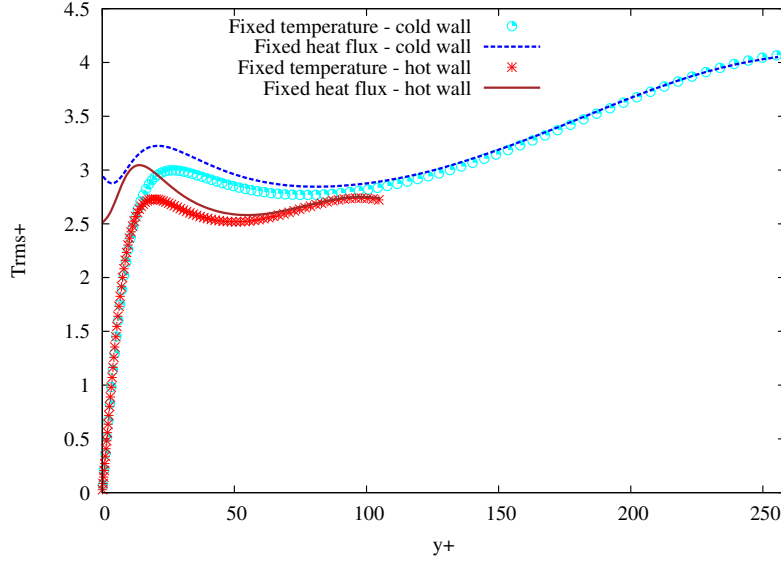


FIGURE 12 : Ecart-type des fluctuations de la température (adimensionnées par la température de frottement T_τ) en fonction de la distance adimensionnelle à la paroi la plus proche $y^+ = (y/h)Re_\tau$.

$$\Phi = \mu \left\{ 2 \left[\left(\frac{\partial U}{\partial x} \right)^2 + \left(\frac{\partial V}{\partial y} \right)^2 + \left(\frac{\partial W}{\partial z} \right)^2 \right] + \left(\frac{\partial U}{\partial y} + \frac{\partial V}{\partial x} \right)^2 + \left(\frac{\partial U}{\partial z} + \frac{\partial W}{\partial x} \right)^2 + \left(\frac{\partial V}{\partial z} + \frac{\partial W}{\partial y} \right)^2 - \frac{2}{3} \left(\frac{\partial U}{\partial x} + \frac{\partial V}{\partial y} + \frac{\partial W}{\partial z} \right)^2 \right\} \quad (49)$$

Sauf mention du contraire, la suite de cet exposé concerne la simulation à températures imposées aux parois avec un ratio de température pariétal $T_2/T_1 = 2$ et un nombre de Reynolds de frottement moyen $Re_{\tau_m} = 180$. D'autres configurations ont été étudiées et seront décrites plus loin. Les moyennes statistiques, notées $\langle . \rangle$, sont effectuées sur des plans horizontaux (xz) et dans le temps.

La moyenne de la puissance entropique générée localement en fonction de la distance au mur froid (Figure 13) est essentiellement concentrée près des parois qui sont le lieu des irréversibilités les plus fortes, et principalement dans la sous-couche visqueuse, correspondant à une distance adimensionnelle à la paroi la plus proche $y^+ = (y/h)Re_\tau \leq 5$, où Re_τ est le nombre de Reynolds de frottement de la paroi considérée. Le profil est asymétrique, la puissance entropique générée présentant des valeurs plus faibles du côté chaud du canal ainsi qu'un maximum situé à $y^+ = 3.4$ qui correspond au point de début de séparation du profil de la vitesse moyenne avec la loi de paroi $\langle U \rangle^+ = y^+$.

L'analyse de la composition de la puissance entropique générée totale $\dot{S}_{gen} [W.K^{-1}]$ montre que cette dernière est essentiellement constituée de la part correspondant à la conduction de la chaleur, la part visqueuse étant négligeable pour le ratio de température et le nombre de Reynolds étudiés. La part conductive provient pour environ 80% de la conduction verticale de la chaleur, les gradients de température horizontaux et transversaux intervenant du fait de leurs fluctuations turbulentes uniquement. Le terme majoritaire, lié au gradient vertical de la température, fait l'objet d'une décomposition en approximations successives (figure 14) afin de déterminer dans quelle mesure les

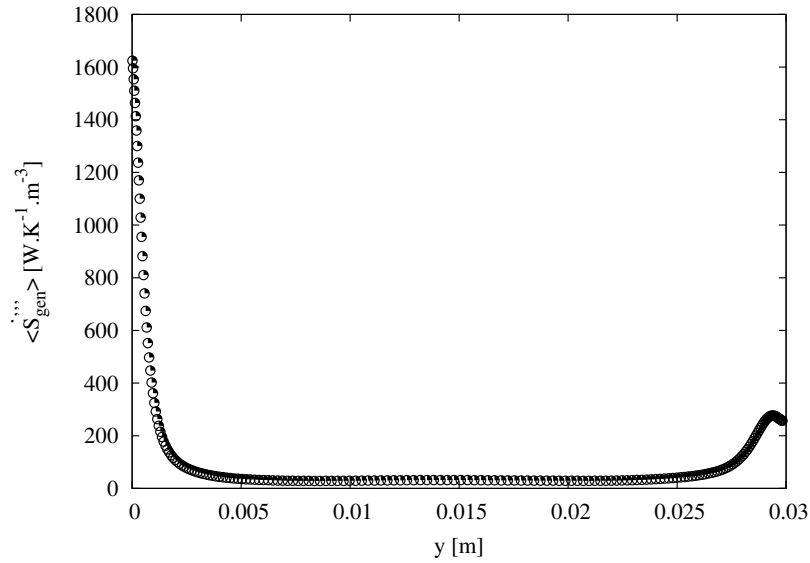
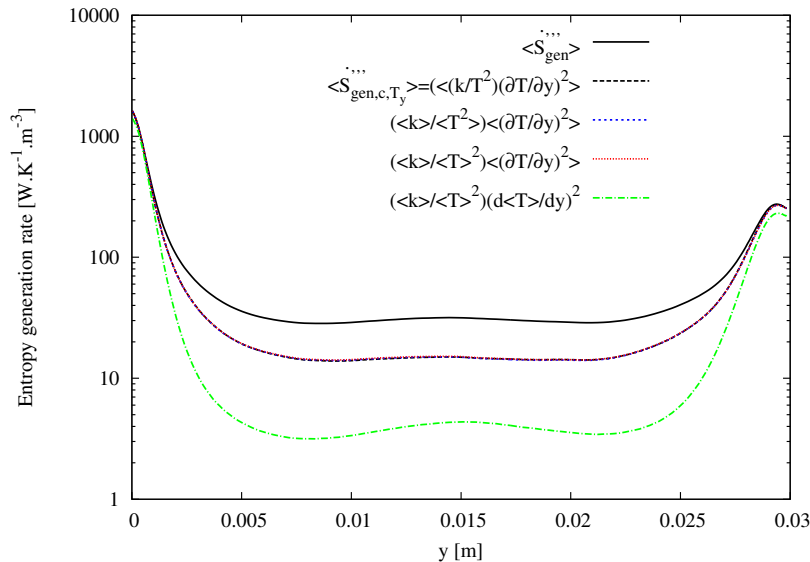


FIGURE 13 : Moyenne de la puissance entropique générée localement.

FIGURE 14 : Approximations successives la puissance entropique générée localement. Le terme noté \dot{S}_{gen,c,T_y}''' correspond à la part provenant de la conduction verticale de la chaleur.

champs moyens (de température, en particulier) peuvent être utilisés dans le calcul de l'entropie générée. Alors que la température et la conductivité thermique moyenne peuvent être employées sans encombre dans le terme k/T^2 , le gradient de la température ne peut pas être estimé à l'aide de la température moyenne sans commettre une erreur importante. L'écart-type des fluctuations turbulentes de ce gradient est significatif et contribue à un écart-type de la puissance entropique générée localement (comprenant tous les termes conductifs et visqueux, moyens et turbulents) qui est du même ordre de grandeur que sa moyenne.

L'analyse de la puissance entropique moyenne générée localement du fait de la conduction verticale de la chaleur (qui est le terme majoritaire comme indiqué précédemment) en fonction de la distance adimensionnée à la paroi la plus proche (y^+) peut

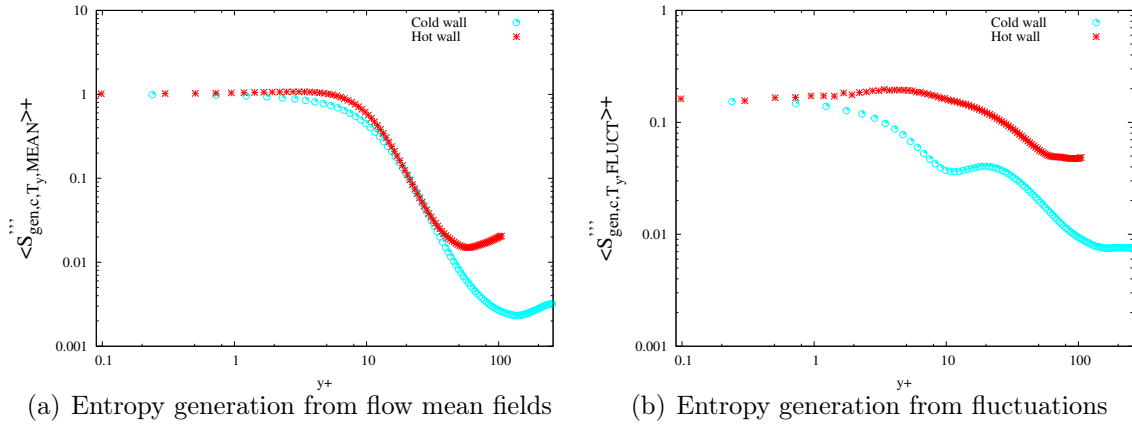


FIGURE 15 : Décomposition de la puissance entropique locale due à la conduction verticale de la chaleur (cf. Eqs. 50 and 51)

être effectuée en distinguant la contribution provenant du champ moyen de température $\dot{S}_{gen,c,T_y,MEAN}'''$ de celle qui provient des fluctuations turbulentes $\dot{S}_{gen,c,T_y,FLUCT}'''$ (embarquant les effets liés aux variances et corrélations de ces fluctuations), comme indiqué dans les équations 50 :

$$\dot{S}_{gen,c,T_y,MEAN}''' = \frac{\langle k \rangle}{\langle T \rangle^2} \left(\frac{d \langle T \rangle}{dy} \right)^2 \quad (50)$$

$$\dot{S}_{gen,c,T_y,FLUCT}''' = \langle \dot{S}_{gen,c,T_y}''' \rangle - \dot{S}_{gen,c,T_y,MEAN}'''$$

$$\langle \dot{S}_{gen,c}''' \rangle^+ = \frac{\langle \dot{S}_{gen,c}''' \rangle}{\langle q_w'' \rangle^2 / (\langle k_w \rangle \langle T_w \rangle^2)} \quad (51)$$

Les puissances entropiques adimensionnelles (normalisées à partir des lois de parois pour les champs moyens tel qu'indiqué dans l'équation 51) sont présentées à la figure 15. Les frontières des différentes sous-couches de l'écoulement turbulent ont une incidence sur les profils correspondants. La concentration des puissances entropiques générées y est apparente dans la sous-couche visqueuse. La part liée au champ moyen de la température (figure 15(a)) chute fortement dans les zones buffer et logarithmiques, puis cette contribution passe par un minimum local avant de remonter légèrement au centre du canal, les profils y présentant une asymétrie entre le côté chaud et le côté froid. En effet, l'asymétrie des conditions aux limites thermiques influence la position de la fin de la zone logarithmique qui est située aux alentours de $y^+ = 70$ du côté chaud et $y^+ = 150$ du côté froid. Aux parois, la part liée aux fluctuations (figure 15(b)) équivaut à environ 20% de la puissance entropique générée localement due à la conduction verticale de la chaleur. Elle présente une asymétrie plus prononcée entre le côté chaud et le côté froid dans lequel une oscillation apparaît à l'intérieur de la zone buffer. Ce phénomène d'oscillation a également été observé dans la littérature [125] [126] sur la base de simulations d'écoulements incompressibles, en chauffage symétrique et pour lesquelles la température est un scalaire passif.

Modifier le ratio de température entre la paroi chaude et la paroi froide, tout en maintenant constant le nombre de Reynolds de frottement moyen influence les puissances entropiques générées (figure 16) : un accroissement de ce rapport induit un

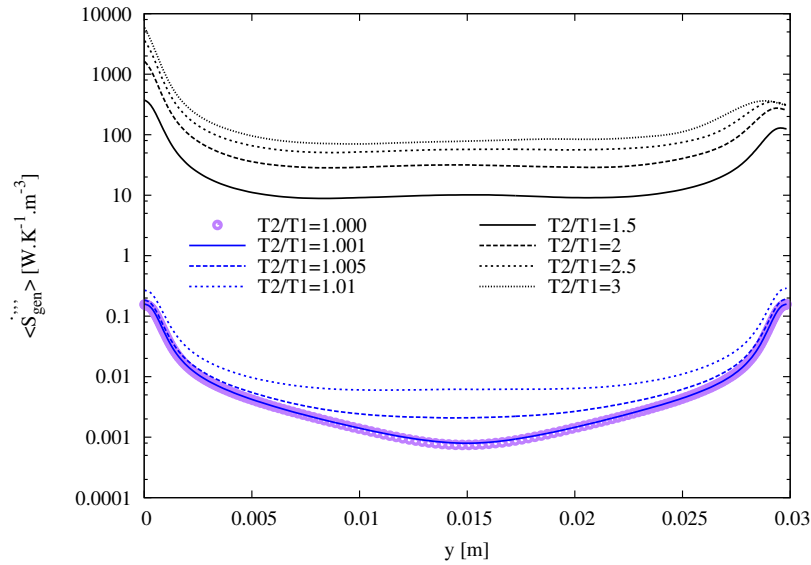


FIGURE 16 : Moyenne de la puissance entropique générée localement pour plusieurs ratios de températures T_2/T_1 entre le mur chaud et le mur froid ($Re_{\tau m} = 180$).

accroissement de ces dernières ainsi qu'une asymétrie plus prononcée entre le côté chaud et le côté froid. A partir de ratios mur chaud / mur froid relativement modestes ($T_2/T_1 \geq 1.005$) les puissances entropiques générées dans une large zone centrale du canal conservent un ordre de grandeur relativement stable. Si l'on fait varier le nombre de Reynolds de frottement moyen (entre 150 et 210) en maintenant constant le ratio de température entre le mur chaud et le mur froid, les puissances entropiques générées aux parois augmentent approximativement en proportion des nombres de Reynolds au carré et en accord avec l'influence du composant majeur (la conduction verticale de la chaleur) et des lois de parois.

Les champs instantanés de puissance entropique générée localement (présentés à la paroi froide dans la figure 17) font apparaître des structures de forme allongée dans le sens de l'écoulement. Ces structures sont d'une taille moyenne plus importante à la paroi chaude. La variabilité spatiale du champ de puissance entropique générée est apparente : sa valeur occupe à la paroi froide un intervalle allant de $200 W.K^{-1}.m^{-3}$ à $12000 W.K^{-1}.m^{-3}$ à l'instant de prise d'image, pour une moyenne d'environ $1620 W.K^{-1}.m^{-3}$

5 Conclusion et perspectives

Dans ce travail de thèse, trois configurations d'écoulement ont fait l'objet d'une étude du champ de puissance entropique générée, toutes en considérant des convections forcées en présence de gradients de température et de conditions aux limites thermiques asymétriques. En premier lieu, la puissance entropique générée dans la couche limite laminaire d'un fluide rencontrant une plaque qui va le cisailer et le chauffer a été effectuée en termes locaux, surfaciques et intégrés entre deux positions le long de la plaque. L'influence du type de conditions aux limites thermiques (température imposée vs densité de flux de chaleur imposée) a été étudiée. De même, la dépendance des puissances entropiques générées locales et totales ainsi que leurs compositions ont été examinées,

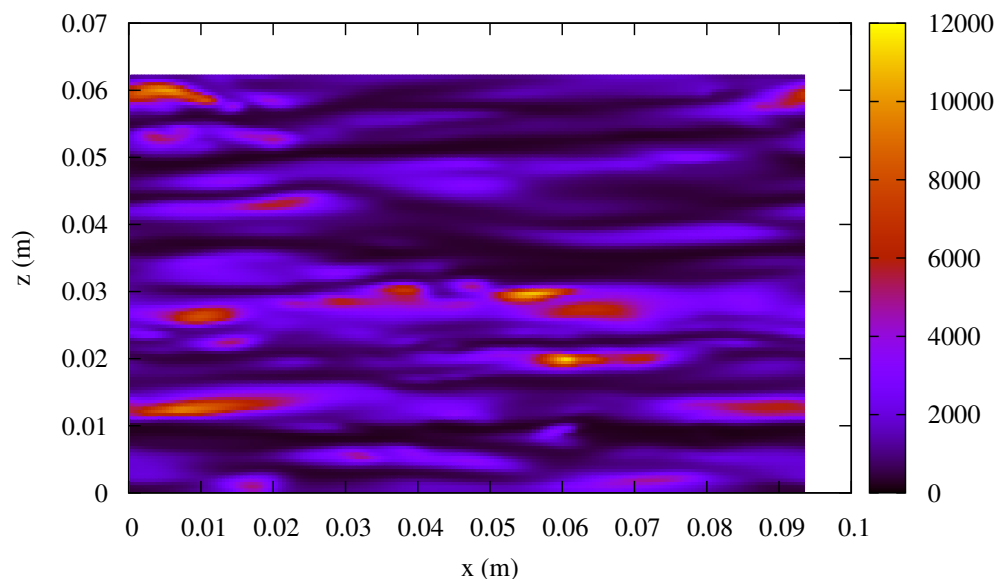


FIGURE 17 : valeur instantanée de la puissance entropique générée localement au mur froid $W.K^{-1}.m^{-3}$.

en fonction du nombre de Reynolds local et du ratio thermique adimensionnel τ égal au rapport de la température de la paroi à l'écart de température entre cette dernière et le fluide entrant. Lorsque la puissance thermique échangée entre la plaque et le fluide est fixée (à partir d'une distance donnée au bord d'attaque), la puissance entropique totale présente un minimum pour une valeur optimale du facteur thermique τ_{opt} . La position de cet optimum n'est pas la même suivant que la plaque est à température ou à densité de flux thermique imposée. Dans ce dernier cas, l'optimum dépend également de la puissance thermique échangée et du point de départ de l'intégration de la puissance entropique le long de la paroi. Lorsque l'écart de température paroi/fluide est important relativement à la température de la plaque (une situation présente dans les récepteurs solaires), réduire cet écart peut apporter une diminution significative de la puissance entropique générée.

Dans une seconde étude, le calcul des variations a été appliqué à un écoulement interne en canal plan dont un tiers d'une des parois chauffe le fluide avec une densité de flux thermique uniforme et constante. Le but est de trouver des champs de vitesse minimisant la puissance entropique générée par conduction de la chaleur (très largement majoritaire dans les cas de figure étudiés) tout en prenant en compte la dissipation visqueuse totale via un facteur pondérateur nommé W_{Φ} . Les champs de vitesse, de température et de puissance entropique générée par conduction et par frottement visqueux ont été étudiés. Plusieurs nombres de Reynolds ont été utilisés et l'influence de la densité de flux thermique imposée à la paroi a également été analysée. Les champs de vitesse obtenus par optimisation variationnelle conduisent à une puissance entropique générée totale inférieure aux cas non optimisés et ce d'autant plus que W_{Φ} est petit. La température est également plus homogène dans le volume de l'écoulement,

sur la plaque chauffante et en sortie du canal. La température maximale de la plaque chaude est abaissée, ce qui constitue un avantage dans le cas des récepteurs solaires pour lesquels les hautes températures et leurs variations induisent des contraintes thermomécaniques et chimiques pouvant endommager les matériaux constituant les parois. Il existe une valeur critique du facteur de pondération $W_{\mathcal{F}}$ déclenchant la transition depuis des profils de vitesse et de température peu perturbés par rapport à une situation sans optimisation vers des champs très perturbés et la présence de vortex. Les résultats décrits brièvement ci-dessus sont qualitativement communs pour différents fluides, différents nombre de Reynolds et conditions aux limites à la paroi d'échange, et d'autres processus d'advection-diffusion, comme la diffusion d'une espèce chimique minoritaire depuis le tiers inférieur du canal, la fraction massique de cette espèce devenant le scalaire transporté au lieu de la température.

Dans la troisième étude, des simulations numériques directes d'un écoulement quasi-compressible turbulent et établi en moyenne ont été effectuées pour un fluide dont les propriétés dépendent de la température, dans un canal plan bi-périodique. Le ratio de températures entre la paroi chaude et la paroi froide est $T_2/T_1 = 2$ et le nombre de Reynolds de friction moyen $Re_{\tau_m} = 180$. L'étude de l'influence du type de condition aux limites thermique (températures vs densité de flux thermique imposée aux parois) sur les statistiques de l'écoulement démontre que les fluctuations de la température présentent un profil différent : elles sont non nulles aux parois lorsque la densité de flux est imposée et plus élevées du côté chaud. La puissance entropique générée localement est essentiellement concentrée près des parois et son profil est asymétrique, le côté froid étant le siège de plus d'irréversibilités. Par ailleurs les transitions entre sous-couches turbulentes (visqueuse, buffer, logarithmique et externe) se reflètent dans le profil de la puissance entropique générée provenant du champ moyen de la température ainsi que sur celui de la part provenant des fluctuations turbulentes. L'étude des différentes approximations de la puissance entropique générée montre que les fluctuations du gradient de la température ne peuvent pas être négligées, l'écart-type relatif en étant élevé. Augmenter le ratio de températures entre le mur chaud et le mur froid contribue à accroître la puissance entropique générée mais également l'asymétrie de son profil. L'accroissement du nombre de Reynolds de frottement moyen a également pour effet d'augmenter les puissances entropiques générées aux parois.

Chacun des trois volets qui viennent d'être résumés peut bénéficier de travaux complémentaires. La compressibilité et la thermo-dépendance du fluide pourraient ainsi être prises en compte dans le modèle de la couche limite laminaire ou encore dans la procédure d'optimisation variationnelle afin d'en analyser l'effet en comparant les champs obtenus. La valeur critique du coefficient de pondération $W_{\mathcal{F}}$ peut également bénéficier de travaux complémentaires (mathématiques par exemple). Il existe probablement un potentiel d'amélioration des récepteurs solaires, lié à la réduction de la puissance entropique qui y est générée via une meilleure homogénéisation du champ de température, en s'inspirant des champs de vitesse proposés par l'optimisation variationnelle : il serait ainsi intéressant d'utiliser les simulations numériques directes d'écoulements turbulents s'approchant de ces champs de vitesses tout en conservant les caractéristiques particulières aux récepteurs solaires (forte anisothermie et température agissant en scalaire actif du fait de la thermo-dépendance du fluide, asymétrie des conditions aux limites thermiques et quasi-compressibilité de l'écoulement).

Acknowledgements

This work was funded by the French "Investments for the future" ("Investissements d'Avenir") programme managed by the National Agency for Research (ANR) under contract ANR-10-LABX-22-01 (Labex SOLSTICE) and the European Union's Horizon 2020 research and innovation programme under grant agreement Number 654663, SOLPART project. This work has benefited from the HPC resources of GENCI-CINES (Grants A0022A05099 and A0042A05099). The author thanks the French CEA for providing the CFD software (TrioCFD).

The author would like to thank his thesis directors for their advice and assistance throughout this work and especially Françoise Bataille for her unfailing scientific and human support, always efficient, relevant, attentive and positive. Gilles Flamant's profound scientific experience was of great help. He allowed this thesis to exist and created the decisive scientific contacts with our colleagues at the University of Tianjin. Adrien Toutant has always been present to discuss and untangle in particular the difficult technical points. Pierre Neveu brought his rigor and interest to go further by questioning the foundations.

The author also thanks the members of the thesis follow-up committee for their attentive listening and their advice and constructive remarks. The referees are thanked for the time they devoted to reading the manuscript and for the relevant remarks and criticisms they provided. Likewise, the author thanks the members of the jury for their listening, their interest in the thesis work, their questions and the improvements and extensions they suggested. The writing of the thesis manuscript and its defense were, thanks to them, an enriching moment.

The author appreciated his stay in the PROMES laboratory and thanks his fellow students and in particular Dorian Dupuy with whom he was able to share a lot and in particular his taste for precision and questioning in theoretical physics. These thanks are also addressed to the computer team with its formidable and always positive efficiency, to the researchers, professors, technicians, members of the administration and management team, postdoctoral researchers, PhD students, ATER and trainees with whom conversations and exchanges have always been pleasant and enriching. Likewise, the Languedoc-Roussillon delegation of the CNRS, the University of Perpignan Via Domitia, its Doctoral School and University Library as well as the Sup'ENR school are thanked for their professionalism and the welcome they have given to the author.

Finally, it was a pleasure to teach numerical methods to the students of the University of Perpignan and the Sup'ENR school: research and teaching are two mutually enriching activities.

Table of contents

Résumé en français	ii
1 Introduction	iii
2 Puissance entropique générée dans une couche limite laminaire	v
3 Optimisation variationnelle d'un écoulement interne	xi
4 Puissance entropique générée dans un écoulement turbulent	xviii
5 Conclusion et perspectives	xxiii
Acknowledgments	xxvii
General introduction	1
1 Context and objectives	3
1.1 Context	3
1.1.1 Energy consumption and renewable energies	3
1.1.2 Concentrated solar plants and solar receivers	5
1.2 General objectives	11
1.3 General governing equations	14
1.3.1 The Navier-Stokes equations	14
1.3.2 The entropy production rate equation	19
2 Entropy production rates in the laminar boundary layer	23
2.1 Introduction	23
2.2 The boundary layer flow governing equations	24
2.2.1 From the Navier-Stokes to the boundary layer equations	25
2.2.2 The similarity equations of the boundary layer	28
2.3 The entropy generation rate equations	29
2.3.1 Entropy production rate equations for an isothermal plate	29
2.3.2 Entropy production rate equations for an isoflux plate	31
2.3.3 Marginal viscous entropy production rates	32
2.4 Physical and numerical model	32
2.5 Results	34
2.5.1 Local entropy production rates	35
2.5.2 Surface entropy production rates	37
2.5.3 Total entropy production rates	39
2.6 The relative importance of the viscous dissipation function	43
2.7 Conclusion and perspectives	51

3	Variational optimization of the internal flow	53
3.1	Convective heat transfer in a gas flow	53
3.1.1	Introduction	53
3.1.2	The governing equations of the flow	54
3.1.3	The entropy production rate equations	55
3.1.4	The variational problem	55
3.1.5	Physical and numerical model	57
3.1.6	Results	57
3.1.7	Conclusion	71
3.2	Application to different advection-diffusion situations	73
3.2.1	Introduction	73
3.2.2	Governing equations	74
3.2.3	Variational problem	75
3.2.4	Physical and numerical setup	77
3.2.5	Heat transfer	78
3.2.6	Mass transfer	86
3.2.7	Robustness of the flow regime transition	89
3.2.8	Conclusion	91
3.3	Conclusion and perspectives	92
4	Entropy generation rates in the turbulent flow	93
4.1	Reference simulations and influence of the thermal boundary condition type	93
4.1.1	Introduction	93
4.1.2	The governing equations of the low Mach flow	95
4.1.3	Physical and numerical model	96
4.1.4	Results	98
4.1.5	Conclusion and perspectives	105
4.2	Analysis of the entropy generation rate in the turbulent flow	107
4.2.1	Introduction	107
4.2.2	Mean and turbulent entropy production rates	107
4.2.3	Influence of the hot to cold wall temperature ratio	116
4.2.4	Influence of the mean friction Reynolds number	116
4.2.5	RMS and correlations	116
4.2.6	Influence of the thermal boundary condition type	120
4.2.7	Instantaneous local entropy generation rates	121
4.2.8	Influence of mesh definition	124
4.2.9	Conclusion	125
	General conclusion	127
	Appendices	129
A	Derivation of the equations of the second Lagrange multiplier and the volume force field	131
B	DNS characteristics	133
	Nomenclature	139

List of figures	145
List of tables	147
Bibliography	168

General introduction

This thesis work is part of research aimed at improving the performance of concentrated solar power plant receivers in which fluid flows are submitted to large temperature gradients and asymmetric thermal boundary conditions. The context and the aims of the study are described in chapter 1 along with the general governing equations of the analyzed flows.

One way to address the improvement of solar receivers consists in analyzing the useful power lost due to thermal and viscous irreversibility by studying the entropy generation rate within the flow. Three different approaches are adopted and presented in the following chapters.

In chapter 2, a detailed study of the entropy generation rates and their minimization in the laminar boundary layer of a heated and sheared fluid is described. The effect of the thermal boundary condition type (fixed temperature vs fixed heat flux density at the plate) on the local and integrated entropy generation rates is analyzed along with the influence of the relative temperature gap between the heated plate and the incoming fluid.

In chapter 3, a flat plate channel flow is considered, the fluid being heated from a part of one of the plates with a constant and uniform heat flux density. Velocity field patterns are found by using the calculus of variations to minimize an objective functional directly related to the entropy generation rate in the channel. The resulting velocity, temperature and entropy generation rate fields are discussed along with the influence of the boundary conditions.

Chapter 4 is dedicated to the study of flow statistics and entropy generation rates in a turbulent quasi-compressible flat-plate channel flow at mean friction Reynolds number 180 submitted to a hot to cold wall temperature ratio $T_2/T_1 = 2$. The fluid viscosity and thermal conductivity vary with the temperature. The influence of the thermal boundary condition type is analyzed. The statistics of the mean and turbulent entropy generation rates are presented along with the influence of the mean friction Reynolds number and the wall temperature ratio.

These four chapters are followed by a nomenclature, the list of figures and tables and the bibliography.

Chapter 1

Context and objectives

This study originated in the search for the optimization of new-generation concentrating solar power plant receivers in order to contribute to more sustainable solutions to the energy challenge facing humanity. This context, as well as the general objectives pursued in this study, are detailed below. The general equations governing the flow of the fluids studied are described: they will then be adapted according to the particular situations analyzed.

1.1 Context

Research in the field of energy production is immediately placed in a global context: a brief overview of global energy production and consumption is presented below, with an emphasis on renewable energies and more particularly on solar energy with a focus on concentrated solar power plants and their receivers.

1.1.1 Energy consumption and renewable energies

Worldwide energy consumption by humanity is constantly increasing. In 2018, the growth in this demand was 2.3% and mainly concerns primary fossil energies (gas, oil and coal), which represent about 70% and contributed to an increase in CO₂ emissions of 1.7% over the same year 2018 [103]. Beyond their direct impact on the emission of greenhouse gases that contribute to the increase in the global temperature [105], fossil fuels, which are still used massively for energy production [192, 234], are non-renewable resources. The same applies to uranium used by the conventional nuclear industry [235] (the contribution of fast breeder reactors to energy sustainability being a subject of debate).

To meet this energy challenge, one of the strategic axis is to develop the use of renewable energy sources, including biomass, solar energy, wind energy, geothermal energy, hydro-power and ocean energy, that may at least partially supplement or replace conventional fossil fuels for electricity production, heating or the production of energy carriers for use in transport. Renewable energy sources can contribute to the mitigation of human driven climate change [71]. They also make it possible to diversify the energy mix and cushion the impact of shocks on conventional fuel markets (which was the case during the 1973 oil crisis, for example), but are therefore also sensitive to market prices for fossil resources [224] (in terms of competitiveness and investment profitability or risk). Renewable energies also have the advantage of being able to be used locally and

at varying scales [151]. Like any energy source, renewable energies have advantages but also disadvantages and another strategic approach to meeting the energy challenge is to reduce energy consumption, for example by using better building design and insulation techniques, more efficient appliances, by developing car-sharing and individual and collective resource-saving attitudes and by improving the efficiency of energy source collection, transformation and distribution.

Renewable energies are growing: in 2016, the share of renewable energies in total final energy consumption is 18.2% (10.4% when excluding the traditional use of biomass), growing by +2.3% over the period from 2005 to 2015 mainly in the power sector (renewable heating or cooling and biofuels grow slowly) [203]. In the European Union, the share of renewable sources was 17.5% of the gross final energy consumption in 2017, compared to 8.5% in 2004 [75] and to be linked to the 20% target set by the EU for 2020. However, there are many barriers and challenges to the development of renewable energies. For example, the intermittent nature of the resource (such as sunshine or wind) may cause a variability of power generation that leads to a difficulty for interconnection with existing electricity grids: this issue can be taken into account, for example, by improving forecasts or by setting up energy storage systems [61] that will smooth production but involve more complexity and additional cost.

Costs are indeed a challenge for relatively new technologies (in their modern form, as renewable energies have long been used by traditional societies). For an investor to get a decent return on investment or payback time, the price at which energy will be sold should follow stable regulations. The primary resource, like sun radiation or wind energy may be free, but upfront capital investment required to set up a production unit can be high (although there is a decreasing trend for some onshore wind or solar PV plants for example) and may require specific financing solutions: in 2018, overnight capital cost for building a conventional gas/oil combined cycle power plant was estimated a little lower than 1000 \$/kW while it was around 1600 \$/kW for an inland wind power plant and, 2000 \$/kW for a tracking PV solar power plant and 4300 \$/kW for a solar thermal power plant [72].

Since the different energy production technologies are in competition, production costs are an essential determinant of market share increase and profitability. Initial capital cost expenditure must be supplemented by operating, maintenance and fuel costs to compare the total cost of a power plant along its lifetime. The Levelized Cost of Electricity (LCOE in Eq. 1.1) allows this comparison and also takes into account present value incomes and costs via a discount rate [214]. Several recent studies note that renewable energies can be competitive with conventional sources: this is the case for utility-scale onshore wind energy and solar PV in some scenarios [138, 104], which proves that renewable energy sector is gaining maturity.

$$LCOE = \frac{\sum_{t=1}^{t=n} \frac{I_t + OM_t + F_t}{(1+r_{disc})^t}}{\sum_{t=1}^{t=n} \frac{E_t}{(1+r_{disc})^t}} \quad (1.1)$$

In the above equation, the following costs are taken into account over the expected lifetime of the plant for each year t : Investment I_t (initial and on going), operation & maintenance OM_t and fuel F_t expenditures are included and are expressed in monetary units (e. g. USD). E_t is the electrical power generated at the output of the plant for

each year t (in kWh or MWh). All amounts are discounted (r_{disc} being the discount rate).

In the USA context, recent estimates for the LCOE of solar thermal power plant with thermal energy storage (CSP-TES) using a molten-salt power tower system are approximately $\$0.10/kWh$. This cost is for projects that are expected to come online in 2020, which represents a reduction of LCOE by half since 2010 when the LCOE for CSP-TES was around $\$0.21/kWh$ [158]. Moreover, power purchase agreements (PPAs) in late 2017 for two international power tower systems that were designed to primarily provide peaking services approached the cost target of $\$0.06/kWh$ for 2020 [78]. This reduction and the US-DOE SunShot program target is illustrated in Fig. 1.1.

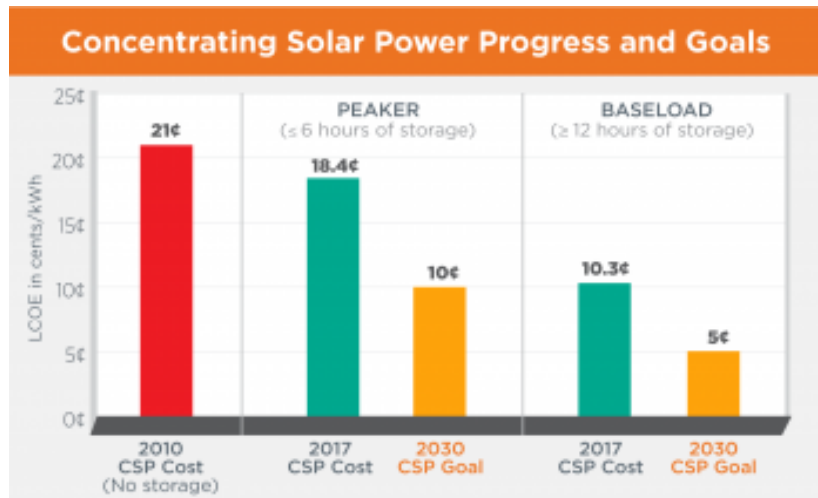


Figure 1.1: Cost reduction of solar thermal electricity [169]

The current decrease of renewable energy costs is driven by several causes among which technological improvements: in the case of CSP power, there is considerable scope for improvement in the search for more technically and economically efficient solutions. The present work is modestly part of this framework.

1.1.2 Concentrated solar plants and solar receivers

There are now two main technologies used to transform the radiation received from the sun into electricity: the direct way is to use the photovoltaic properties of semiconductor materials and will not be developed later in this presentation. The second technology, that of concentrated solar power plants (CSP), consists in using a field of mirrors judiciously arranged to collect solar radiation over a large area and concentrate it towards a receiver with a much smaller surface area (depending on the geometry of the mirrors [159], the concentration ratio ranges from approximately 30 in linear Fresnel collectors [117] to around 10000 [150] for solar furnaces or parabolic dishes). The focused solar power is then absorbed by the receiver and transferred to a working fluid (HTF: Heat Transfer Fluid) that will be used directly (in the case of water/steam for example) or via an exchanger (in the case of molten salts for example) in order to feed a thermodynamic cycle that will supply a turbine connected to a generator, the latter finally delivering electricity from the power plant. In order to cope with the intermittent nature of the solar resource, a thermal energy storage system is often interposed

between the solar field (essentially comprising the optical concentration devices and the receiver) and the thermodynamic cycle [218]. The possibility of easily storing heat and using this tank when solar radiation is low or absent (at night or during cloudy periods) is one of the advantages of solar thermal power plants. Another method of smoothing power generation and fitting electricity supply to the demand is to add a backup system using a fossil fuel that is activated when it is necessary to supplement the solar energy power (in hybrid solar gas-turbine power plants for example [232, 156]).



Figure 1.2: THEMIS Solar Power Plant [191]

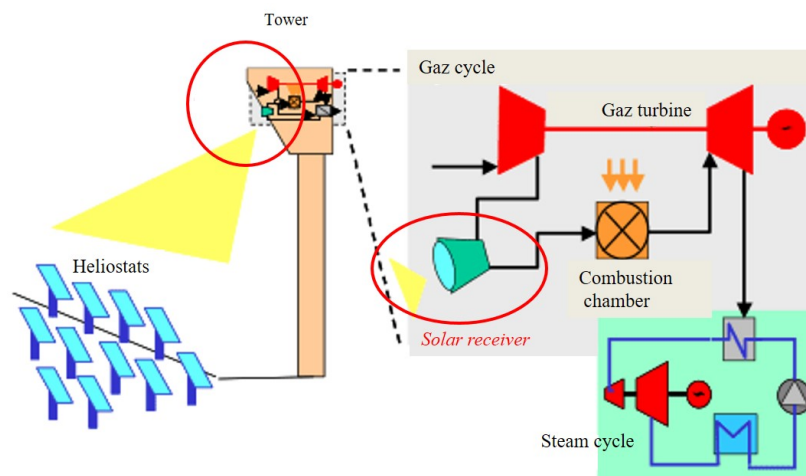


Figure 1.3: PEGASE Project [133]

There are different types of concentrated solar power plants that differ according to the geometry of the solar field, the type of heat transfer fluid, the type of thermodynamic cycle, etc. With regard to the geometry of the solar field, four main technologies are used [245]: the most widespread, called Parabolic Trough, consists of alignments

of parabolic trough mirrors that concentrate solar radiation towards linear absorber tubes in which the thermal transfer fluid flows.

Then comes the Solar Power Towers technology which is based on a field of steerable mirrors, called heliostats, that reflect the sun's rays towards the top of a tower in which a central receiver is located, where the exchange with the heat transfer fluid takes place. An example of such a configuration, intended in particular for the research work of the PROMES - CNRS UPR 8521 laboratory, such as the PEGASE project, is the THEMIS solar power plant located in Targasonne in the Catalan Pyrenees in France (Fig. 1.2): a typical research configuration consists of a solar field of about 100 heliostats covering an area of about $50m^2$ that track the sun and concentrate the solar radiation towards a receiver located at a height of about 100 meters [88]. In the PEGASE project (Fig. 1.3), pressurized air is incoming at $350\text{ }^\circ\text{C}$ and is brought to $750\text{ }^\circ\text{C}$ and then additional heat is provided by combustion to supply a gas turbine at the set temperature of about $1000\text{ }^\circ\text{C}$ regardless of sunlight. The gas thermodynamic cycle (Brayton type) is combined with a steam cycle (Rankine type) to take advantage of the temperature at the turbine outlet and improve the overall efficiency of the installation. The PEGASE project has been launched more than ten years ago. In 2019, it is developed in the form of two options funded by EC H2020 program. The POLYPHEM project that proposes a technology consisting in a solar-driven micro gas turbine (40 kW_{el}) as top cycle and an Organic Rankine Cycle (20 kW_{el}) as bottom cycle. A 2 MWh thermal storage being integrated between the two cycles. The Next-CSP project that aims to develop and integrate of a new technology based on the use of high temperature ($800\text{ }^\circ\text{C}$) particles as heat transfer fluid and storage medium. The project will demonstrate the technology at a significant size (3 MW_{th} solar receiver and 1.2 MW_{el} gas turbine).

In addition to the Parabolic Trough and Solar Tower technologies, there are also two much less common geometries: Fresnel linear reflectors, consisting of long rows of flat (or slightly curved) reflective strips that approximate a parabolic trough mirror and reflect solar radiation to a linear receiver. Finally, the so-called Parabolic Dish geometry consists of a parabolic mirror that concentrates the collected solar power towards a focal point where a Stirling engine can be placed, for example.

Several types of heat transfer fluids and working fluids are used in concentrated solar power plants. In some configurations, the same fluid is used in the solar receiver (HTF) and in the thermodynamic cycle (Working Fluid): this is the case for air for example or in systems with direct steam generation (DSG). In other cases, the heat transfer fluid flows in a primary circuit and an exchanger ensures the transfer of heat to the working fluid of the secondary circuit, which is generally using steam. The thermal transfer fluid can also be used in the thermal storage facilities (like large insulated tanks).

The two main transfer fluids are thermal oils (which are by far the majority choice for parabolic trough power plants) and molten salts (NaNO_3 and KNO_3) widely used in tower power plants. Among the qualities required for HTF are: low cost, high thermal conductivity, low viscosity, low corrosive effect on walls, low degree of degradation at high temperature, high heating capacity (for thermal storage purposes), high level of safety for the environment and the teams working in the plant. The thermal transfer fluid determines the minimum and maximum working temperatures [140]: thermal oils must not exceed approximately $400\text{ }^\circ\text{C}$. As for molten salts, their maximum working temperature depends on their composition and is between $400\text{ }^\circ\text{C}$ and $600\text{ }^\circ\text{C}$ approximately. Molten salts also have a minimum temperature below which they solidify

(Solar Salt melting point is 220 °C [236]) and are therefore no longer usable. However, the efficiency of the thermodynamic cycle will depend in particular on the high temperature of the working fluid and thermal transfer fluids are therefore studied to reach high temperatures. This is the case for molten metals, for example, but they present an explosion risk. Another track that is the subject of intensive research concerns dense suspensions of particles and circulating fluidized beds [81]. Finally, the use of air [91] an abundant and free resource, non-polluting and without safety risk (except for the management of high pressures) that can be used as HTF and Working Fluid in a gas turbine, allows temperatures above 1000 °C to be reached. Another option to achieve these high temperatures is to use Helium or supercritical CO₂ [56, 98]. The overall efficiency of a solar power plant depends synthetically on the optical efficiency of the radiation collection and concentration system η_{col} , the efficiency of the solar receiver η_{rec} (transformation of radiation to latent and/or sensitive heat) and the efficiency of the thermodynamic cycle(s) and more generally of the power block η_{pb} . The type of cycle used depends in particular on the geometry of the solar field and the thermal transfer and working fluids because these elements determine in particular the operating temperatures of the cycle and the theoretical Carnot efficiency η_c (of course, the actual efficiency of operating cycles is lower). For example, the Parabolic Dish geometry allows to reach high solar concentration and receiver temperature at the focal point and the use of a sterling cycle (in a Stirling engine) is indicated [193]. The two basic thermodynamic cycles commonly used are of the Rankine or Brayton type. In the Rankine cycle, a liquid is pressurized, heated and vaporized before expanding in a turbine to produce mechanical work that is immediately transformed into electricity and then, the fluid is cooled before starting the next cycle. In the Brayton cycle, similar steps are followed but without phase change (the fluid remains in a gaseous state throughout the cycle) and at higher temperatures. Sub-critical Rankine cycles, which are very widespread, reach yields of around 37%-42% [67]. In order to increase this efficiency, several paths are followed aiming at efficiencies of around 50%, for example: the use of super-critical Brayton (s-CO₂) or Brayton-type cycles with Helium as well as the use of several heating phases. Another approach is to combine a high temperature cycle with one or more low temperature cycles, the latter using in particular ORC (Organic Rankine Cycle) cycles.

In addition to the influence of the compound yield $\eta_{col}\eta_{rec}$ on the profitability of a concentrated solar power plant, the solar field represents a majority share of the initial capital investment (e.g. 35% to 49% for parabolic trough plants, including about 7% for the receiver, and just under 50% for tower plants, including about 15% for the receiver [106]). Each segment of the power plant deserves to be optimized and, as the orders of magnitude just mentioned show, the solar receiver plays a key role in this optimization process, particularly in tower power plants.

Areas for improvement of power tower receivers include: research into surface coatings and selective materials (with good absorptivity in the solar spectrum but also low emissivity in the infrared to limit radiation loss), definition of configurations limiting convection losses to the environment, research into materials capable of withstanding high temperatures under high flux concentrations (e.g. more than 650 °C under 1000 suns) and optimization of exchanges with the transfer fluid. Among the most important potential for cost reduction and improvement of the LCOE is the focus on defining receivers that can be operated sustainably at high temperatures [127].

Indeed, a high surface temperature for the receiver theoretically provides a higher

temperature working fluid at the inlet of the thermodynamic cycle, which will therefore have a higher efficiency. However, there are two main limiting factors to the race to high temperatures: the first concerns degradations that reduce the service life or performance of receiving surfaces due to thermo-mechanical constraints imposed on materials (especially since the intensity of concentrated solar flux can change rapidly when a cloud passes, for example) and due to chemical transformations such as surface oxidation. This is why the behavior of these materials is studied at high temperatures and why research is being conducted on compositions and surface treatments that are resistant over time. It is also interesting to look for ways to reduce the surface temperature (and equalize it as much as possible, while keeping the total heat transfer constant).

The second limiting factor comes from the following fact: the increase in surface temperature (useful to improve the thermodynamic efficiency of the downstream cycle η_{th}) also increases losses to the environment, particularly due to radiative transfers. The combined efficiency, taking into account the radiative efficiency of the receiver and that of a downstream Carnot cycle, results in a dependence on the efficiency of the CSP power plant η_{csp} in bell form (Fig. 1.4) and indicates an optimal surface temperature for a given concentration factor [130].

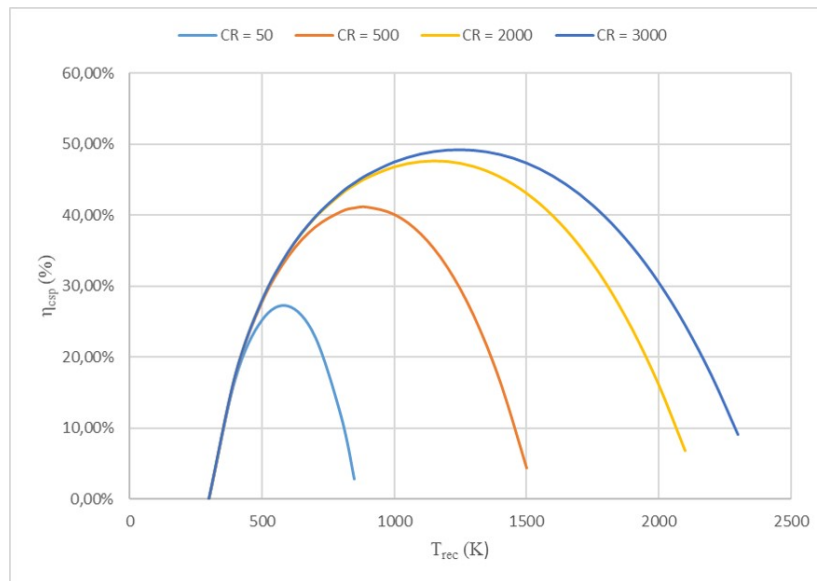


Figure 1.4: Influence of concentration ratio (CR) and the receiver surface temperature on the theoretical performance of a CSP plant

There are a wide variety of receiver technologies available to equip solar tower power plants (also known as CRS: Central Receiver Systems): they differ according to the type of thermal transfer fluid to be heated (liquid, water/steam, gas, solid particles) but also according to the flow geometry (external vs cavity and volumetric vs surface receivers).

In the external receiver configuration (this is case, for example, in the Gemasolar Thermosolar Plant, located in Spain and pictured in Fig. 1.5), the absorbing surfaces are openly exposed on the external surface (which facilitates irradiation by a solar field surrounding the solar tower) while in the case of cavity receivers, the tubes or heat exchange surfaces line the bottom of a cavity. This latter configuration imposes a polar

solar field (favorably oriented to target the entrance of the cavity) but limits radiative and convective losses in the environment, which is an advantage for high temperature receivers.



Figure 1.5: Gemasolar Thermosolar Plant [226]

Solar surface receivers (often tubular) consist of channels that carry the transfer fluid and which outer surface is irradiated by the concentrated solar flux (one illustrating example is provided in Fig. 1.6, which describes the architecture of the solar receiver of the Solar One power plant, now closed but whose principle - external cylindrical tubular geometry - has been used for the following generations of power plants like the Gemasolar Thermosolar plant already mentioned). These walls absorb some of this radiation (the losses concern the radiative emission of the surface and the convection loss with the surrounding air) and transmit it by conduction to the fluid flowing through the channels. Tubular receivers are used in molten-salt and water/steam power plants and are also designed for gas flow (air, $s\text{-CO}_2$). Volumetric receivers have a different exchange mode, mainly adapted to gases: they are made of porous materials (metallic, ceramic or silicon carbide) that are heated by the concentrated solar flux and the transfer fluid flows through this porous structure [13].

Finally, particle-based receivers are a special class and are the subject of intensive research [99]: a falling curtain of particles can be directly irradiated (free-falling particle receivers) or subjected to a more complex fall trajectory by adding obstacles that will slow them down and increase their residence time in the exposed area. Particles can also descend while rotating in a drum (rotating kiln). Finally, fluidized particles can be directly irradiated while circulating in a tube or circulate around a network of irradiated tubes and thus be heated indirectly [99].

The previous review is related to power production using solar concentrating systems. Let us notice that this technology produces primarily heat at various temperature ranges. Consequently, this heat can be used to drive chemical reactions. If the chemical reaction occurs in the solar receiver, it is also a chemical reactor (SOLPART H2020 project). Therefore, the theoretical work proposed in the next sections can be extended to solar receivers-reactors provided some additional efforts to account for the chemical kinetics.

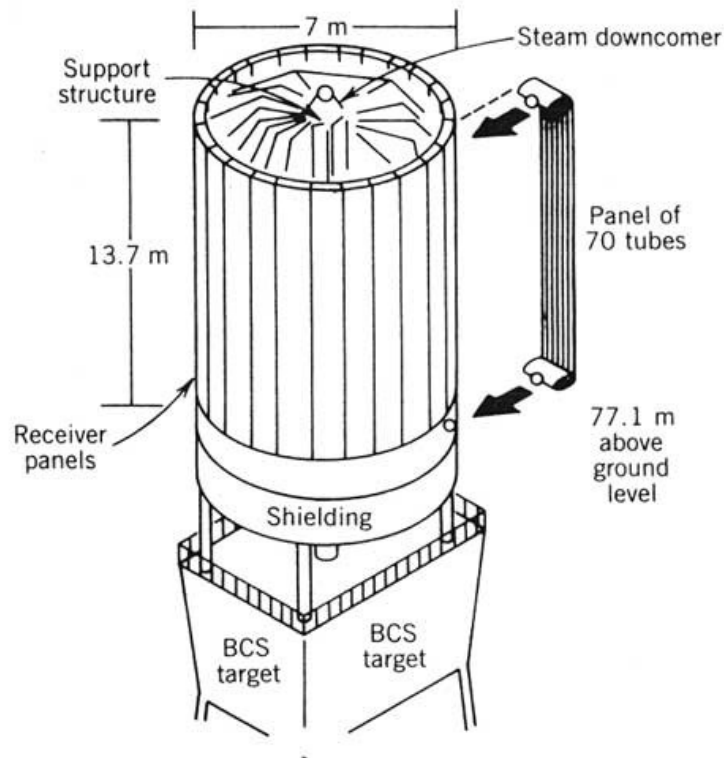


Figure 1.6: Solar One central receiver [219]

1.2 General objectives

For the reasons given in chapter 1.1.2, we are particularly interested in this thesis work in the tower power plants using air as a thermal transfer fluid and with a central surface receptor (whether external or in a cavity). To simplify, it is considered that the fluid flows between two parallel flat plates at different temperatures, one of which having its outer surface exposed to concentrated solar radiation. Some of the power received by radiation is transmitted to the fluid leaving the channel at a higher temperature but also at a lower pressure due to viscous friction within the channel.

To optimize this exchanger, it is desirable to intensify the heat exchange between the fluid and the wall without increasing the pressure drop between the inlet and outlet of the channel, because this corresponds to parasitic energy consumption. For example, let us suppose that fins are inserted inside the channel: the heat exchange surface will be extended and will promote heat exchange, but the pressure drop will also be increased due to a larger friction surface and the presence of flow obstacles. Thus, one of the optimization criteria will be improved (heat exchange) while the other will be degraded (pressure drop). One way to address this dilemma and to rationalize the trade-off between these two opposing effects, is to use a common unit of measurement to assess lost available power related to the different irreversible phenomena occurring within the flow. This common unit can be the entropy generated within the channel, as demonstrated by the research works using the Entropy Generation Minimization (EGM) method [26]. This is why the general framework of our work consists in better estimating, understanding and minimizing the entropy generation rate, also named

generated entropic power (in $[W.K^{-1}]$).

The relationship between the entropy generation rate and the lost available power can be illustrated by Gouy-Stodola's theorem [93, 94, 95] as follows: suppose that an open thermodynamic system Σ (Fig. 1.7) exchanges heat, work and matter with the environment. To simplify the point, it is assumed that heat exchanges occur with only one reservoir at room temperature T_{amb} . The first and second law of thermodynamics for this open system write (using the total enthalpy function h^t):

$$\frac{dE_{\Sigma}}{dt} = \dot{Q} + \dot{W} + \sum_{\substack{\text{inlet} \\ \text{ports}}} \dot{m}_{in} h_{in}^t - \sum_{\substack{\text{outlet} \\ \text{ports}}} \dot{m}_{out} h_{out}^t \quad [W] \quad (1.2)$$

$$h^t = h + \frac{1}{2}V^2 + gz \quad (1.3)$$

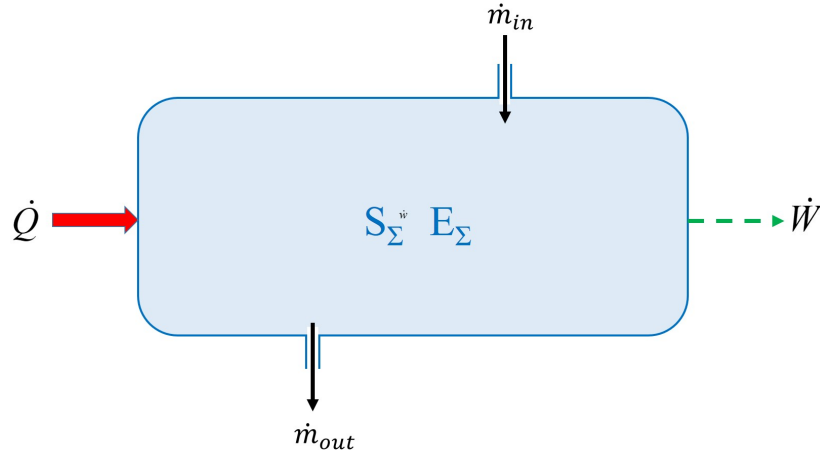


Figure 1.7: Open system Σ to illustrate the Gouy-Stodola theorem

$$\frac{dS_{\Sigma}}{dt} = \frac{\dot{Q}}{T_{amb}} + \sum_{\substack{\text{inlet} \\ \text{ports}}} \dot{m}_{in} s_{in} - \sum_{\substack{\text{outlet} \\ \text{ports}}} \dot{m}_{out} s_{out} + \dot{S}_{gen} \quad [W.K^{-1}] \quad (1.4)$$

$$\dot{S}_{gen} \geq 0 \quad (1.5)$$

One can deduce from the above equations that the maximum power that can be obtained from this system, is reached when $\dot{S}_{gen} = 0$. Let us suppose that the system Σ produces work (\dot{W} is negative) and let us define $\dot{W}^+ = -\dot{W}$ this power accounted positively. The maximum deliverable power is (by eliminating \dot{Q} between equations 1.2 and 1.4):

$$\dot{W}_{max}^+ = \sum_{\substack{\text{inlet} \\ \text{ports}}} \dot{m}_{in} (h_{in}^t - T_{amb} s_{in}) - \sum_{\substack{\text{outlet} \\ \text{ports}}} \dot{m}_{out} (h_{out}^t - T_{amb} s_{out}) - \frac{d(E_{\Sigma} - T_{amb} S_{\Sigma})}{dt} \quad (1.6)$$

The power lost due to irreversibilities is the difference between the maximum power \dot{W}_{max}^+ and the actual power delivered by the system \dot{W}_{actual}^+ (the opposite of the negative value \dot{W}):

$$\dot{W}_{lost}^+ = \dot{W}_{max}^+ - \dot{W}_{actual}^+ = T_{amb} \left(\frac{dS_{\Sigma}}{dt} - \frac{\dot{Q}}{T_{amb}} - \sum_{\substack{inlet \\ ports}} \dot{m}_{in} s_{in} + \sum_{\substack{outlet \\ ports}} \dot{m}_{out} s_{out} \right) \quad (1.7)$$

According to Eq. (1.4), the quantity in brackets in Eq. (1.7) is equal to the entropy generation rate, therefore:

$$\dot{W}_{lost}^+ = T_{amb} \dot{S}_{gen} \geq 0 \quad (1.8)$$

Thus, the lost available power is equal to T_{amb} multiplied by the entropy generation rate in the system Σ . This magnitude is always positive. If the system receives work, \dot{W}_{lost}^+ represents the amount of additional power that actually had to be done on the system compared to the lower value that would correspond to a reversible exchange. An accounting of the maximum useful power that can be obtained from a system as well as the available power lost during thermodynamic transformations can also be systematically developed using the notion of exergy, which expression $h_{in/out}^t - T_{amb} s_{in/out}$ appears in Eq.1.6 (the rate of exergy destruction being proportional to the rate of entropy generation). Comparing reversible and irreversible processes can be complex, especially in an unsteady and non-cyclical situation. In the above discussion, it is assumed that the processes to be compared differ only in their levels of irreversibility and in the values of the thermal power \dot{Q} exchanged with the surrounding environment and the power produced \dot{W}^+ , all other things being equal. Real-life situations can be more complex. For example, several thermal reservoirs may be in contact with the system and the trajectories followed by E_{Σ} and S_{Σ} may be different over time. Similarly, the outgoing flows may differ between the two processes being compared. Nevertheless, entropic (and exergetic) analysis remains applicable to these more complex situations as described in [38].

The calculation of the entropy generation rate within a flow can be carried out according to two different approaches: first, the locally generated entropic power can be calculated at each point of the studied volume (in $[W.K^{-1}.m^{-3}]$) and then an integration can be performed to calculate the total generated entropic power. This approach enables to map the entropy generation and identify the channel regions corresponding to the most important productions. It also makes it possible to analyze the distribution of entropy generation according to its composition (for example: its share linked to thermal transfer and its share linked to viscous friction). The second approach consists in starting from an entropy balance by considering the flows and quantities at the boundaries of the domain (for example, the heat flux density and the temperature) and the evolution of the total entropy over time (if the flow is not steady) in order to deduce the total entropy generation rate. This approach is often based on correlations because the values of temperature and velocity gradients at the walls, for example, depend on the nature of the flow.

Once the total entropy generation rate is known, it is useful to examine its dependence on various flow parameters, which may be geometric (e.g. the diameter of a tube or the shape of its cross-section), dynamic (e.g. Reynolds number), thermal (e.g. the temperature difference between the hot plate and the cold plate). In addition, by adding energy constraints (e.g. the total thermal power exchanged), optimal parameter values can be sought (i.e., minimizing the total entropy generation rate).

The aims of the present study are: to calculate the locally generated entropic power field, to analyze its distribution in the flow space and its composition, to study how it is influenced by boundary conditions (especially thermal) and to investigate how the total entropy generation rate can be minimized.

However, the complexity of the flows encountered in solar receivers requires that the difficulty be split, even if one adopts a simplified geometry. In an airborne surface receiver, the flow is generally turbulent, compressible, subject to high thermal gradients and asymmetric boundary conditions, and the fluid is thermo-dependent [8, 9, 29, 211, 63, 68, 69]. That is why three situations have been studied in this thesis work: each of them sheds a different light on the problem of entropy production in a non-isothermal flow subjected to asymmetric thermal boundary limits, while also embedding its own simplifications in relation to reality.

In the first configuration, developed in chapter 2 the laminar boundary layer is used as a sandbox to study the influence of the thermal boundary conditions by allowing easy variation of the parameters in the context of a simplified flow model that can be used as a reference when dealing with more realistic flows. This work has been published in the *Journal of Thermophysics and Heat Transfer* [12] and much of the content has been included in the present thesis, with some additional details on the derivation of the boundary layer equations and on a discussion on the order of magnitude of the viscous dissipation function.

In chapter 3 a variational optimization is performed for an internal flow in a channel in which part of one of the two walls is heated with an imposed heat flow density. The objective here is to examine a method whose field of application is much broader than the optimization of solar receivers.

Finally, in chapter 4, the analysis of a turbulent quasi-compressible flow in a bi-periodic plane channel for a thermo-dependent fluid is performed, in order, on the one hand, to know the influence of the thermal boundary condition (fixed wall temperatures vs fixed wall heat flux densities), which has been published in the *Journal of Heat and Fluid Flow* [11] and, on the other hand, to lay the foundations for a statistical analysis of the entropy generation rate in a thermally asymmetric flow.

1.3 General governing equations

The general equations that will serve as a basis for the models presented below are explained. First of all, the Navier-Stokes equation system is the basis for the numerical calculation of flows. In addition, the general equation of the local entropy generation rate at a flow point is also described.

1.3.1 The Navier-Stokes equations

Let us consider the flow of a homogeneous single-phase and non-reactive fluid without any volumetric energy source (corresponding, for example, to the direct absorption of radiation by the fluid) and within the framework of classical mechanics (macroscopic and non-relativist). The local equations of a the flow are recalled below. They are expressed in Cartesian coordinates in a Galilean reference frame and use the Einstein convention for repeated indexes. These equations can be obtained either by considering a small fluid parcel (material domain or material region) in motion and by using

material or substantial derivatives and the Leibnitz-Reynolds transport theorem [189], or by considering a small fixed control volume and by applying integral balances (i.e: the variation of an additive quantity in a control volume comes from the input and output flows as well as from possible source terms) [27].

$$\frac{\partial \rho}{\partial t} + \frac{\partial(\rho u_j)}{\partial x_j} = 0 \quad (1.9)$$

$$\frac{\partial(\rho u_i)}{\partial t} + \frac{\partial(\rho u_i u_j)}{\partial x_j} = \rho f_i + \frac{\partial \sigma_{ij}}{\partial x_j} \quad (1.10)$$

$$\frac{\partial(\rho e_M)}{\partial t} + \frac{\partial(\rho e_M u_j)}{\partial x_j} = \rho u_j f_j + \frac{\partial(\sigma_{ij} u_i)}{\partial x_j} - \frac{\partial q_i}{\partial x_i} \quad (1.11)$$

In this set of equations, x_i are the Cartesian coordinates ($i \in \{1, 2, 3\}$) of the point where all quantities are evaluated at the time t : u_i are the components of the velocity, ρ is the density, f_i are the components of the specific volume force (in N kg^{-1}), σ_{ij} are the components of the stress tensor, e_M is the specific total energy (in J kg^{-1}) and q_i are the components of the heat flux vector. The specific mechanical energy here is the sum of the specific internal energy and the specific kinetic energy (the potential energy from conservative forces is treated as mechanical powers in the term $\rho u_i f_i$). The stress tensor can be broken down into two parts: a spherical part showing the local thermodynamic pressure P and a part related to the stresses from the fluid movement, called the viscous stress tensor τ_{ij} (δ_{ij} being the Kronecker delta):

$$\sigma_{ij} = -P\delta_{ij} + \tau_{ij} \quad (1.12)$$

These equations are already very general and correspond to the conservation of mass (eq. 1.9), the conservation of momentum or the fundamental equation of dynamics (eq. 1.10) and the first principle of thermodynamics (eq. 1.11). However, they are based on the continuous medium assumption described below. In addition, it is possible to reduce the number of fundamental principles used to deduce equations 1.9 to 1.11 because the conservation of mass as well as that of momentum can be derived from the first principle of thermodynamics by imposing the Galilean invariance as described in [114].

Although a fluid may appear as a continuous medium from a macroscopic point of view, it is actually composed of atoms and molecules in endless relative motion. A first way to study the motion of a fluid can be to use the equations of motion of each individual atom or molecule (e. g. in the molecular dynamics approach) and then to use statistical methods to obtain information on the macroscopic behavior of the fluid (kinetic and statistical fluid theory). However, it is often not necessary to go to the molecular scale to obtain useful information because there is a general interest in the movement of parts of the fluid domain (named fluid parcels) that are small compared to the dimensions of the equipment (flow channel, turbine blades, etc.) but which are already composed of a very large number of molecules. This is why the so-called continuous medium approach (the continuum hypothesis) is commonly adopted and it is considered that all useful quantities (density, velocity, temperature, etc.) can be assigned to each point of the fluid domain and derived in order to calculate gradients, divergences, curl, for example (except at possible discontinuity points, as in shock waves or liquid free surface, for example). There is a criterion, the number of Knudsen

(Kn), to determine whether the continuous medium mechanics approach is valid or whether it should be preferred to the statistical mechanics approach. This is the ratio (Eq. 1.13) between a length L_{micro} characteristic at the molecular scale (e. g. the average free path of the molecules composing the fluid) and a flow characteristic length L_{macro} (e. g. the height of the channel). When $Kn < 10^{-3}$, the assumption of the continuous medium can be used [84].

$$Kn = \frac{L_{micro}}{L_{macro}} \quad (1.13)$$

For example, an air flow in a channel of height $5 \times 10^{-3}m$ under a pressure of 1 atm at the temperature of 300 K corresponds to a Knudsen number of $\approx 1.3 \times 10^{-5}$. In the situations that will be mentioned later, the number of Knudsen will be small enough for the continuum hypothesis to be applied.

The second hypothesis that will be used hereafter is that of local thermodynamic equilibrium (in particular in order to apply the equations of state of fluids or Fourier's law): fluid flow processes are generally out-of-equilibrium situations and the thermodynamics of irreversible processes should a priori be applied to them. However, it is possible to apply classical thermodynamics (which is concerned with balanced systems or processes approximated by a succession of equilibrium situations) provided that certain constraints are respected. For this purpose, it is necessary that, at the scale of the fluid parcel, a thermodynamic equilibrium be established, making it possible to give at each instant (in the macroscopic sense) a value to the thermodynamic quantities characterizing this small system (such as its temperature, for example). This requires that the characteristic duration of the flow at the macroscopic scale τ_{macro} is much greater than the characteristic duration at the microscopic scale τ_{micro} (equilibrium relaxation time) and therefore the ratio $\frac{\tau_{micro}}{\tau_{macro}}$ can be used as a criterion, transposing the number of Knudsen to a characteristic time ratio and similar to the Deborah number: when this ratio is well below 1, changes at the macroscopic level are slow enough for the fluid parcel to relax to a state of thermodynamic equilibrium in a rapid time compared to the macroscopic duration scale. In the rest of this presentation it is considered, as is usually done, that the hypothesis of local thermodynamic equilibrium applies (especially since there is no involvement of any chemical reaction, rarefied gas, shock phenomenon or viscoelastic environment [215]).

From the general equations 1.9 to 1.11, it is possible to deduce other useful equations: multiplying by u_i the equation 1.10 leads to equation 1.14 showing the specific kinetic energy (per unit mass) $e_K = \frac{1}{2}u_i u_i$. This equation expresses the kinetic energy theorem and its RHS can be developed to make terms corresponding to the volume powers due to external forces (volume, surface pressure-related, surface viscosity-related) and internal forces (pressure-related and viscosity-related) more clearly visible as in Eq. 1.15.

$$\frac{\partial(\rho e_K)}{\partial t} + \frac{\partial(\rho e_K u_j)}{\partial x_j} = \rho u_i f_i + u_i \frac{\partial \sigma_{ij}}{\partial x_j} \quad (1.14)$$

$$\frac{\partial(\rho e_K)}{\partial t} + \frac{\partial(\rho e_K u_j)}{\partial x_j} = \rho u_i f_i - \frac{\partial(P u_i)}{\partial x_i} + \frac{\partial(\tau_{ij} u_i)}{\partial x_j} + P \frac{\partial u_i}{\partial x_i} - \tau_{ij} \frac{\partial u_i}{\partial x_j} \quad (1.15)$$

From Equations 1.11 and 1.14 one can derive by difference the equation of the specific internal energy e_I :

$$\frac{\partial(\rho e_I)}{\partial t} + \frac{\partial(\rho e_I u_j)}{\partial x_j} = -P \frac{\partial u_i}{\partial x_i} + \tau_{ij} \frac{\partial u_i}{\partial x_j} - \frac{\partial q_j}{\partial x_j} \quad (1.16)$$

Using the relationship $h = e_I + \frac{P}{\rho}$ and Equation 1.16 leads to the equation of the specific enthalpy:

$$\frac{\partial(\rho h)}{\partial t} + \frac{\partial(\rho h u_j)}{\partial x_j} = \frac{\partial P}{\partial t} + u_j \frac{\partial P}{\partial x_j} + \tau_{ij} \frac{\partial u_i}{\partial x_j} - \frac{\partial q_j}{\partial x_j} \quad (1.17)$$

In the three previous equations, relating to energy, a term appears that will be important for subsequent discussions on entropy production: the viscous dissipation function Φ :

$$\Phi = \tau_{ij} \frac{\partial u_i}{\partial x_j} \quad (1.18)$$

The examination of Equations 1.9 to 1.11 leads to the conclusion that 5 equations are available (Equation 1.10 corresponds in fact to three equations relating to projections on the axes of the Cartesian reference frame) for a total of 14 unknown scalars (density, the three components of the velocity, the six components of the viscous stress tensor - which is symmetrical, the specific total energy and the three components of the heat flux density vector). It is therefore necessary to add several equations to close the differential system. These supernumerary relationships involve setting assumptions about fluid behavior and therefore choosing a model. There are several of them and the next development is the one that will be useful to us later: the Navier-Stokes model.

In this model, the fluid is considered as Newtonian: the fluid is isotropic (has no preferred direction) and the tensor of viscous stresses depends linearly on the components of the strain rate tensor (defined in Eq. 1.19), which is a generalization of the behavior expressed by Newton in his book *Philosophiae Naturalis Principia Mathematica* [178].

$$S_{ij} = \frac{1}{2} \left(\frac{\partial u_i}{\partial x_j} + \frac{\partial u_j}{\partial x_i} \right) \quad (1.19)$$

This linear relationship (eq. 1.20) shows two quantities μ and μ' , called dynamic viscosity and second coefficient of viscosity respectively, that characterize the behavior of the fluid when it is subjected to deformation stresses.

$$\tau_{ij} = \mu \left(\frac{\partial u_i}{\partial x_j} + \frac{\partial u_j}{\partial x_i} \right) + \mu' \frac{\partial u_k}{\partial x_k} \delta_{ij} = 2\mu S_{ij} + \mu' \text{tr}(S_{kl}) \delta_{ij} \quad (1.20)$$

Then the Stokes hypothesis (Eq. 1.21) is used to link the dynamic viscosity to the second viscosity coefficient to ensure that the tensor trace of the viscous stresses vanishes (the bulk viscosity is then also zero). This hypothesis is generally accepted but it should be known that it is the subject of debate and research and is not necessarily perfectly verified (for dense or polyatomic fluids for example).

$$\mu' = -\frac{2}{3}\mu \quad (1.21)$$

Taking into account Equations 1.20 and 1.21, the equation of the conservation of momentum 1.10 becomes:

$$\frac{\partial(\rho u_i)}{\partial t} + \frac{\partial(\rho u_i u_j)}{\partial x_j} = \rho f_i - \frac{\partial P}{\partial x_i} + 2 \frac{\partial(\mu S_{ij})}{\partial x_j} - \frac{2}{3} \frac{\partial(\mu \frac{\partial u_k}{\partial x_k})}{\partial x_i} \quad (1.22)$$

In the present thesis work, we will not deal with heat exchanges by radiation. Similarly, the fluid is considered non-reactive (whether from a chemical or nuclear perspective) and single-phase. Thus, the energy equation does not contain additional source terms that would account for heat released or absorbed by a chemical or nuclear reaction, nor does it contain terms that represent the absorption by the fluid of radiation that would pass through it. The only mode of heat exchange considered is heat conduction, for which the phenomenological law used is Fourier's law, considering a scalar (isotropic) thermal conductivity k :

$$q_i = -k \frac{\partial T}{\partial x_i} \quad (1.23)$$

From Gibbs' phase rule, the specific enthalpy depends on two independent intensive variables $h(P, T)$ and its variation can be written as follows, by introducing the specific heat capacity at constant pressure C_p and $\beta = -\frac{1}{\rho} \frac{\partial \rho}{\partial T}$ the (volumetric) coefficient of thermal expansion:

$$dh = \frac{\partial h}{\partial T} dT + \frac{\partial h}{\partial P} dP = C_p dT + \frac{1 - \beta T}{\rho} dP \quad (1.24)$$

By using the relationships 1.24 and 1.23 and considering as will be done later that C_p is practically constant over the considered temperature range, one obtains from Equation 1.17 the following relationship, concerning the temperature in the flow:

$$\frac{\partial(\rho C_p T)}{\partial t} + \frac{\partial(\rho C_p T u_j)}{\partial x_j} = \beta T \left(\frac{\partial P}{\partial t} + u_j \frac{\partial P}{\partial x_j} \right) + \tau_{ij} \frac{\partial u_i}{\partial x_j} + \frac{\partial}{\partial x_j} \left(k \frac{\partial T}{\partial x_j} \right) \quad (1.25)$$

In addition, the viscous dissipation function becomes:

$$\Phi = \tau_{ij} \frac{\partial u_i}{\partial x_j} = 2\mu S_{ij} S_{ij} - \frac{2}{3} \mu \left(\frac{\partial u_k}{\partial x_k} \right)^2 \quad (1.26)$$

This expression, when developed according to the components of the velocity vector and the position vector ($u = u_1, v = u_2, w = u_3; x = x_1, y = x_2, z = x_3$) results in:

$$\Phi = \mu \left\{ 2 \left[\left(\frac{\partial u}{\partial x} \right)^2 + \left(\frac{\partial v}{\partial y} \right)^2 + \left(\frac{\partial w}{\partial z} \right)^2 \right] + \left(\frac{\partial u}{\partial y} + \frac{\partial v}{\partial x} \right)^2 + \left(\frac{\partial u}{\partial z} + \frac{\partial w}{\partial x} \right)^2 + \left(\frac{\partial v}{\partial z} + \frac{\partial w}{\partial y} \right)^2 - \frac{2}{3} \left(\frac{\partial u}{\partial x} + \frac{\partial v}{\partial y} + \frac{\partial w}{\partial z} \right)^2 \right\} \quad (1.27)$$

Equations 1.9, 1.22 and 1.25 correspond to 5 scalar equations and involve 9 unknown scalars (density, the three components of the velocity, pressure, temperature, dynamic viscosity, thermal conductivity and the compressibility coefficient β as C_p is considered as a constant). In order to close this system of equations, 4 additional equations are required: the equation of state of the fluid $\rho = \rho(P, T)$, the equation $\beta = -\frac{1}{\rho} \frac{\partial \rho}{\partial T}$, which

allows to derive β and the equations relating k and μ to the temperature (and possibly to the pressure, for liquids in particular [209]).

In the rest of this presentation we will start from Equations 1.9, 1.22 and 1.25 by specializing them according to the situation: in some specific cases the fluid will be considered incompressible (ρ will be invariable) or its dynamic viscosity or thermal conductivity will be constant and these symbols can if necessary be taken out from the derivatives in Equations 1.22 and 1.25. The fluid will sometimes be considered to be a perfect gas with $\beta = 1/T$.

To conclude this chapter, it is important to note that the equations governing fluid flows can be formulated in different ways: they have been presented in indexed form but they can also be expressed using differential operators or tensor operations (whose notation may however vary according to the authors). The terms in divergence form have also been revealed as much as possible, because this facilitates the application of Stokes or Green-Ostrogradski type theorems when switching to volume integrals. Finally, the usual partial derivatives are used and not the material substantial derivative (which can also be noted differently depending on the authors). Subsequently, these condensed forms will sometimes be used (especially the ∇ operator) in order to lighten some formulas.

1.3.2 The entropy production rate equation

Intensive use will be made of the following expression of the local entropy generation rate (for a homogeneous, non-reactive and electrically non-conductive fluid):

$$\dot{S}_{gen}''' = \frac{k}{T^2}(\nabla T)^2 + \frac{\Phi}{T} = \frac{k}{T^2} \frac{\partial T}{\partial x_i} \frac{\partial T}{\partial x_i} + \frac{\mu}{T} (2S_{ij}S_{ij} - \frac{2}{3}(\frac{\partial u_k}{\partial x_k})^2) \quad (1.28)$$

This expression is obtained by combining the first and second principles of thermodynamics: starting from Equation 1.17 derived from the first principle, and taking into account the thermodynamic relationship $dh = Tds + (1/\rho)dP$ and Fourier's law, one obtains a transport equation for the specific entropy s :

$$\frac{\partial(\rho s)}{\partial t} + \frac{\partial(\rho s u_j)}{\partial x_j} = \frac{\Phi}{T} + \frac{1}{T} \frac{\partial}{\partial x_j} (k \frac{\partial T}{\partial x_j}) \quad (1.29)$$

In addition, the application of the second principle to a fluid moving parcel (closed system) or to a small fixed control volume (open system) leads to Eq. 1.30. Finally, the combination of the Equations 1.29 and 1.30 leads to Equation 1.28

$$\frac{\partial(\rho s)}{\partial t} + \frac{\partial(\rho s u_j)}{\partial x_j} = \dot{S}_{gen}''' + \frac{\partial}{\partial x_j} (k \frac{\partial T}{\partial x_j}) \quad (1.30)$$

In order to demonstrate Eq. 1.30, let us consider a small fixed open rectangular parallelepiped control volume CV with dimensions dx , dy and dz (Fig. 1.8). The second principle of thermodynamics writes:

$$\dot{S}_{gen} = \frac{dS_{CV}}{dt} - \sum \frac{\dot{Q}_i}{T_i} - \left(\sum_{\substack{inlet \\ ports}} \dot{m}_{in} s_{in} - \sum_{\substack{outlet \\ ports}} \dot{m}_{out} s_{out} \right) \geq 0 \quad (1.31)$$

The total entropy generation rate in CV can be expressed as a function of its density per unit volume:

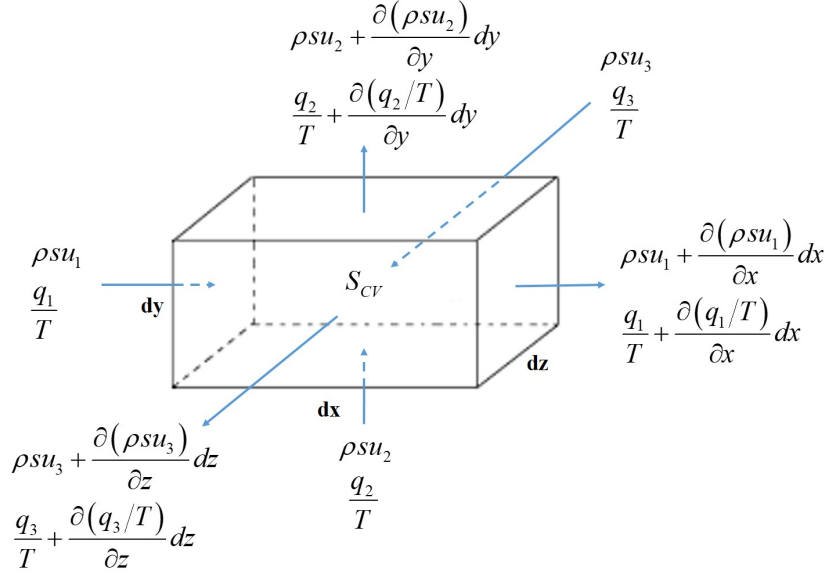


Figure 1.8: Elementary control volume CV to illustrate Eq. 1.30 demonstration

$$\dot{S}_{gen} = \dot{S}_{gen}''' dx dy dz \quad (1.32)$$

Similarly, the rate of variation of the total CV entropy over time writes:

$$\frac{dS_{CV}}{dt} = \frac{\partial(\rho s)}{\partial t} dx dy dz \quad (1.33)$$

In addition, the second RHS term in Eq. 1.31 corresponds to the net output entropy flux related to heat transfers through the elementary surfaces $dx dy$, $dx dz$ and $dy dz$. which can be expressed in the first order as follows (q_1 , q_2 and q_3 being the components of the heat flow rate vector in [W]):

$$-\sum \frac{\dot{Q}_i}{T_i} \approx \left(\frac{\partial(q_1/T)}{\partial x} dx \right) dy dz + \left(\frac{\partial(q_2/T)}{\partial y} dy \right) dx dz + \left(\frac{\partial(q_3/T)}{\partial z} dz \right) dx dy \quad (1.34)$$

Similarly, the combination of the third and fourth RHS terms in Equation 1.31 expresses the net entropy flux due to the material flows passing through these same elementary surfaces (where u_1 , u_2 and u_3 being the components of the velocity vector):

$$-\left(\sum_{\substack{\text{inlet} \\ \text{ports}}} \dot{m}_{in} s_{in} - \sum_{\substack{\text{outlet} \\ \text{ports}}} \dot{m}_{out} s_{out} \right) \approx \left(\frac{\partial(\rho s u_1)}{\partial x} dx \right) dy dz + \left(\frac{\partial(\rho s u_2)}{\partial y} dy \right) dx dz + \left(\frac{\partial(\rho s u_3)}{\partial z} dz \right) dx dy \quad (1.35)$$

By injecting Eqs. 1.32 to 1.35 into Equation 1.31 and then dividing by the elementary volume $dx dy dz$ and replacing the heat flows with their expression derived from Fourier's law, one obtains the desired Equation 1.30.

The locally generated entropic power in Equation 1.28 is the sum of two terms: the first one is related to the temperature gradient and expresses the generation of entropy corresponding to heat transfer across finite temperature differences in the three Cartesian

directions (longitudinal, normal and transversal). The second term is a function of the different components of the tensorial gradient of the velocity vector and accounts for the viscous dissipation phenomena within the flow.

In more general situations, where other irreversible phenomena may occur (such as chemical reactions, for example), additional terms should be added in Eq. 1.28. This will be done in Chapter 3 when mass diffusion in a fluid composed of two chemical species is studied.

Chapter 2

Entropy production rates in the laminar boundary layer

2.1 Introduction

As announced in Chapter 1.2, this study is part of the thermodynamic optimization of heat exchangers and in particular of surface solar receivers in concentrated solar power systems in which a high flux solar beam heats a wall that transfers the absorbed power to a heat transfer fluid. However, this work has a fundamental aspect and its scope of application is broader: the objective is to conduct a detailed analysis of the entropic power generated in a laminar boundary layer with a focus on the influence of the thermal boundary condition type and intensity. The results can be used as a reference model when dealing with non-isothermal flows in heat exchangers for example, or in areas where the boundary layer control is essential, such as aeronautics. The entropy generation (time) rate is calculated and analyzed in order to set a detailed reference in a simplified model while taking into account heat flux density boundary conditions (in addition to fixed temperature boundaries) and a wide range of thermal gaps (up to $T_{hot}/T_{cold} = 2$) in order to address solar receivers.

Flat plate boundary layer is a reference model for sheared convective flow with active research in a broad variety of academic and application domains like, to name but a few: mixed convection over a permeable plate [153], hypersonic flows and viscous heating [146] or flow control [233], with studies both theoretical and numerical [43] [238] or experimental [213] [19]. Boundary layer analysis and control is an essential field in aeronautics [18, 92, 167, 188, 204, 240], with a view, for example, to delay or prevent its separation [83, 160, 161] and to improve lift [59]. The laminar boundary layer is also being investigated and many studies are analyzing ways to delay the transition from laminar to turbulent regimes in order to reduce drag forces [22, 52, 77, 113, 176, 225]. Heat exchange between the fluid and the aircraft is also an area of interest [239] whether it concerns aerodynamic heating (in supersonic/hypersonic flight [177] or for reentry vehicles [145]), lift and drag improvements [124, 152] or heating parts of the aircraft to prevent the formation of ice [62]. The boundary layer model allows to deal with different thermal boundary conditions like isothermal or isoflux plates and in simplified reference cases like steady-state two-dimensional incompressible flow of a fluid with constant properties, semi-analytical computations can be readily performed. For all these reasons, the boundary layer model is helpful in analyzing the impact of changing parameters without requiring expensive computation resources. In this study this

model has been used as a sandbox to analyze entropy generation and minimization in forced convective flows.

The analysis of the entropy generation field and the reduction of entropy generation or exergy destruction [173, 174, 26] are valuable tools used to optimize systems [4, 28, 25, 79, 196, 55]. Entropy generation minimization [24] can help in optimizing convective heat exchange and in suggesting optimal design set-up [23] [24] [107] [141]. However, actual exchangers may not be able to work at the theoretical optimal point for technical or economic reasons. In solar receivers of concentrated solar power plants (CSP), the ratio between hot and cold wall temperatures can be around 2 or more, leading to high entropy generation rates. It is therefore useful to understand where the highest rates are located and what are the factors influencing entropy generation in order to assess how a better design reducing entropy can improve the receiver efficiency, even if it is merely located a little closer to the optimum value of design parameters (like shape or thermal settings). Moreover, in solar receivers, three-dimensional turbulent quasi-compressible flows of thermo-dependent fluids occur with high temperature gradients and asymmetrical thermal boundary conditions [8] [9] [29] [211] [63] [68] [69] and require significant computing resources for a single simulation [230]. It is useful to adopt a step-by-step approach to this complexity when dealing with the entropy generation analysis and minimization in order to be able to discriminate the effects of each characteristic of the flow and to vary freely the key parameters (in particular: the temperature gap between the hot and the cold plate) and over a wide range of values. For all the above reasons, the boundary layer model has been used in the simplified case of a laminar and incompressible flow over a flat plate in order to calculate and analyze the local entropy generation rate and its composition at any point in the flow and the total entropy generation rate between two positions along the plate. If the thermal power exchanged between the heating plate and the fluid is fixed, there is a minimum of the total entropy generation rate for an optimal set of control variable values (see for example [23] when considering the entire length of the plate). Varying the thermal boundary condition type has a major influence on the position of this optimum.

In the present study we consider the total entropy generation rate over a length interval along the plate and analyze how this optimum depends on the total heat power transferred and on the distance of the exchange section from the leading edge. While performing this study, we took care of the following points. Firstly, the temperature gap is not neglected when compared to the plate temperature. This allows to set a reference for high temperature gap flows in a simplified model. Secondly, the behavior of the solution of the model has also been studied near the leading edge in order to know its asymptotic trend and because some contributions to the entropy generation rate grow to infinity when reaching the leading edge. Thirdly, all contributors in heat transfer and viscous friction entropy generation have been considered at first, in order to determine which of them are negligible.

2.2 The boundary layer flow governing equations

The laminar boundary layer equations are a useful simplification of the general flow equations of a fluid (see Chapter 1.3). They have their origin in the pioneering work carried out by Ludwig Prandtl [195] at the beginning of the 20th century. The derivation of these equations is presented in the following sections.

2.2.1 From the Navier-Stokes to the boundary layer equations

We consider the steady two-dimensional laminar flow of an incompressible fluid (ρ is uniform and constant and $\beta = 0$) with constant properties (C_p , μ , k are uniform and constant) over a semi-infinite flat plate. We assume there is no volume force or heat source and no radiative thermal transfer. Viscous heating is also neglected (see section 2.6 for a discussion on this topic). The fluid arrives at a fixed temperature T_∞ and velocity U_∞ and is both sheared and heated by the plate. Since the velocity is zero in contact with the wall (no-slip condition), friction forces slow the flow in a thin area near the plate called the boundary layer (Fig. 2.1). The longitudinal velocity, being zero at the wall, increases with the value of the ordinate by approaching the inlet velocity U_∞ but there is no clear separation between the boundary layer zone and the free flow zone and the thickness of the (dynamic) boundary layer is conventionally defined by ordinate δ where $u = 0.99U_\infty$. It is also near the wall that the strongest temperature gradients are located, which makes it possible to define a thermal boundary layer and its corresponding thickness δ_T for which the temperature difference with respect to the wall is 99% of the total temperature difference between the wall and the free flow.

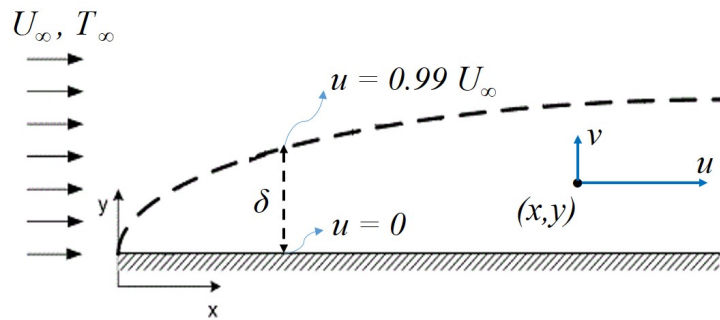


Figure 2.1: Boundary layer over a flat plate

Taking into account the key assumptions mentioned above (incompressibility, constant properties, etc.), it is first possible to simplify the equation Eqs. 1.9, 1.22 and 1.25, which become:

$$\frac{\partial u}{\partial x} + \frac{\partial v}{\partial y} = 0 \quad (2.1)$$

$$u \frac{\partial u}{\partial x} + v \frac{\partial u}{\partial y} = -\frac{1}{\rho} \frac{\partial P}{\partial x} + \nu \left(\frac{\partial^2 u}{\partial x^2} + \frac{\partial^2 u}{\partial y^2} \right) \quad (2.2)$$

$$u \frac{\partial v}{\partial x} + v \frac{\partial v}{\partial y} = -\frac{1}{\rho} \frac{\partial P}{\partial y} + \nu \left(\frac{\partial^2 v}{\partial x^2} + \frac{\partial^2 v}{\partial y^2} \right) \quad (2.3)$$

$$u \frac{\partial T}{\partial x} + v \frac{\partial T}{\partial y} = \alpha \left(\frac{\partial^2 T}{\partial x^2} + \frac{\partial^2 T}{\partial y^2} \right) \quad (2.4)$$

In the above equations, the common notation for two-dimensional flows is used, where $u(x, y)$ represents the longitudinal component of the velocity (parallel to the plate and the x axis, the abscissa being counted from the leading edge of the plate) and $v(x, y)$ is its normal component to the plate, the ordinates being counted from the plate (thus $u = u_1$, $v = u_2$, $x = x_1$, $y = x_2$). $T(x, y)$ is the temperature of the fluid. In

addition, $\nu = \mu/\rho$ is the kinematic viscosity of the fluid and $\alpha = k/(\rho C_p)$ is its thermal diffusivity.

The system of equations 2.1 to 2.4 may be simpler than the general system presented in Chapter 1.3.1, but it remains a daunting task to solve. Ludwig Prandtl's contribution was a major step towards further simplifying the equations governing the flow by taking into account the specificities of the boundary layer and by analyzing the orders of magnitude of the different terms in the above equations. The keystone of this reasoning is that the thickness of the boundary layer δ is small compared to the characteristic length of the flow L (such as the plate length considered) and this is all the more true as the Reynolds number $Re = U_\infty L/\nu$ is high.

In order to conduct this reasoning on the orders of magnitude of the different terms, the first step consists in making these equations dimensionless. The following dimensionless quantities are defined (T_w being the temperature of the plate):

$$x^\times = \frac{x}{L}, \quad y^\times = \frac{y}{L}, \quad u^\times = \frac{u}{U_\infty}, \quad v^\times = \frac{v}{U_\infty}, \quad P^\times = \frac{P}{\rho U_\infty^2}, \quad T^\times = \frac{T_w - T}{T_w - T_\infty} \quad (2.5)$$

Injecting Eqs. 2.5 into Eqs. 2.1 to 2.4 leads to the following dimensionless equations (where $Pr = \nu/\alpha$ is the Prandtl number):

$$\frac{\partial u^\times}{\partial x^\times} + \frac{\partial v^\times}{\partial y^\times} = 0 \quad (2.6)$$

$$u^\times \frac{\partial u^\times}{\partial x^\times} + v^\times \frac{\partial u^\times}{\partial y^\times} = -\frac{\partial P^\times}{\partial x^\times} + \frac{1}{Re} \left(\frac{\partial^2 u^\times}{\partial (x^\times)^2} + \frac{\partial^2 u^\times}{\partial (y^\times)^2} \right) \quad (2.7)$$

$$u^\times \frac{\partial v^\times}{\partial x^\times} + v^\times \frac{\partial v^\times}{\partial y^\times} = -\frac{\partial P^\times}{\partial y^\times} + \frac{1}{Re} \left(\frac{\partial^2 v^\times}{\partial (x^\times)^2} + \frac{\partial^2 v^\times}{\partial (y^\times)^2} \right) \quad (2.8)$$

$$u^\times \frac{\partial T^\times}{\partial x^\times} + v^\times \frac{\partial T^\times}{\partial y^\times} = \frac{1}{Re Pr} \left(\frac{\partial^2 T^\times}{\partial (x^\times)^2} + \frac{\partial^2 T^\times}{\partial (y^\times)^2} \right) \quad (2.9)$$

In the boundary layer, the order of magnitude (OM) of u^\times , x^\times and $\frac{\partial u^\times}{\partial x^\times}$ is 1, while the OM of y^\times is $\delta^\times = \delta/L$. From the continuity equation 2.6, it follows that the OM of v^\times is δ^\times . As $\delta^\times \ll 1$, the OM of the normal component of the velocity is small when compared to the OM of the longitudinal velocity.

In addition, the OM of $\frac{\partial^2 u^\times}{\partial (x^\times)^2}$ is 1 while the OM of $\frac{\partial^2 u^\times}{\partial (y^\times)^2}$ is $1/(\delta^\times)^2$ which is thus the majority in the viscous term of Eq. 2.7 and $\frac{\partial^2 u^\times}{\partial (x^\times)^2}$ will now be neglected. In the boundary layer, the viscous and inertial effects are in competition and are of the same order of magnitude: for this to be reflected in Eq. 2.7, it is necessary that the OM of $\frac{1}{Re}$ be $(\delta^\times)^2$ (because the inertial terms in the LHS of this equation are of order of magnitude 1). Therefore, the order of magnitude of δ^\times is $\frac{1}{\sqrt{Re}}$.

In Eq. 2.8, the terms in the LHS as well as the viscous terms are of order of magnitude δ^\times . This implies that the OM of $\frac{\partial P^\times}{\partial y^\times}$ is also δ^\times , which means that the pressure depends practically only on x and $\frac{\partial P^\times}{\partial x^\times} \approx \frac{dP^\times}{dx^\times}$.

At this point of the reasoning, it is possible to rewrite Eqs. 2.7 to 2.8 into dimensional quantities while eliminating the terms that are neglected for the reasons just given:

$$u \frac{\partial u}{\partial x} + v \frac{\partial u}{\partial y} = -\frac{1}{\rho} \frac{dP}{dx} + \nu \frac{\partial^2 u}{\partial y^2} \quad (2.10)$$

For the sake of simplicity, let us consider a flow without free stream pressure gradient. P depends only on x and $\frac{dP}{dx}$ vanishes in the free stream area and in the boundary layer. Thus Eq. 2.10 finally takes the form:

$$u \frac{\partial u}{\partial x} + v \frac{\partial u}{\partial y} = \nu \frac{\partial^2 u}{\partial y^2} \quad (2.11)$$

It is now necessary to conduct the same type of order of magnitude analysis for the temperature equation (Eq. 2.9). The OM of T^\times is 1. For temperature derivatives, it must be taken into account that T^\times goes from 0 to almost 1 over the thickness of the thermal boundary layer $\delta_T^\times = \frac{\delta_T}{L}$, which may be different from the dynamic boundary layer thickness δ^\times . In the viscous term of Eq. 2.9, the OM of $\frac{\partial^2 T^\times}{\partial (x^\times)^2}$ and $\frac{\partial^2 T^\times}{\partial (y^\times)^2}$ are 1 and $\frac{1}{(\delta_T^\times)^2}$ respectively, which means that the latter term is largely predominant and will be the only one retained. Once switched back to dimensioned magnitudes and taking into account the simplification just given, Eq. 2.9 becomes:

$$u \frac{\partial T}{\partial x} + v \frac{\partial T}{\partial y} = \alpha \frac{\partial^2 T}{\partial y^2} \quad (2.12)$$

To conclude, in the boundary layer created just above the plate and when no pressure gradient exists in the free-stream area of the flow, a reasoning on the orders of magnitudes leads to a simplified form of the Navier-Stokes equations which now read [208]:

$$\frac{\partial u}{\partial x} + \frac{\partial v}{\partial y} = 0 \quad (2.13)$$

$$u \frac{\partial u}{\partial x} + v \frac{\partial u}{\partial y} = \nu \frac{\partial^2 u}{\partial y^2} \quad (2.14)$$

$$u \frac{\partial T}{\partial x} + v \frac{\partial T}{\partial y} = \alpha \frac{\partial^2 T}{\partial y^2} \quad (2.15)$$

with the following boundary conditions for the velocity:

$$u(x, 0) = 0, \quad v(x, 0) = 0, \quad \lim_{y \rightarrow \infty} u(x, y) = U_\infty \quad (2.16)$$

For the temperature, two boundary conditions will be analyzed hereafter: the isothermal plate in Eq. 2.17 (if the temperature of the plate is fixed at a constant and uniform value T_w) and the isoflux plate in Eq. 2.18 (if the heat flux density at the plate is fixed at a constant and uniform value q'').

$$T(x, 0) = T_w, \quad \lim_{y \rightarrow \infty} T(x, y) = T_\infty \quad (2.17)$$

$$-k \left. \frac{\partial T}{\partial y} \right|_{y=0} = q'', \quad \lim_{y \rightarrow \infty} T(x, y) = T_\infty \quad (2.18)$$

2.2.2 The similarity equations of the boundary layer

In order to solve the above equations, the similarity of longitudinal velocity (x-component) and temperature profiles along the plate is assumed [116]. The dimensionless η variable is defined in Eq. 2.19 and combines x and y coordinates. Two dimensionless functions of η are also introduced in Eqs. 2.20 and 2.22. The $f(\eta)$ function is linked to the stream function ψ (see Eqs. 2.21) and the $\theta(\eta)$ function defines a dimensionless temperature gap between the fluid temperature T and the plate temperature T_w at the same x position along the plate.

$$\eta = y\sqrt{\frac{U_\infty}{\nu x}} \quad (2.19)$$

$$\psi = \sqrt{U_\infty \nu x} f(\eta) \quad (2.20)$$

$$u = \partial\psi/\partial y, \quad v = -\partial\psi/\partial x \quad (2.21)$$

$$\theta(\eta) = \frac{T_w - T}{T_w - T_\infty} \quad (2.22)$$

By definition of the stream function ψ , the continuity equation (Eq. 2.13) is automatically verified. Injecting Eqs. 2.19 to 2.21 into Eq. 2.14 leads to the Blasius equation [37, 170] for the f function, where the $(.)'$ superscript stands for the successive derivatives of any function with respect to variable η :

$$f''' + \frac{1}{2}ff'' = 0 \quad (2.23)$$

The boundary conditions in Eqs. 2.16 become:

$$f(0) = 0, \quad f'(0) = 0, \quad \lim_{\eta \rightarrow \infty} f(\eta) = 1 \quad (2.24)$$

Solving Eqs. 2.23 and 2.24 allows to find f , then ψ and finally u and v . The values of f have been tabulated in the scientific literature and are independent on the type of thermal boundary condition applied at the plate, because in the case of a fluid with constant properties (ρ and μ , in particular), the dynamical and thermal equations are independent. The corresponding equation for the dimensionless temperature θ depends on the thermal boundary condition type and the isothermal and isoflux plate cases are presented separately in the sections below.

Isothermal plate

When the temperature of the plate is set at a fixed value T_w , injecting Eqs. 2.19 to 2.22 into Eq. 2.15 gives the following equation for $\theta(\eta)$, $Pr = \nu/\alpha$ being the Prandtl number:

$$\theta'' + \frac{1}{2}Pr f\theta' = 0 \quad (2.25)$$

The boundary conditions also become:

$$\theta(0) = 0, \quad \lim_{\eta \rightarrow \infty} \theta(\eta) = 1 \quad (2.26)$$

As f is found by Eqs. 2.23 and 2.24, θ is found using Eqs. 2.25 and 2.26 and finally, the temperature is derived by using Eq. 2.22.

Isoflux plate

When the heat density flux is set to a fixed uniform and constant value at the plate, the similarity of temperature profiles along the plate implies a $Re_x^{1/2}$ dependence of the temperature gap between the plate and the free stream. Indeed, the heat flux density is given by Eq. 2.27 and is constant along the plate only if the temperature gap $T_w - T_\infty$ is proportional to the square root of the abscissa as in Eq. 2.28.

$$q'' = -k \left. \frac{\partial T}{\partial y} \right|_{y=0} = k(T_w - T_\infty) \theta'(0) \left(\frac{U_\infty}{\nu x} \right)^{\frac{1}{2}} \quad (2.27)$$

$$\Delta T = T_w - T_\infty = Nx^{\frac{1}{2}} \quad (2.28)$$

Using Eqs. 2.22 and 2.28 allows to express T as a function of θ , x , N , and T_∞ , the two latter being constant when x or y varies. Eqs. 2.19 to 2.22 are then injected into Eq. (2.15), which provides the following ordinary differential equation for $\theta(\eta)$ (Eq. 2.29) that includes an additional term when compared to the isothermal case (Eq. 2.25). An alternative approach is provided in [27] by defining a different θ function and deriving a differential equation that is consistent with Eq. 2.29.

$$\theta'' + \frac{1}{2} Pr f \theta' + \frac{1}{2} Pr f'(1 - \theta) = 0 \quad (2.29)$$

In addition, the boundary conditions in Eqs. 2.26 are still true and can be used in order to find $\theta(\eta)$.

2.3 The entropy generation rate equations

The local entropy generation rate by unit of volume at any point in the flow is given by [26]:

$$\dot{S}_{gen}''' = \frac{k(\nabla T)^2}{T^2} + \frac{\phi}{T} \quad (2.30)$$

ϕ is the viscous dissipation term in the equation of energy and is given by the following expression for a two-dimensional incompressible flow:

$$\phi = \mu \left\{ 2 \left[\left(\frac{\partial u}{\partial x} \right)^2 + \left(\frac{\partial v}{\partial y} \right)^2 \right] + \left(\frac{\partial u}{\partial y} + \frac{\partial v}{\partial x} \right)^2 \right\} \quad (2.31)$$

2.3.1 Entropy production rate equations for an isothermal plate

Injecting f and θ functions into Eq. 2.30 and keeping in the value of ϕ the main term $(\partial u / \partial y)^2$ only, leads to Eq. 2.32. The further multiplication by the dimensionless factor $\nu^2 / (kU_\infty^2)$ provides the expression of the dimensionless local entropy generation rate at any point in the flow in Eq. 2.33.

$$\dot{S}_{gen}''' = \frac{k\theta'^2}{(\tau - \theta)^2} \frac{U_\infty}{\nu x} \left(\frac{\eta^2}{4Re_x} + 1 \right) + \frac{\mu U_\infty^3}{\Delta T (\tau - \theta) \nu x} f''^2 \quad (2.32)$$

$$S_3 = \frac{\theta'^2}{Re_x (\tau - \theta)^2} \left(\frac{\eta^2}{4Re_x} + 1 \right) + \frac{Pr Ec}{Re_x (\tau - \theta)} f''^2 \quad (2.33)$$

In this formula, $Re_x = U_\infty x / \nu$ is the local (or longitudinal) Reynolds number, $Ec = U_\infty^2 / (C_p \Delta T)$ is the Eckert number and $\tau = T_w / \Delta T > 1$ is a dimensionless thermal parameter accounting for the relative importance of the temperature gap between the fluid and the plate ($\Delta T = T_w - T_\infty$) in relation to the temperature of the plate.

S_3 is a sum of three terms, accounting successively and respectively for the entropy generation rate by horizontal heat conduction $S_{3,ch}$, by vertical heat conduction $S_{3,cv}$ and by viscous friction $S_{3,f}$:

$$S_{3,ch} = \frac{\theta'^2}{Re_x (\tau - \theta)^2} \left(\frac{\eta^2}{4Re_x} \right) \quad (2.34)$$

$$S_{3,cv} = \frac{\theta'^2}{Re_x (\tau - \theta)^2} \quad (2.35)$$

$$S_{3,f} = \frac{Pr Ec}{Re_x (\tau - \theta)} f''^2 \quad (2.36)$$

Integrating \dot{S}_{gen}''' along the vertical direction from the plate ($y = 0$) to the free stream area ($y \rightarrow \infty$) gives the entropy generation rate by unit of plate surface \dot{S}_{gen}'' [$W.K^{-1}m^{-2}$] (Eq. 2.37) and its dimensionless value (Eq. 2.38) with the $\nu / (kU_\infty)$ factor.

$$\dot{S}_{gen}'' = \frac{kU_\infty}{\nu} \left(\frac{\Omega_{ch}}{4Re_x} + \Omega_{cv} + Pr Ec \Omega_f \right) Re_x^{-\frac{1}{2}} \quad (2.37)$$

$$S_2 = \left(\frac{\Omega_{ch}}{4Re_x} + \Omega_{cv} + Pr Ec \Omega_f \right) Re_x^{-\frac{1}{2}} \quad (2.38)$$

The Ω_{ch} , Ω_{cv} and Ω_f terms depend on the τ parameter and result from the integration of functions of η :

$$\Omega_{ch} = \int_0^\infty \frac{\theta'^2 \eta^2}{(\tau - \theta)^2} d\eta \quad (2.39)$$

$$\Omega_{cv} = \int_0^\infty \frac{\theta'^2}{(\tau - \theta)^2} d\eta \quad (2.40)$$

$$\Omega_f = \int_0^\infty \frac{f''^2}{\tau - \theta} d\eta \quad (2.41)$$

Finally, the integration of \dot{S}_{gen}'' between two longitudinal positions a and b along the plate leads to the entropy generation rate by unit of transversal length \dot{S}_{gen}' [$W.K^{-1}m^{-1}$] (Eq. 2.42) for the boundary layer between these two abscissa (accounted by their related local Reynolds numbers Re_a and Re_b). Its dimensionless counterpart S_1 is derived by dividing \dot{S}_{gen}' by the thermal conductivity k (Eq. 2.43).

$$\begin{aligned}\dot{S}'_{gen} &= \frac{k}{2}(Re_a^{-\frac{1}{2}} - Re_b^{-\frac{1}{2}})\Omega_{ch} \\ &+ 2k(Re_b^{\frac{1}{2}} - Re_a^{\frac{1}{2}})(\Omega_{cv} + PrEc\Omega_f)\end{aligned}\quad (2.42)$$

$$\begin{aligned}S_1 &= \frac{1}{2}(Re_a^{-\frac{1}{2}} - Re_b^{-\frac{1}{2}})\Omega_{ch} \\ &+ 2(Re_b^{\frac{1}{2}} - Re_a^{\frac{1}{2}})(\Omega_{cv} + PrEc\Omega_f)\end{aligned}\quad (2.43)$$

Like S_3 or S_2 , S_1 is the sum of three terms accounting for the horizontal conduction of heat $S_{1,ch} = \frac{1}{2}(Re_a^{-\frac{1}{2}} - Re_b^{-\frac{1}{2}})\Omega_{ch}$, the vertical conduction of heat $S_{1,cv} = 2(Re_b^{\frac{1}{2}} - Re_a^{\frac{1}{2}})\Omega_{cv}$ and the viscous friction $S_{1,f} = 2(Re_b^{\frac{1}{2}} - Re_a^{\frac{1}{2}})PrEc\Omega_f$.

Equations 2.33, 2.38 and 2.43 allow to analyze the behavior and the composition of the entropy generation rate as a function of dynamical and thermal variables.

2.3.2 Entropy production rate equations for an isoflux plate

For an isoflux plate Eq. 2.30 leads to the following expressions of the entropy generation rate by unit of volume and of its dimensionless form:

$$\begin{aligned}\dot{S}'''_{gen} &= \frac{k\theta'^2}{(\tau - \theta)^2} \frac{U_\infty}{\nu x} \left(\left(\frac{\eta\theta' - \theta + 1}{\theta'} \right)^2 \frac{1}{4Re_x} + 1 \right) \\ &+ \frac{\mu U_\infty^3}{\Delta T(\tau - \theta)\nu x} f''^2\end{aligned}\quad (2.44)$$

$$\begin{aligned}S_3 &= \frac{\theta'^2}{Re_x(\tau - \theta)^2} \left(\left(\frac{\eta\theta' - \theta + 1}{\theta'} \right)^2 \frac{1}{4Re_x} + 1 \right) \\ &+ \frac{PrEc}{Re_x(\tau - \theta)} f''^2\end{aligned}\quad (2.45)$$

As for the isothermal plate, integrating along the vertical line gives the entropy generation rates by unit of plate surface.

$$\dot{S}''_{gen} = \frac{kU_\infty}{\nu} \left(\frac{\Omega_{ch}}{4Re_x} + \Omega_{cv} + PrEc \Omega_f \right) Re_x^{-\frac{1}{2}} \quad (2.46)$$

$$S_2 = \left(\frac{\Omega_{ch}}{4Re_x} + \Omega_{cv} + PrEc \Omega_f \right) Re_x^{-\frac{1}{2}} \quad (2.47)$$

$$\Omega_{ch} = \int_0^\infty \frac{(\eta\theta' - \theta + 1)^2}{(\tau - \theta)^2} d\eta \quad (2.48)$$

$$\Omega_{cv} = \int_0^\infty \frac{\theta'^2}{(\tau - \theta)^2} d\eta \quad (2.49)$$

$$\Omega_f = \int_0^\infty \frac{f''^2}{\tau - \theta} d\eta \quad (2.50)$$

Although Eqs. 2.46, 2.47, 2.49 and 2.50 have an identical form than the corresponding equations already given for the isothermal plate, it must be kept in mind the following key differences: first, the θ functions are different. Secondly, Ω_{ch} , Ω_{cv} , Ω_f now depend on x because τ is now a function of the longitudinal position. Thirdly, the Eckert number Ec also depends on x .

The entropy generation rate per unit of transversal length is then integrated numerically:

$$\dot{S}'_{gen} = \int_a^b \dot{S}''_{gen} dx \quad (2.51)$$

$$S_1 = \frac{\dot{S}'_{gen}}{k} \quad (2.52)$$

2.3.3 Marginal viscous entropy production rates

Up to now, marginal terms in the viscous dissipation term ϕ have not been taken into account. To the best of our knowledge, these terms have not been described before. In addition to $S_{3,f}$ in Eq. 2.36, the following contributors to the entropy generation by viscous friction are:

$$S_{3,f,marg1} = \frac{PrEc}{Re_x^2(\tau - \theta)} \eta^2 f'^2 \quad (2.53)$$

$$S_{3,f,marg2} = \frac{PrEc}{16Re_x^3(\tau - \theta)} (\eta^2 f'' + \eta f' - f)^2 \quad (2.54)$$

$$S_{3,f,marg3} = -\frac{PrEc}{2Re_x^2(\tau - \theta)} f'' (\eta^2 f'' + \eta f' - f) \quad (2.55)$$

These dimensionless terms correspond respectively to $\frac{2\mu}{T} [(\frac{\partial u}{\partial x})^2 + (\frac{\partial v}{\partial y})^2]$, $\frac{\mu}{T} (\frac{\partial v}{\partial x})^2$, and $\frac{2\mu}{T} (\frac{\partial u}{\partial y} \frac{\partial v}{\partial x})$. The total contribution of viscous friction to the local entropy generation rate is then:

$$S_{3,f-total} = S_{3,f} + S_{3,f,marg1} + S_{3,f,marg2} + S_{3,f,marg3} \quad (2.56)$$

The form of equations 2.53 to 2.56 is the same whether the plate is kept at a fixed temperature or at a fixed heat flux density.

2.4 Physical and numerical model

In order to solve Eqs. 2.23 and 2.25 or 2.29, a 4th order Runge-Kutta scheme has been applied [121]. Values of η in the range [0;10] have been discretized with 1000 nodes and $\eta = \infty$ has been replaced by $\eta = 10$ in the boundary conditions at infinity [16]. The function $f(\eta)$ and its first and second derivatives (Fig. 2.2) have been checked against tabulated values available in the literature [87, 116, 110]. The value of $\theta'(0)$ has also been checked against Churchill and Ozoe correlations [53, 54] for values of Pr number between 0.1 and 10 and are also in excellent agreement (Fig. 2.3). We have applied the laminar boundary layer model solved by adopting the similarity approach when $Pr = 1$:

the corresponding local friction coefficient $C_{f_x} = 2f''(0)Re_x^{-1/2}$ leads to a total drag coefficient (Blasius drag law) valid for laminar flows [208]. The local Nusselt number $Nu = \theta'(0)Re_x^{1/2}$ is in accordance with the literature [53, 54]. Numerical integration of Ω in Eqs. 2.39, 2.40, 2.41, 2.48, 2.49, 2.50, and S_1 in Eq. 2.51 have been performed by using the Simpson's rule.

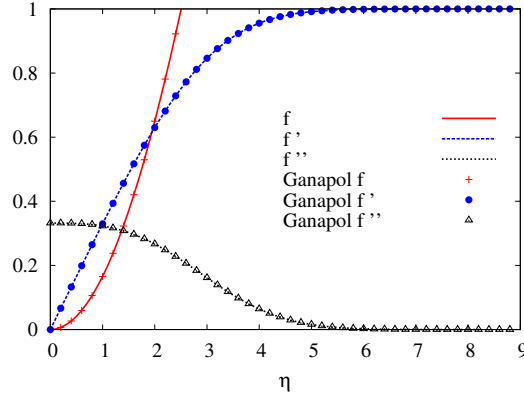


Figure 2.2: Functions f , f' and f'' cross-checked with Ganapol [87]

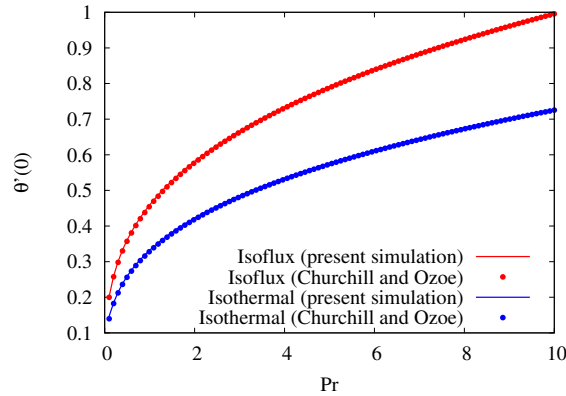


Figure 2.3: $\theta'(0)$ cross-checked with Churchill and Ozoe [53, 54]

For all simulations, $Pr = 1$. In order to be able to compare isothermal and isoflux simulations, with different values of the thermal ratio τ , a fixed reference position along the plate is set once for all and named x_{ref} . At this reference position $Re_{ref} = Re(x_{ref}) = 1000$ and the plate temperature is set to $T_{w,ref} = T_w(x_{ref}) = 1000K$. For each simulation a value of $\tau_{ref} = \tau(x_{ref})$ is set at the reference position and the corresponding values of $\Delta T_{ref} = \Delta T(x_{ref})$ and $Ec_{ref} = Ec(x_{ref})$ are then known. In order to keep U_∞ to the same value for all simulations while τ_{ref} is changed, the ratio $Ec_{w,ref} = U_\infty^2 / (C_p T_{w,ref}) = Ec_{ref} / \tau_{ref}$ is set to the fixed value 0.005 (e.g.: if $\tau_{ref} = 2$, $Ec_{ref} = 0.01$ at the reference position $Re_{ref} = 1000$). For an isothermal plate, T_w , τ , ΔT , and Ec are constant along the plate. For an isoflux plate they depend on Re_x and obey the following equations:

$$T_w(Re_x) = \frac{T_{w,ref}}{\tau_{ref}} \left(\tau_{ref} - 1 + \sqrt{\frac{Re_x}{Re_{ref}}} \right) \quad (2.57)$$

$$\Delta T(Re_x) = \frac{T_{w,ref}}{\tau_{ref}} \sqrt{\frac{Re_x}{Re_{ref}}} \quad (2.58)$$

$$Ec(Re_x) = Ec_{w,ref} \tau_{ref} \sqrt{\frac{Re_{ref}}{Re_x}} \quad (2.59)$$

$$\tau(Re_x) = 1 + (\tau_{ref} - 1) \sqrt{\frac{Re_{ref}}{Re_x}} \quad (2.60)$$

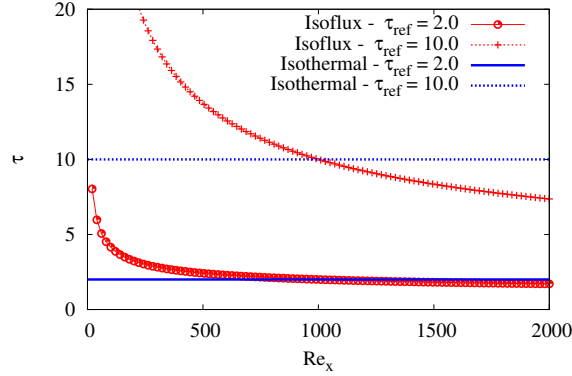


Figure 2.4: Variation of τ as a function of Re_x

When going further from the leading edge, the wall temperature and the temperature gap increase while there is a decrease of the Ec number and of τ (see Fig. 2.4), the latter approaching 1 when Re_x approaches infinity

2.5 Results

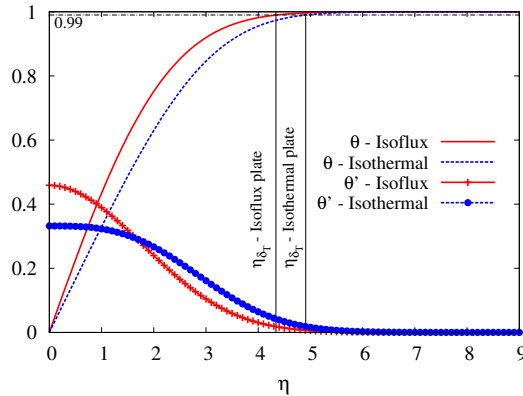


Figure 2.5: θ and θ' functions for an isothermal and an isoflux plate

The functions $\theta(\eta)$ in the isothermal and isoflux cases are derived from different differential equations (Eqs. 2.25 and 2.29 respectively) that lead to distinct solutions (Fig. 2.5) and different values of $\theta'(0)$ in particular: at a given position along the plate and with the same temperature gap, the temperature gradient is higher at the plate in the isoflux case. The thermal boundary layer thickness is also smaller in the isoflux case (even if $Pr = 1$).

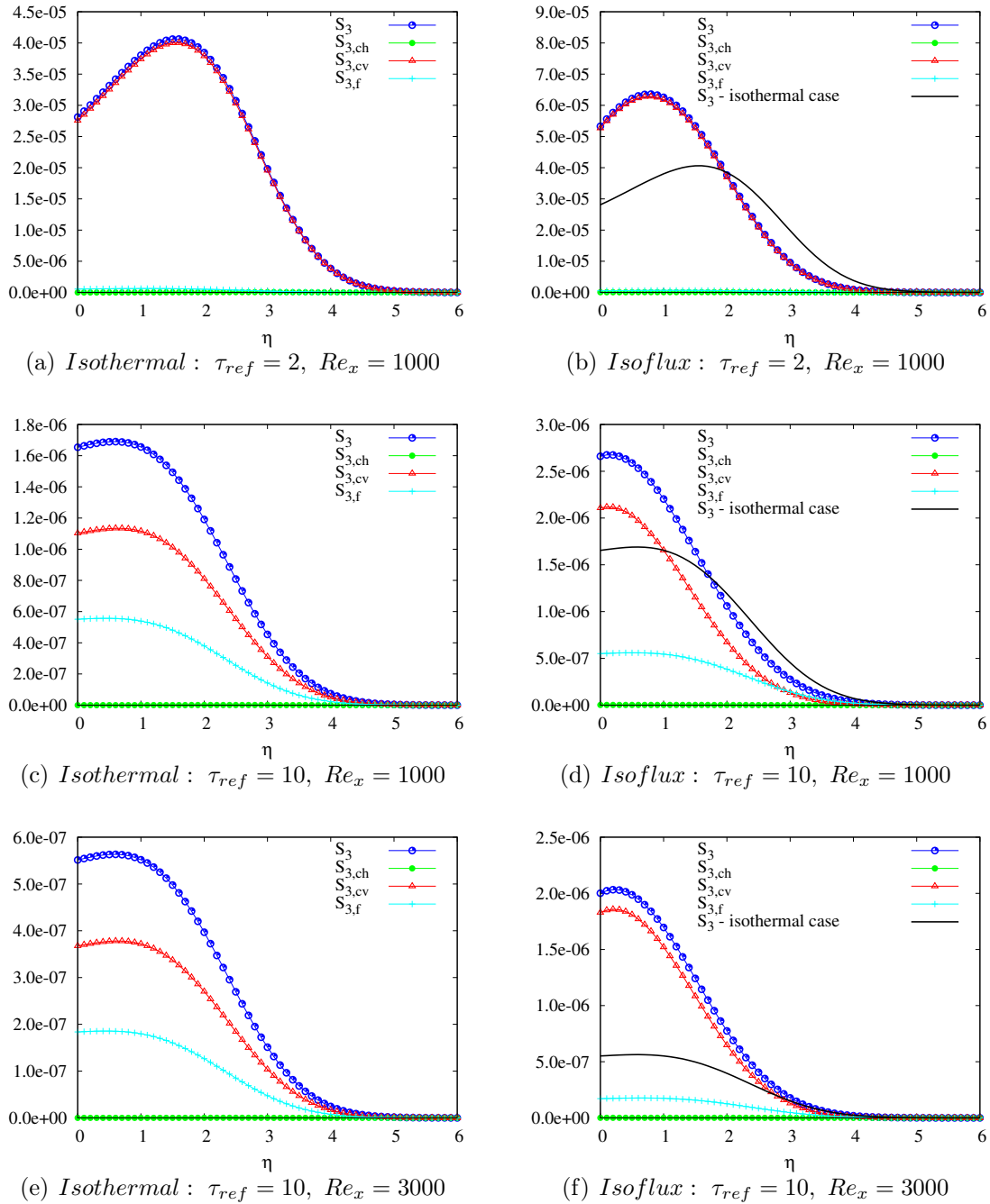


Figure 2.6: Local entropy generation rate. Isothermal (left) and Isoflux (right). The isothermal curve S_3 is also plotted as a reference on the corresponding isoflux chart (black plain line).

2.5.1 Local entropy production rates

The dimensionless local entropy generation rate S_3 depends on the thermal ratio τ_{ref} , on the local Reynolds number Re_x and on the type of thermal boundary condition, as shown in Figs. 2.6. The entropy generation rate at the plate is strictly positive because of the non-zero local temperature gradient. It increases to a local maximum and then decreases and vanishes when reaching the isentropic free stream. The temperature gradient reaches its τ maximum at the plate and then decreases when η increases. The

presence of a maximum in entropy generation rate above the plate comes from the rate of decrease of the square of temperature: near the plate, the temperature ($T = T_w - \theta\Delta T$) decreases rapidly while its gradient has a small negative slope (see Fig. 2.5) and this contributes to an increase of the entropy generation rate. Further from the plate, the rate of decrease of the gradient becomes higher than the one of the temperature and the entropy generation rate decreases. As will be shown hereafter, the location of the maximum of S_3 depends on the value of τ_{ref} . Local entropy generation rate profiles as a function of the dimensionless distance from the wall can be compared with those presented by several authors who studied the boundary layer in different configurations and show a similarity of form [210, 206]. This is the case, in particular, about the existence of a local maximum of entropy generation rate by unit of volume, whose distance from the wall depends on the boundary conditions [155, 74]. A check has been made with [155]: The equations of the dimensionless entropy generation rate are equivalent and the position of the maximum on local entropy generation are compatible.

At a given position along the plate, increasing τ_{ref} , which means decreasing the relative importance of the temperature gap, leads to a decrease of S_3 whatever the boundary condition type (Fig. 2.6(c) vs Fig. 2.6(a) and Fig. 2.6(d) vs Fig. 2.6(b)). Greater values of τ_{ref} also bring the local maximum of $S_3(\eta)$ closer to the plate: for high values of τ_{ref} and not too close to the leading edge (where horizontal conduction and usually marginal viscous terms are no longer negligible), the main contribution to the entropy generation rate comes from the main viscous friction component $S_{3,f}$ which is strictly decreasing and has its maximum located at the plate.

If τ_{ref} is fixed and the position along the plate varies, an increase of Re_x corresponds to a decrease of the local entropy generation rate (Fig. 2.6(e) vs Fig. 2.6(c) and Fig. 2.6(f) vs Fig. 2.6(d)).

For a given τ_{ref} and a given position along the plate, S_3 depends on the boundary condition type. In the case of an isoflux plate, the position of the local maximum of $S_3(\eta)$ is closer to the wall and it is the same for the vanishing point as the thermal boundary layer thickness is smaller for the isoflux case (compare left vs right columns in Figs. 2.6). Far from the leading edge and near the plate S_3 is greater in the isoflux case. The crossing point value of η where S_3 is the same whatever the boundary condition type increases when Re_x increases.

The composition of S_3 also depends on τ_{ref} and Re_x . The relative importance of the viscous part is greater when τ_{ref} increases and the proportion increase depends on the boundary condition type (Fig. 2.6(c) vs Fig. 2.6(a) and Fig. 2.6(d) vs Fig. 2.6(b)).

The influence of Re_x on the relative values of the components of the local entropy generation rate also depends on the boundary condition type. For an isothermal plate, the main effect appears when getting closer to the leading edge where the horizontal conduction part becomes no longer negligible and puts the local maximum a bit further from the wall as shown in Fig. 2.7(a). Moreover, the additional terms (see Eqs. 2.53, 2.54, and 2.55) contributing to the viscous friction entropy generation rate are no longer negligible: this can be seen in the same figure where the total viscous friction effect $S_{3,f-total}$ is shown along with the usual computation $S_{3,f}$ that neglects the otherwise marginal terms.

For an isoflux plate, the major effect of increasing Re_x is the decrease of the relative contribution of the viscous component. This effect appears all the more near the edge as the parameter τ_{ref} is smaller. Close to the leading edge, marginal contributors to

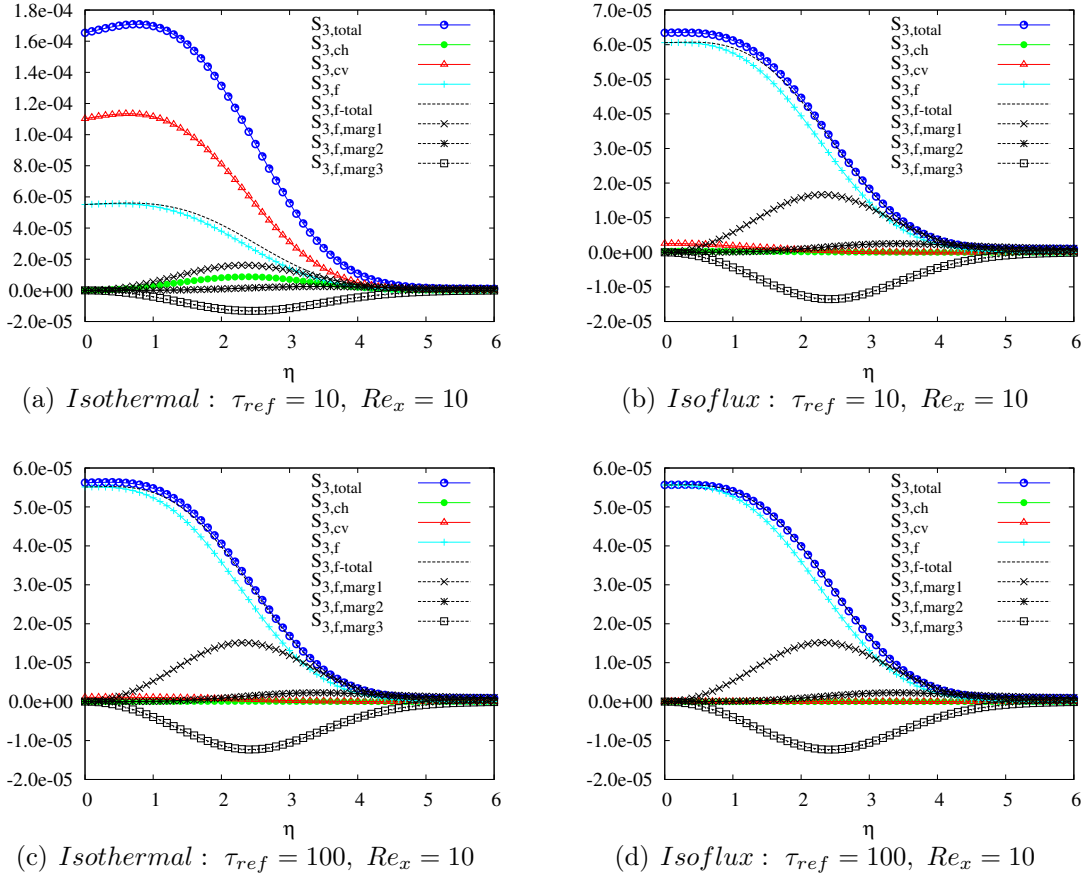


Figure 2.7: Local entropy generation rate. Isothermal (left) and Isoflux (right), showing all marginal viscous friction contributors.

viscous friction entropy generation become visible (Fig. 2.7(b)) as in the isothermal case. However, for an isoflux plate, the horizontal conduction term stays negligible even for low values of Re_x .

The marginal viscous friction terms (Figs. 2.7) become visible near the leading edge: they contribute positively ($S_{3,f,marg1}$ and $S_{3,f,marg2}$) or negatively ($S_{3,f,marg3}$, because the wall normal component of the velocity decreases with the abscissa for a fixed ordinate) to the entropy generation rate, the sum of all the contributors to the viscous friction entropy generation rate (marginal or not) being positive. As can be seen in Figs. 2.7(b), 2.7(c), and 2.7(d), $S_{3,f,marg2}$ can be non zero when moving far from the plate and reaching the free stream zone. This term is related to the longitudinal derivative of the vertical velocity component (Eq. 2.54): the Blasius boundary layer model leads to a non-zero vertical component of the velocity in the free stream area [208] and to a non zero longitudinal derivative of this component. $S_{3,f,marg2}$ reaches an asymptotic value when $\eta \rightarrow \infty$ that goes closer to zero when Re_x is increased.

2.5.2 Surface entropy production rates

The dimensionless surface entropy generation rate S_2 depends on τ_{ref} and on the position along the plate. For a given Re_x and whatever the thermal boundary condition type, increasing τ_{ref} leads to a decrease of S_2 .

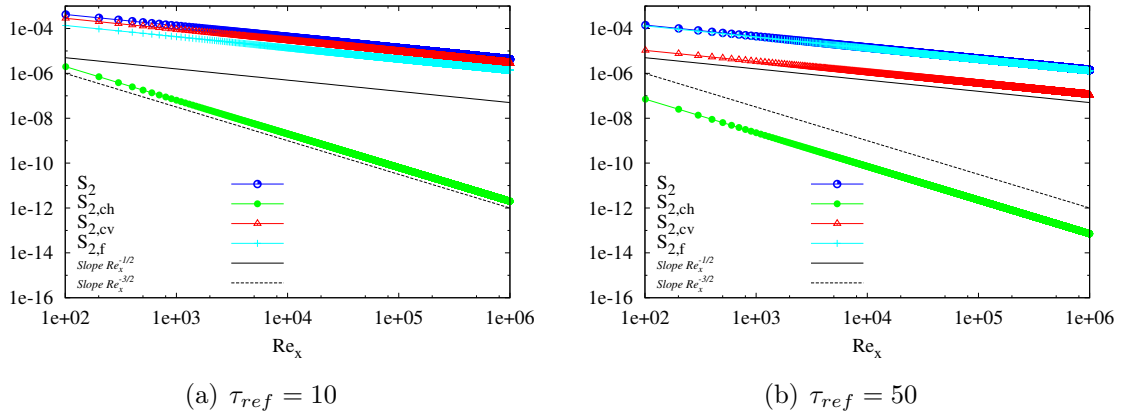


Figure 2.8: Isothermal plate surface entropy generation rates for two values of τ_{ref} and Re_x from 100 to 1000000

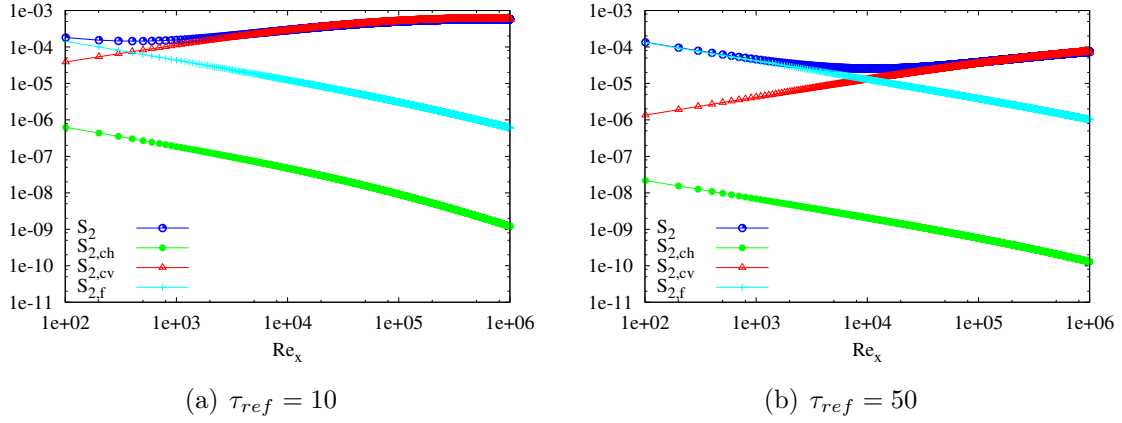


Figure 2.9: Isoflux plate surface entropy generation rates for two values of τ_{ref} and Re_x from 100 to 1000000

For an isothermal plate and a given τ_{ref} , going further from the leading edge, i.e. increasing Re_x , leads to lower surface entropy generation rates as exhibited in Figs. 2.8(a) and 2.8(b) (the behavior of S_2 is shown for values up to $Re_x = 10^6$, i.e. above the usual critical Reynolds number around 5×10^5 , in order to reveal asymptotic trends. Moreover, critical Reynolds up to 3×10^6 can be observed [244]). Indeed, all Ω integrals (Eqs. 2.39, 2.40 and 2.41) stay constant and neither τ nor Pr or Ec number vary along the wall. Thus, the horizontal conduction part of the entropy generation is inversely proportional to $(Re_x)^{3/2}$ and the vertical conduction like the friction parts are inversely proportional to $(Re_x)^{1/2}$. The boundary layer thickness increases while the temperature gap stays constant when moving further from the leading edge. This causes the entropy generation rate coming from the vertical conduction to be smaller. A similar reasoning explains the decrease of the major contributor to the viscous friction entropy generation rate ($S_{3,f}$) as the dynamic boundary layer thickness increases for a constant longitudinal speed gap between the plate and the free stream flow. In fact, all terms, including marginal ones are decreasing, some at high rates (like $S_{3,f,marg2}$).

For an isoflux plate, the dependence of S_2 on Re_x is more complex and is the result of the competition of two opposite causes. As shown in Fig. 2.9(a) and 2.9(b), near

the leading edge, S_2 is a decreasing function of Re_x and reaches a local minimum (around $Re_x = 400$ for $\tau_{ref} = 10$ and around $Re_x = 11500$ for $\tau_{ref} = 50$). Then, S_2 increases with the distance from the leading edge and reaches a local maximum (around $Re_x = 640000$ for $\tau_{ref} = 10$), after which it starts decreasing again. The position of the local maximum and minimum are all the more distant from the leading edge so as τ_{ref} is high. Increasing Re_x leads to two opposite effects: on the one hand, τ decreases (see Eq. 2.60) and corresponds to higher temperature gaps, pushing up entropy generation rates coming from the vertical conduction of heat. On the other hand, the boundary layer thickness increases when Re_x is higher and this contributes to a reduction of the entropy generation rate. The actual trend thus depends on the combination of these two effects. Far from the leading edge (when $Re_x \gtrsim 640000$ if $\tau_{ref} = 10$, for example), the major contributor to the surface entropy generation rate comes from the vertical conduction of heat and the decrease of $S_2(Re_x)$ is mainly due to the boundary layer increase while $\tau(Re_x)$ is quite flat (Eq. 2.60). For intermediate Re_x , the vertical conduction component is still the main contributor but it is increasing with Re_x because $\tau(Re_x)$ is now decreasing quickly with the abscissa (the relative value of the temperature gap in relation to the wall temperature is growing fast). Near the leading edge (when $Re_x \lesssim 400$ if $\tau_{ref} = 10$, for example), the main contributor to the surface entropy generation rate is the viscous friction term which is decreasing with Re_x and causes the surface entropy generation rate to decrease alongside.

2.5.3 Total entropy production rates

The dimensionless total entropy generation rate between two positions Re_a and Re_b along the plate is a strictly decreasing function of τ_{ref} . For an isoflux plate (Fig. 2.10), the abscissa of the crossing point of the viscous and the conduction parts is increasing when the integration interval $[Re_a; Re_b]$ is located further from the leading edge. This can occur because Re_a is greater with the same interval length (Fig. 2.10(b) vs 2.10(a)) or because the length of the interval is greater with the same starting Re_a (Fig. 2.10(c) vs 2.10(a)).

When the total thermal power (q_1 in dimensionless form: see Eq. 2.61) exchanged between the plate and the fluid, starting from a given position Re_a , is fixed, the dimensionless total entropy generation rate S_1 exhibits a minimum of entropy generation for an optimum value of τ_{ref} named τ_{opt} (Fig. 2.11).

$$q_1 = \frac{q'}{kT_{w,ref}} \quad (2.61)$$

For high values of τ_{ref} , the main contribution to the entropy generation comes from the viscous friction. The temperature gap between the plate and the fluid is small alongside and to keep the fixed thermal power, the exchange length must be increased. These two factors combine to produce high entropy generation rates. On the other hand, when τ_{ref} is small, the major contributor is the thermal conduction that occurs across high temperature gaps and this leads also to high entropy generation rates. These two opposite trends lead to an intermediate value of τ_{ref} where they are balanced (the sum of their derivatives with respect to τ_{ref} is zero) and where the entropy generation rate is minimum.

The total entropy generation rates between two longitudinal positions along the plate when the exchanged heat power is fixed can be compared with a reference model

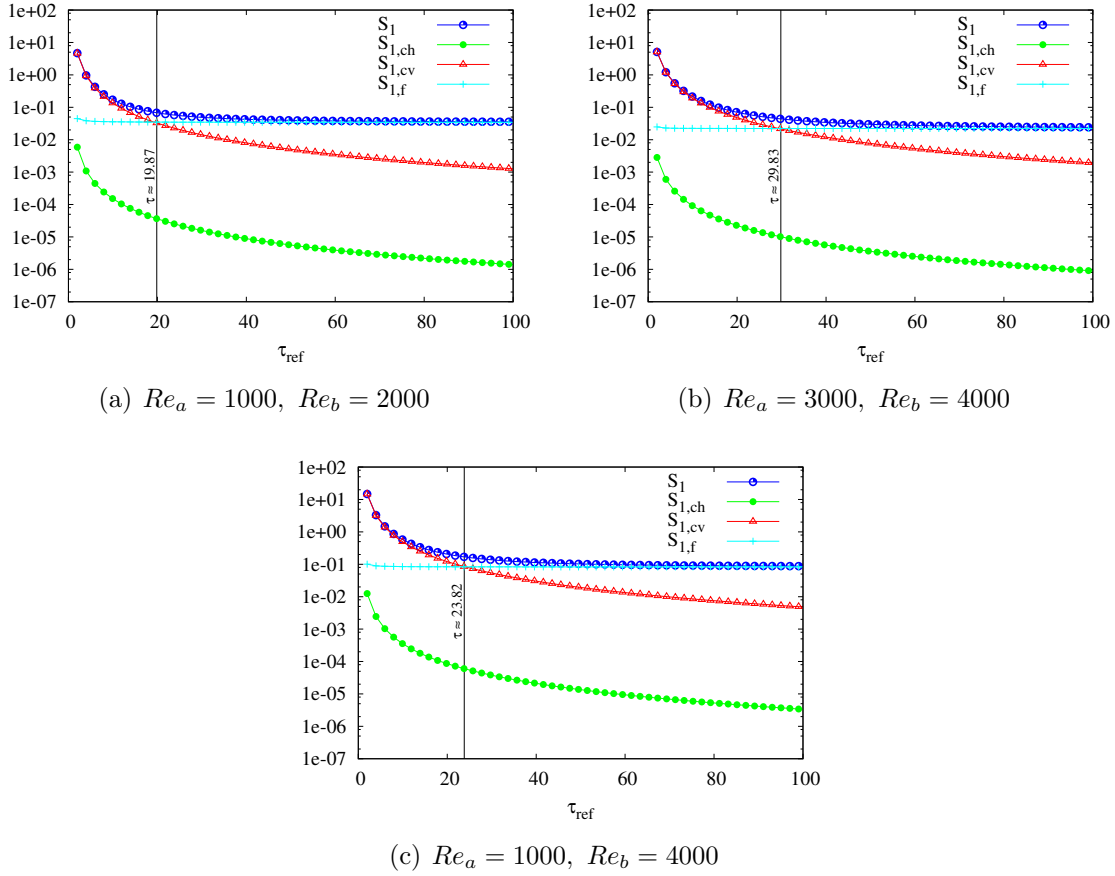


Figure 2.10: Isoflux plate total entropy generation rate between two positions Re_a and Re_b

that adopts useful simplifications [23], namely that the generation of entropy by horizontal conduction is neglected and the temperature difference between the fluid and the plate is considered small enough to be neglected in comparison to the temperature (Fig. 2.12). For large values of τ (above ≈ 15), there is a convergence with the simplified model. The gap is growing rapidly for very small values (below ≈ 5), but in this case, the thermo-dependence of the fluid should normally be taken into consideration in the two compared models. In the intermediate range of τ values, the model presented in this study, which does not neglect ΔT in front of T , would be more appropriate.

The optimal value of τ_{ref} depends on the thermal boundary condition type. As an example, when $q_1 = 26.67$ and $Re_a = 1000$, the optimum value of τ_{ref} is around 15 for an isothermal plate and about 132 for an isoflux plate. This demonstrates that the boundary condition type has a major influence on the behavior of $S_1(\tau_{ref})$ when an energetic constraint is set. Moreover, in the isothermal case, stepping further from the optimum value has a significant influence on the generated entropy because of the relatively small radius of curvature of the curve at this point (see Fig. 2.11 around $\tau_{ref} = 15$). In the isoflux case, $S_1(\tau_{ref})$ is almost flat in a large interval centered on the optimal value of τ and operating values of τ_{ref} can be distant from the optimum value without increasing the total entropy generation rate in a major proportion (see Fig. 2.11 in the interval $\tau_{ref} = 90$ to 200, where S_1 defers from the optimum value by no more than 2%). Whatever the boundary condition type, the negative slope of the

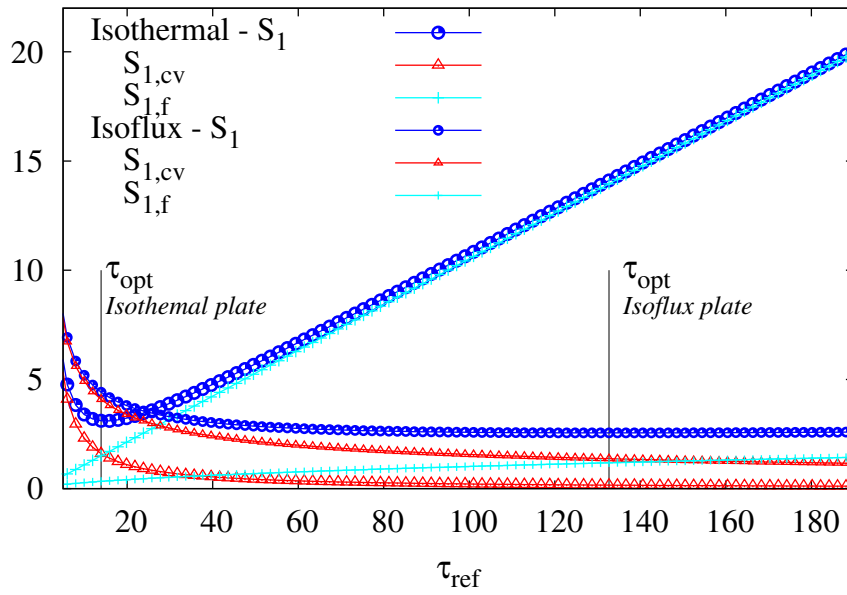


Figure 2.11: Total entropy generation rate starting at $Re_a = 1000$ with $q_1 = 26.67$ (τ_{ref} spreads from 5 to 190.)

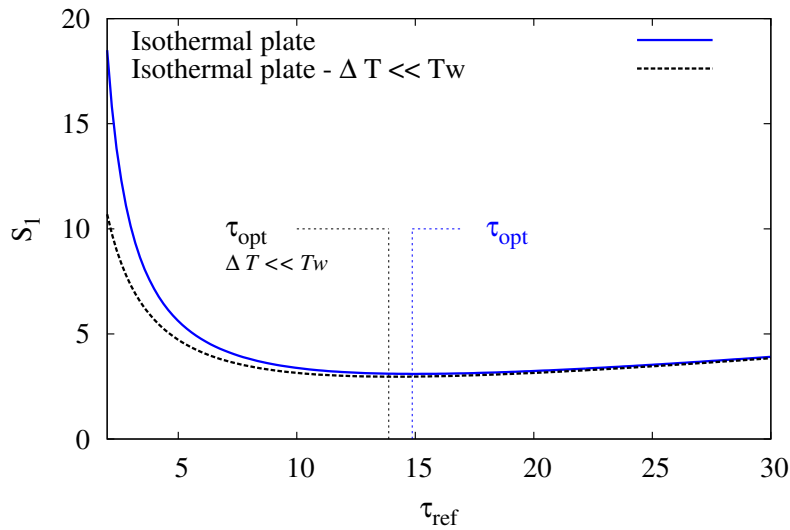
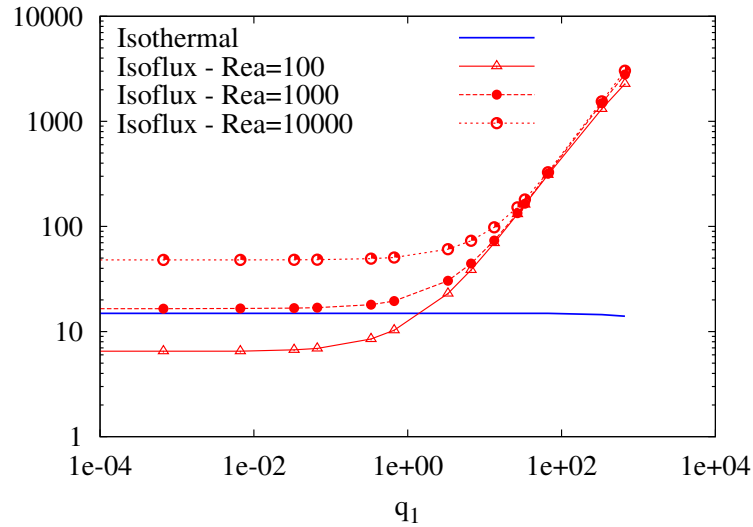
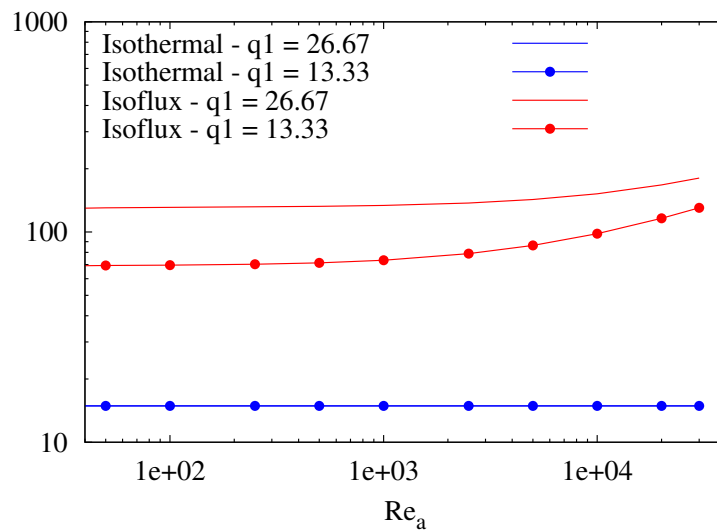


Figure 2.12: Isothermal plate ($Re_a = 1000$, $q_1 = 26.67$, $2 \leq \tau_{ref} \leq 30$): Comparison with a model where $\Delta T \ll T_w$

total entropy generation rate is rather steep for low values of τ_{ref} (see Fig. 2.11 for $\tau_{ref} \lesssim 10$) and this could have a major effect for highly non-isothermal applications, like receivers of concentrated solar power plants: moving to bigger values of τ_{ref} can reduce the total entropy generation rate significantly. Nevertheless, it must be kept in mind that this is observed in the case of a simplified model that is used as a reference and has to be confirmed for a thermo-dependent fluid.

Another major difference comes from the thermal boundary condition type : for an isothermal plate, the optimum value of τ_{ref} appears to be independent on the

Figure 2.13: τ_{opt} as a function of q_1 Figure 2.14: τ_{opt} as a function of Re_a

integration starting point Re_a and on the exchanged thermal power q_1 . For an isoflux plate, τ_{opt} increases when q_1 increases (Fig. 2.13) and the larger the thermal power to evacuate between the plate and the fluid, the lesser the optimal relative temperature gap at the reference point must be. In the isoflux plate case τ_{opt} is also an increasing function of Re_a (Fig. 2.14).

2.6 The relative importance of the viscous dissipation function

Until now, the viscous dissipation function Φ has been neglected in the energy equation. It is legitimate to ask whether this is justified and what impact the absence of this term may have on the solution temperature field. It is also useful to justify why Φ could be neglected in the energy equation while keeping it for the calculation of the entropy generation rate. The purpose of this chapter is to provide some answers to these questions.

Let us consider the case of the steady two-dimensional flow in a laminar boundary layer over an isothermal flat plate, for an incompressible fluid with constant properties and without pressure gradient in the free flow (U_∞ is constant in the free flow). With this set of assumptions, the boundary layer energy equation writes (the viscous dissipation term is not neglected and is considered for its majority part in the boundary layer):

$$\rho C_p (u \frac{\partial T}{\partial x} + v \frac{\partial T}{\partial y}) = k \frac{\partial^2 T}{\partial y^2} + \mu (\frac{\partial u}{\partial y})^2 \quad (2.62)$$

The dimensionless quantities are defined in Eqs. 2.63 [208], which leads to the dimensionless equation in Eq. 2.64:

$$x^\times = \frac{x}{L}, \quad y^\times = \frac{y}{L} \sqrt{Re}, \quad u^\times = \frac{u}{U_\infty}, \quad v^\times = \frac{v}{U_\infty} \sqrt{Re}, \quad T^\times = \frac{T_w - T}{T_w - T_\infty} \quad (2.63)$$

$$u^\times \frac{\partial T^\times}{\partial x^\times} + v^\times \frac{\partial T^\times}{\partial y^\times} = \frac{1}{Pr} \frac{\partial^2 T^\times}{\partial (y^\times)^2} + Ec (\frac{\partial u^\times}{\partial y^\times})^2 \quad (2.64)$$

The ratio between the viscous and conductive terms in Eq. 2.64 is:

$$Pr Ec \frac{(\frac{\partial u^\times}{\partial y^\times})^2}{\frac{\partial^2 T^\times}{\partial (y^\times)^2}} \quad (2.65)$$

For a fluid like air, which Prandtl number is not far from 1, the order of magnitude of the ratio in Eq. 2.65 is $Pr Ec$ as within the boundary layer, each of the terms in the fraction has an order of magnitude ≈ 1 . Thus the viscous and conductive terms in the equation of the energy are in a ratio equal to the Brinkman number Br :

$$Br = Pr Ec = \frac{\mu U_\infty^2}{k \Delta T} \quad (2.66)$$

In an air solar receiver case with $\Delta T = 500K$, $Pr = 0.7$, $U_\infty = 40 \text{ m.s}^{-1}$, $C_p = 1005 \text{ J.K}^{-1}.\text{kg}^{-1}$, the Brinkman number is around $2 \times 10^{-3} \ll 1$ and it is possible to neglect the viscous dissipation term when solving the temperature equation. This would not be the case for high Mach flows or very viscous fluids, for example [36].

Let us now examine the entropy generation rate:

$$\dot{S}_{gen}''' = \frac{k(\nabla T)^2}{T^2} + \frac{\phi}{T} \approx \frac{k}{T^2} (\frac{\partial T}{\partial y})^2 + \frac{\mu}{T} (\frac{\partial u}{\partial y})^2 \quad (2.67)$$

By multiplying this expression by $\frac{\nu^2}{kU_\infty^2}$ in order to use a dimensionless form of the entropy generation rate (S_3) and replacing T , u and y by their expressions as functions of T^\times , u^\times and y^\times , one gets the following expression for the dimensionless entropy generation rate (where $\tau = T_w/(T_w - T_\infty)$):

$$S_3 = \frac{1}{Re(\tau - T^\times)^2} \left(\frac{\partial T^\times}{\partial y^\times} \right)^2 + \frac{PrEc}{Re(\tau - T^\times)} \left(\frac{\partial u^\times}{\partial y^\times} \right)^2 \quad (2.68)$$

This dimensionless entropy generation rate includes two terms, one viscous and the other conductive, their ratio being:

$$PrEc(\tau - T^\times) \left(\frac{\frac{\partial u^\times}{\partial y^\times}}{\frac{\partial T^\times}{\partial y^\times}} \right)^2 \quad (2.69)$$

The order of magnitude of this ratio is $PrEc(\tau - T^\times)$. Thus the viscous and conductive terms in the equation of the entropy generation rate are in a ratio equal to the $Br(\tau - T^\times)$. If $\tau \gg 1$, this order of magnitude becomes $PrEc \times \tau$ which can be very different from the ratio found for the energy terms.

In the case of flows for which $\tau \gg 1$ and $Br \ll 1$, one could encounter situations where the viscous dissipation term could be neglected in the equation of energy but not in the calculation of the generated entropic power.

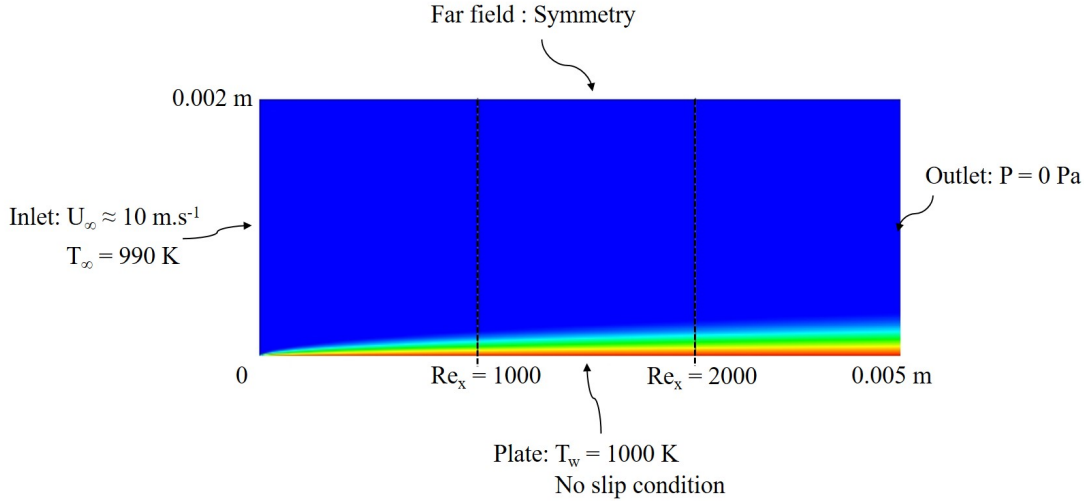


Figure 2.15: Simulation1 and Simulation2 boundary conditions

In order to study this case more closely, two boundary layer simulations were performed by solving the incompressible Navier-Stokes equations with the ANSYS Fluent software, in a 5 mm long \times 2 mm high domain, containing 500×200 mesh cells and with the following conditions (Fig. 2.15): $U_\infty = 10.02497$ m.s⁻¹, $T_\infty = 990$ K, $T_w = 1000$ K, $C_p = 1005$ J.K⁻¹.kg⁻¹, $k = 1.5 \times 10^{-2}$ W.m⁻¹.K⁻¹, $\mu = 1.4925 \times 10^{-5}$ Pa.s. Therefore, the Brinkman number is $Br = 0.01$ and its product by τ is $Br.\tau = 1$. Under these conditions, it is expected that the orders of magnitude of the viscous and conductive

components in the entropy generation rate are identical and that, in addition, the viscous dissipation term in the energy equation is negligible (around 1% of the conductive term).

In the first simulation (Simulation1), the energy equation is solved without taking into account Φ . In the second (Simulation2), the viscous dissipation term is kept in the energy equation. The comparison between these two simulations addresses the temperature field, the entropy generation rates and the energy and entropy balances (carried out in a control volume limited below by the plate, above by a border located "far" from the boundary layer, at the entrance by the plane $Re_x = 1000$ and at the exit by the plane $Re_x = 2000$). The values are expressed with a number of decimal places allowing to show the differences between two executions of the code with different settings: this does not mean that the real accuracy of the simulation is of this order of magnitude.

Table 2.1: Entropy generation rate by unit of transversal length [$W.K^{-1}.m^{-1}$]

	$\dot{S}'_{gen,c}$	$\dot{S}'_{gen,f}$
Simulation 1	1.1115×10^{-5}	1.546457×10^{-5}
Simulation 2	1.1139×10^{-5}	1.546460×10^{-5}

The entropy generation rates are presented in Table 2.1 and are very close between the two simulations (the relative difference being slightly more pronounced in relative terms for the entropy generation by conduction, i.e.: 0.22% for Simulation2 compared to Simulation1).

In addition, the ratio between the entropy generation rate by viscous friction $\dot{S}'_{gen,f}$ and the one generated by conduction $\dot{S}'_{gen,c}$ is 1.39. The entropic power created by viscous effect is not negligible at all in these cases. The dimensionless parameter $Br.\tau = 1$ predicts that the orders of magnitude of the entropy generation rates created by conduction and by viscous friction are the same and this is indeed the case ($10^{-5} W.K^{-1}.m^{-1}$).

The temperature profiles as a function of the distance to the wall, taken at the abscissa $Re_x = 1000$, $Re_x = 2000$ and at the output ($Re_x = 2949$) (Fig. 2.16) indicate that the temperature fields are almost identical between the two simulations. The temperature difference between the two simulations is also shown and does not exceed 0.014 K (Fig. 2.17). Thus, neglecting the viscous dissipation term when solving the energy equation has a negligible impact on the resulting temperature field.

The mass balance between $Re_x = 1000$ and $Re_x = 2000$ does not show any discrepancy (incoming and outgoing mass flow rates are equal up to the 9th decimal and are about $0.0176 kg.s^{-1}$ for both simulations). The momentum balances show a relative deviation of 0.65% (for the longitudinal projection) and 0.66% (for the normal projection to the wall). The absolute deviation is the gap between the net flux of momentum (outgoing minus incoming) on the one hand, and the sum of the pressure and viscous forces acting on the fluid, on the other hand. The relative deviation is to relate this

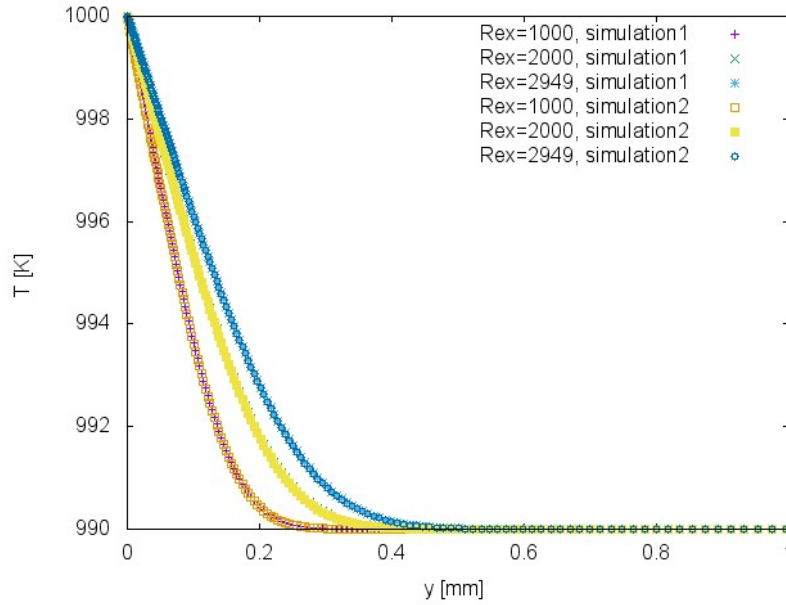


Figure 2.16: Temperature as a function of the distance to the wall

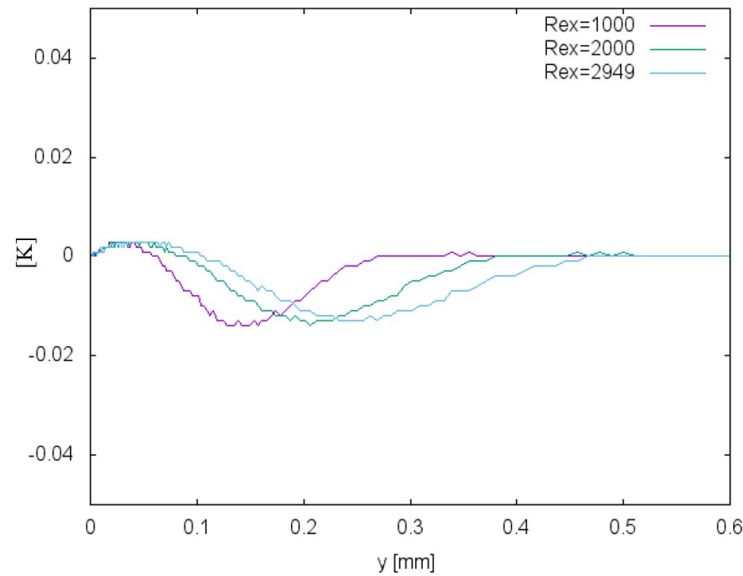


Figure 2.17: Temperature gap between Simulation1 and Simulation2 as a function of the distance to the wall

absolute gap to the net flux of momentum. If the absolute deviation on the longitudinal projection of the momentum balance is related to the incoming momentum flux, for example, the relative deviation is only 0.01%.

The internal energy balance in the control volume is presented in Table 2.2: It can be seen that the relative error in the internal energy balance is less than 1% and is of similar importance for both simulations. If the absolute deviation is related to the incoming flux, the relative deviation is less than 10^{-4} %. The absolute error is about $9 \times 10^{-3} \text{ W.m}^{-1}$, a value that is of the same order of magnitude as the viscous dissipation term (about $1.5 \times 10^{-2} \text{ W.m}^{-1}$). Simulation1 is solved by neglecting the

viscous dissipation term in the energy equation and it is also possible to compute the balance deviation without this term by performing the A-B difference in table 2.2 (although the velocity field actually calculated results in a non-zero value of this dissipation). The absolute error is then higher but keeps the same order of magnitude ($10^{-2} W.m^{-1}$). In addition, the ratio between viscous and conductive heating is about 0.011, in good agreement with the value predicted by the Brinkman number (10^{-2}).

Table 2.2: Internal energy balance by unit of transversal length [$W.m^{-1}$]

	Simulation 1	Simulation 2
(A) Net convective flux (out - in)	1.43	1.426
(B) Net conductive flux (out - in)	1.40576	1.40144
(C) Viscous dissipation	0.01541	0.01541
Absolute deviation (A-B-C)	0.00884	0.00915
Relative deviation (A-B-C)/A	0.62%	0.64%
Viscous/conduction ratio (C/B)	0.01096	0.01099

It is also interesting to examine the deviation found in the equation actually solved by Fluent (Eq. 2.70): the absolute deviation is still around $10^{-2} W.m^{-1}$ and the relative deviation around 1% (less than 10^{-4} % if related to the incoming convective flux of total energy).

$$\nabla \cdot (\mathbf{V}(\rho e_M + P)) = \nabla \cdot (k \nabla T + \bar{\bar{\tau}} \cdot \mathbf{V}), \quad e_M = h - \frac{P}{\rho} + \frac{|\mathbf{V}|^2}{2} \quad (2.70)$$

The entropy balance in the control volume is presented in Table 2.3: the relative deviation in the entropy balance is also less than 1% (and less than 10^{-4} % if related to the incoming convective flux of entropy). The creation of entropy is about 2% of the net conductive flux or the net convective flux.

In order to qualify the numerical convergence, it can be noted that the evolution of internal energy and entropy fluxes (entering at $Re_x = 1000$ and leaving at $Re_x = 2000$) as a function of the residue for the energy equation stabilize from 10^{-11} (Figs. 2.18 and 2.19). The relative deviation in the internal energy and entropy balances is reduced to less than 1% also from 10^{-11} (Fig. 2.20). Simulations were conducted to a residue of 10^{-16} .

Finally, in order to study the influence of the mesh, two additional simulations were carried out with a mesh twice as fine in the normal direction to the wall. The above conclusions remain valid and so do the orders of magnitude. The balances are slightly improved: the momentum balance in the normal direction goes from 0.66% to 0.61% in relative deviation. The entropy and internal energy balances are also improved: the relative deviations are 0.60% and 0.55% respectively, instead of the previous 0.67% and 0.62% for Simulation1.

Table 2.3: Entropy balance by unit of transversal length [$W.K^{-1}.m^{-1}$]

	Simulation 1	Simulation 2
(A) Net convective flux (out - in)	0.00144	0.00144
(B) Net conductive flux (out - in)	0.00141	0.00140
(C) Entropy generation	2.65795×10^{-5}	2.66038×10^{-5}
Absolute deviation (A-B-C)	9.67285×10^{-6}	8.97109×10^{-6}
Relative deviation (A-B-C)/A	0.67%	0.62%

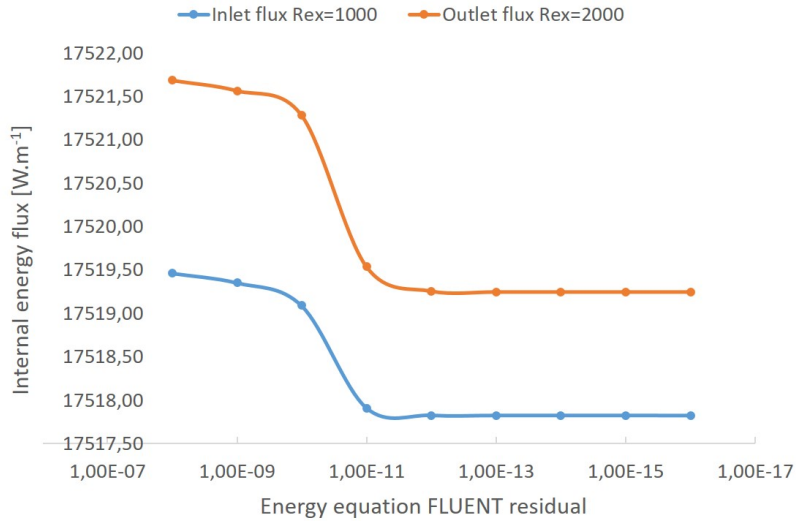


Figure 2.18: Internal energy (convective) fluxes as functions of the energy equation residual

To summarize, the theoretical analysis (in the particular case of the laminar steady state boundary layer of an incompressible fluid with constant thermo-physical properties) indicates that the relative importance of the viscous dissipation function compared to the conductive term in the heat equation is in the order of the Brinkman number. Moreover, the relative importance of the entropic power created by viscous effect compared to the production by heat conduction is in the order of the Brinkman number multiplied by the dimensionless thermal ratio τ (as long as τ is well above 1). A pair of simulations, with $Br = 0.01$ and $Br.\tau = 1$, one of which taking into account the viscous dissipation term in the energy equation and the other not, confirm the theoretical analysis: neglecting the viscous dissipation term when solving the energy equation only modifies the temperature field in an extremely weak way. In addition, the entropy generation rate due to viscous friction is not negligible (it is even more important than the heat conduction part), both being of the same order of magnitude.

The total viscous dissipation is about 1% of the internal energy net convective flux

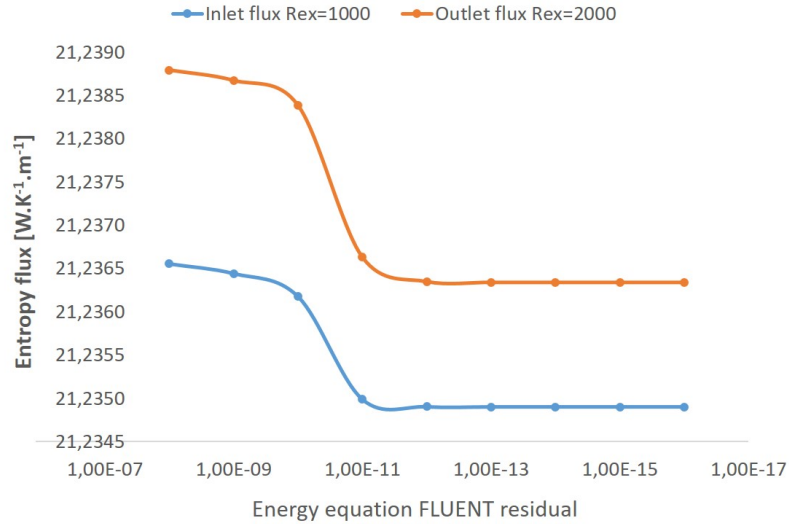


Figure 2.19: Entropy (convective) fluxes as functions of the energy equation residual

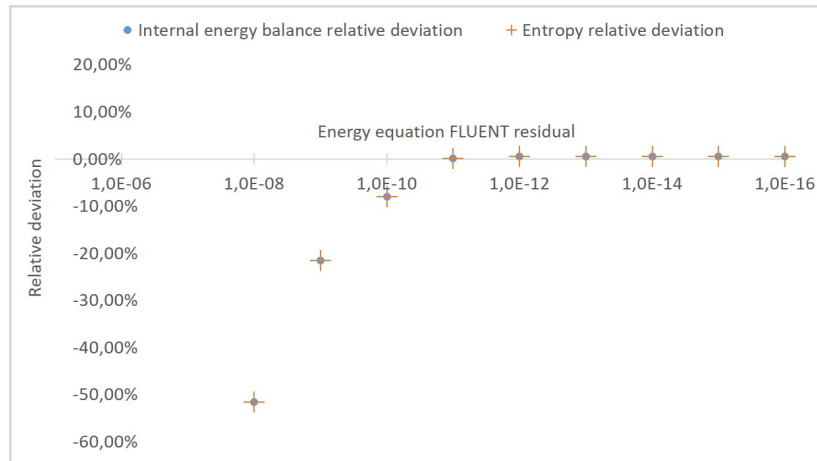


Figure 2.20: Internal energy and entropy balance relative deviation as functions of the energy equation residual

and the total generated entropic power is around 2% of the entropy net convective (or conductive) flux. Although the physical balance errors are relatively small (when compared to the net fluxes), viscous dissipation and entropy generation are of the same order of magnitude as the absolute errors in the internal energy and entropy balances respectively. This observation deserves further analysis because the calculated entropy generation rate could be of little physical significance due to numerical errors. For this reason, it is useful to make a comparison with the numerical model based on the Blasius equation and presented in detail in chapters 2.3 to 2.5.

To carry out this comparison, four simulations are performed by combining two values of the thermal ratio τ ($\tau = 2$ or $\tau = 100$) and the two boundary condition types (isothermal or isoflux plate). When $\tau = 2$, the input velocity is set at $\approx 71 \text{ m.s}^{-1}$ and the integration is performed between $Re_x = 10000$ and $Re_x = 20000$ and if $\tau = 100$, the input velocity is set at $\approx 10 \text{ m.s}^{-1}$ and the integration is performed between $Re_x = 1000$ and $Re_x = 2000$. The corresponding entropy generation rates are presented in table 2.4 and compared with the solutions of the boundary layer equations with the Blasius

equation: they are close and in any case of the same order of magnitude. Therefore, the deviation observed in the entropy balance is not concentrated in the calculation of the entropy generation rate but more likely spread over the different terms of this balance.

Table 2.4: Entropy generation rate by heat conduction and by viscous friction, by unit of transversal length [$W.K^{-1}.m^{-1}$]

Boundary condition	τ_{ref}	Equations	$\dot{S}'_{gen,c}$	$\dot{S}'_{gen,f}$
Fixed T_w	2	Blasius	0.14097	0.00211
		Navier-Stokes	0.14772	0.00264
Fixed T_w	100	Blasius	1.0346×10^{-5}	1.0300×10^{-5}
		Navier-Stokes	1.1164×10^{-5}	1.5465×10^{-5}
Fixed q''	2	Blasius	0.77142	0.00132
		Navier-Stokes	0.77039	0.00167
Fixed q''	100	Blasius	1.8955×10^{-5}	1.0308×10^{-5}
		Navier-Stokes	1.6939×10^{-5}	1.5472×10^{-5}

The relative gap between the Blasius solution and the Navier-Stokes simulation is more pronounced for the entropy generation rate by viscous friction and is to be related to the different $u(y)$ profiles of the longitudinal velocity as a function of the ordinate. These profiles are presented in Fig. 2.21 for the case $\tau = 2$ at the domain output ($Re_x \approx 20850$): whereas in Blasius' solution the longitudinal velocity increases asymptotically towards U_∞ , the Navier-Stokes solution presents an overshoot close to the wall, the velocity becoming higher than U_∞ and then decreasing to reach value. This overshoot accounts for a phenomenon that is not captured by the classical laminar boundary layer model concerning the displacement thickness of the boundary layer [60]. In the Navier-Stokes solution, the velocity gradients are stronger and the entropy generation rates by viscous friction as well.

As for the temperature profiles, whether the thermal boundary condition at the wall is of the fixed temperature or fixed heat flux density type, the Blasius and Navier-Stokes solutions provide close results (Figs. 2.22 and 2.23). However, the temperatures obtained with the Navier-Stokes equations are slightly lower than those of the Blasius approximation.

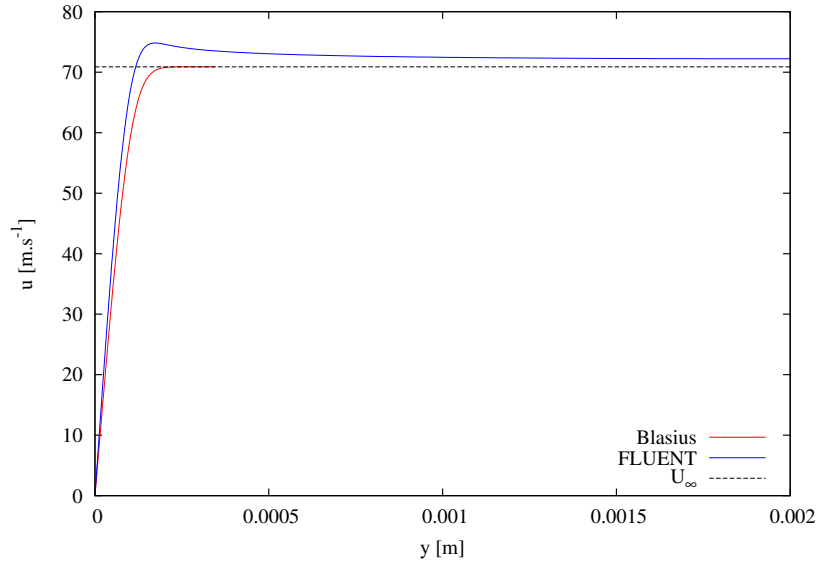


Figure 2.21: Comparison between Blasius and Navier-Stokes longitudinal velocity ($\tau = 2$ and $Re_x = 20850$)

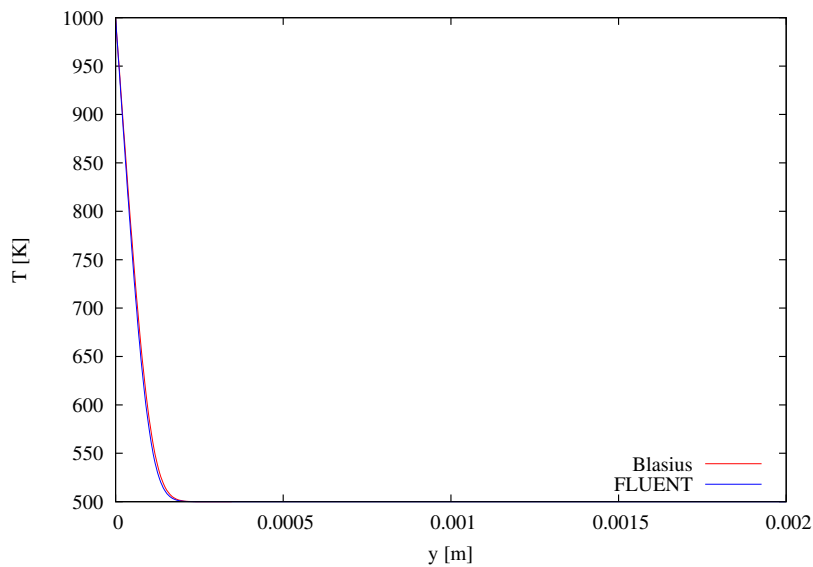


Figure 2.22: Comparison between Blasius and Navier-Stokes temperature at $Re_x = 20850$ when $\tau = 2$ and the temperature of the plate is fixed

2.7 Conclusion and perspectives

This study presents the local, surface and total generation rates in the boundary layer above a flat plate with two different thermal boundary conditions: the isothermal case when the plate temperature is fixed on the one hand, and the isoflux case when the plate heat flux density is fixed on the other hand. In addition to the longitudinal Reynolds number, the Prandtl number and the Eckert number, the entropy generation rate depends on the ratio, here named τ , between the plate temperature and the temperature gap between the plate and the free stream flow (considered at a common reference point for all simulations in the study). This thermal ratio has a direct influence on the magnitude and on the composition of the entropy generation rates,

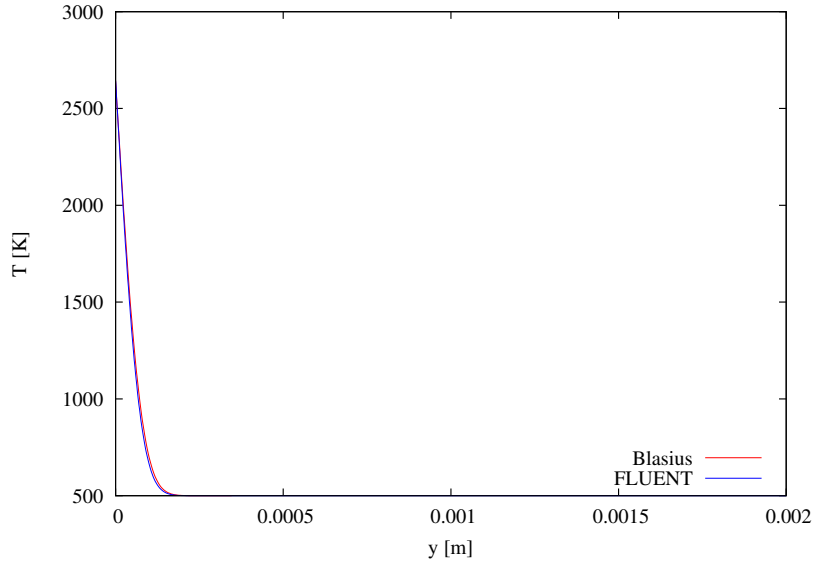


Figure 2.23: Comparison between Blasius and Navier-Stokes temperature at $Re_x = 20850$ when $\tau = 2$ and the heat flux density of the plate is fixed

the effects being different depending on the plate thermal boundary condition type. When an energetic constraint is applied (by fixing the total thermal power exchanged between the plate and the fluid), there is an optimum value of τ for which the total entropy generation rate is minimum (and this has also been observed for $Pr = 0.71$, a value corresponding to air at about $300K$). This optimum value of τ is independent on the total heat power exchanged or on the integration starting point along the plate for an isothermal plate. On the contrary, when the heat flux density is fixed at the plate, the optimum τ increases with the integration starting point or the exchanged thermal power.

For small values of τ (i.e., if the temperature difference is large when related to the temperature of the heated plate), a change in the relative temperature gap has a significant effect on the entropy generation rate. In solar receivers, temperature gradients are precisely high and this should motivate the search for solutions to better homogenize the temperature field of the flow. This will be done in Chapter 3 by applying the calculus of variations to search for velocity fields minimizing the entropy generation rate (mainly due to heat transfer) in a flat channel.

Chapter 3

Variational optimization of the internal flow

In this chapter, internal flat-plate channel flows are considered and optimized velocity and scalar field patterns are found by applying variational optimization technique to heat or mass transfer enhancement. In section 3.1, the fluid is air and heat transfer optimization is studied. In section 3.2, the same general optimization approach is applied to water and two different advection-diffusion processes are examined: heat transfer on the one hand and mass diffusion on the other hand. Moreover, the influence of boundary conditions such as the inlet velocity and the heat or mass flux density is analyzed.

3.1 Convective heat transfer in a gas flow

3.1.1 Introduction

Improving heat transfer in convective flows is a vast and active area of research that has applications in many industrial fields like nuclear [163] or solar [50] [63] [58] power plants, process industry [144], chemical engineering [32], air-conditioning or cooling of electronic systems [142] and automotive [102] or aerospace [220] industries to name but a few. To enhance heat transfer, many methods have been studied, generally classified according to whether they are active, passive or using a combination of the latter. Active methods require external energy supply to maintain the enhancement mechanism [134]: they can be based upon ultrasound [42], wall morphing [243] [132] and vibrating walls [64] including piezoelectric fans, impingement jets [172] [187] or sprays [100] [122], and electric field force on a dielectric fluid [137]. Heat transfer improvement passive methods are based upon three main techniques. Inserts can be placed in the fluid path to extend the exchange surface, redirect the flow, break boundary layers and promote mixing, swirl, vortexes and turbulence. There is a wide variety of inserts [131] [148]: twisted tapes, coiled wires, conical rings, helical screws and also fins, baffles or ribs. Combinations of techniques such as perforated twisted tapes or those with cut or corrugated edges have also been studied. Another passive method consists in using coatings or surface roughening [49] [76]. Finally, improving heat transfer can also be performed by changing the characteristics of the fluid (its heat capacity, viscosity and thermal conductivity), one active area of research being the use of nanofluids [180, 96, 115] (i.e. a fluid containing nanoparticles, whose sizes are $< 100 \text{ nm}$). Nanoparticles

can be made of a metal (e.g. Au or Cu), a metal oxide (e.g. TiO₂, Fe₃O₄, CuO, Al₂O₃) or other chemical substances (e.g. SiC, Carbon nanotubes) dispersed in a fluid, in particular: water, oil, molten salts or ethylene-glycol. The use of nanoparticles can be combined with passive [2] or active [136] methods and applied for example in the nuclear [147] or solar industry [30]. Higher size (micro-metric) particle suspensions are also promising to improve the performance of concentrated solar power plants [143] [86] [81].

Whatever the method used to increase heat exchange, it is necessary to ensure that this improvement is not accompanied by the harmful degradation of another performance criterion. In particular, one of the challenges in optimizing forced convective heat transfers is the balance between intensifying thermal exchange while minimizing or controlling pressure drop increase, both having to be taken into account [17] [51]. One way to address this trade-off consists in minimizing the entropy generation rate, which includes all the available power lost due to irreversibility in the flow whether it comes from the viscous friction responsible for the pressure drop or from the conduction phenomena through finite temperature differences [26] [24] [107]. As total viscous dissipation is related to the drop in pressure that can be a constrained element in industrial applications, it is also interesting to seek a minimization of the entropic power generated while maintaining control of total viscous dissipation [141] [10], which can be done by using a weighted objective functional.

In this study, we consider situations where the entropy generation rate by heat transfer is largely dominant when related to the viscous friction generated entropic power (which corresponds to $Be \approx 1$, where Be is the thermodynamic Bejan number [14]). We look for velocity and temperature fields that minimize a functional objective combining the entropic power generated by the dominant factor (i. e. heat conduction) on the one hand and the total viscous dissipation on the other hand, the latter being weighted by a factor that can be freely fixed in order to give more or less weight to the pressure drop in the optimization process. Several simulations were carried out for three Reynolds number values, by varying this total viscous dissipation weighting factor, in order to observe its influence on the entropy generation rates as well as on key physical variables such as the temperature of the heated wall, the total viscous dissipation, the maximum temperature and velocity in the channel and the outlet mean temperature.

3.1.2 The governing equations of the flow

We consider the two-dimensional steady-state incompressible flow of a Newtonian fluid with constant properties. Viscous heating and gravity are neglected and there is no source term in the energy equation nor any radiative exchange. Taking into account these assumptions, the conservation of mass, momentum and energy lead respectively to the following equations [189]:

$$\nabla \cdot \mathbf{V} = 0 \quad (3.1)$$

$$\rho \mathbf{V} \cdot \nabla \mathbf{V} = -\nabla P + \mu \nabla^2 \mathbf{V} + \mathbf{F} \quad (3.2)$$

$$\mathbf{V} \cdot \nabla T = \frac{k}{\rho C_p} \nabla^2 T \quad (3.3)$$

In this set of equations, \mathbf{V} is the velocity vector of the fluid, ρ its density, P its pressure, μ its dynamic viscosity, T its temperature, k its thermal conductivity, C_p its thermal capacity at constant pressure and \mathbf{F} is a volume force field that will be used in the optimization process described below: the volume force is an intermediary allowing to act on the velocity field in order to optimize the objective functional and the heat transfer.

3.1.3 The entropy production rate equations

The local entropy generation rate (by unit of volume) can be calculated using the following expression, where Φ is the viscous dissipation function [26]:

$$\dot{S}_{gen}''' = \frac{k}{T^2}(\nabla T)^2 + \frac{\Phi}{T} \quad (3.4)$$

$$\Phi = \mu \left\{ 2 \left[\left(\frac{\partial u}{\partial x} \right)^2 + \left(\frac{\partial v}{\partial y} \right)^2 \right] + \left(\frac{\partial u}{\partial y} + \frac{\partial v}{\partial x} \right)^2 \right\} \quad (3.5)$$

3.1.4 The variational problem

Objective functionals

Finding a minimum of a linear combination of the following two terms (Ω being the control volume) results in minimizing the generation of entropy by heat conduction while taking into account the total viscous dissipation:

$$J = \iiint_{\Omega} \left(\frac{k}{T^2}(\nabla T)^2 + W_{\Phi}\Phi \right) .d\Omega \quad (3.6)$$

In Eq. 3.6, W_{Φ} is a weighting factor allowing to control the relative importance given to the viscous dissipation. W_{Φ} can be seen as a weighting factor in a multi-objective optimization problem. Minimizing the entropy generation rate and the pressure drop, while these two objectives are contradictory, does not lead to a single solution. The use of a weighting factor allows to find a whole range of optimized trade-offs: with high values of W_{Φ} , the emphasis is on the reduction of pressure drop (and more precisely of the total viscous dissipation Φ_{tot} , which corresponds to the mechanical power required to maintain the flow). Conversely, small values of W_{Φ} correspond to a focus on minimizing the entropy generation rate in the channel. Each value of W_{Φ} leads to an optimal velocity field that minimizes differently the two contradictory objectives pursued since they are assigned different weighting factors.

The constraints expressed by the mass and energy conservation equations (Eqs. 3.1 and 3.3) are taken into account through two Lagrange multipliers (respectively λ_1 and λ_2 that are functions of the x and y coordinates). This leads to the following Lagrangian criterion to minimize:

$$J^* = \iiint_{\Omega} \left\{ \frac{k}{T^2}(\nabla T)^2 + W_{\Phi}\Phi + \lambda_2 \left[\frac{k}{\rho C_p} \nabla^2 T - \mathbf{V} \cdot \nabla T \right] + \lambda_1 \nabla \cdot \mathbf{V} \right\} .d\Omega \quad (3.7)$$

The function to be minimized (the entropy generation rate due to heat transfer and the viscous dissipation combined linearly in order to cope with a multi-objective optimization problem) is a functional (a function of functions, which is also non-linear) and the solution sought is a set of functions of the position (the velocity vector field and the scalar field) and not a simple number or even a single vector or tensor. These solution fields must also comply with the conservation equations (also non-linear) and the boundary conditions. One way to find the minimum of the functional could be to use iterative search algorithms (starting from an initial possible field and trying to get closer to the minimum by calculating gradients and penalty functions, for example) or methods based on meta-heuristics (such as genetic approaches) [199]. This implies to carry out a potentially high number of resolutions of the fluid flow equations and of evaluations of the objective functional. On the other hand, the calculus of variations allows to transform the optimization problem into a system of differential equations [90] [231] (the Euler-Lagrange equations) and the optimization is therefore carried out mathematically and not numerically. One single numerical resolution of the resulting differential equation system is then carried out to find the velocity and scalar fields. In this method, the standard procedure for taking into account the equality constraints that must be respected by the solutions (here: the conservation equations) is done using Lagrange multipliers.

Resulting equations

The expression of the volume force field is obtained by equaling to zero the first variation of J^* with respect to the components u and v of the velocity in order to deduce the corresponding Euler-Lagrange equations and taking into account the equation of the conservation of momentum (Eq. 3.2):

$$\mathbf{F} = \frac{\lambda_2}{2W_\Phi} \nabla T + \rho \mathbf{V} \cdot \nabla \mathbf{V} \quad (3.8)$$

Making the first variation of J^* with respect to T vanish leads to a transport-like equation for the λ_2 Lagrange multiplier:

$$\nabla \cdot \left(\rho \mathbf{V} \lambda_2 - \frac{-k}{C_p} \nabla \lambda_2 \right) = \frac{2k\rho}{T} \nabla \cdot \left(\frac{\nabla T}{T} \right) \quad (3.9)$$

The boundary conditions applicable to equation Eq. 3.9 depend on those concerning the temperature: if the temperature is imposed on a boundary of the domain, Eq. 3.10 applies and if the heat flux density is imposed, Eq. 3.11 must be taken into account (where $\partial/\partial n$ is the normal derivative to the boundary):

$$\lambda_2 = 0 \quad (3.10)$$

$$\frac{\partial \lambda_2}{\partial n} = \frac{2\rho C_p}{T^2} \frac{\partial T}{\partial n} \quad (3.11)$$

Finally, the differential equation system to be solved consists in Eqs. 3.1 to 3.3 (supplemented by boundary conditions for temperature, velocity and/or pressure) and Eqs. 3.8 and 3.9 (supplemented by the boundary conditions in Eqs. 3.10 or 3.11). The λ_1 Lagrange multiplier is not necessary but can be computed by:

$$\nabla \lambda_1 = -2W_{\Phi} \nabla P \quad (3.12)$$

The derivation of Eqs. 3.8, 3.9 and 3.12 from the calculus of variations is provided in Appendix A.

3.1.5 Physical and numerical model

The fluid is dry air, flowing between two transversely infinite flat plates (Fig. 3.1) that are impermeable and comply with the no-slip boundary condition. The walls are adiabatic except for the central third of the lower wall which is subjected to a uniform and constant heat flux density (1000 W.m^{-2}) in order to heat the fluid. The domain dimensions are $30 \text{ mm} \times 5 \text{ mm}$ and a uniform 1200×200 mesh is applied. At the inlet, the velocity and the temperature of the fluid are fixed and at the outlet, the gage pressure is set to zero.

The ANSYS Fluent 15.0 code is used to solve the flow equations with the SIMPLE velocity-pressure coupling algorithm. Additional scripts (UDF) have been developed to solve the additional λ_2 equation (Eq. 3.9) and to define the \mathbf{F} volume force field that is applied in the central area of the domain (between $x = 10 \text{ mm}$ and $x = 20 \text{ mm}$) in order to avoid side effects and to keep simple inlet and outlet boundary conditions.

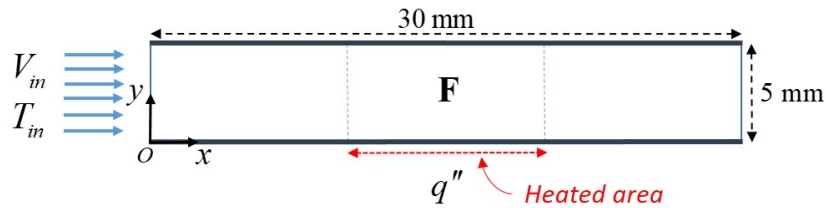


Figure 3.1: Domain characteristics.

For pressure and energy, second-order discretization schemes are applied. Momentum is solved with a QUICK scheme and λ_2 is solved with a first order scheme.

About forty simulations were performed, divided into three groups corresponding to three Reynolds number (based upon the channel height): $Re = 20$, $Re = 30$ and $Re = 320$, obtained by varying the inlet velocity V_{in} . In each group several values of the weighting factor W_{Φ} were tested, the global span of values ranging from $W_{\Phi} \approx 0.54 \text{ K}^{-1}$ to $W_{\Phi} \approx 1.23 \times 10^5 \text{ K}^{-1}$ so as to provide a wide range of situations from cases where viscous dissipation is of significant importance in optimizing the objective functional to cases where its relative weight is a priori negligible. In all simulation the inlet temperature is set to $T_{in} = 300 \text{ K}$.

3.1.6 Results

Entropy production rates and improvement factors

As shown in Fig. 3.2 (each point corresponding to a different simulation, as is the case for the following graphs), whatever the value of W_{Φ} , the optimized cases lead to a reduced total entropy generation rate in the channel, when compared to the case with no optimization, the relative reduction being quantified by using an improvement

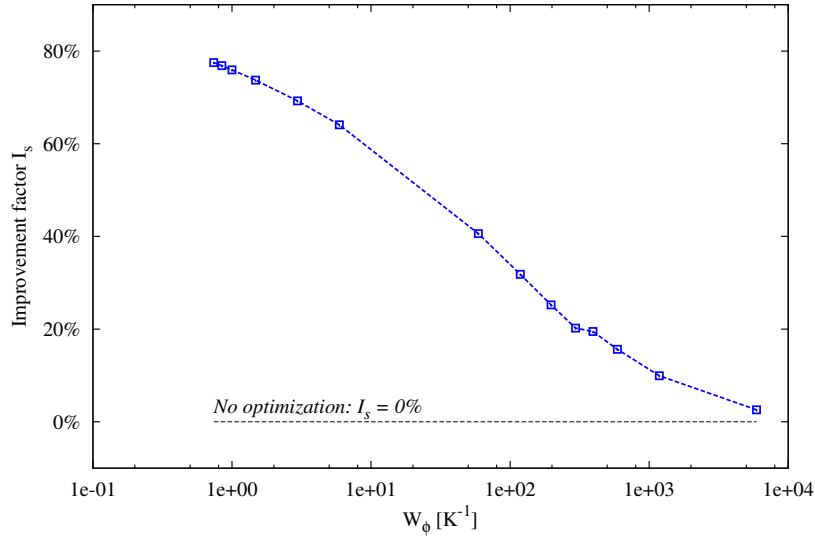


Figure 3.2: Improvement factor I_S (Eq. 3.13) as a function of W_{Φ} . $Re = 30$.

factor I_S (Eq. 3.13) that is increasing when W_{Φ} decreases. For high values of W_{Φ} ($10^5 K^{-1}$ or more), the improvement factor is near zero. For $W_{\Phi} = 1 K^{-1}$, I_S is around 74% when $Re = 30$.

$$I_S = 1 - \frac{\dot{S}_{gen, optimized}}{\dot{S}_{gen, no optimization}} \quad (3.13)$$

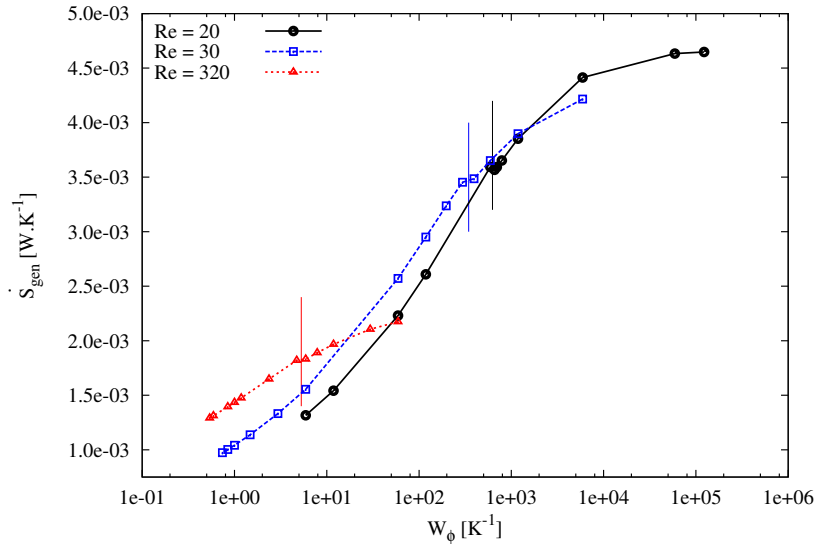


Figure 3.3: Total entropy generation rate \dot{S}_{gen} as a function of W_{Φ}

The total entropy generation rate increases with W_{Φ} (Fig. 3.3). For high values of W_{Φ} , the slope of the curve is small and approaches zero. The slope is higher for intermediate values of the weighting factor and it flattens when reaching small values of W_{Φ} . An unevenness of the slope also appears (it is embodied by vertical lines in Fig. 3.3), whose localization depends on the Reynolds number: the higher the

Reynolds number, the lower the value of W_{Φ} for which this irregularity occurs (around $W_{\Phi} = 325 \text{ K}^{-1}$ if $Re = 30$ and around $W_{\Phi} = 5 \text{ K}^{-1}$ when $Re=320$).

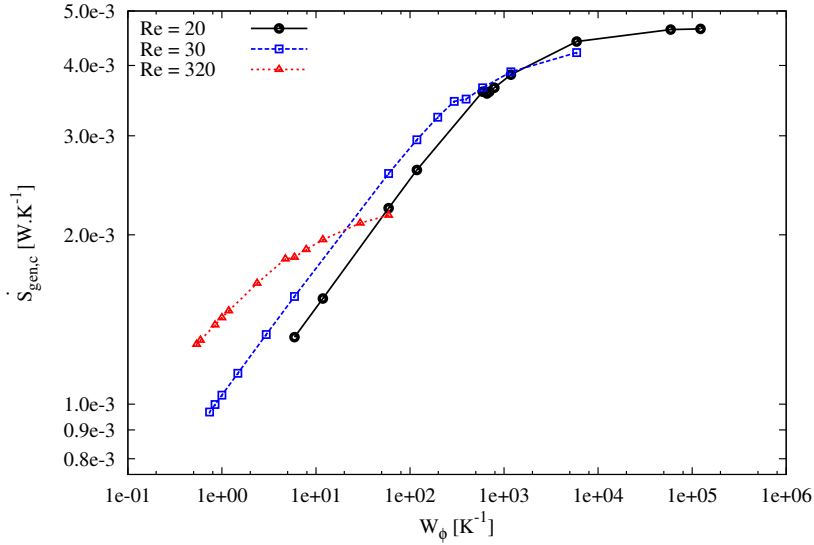


Figure 3.4: Entropy generation rate due to heat conduction $\dot{S}_{gen,c}$ as a function of W_{Φ}

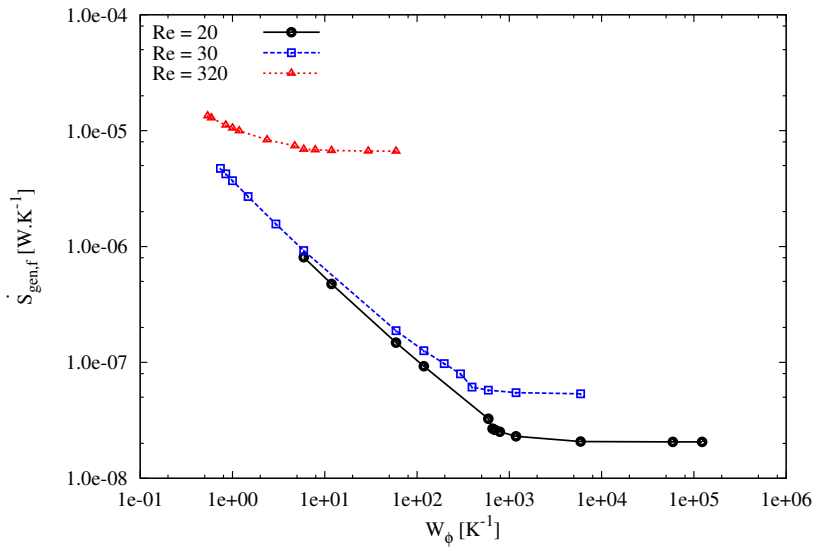


Figure 3.5: Entropy generation rate due to viscous friction $\dot{S}_{gen,f}$ as a function of W_{Φ}

The entropy generation rate in the channel is the sum of heat conduction ($\dot{S}_{gen,c}$, in Fig. 3.4) and viscous friction ($\dot{S}_{gen,f}$, in Fig. 3.5) contributors. The order of magnitude of the heat conduction part is the $mW.K^{-1}$ while the viscous part ranges between $\approx 10 \text{ nW.K}^{-1}$ and $\approx 10 \text{ }\mu\text{W.K}^{-1}$, depending on the Reynolds number. Because of the very small relative importance of the viscous part in comparison to the heat conduction part, the entropy generation rate by heat conduction is almost equal to the total entropy generation rate. The entropy generation rate by viscous friction (Fig. 3.5) is increasing when W_{Φ} decreases because the total viscous dissipation Φ_{tot} is increasing (Fig. 3.6), while the temperature remains in the order of 300 K . This means that

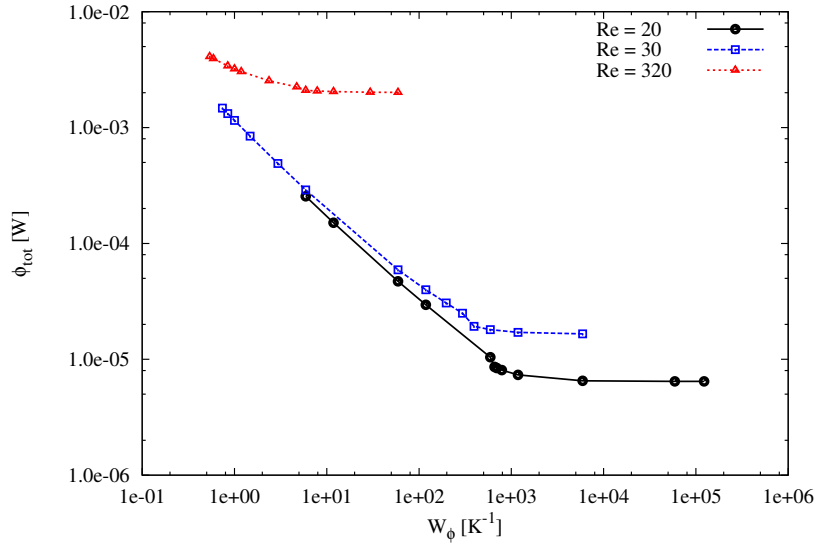


Figure 3.6: Total viscous dissipation Φ_{tot} as a function of W_{Φ}

the improvement observed on heat conduction entropy generation (and on the total entropy generation rate) is gained at the expense of an increase of the total viscous dissipation and correlatively of the viscous entropy generation rate, which remains however relatively small.

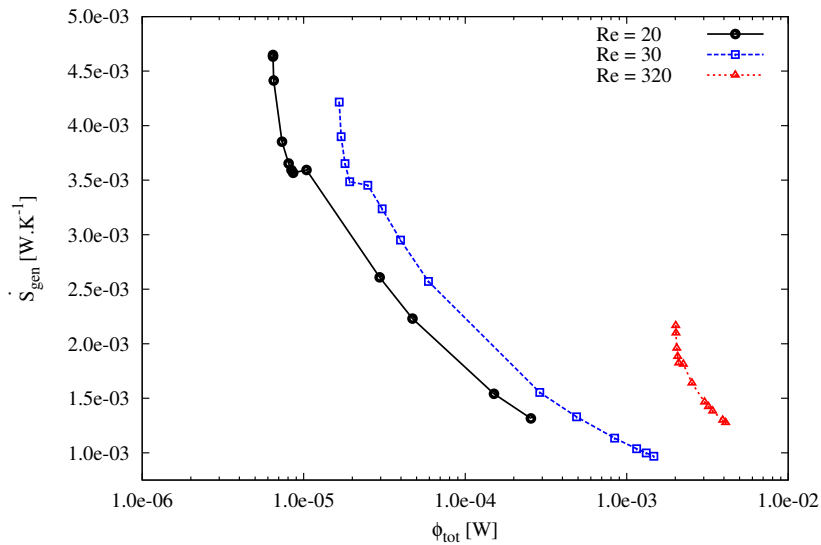
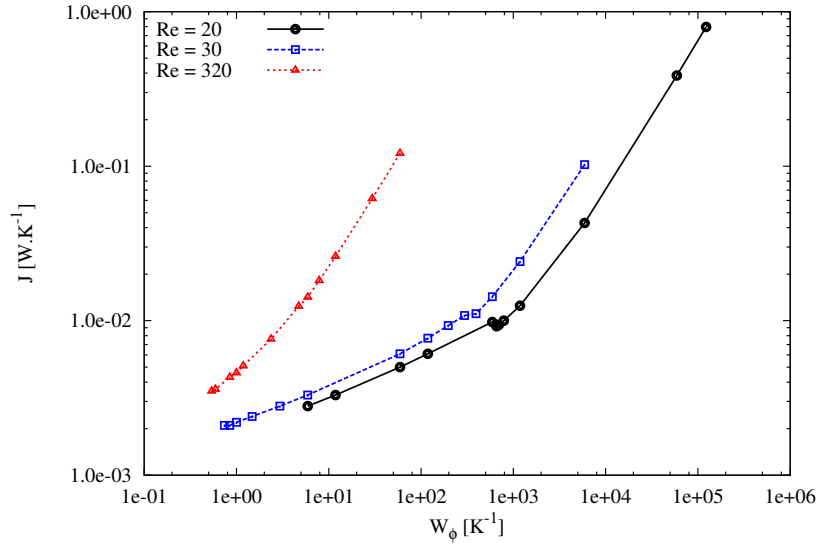


Figure 3.7: Total entropy generation rate \dot{S}_{gen} as a function of the total viscous dissipation Φ_{tot}

The decreasing behavior of the total entropy generation rate when the total viscous dissipation increases is even clearer when observing the direct relationship between these two physical integrals (Fig. 3.7). The viscous related quantities $\dot{S}_{gen,f}$ and Φ_{tot} in Figs. 3.5, 3.6 and 3.7 exhibit the irregularity already observed in Fig. 3.3, which is particularly visible when $Re = 20$ or $Re = 30$.

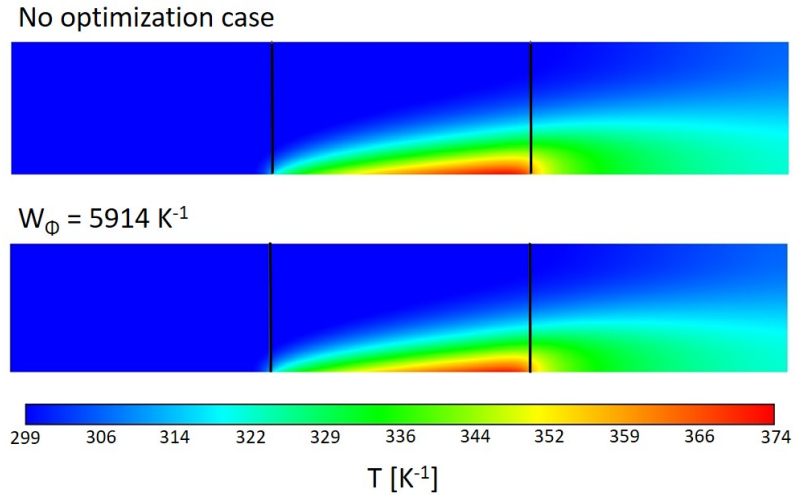
The weighted objective functional J is an increasing function of W_{Φ} (see Fig. 3.8) even for high values of the weighting factor. Indeed, when W_{Φ} gets high in Eq. 3.6, the

Figure 3.8: J objective functional as a function of W_ϕ

entropy generation rate by heat conduction (Fig. 3.4) and the total viscous dissipation (Fig. 3.6) stabilize, while the weighting factor W_ϕ increases.

Flow regimes

Depending on the value of W_ϕ , the velocity and temperature fields exhibit different profiles [10], being more or less perturbed when compared to the case where no optimization is applied at all.

Figure 3.9: Temperature field with no optimization and when $W_\phi = 5914 K^{-1}$. ($Re = 30$)

For high values of W_ϕ , for example $5914 K^{-1}$, the temperature and velocity fields are very similar to the case where no optimization is applied (see figs. 3.9 and 3.10, where the abscissa at the beginning and end of the heated zone are materialized by two black vertical lines). Nevertheless, the optimization process has already an influence:

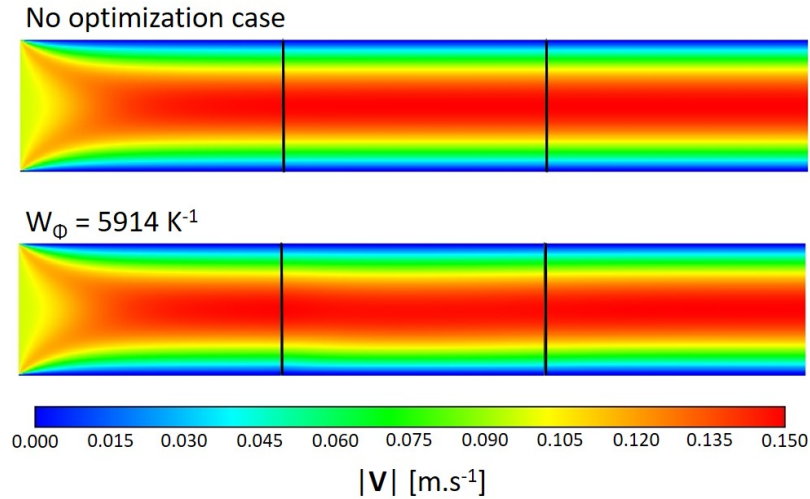


Figure 3.10: Velocity magnitude field with no optimization and when $W_{\Phi} = 5914 K^{-1}$. $Re = 30$)

when $Re = 30$, the maximum temperature in the channel without optimization is $373.5 K$ and $372.2 K$ when $W_{\Phi} = 5914 K^{-1}$.

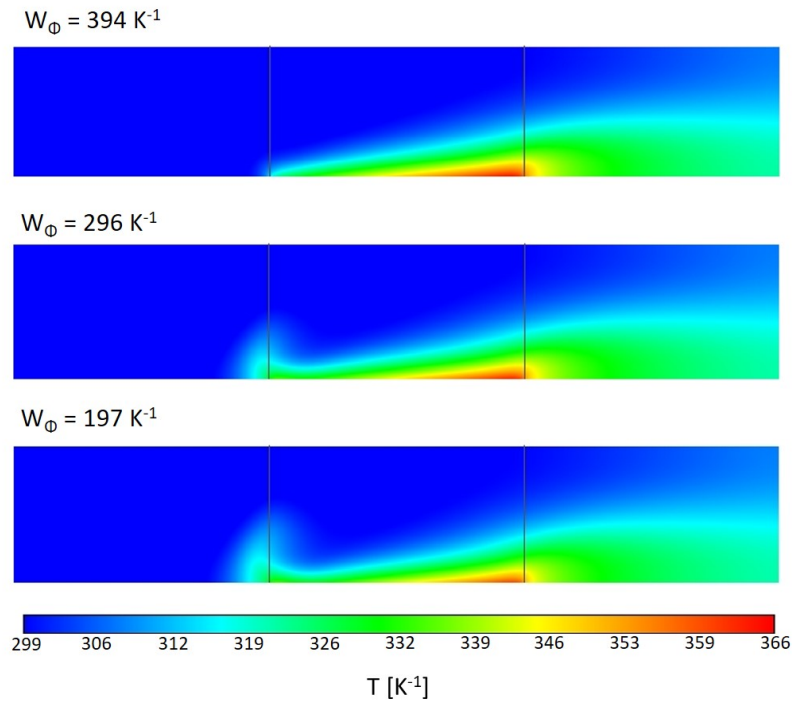


Figure 3.11: Temperature field for $W_{\Phi} = 394 K^{-1}$, $296 K^{-1}$ and $197 K^{-1}$. $Re = 30$.

For smaller values of W_{Φ} , the influence of the optimization process becomes evident and the perturbation level (when compared to the case where no optimization is performed) increases as W_{Φ} decreases (see Figs. 3.11 and 3.12): if $W_{\Phi} = 394 K^{-1}$, the temperature profile exhibits a squeeze above the heated zone and this phenomenon becomes more pronounced as W_{Φ} decreases. At $W_{\Phi} = 296 K^{-1}$ and even more at $W_{\Phi} = 197 K^{-1}$, a protrusion appears above the beginning of the heated area.

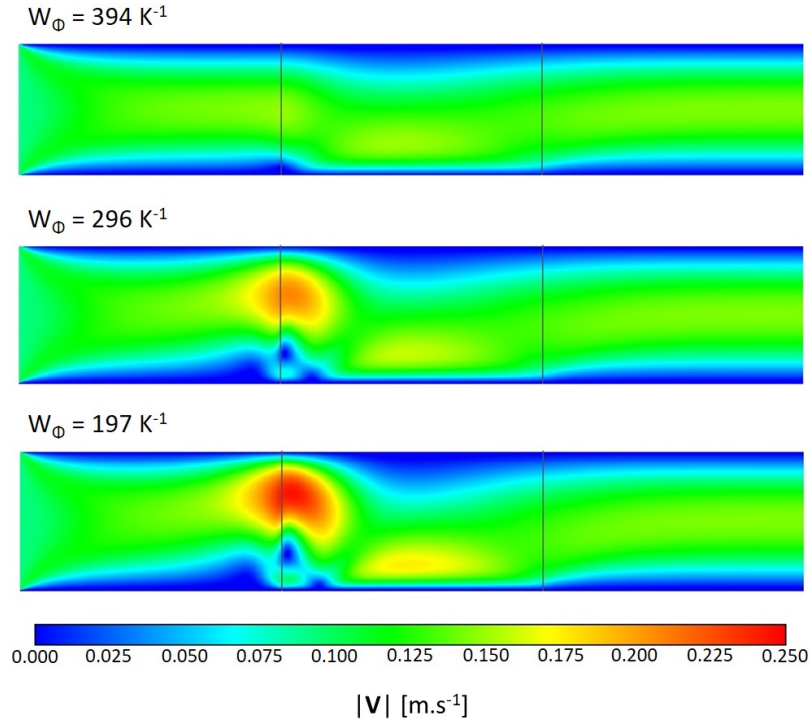


Figure 3.12: Velocity magnitude field for $W_{\Phi} = 394 K^{-1}$, $296 K^{-1}$ and $197 K^{-1}$. $Re = 30$.

The velocity magnitude field at $W_{\Phi} = 394 K^{-1}$ is also stuck towards the bottom plate and this observation is still valid when decreasing W_{Φ} . Moreover, as W_{Φ} gets smaller, areas of the channel exhibit higher velocities, in particular around the beginning of the heated zone (above a round structure circling an area of small velocities which looks like a vortex) and in a large central part of the heated segment above the bottom plate. The transition between the slightly perturbed velocity and temperature fields (when $W_{\Phi} = 394 K^{-1}$, for example) and the highly perturbed ones (when $W_{\Phi} = 296 K^{-1}$, for example) take place at $W_{\Phi} = 325 K^{-1}$ and corresponds to the irregularity previously observed in the entropy generation rate profiles in particular.

The stream function presented in Fig. 3.13 confirms the presence of a vortex (also found in [141] for a turbulent flow of heated air subject to variational optimization) in the initial part of the heated segment as soon as W_{Φ} is small enough: there is no apparent vortex when $W_{\Phi} = 1183 K^{-1}$ and a single vortex is clearly visible if $W_{\Phi} = 197 K^{-1}$. for a smaller value like $W_{\Phi} = 1 K^{-1}$, the main vortex at the heated zone entry is larger and exhibits a more complex shape. Furthermore, additional recirculating vortexes appear above the heated zone.

A zoom of the velocity vector above and around the central heated zone of the channel is presented in Fig. 3.14) along with a schematic representation of the main flow directions and of the rotational directions of the vortexes (the + sign meaning that the vortex has a clockwise rotation). The main vortex, located near the entry of the heated zone, collects a part of the heated fluid and transfers it to the accelerated area above the vortex. Then, the flow is stucked towards the heated segment of the bottom plate. As can be seen in Figs. 3.13 and 3.14, when $W_{\Phi} = 197 K^{-1}$, the center of the main vortex is located just after the beginning abscissa of the heated zone.

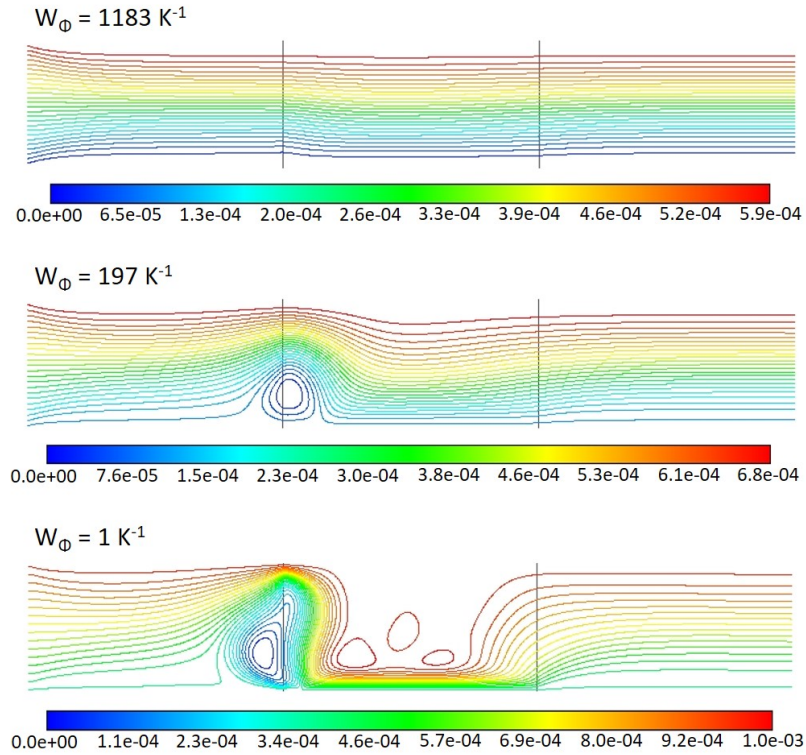


Figure 3.13: Stream function $[kg.s^{-1}]$. $Re = 30$.

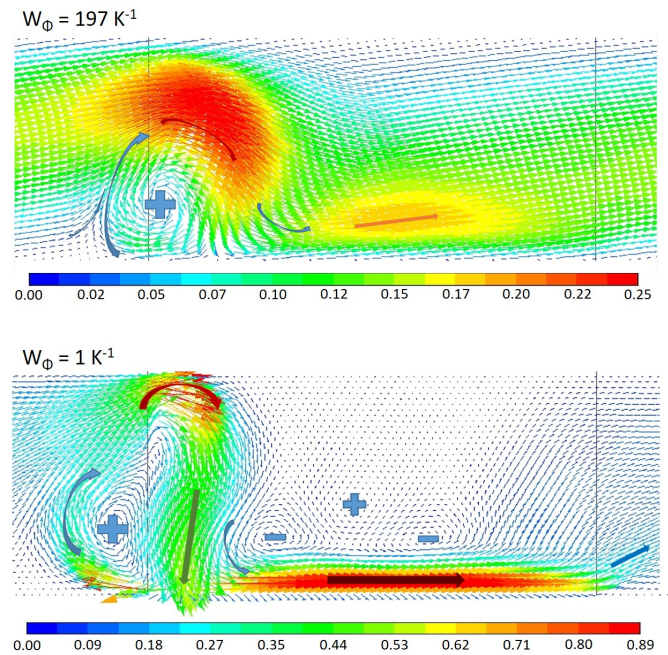


Figure 3.14: Velocity vector (zoom) with an indication of the main flow directions and of the rotational direction of vortices: " + " means clockwise. $Re = 30$.

Nevertheless, for low values of W_Φ , this center is located before this abscissa (this is the case when $W_\Phi = 1 \text{ K}^{-1}$, but also when $W_\Phi = 6 \text{ K}^{-1}$ for instance). The vertical extension of the main vortex increases when W_Φ decreases and so does the barycentric

position of the accelerated area above the vortex: when $W_{\Phi} = 1 \text{ K}^{-1}$ (Fig. 3.14), this high speed area is very close to the top plate of the channel.

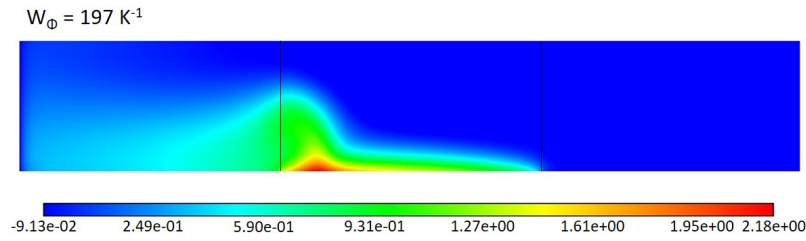


Figure 3.15: λ_2 Lagrange multiplier [$J.m^{-3}.K^{-2}$] field ($Re = 30$).

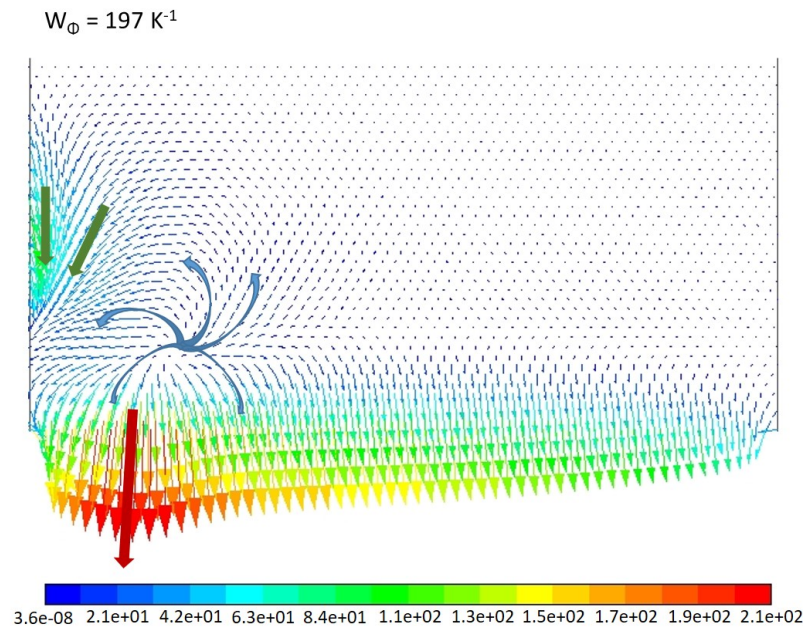


Figure 3.16: Force field \mathbf{F} applied above the heated segment area [$N.m^{-3}$] ($Re = 30$).

The Lagrange multiplier λ_2 field is presented in Fig. 3.15 when $W_{\Phi} = 197 \text{ K}^{-1}$. The highest values are concentrated in the first third of the heated area and mainly close to the plate. This is to be related to the magnitude of the corresponding force field \mathbf{F} presented in Fig. 3.16. Indeed, high λ_2 values contribute to the increase of the first term of the expression defining \mathbf{F} in Eq. 3.8 and this term also involves the temperature gradient that reaches high values near the heated plate segment. The main effect of the force field applied in the central third of the channel is to push down the fluid in the direction of the plate and to the starting point of the heated segment. Moreover, the force field tends to squeeze the flow and to crutch the thermal boundary layer above the heated segment of the bottom plate. As can be seen in Figs. 3.12, 3.13, 3.14 and 3.16, there is a strong relationship between the applied force field and the velocity vector.

The local entropy generation rate fields by heat conduction and by viscous friction are presented in Figs. 3.17 and 3.18 respectively (the latter using a logarithmic color scale for the sake of visibility). Significant entropy generation rates by heat conduction

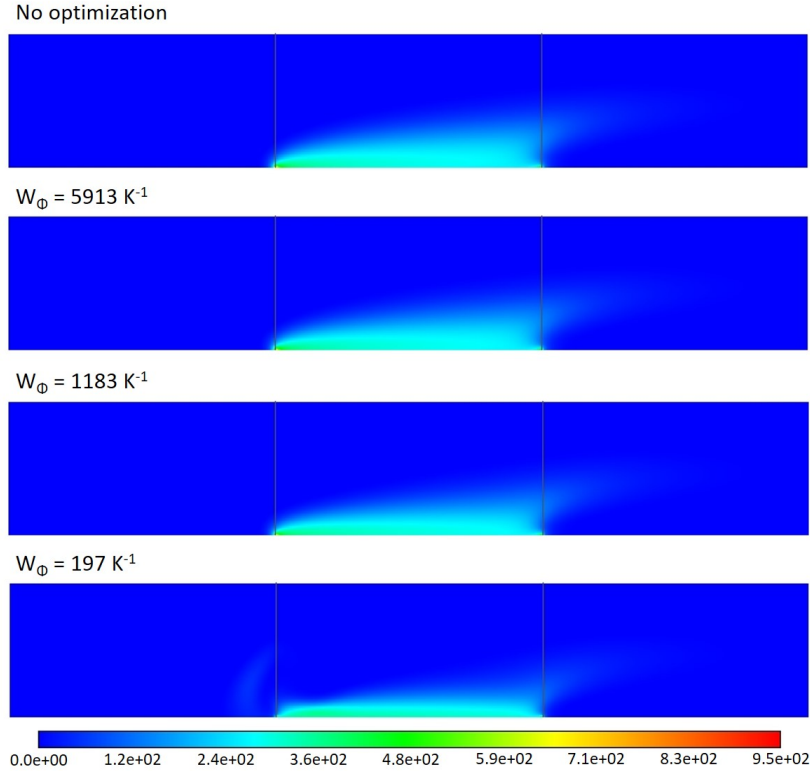


Figure 3.17: Local entropy generation rate by heat conduction in $[W.K^{-1}.m^{-3}]$ for $W_\phi = 5913 K^{-1}$, $1183 K^{-1}$, $197 K^{-1}$ and when no optimization is applied.

are located above the heated segment and are mainly due to the vertical conduction of heat. A convective trail appears at the exit of the heated zone. As W_ϕ decreases, the region of higher entropy generation rate by heat conduction is flattened and closer to the bottom plate. For values of W_ϕ small enough to make appear the thermal protrusion before the beginning of the heating zone, a plume appears in this area (see figs. 3.11 and 3.17 when $W_\phi = 197 K^{-1}$). The behavior of the local entropy generation rate by viscous friction is more complex (Fig. 3.18). The highest entropy generation rates by viscous friction are located at the channel inlet wall ordinates $y = 0$ and $y = H$ because of the discontinuity of the velocity that changes from U_{in} to zero at the walls. Just after this entry zone, the main viscous dissipation comes generally from areas close to the walls, at least when the velocity field is not too disturbed. Concentrating mainly to the part of the channel located above the heated segment, the perturbation of the entropy generation rate field by viscous friction becomes apparent even for high values of the weighting factor, like $W_\phi = 5913 K^{-1}$ or $W_\phi = 1183 K^{-1}$: the narrow longitudinal region of low entropy generation rate located in the center of the channel is deviated when crossing the entry of the heated zone and even almost broken when $W_\phi = 1183 K^{-1}$. For lower values ($W_\phi = 197 K^{-1}$), the entropy generation rate by viscous friction (and the viscous dissipation) is more perturbed and higher generation rates concentrate above the heated segment but also at the top wall around $x = 10 mm$ and along a closed curve enclosing the main velocity vortex. Indeed, the velocity field pattern is the main contributor to the complex shape of the entropy generation rate by viscous friction because the temperature field is simpler and kept in a smaller relative interval of values.

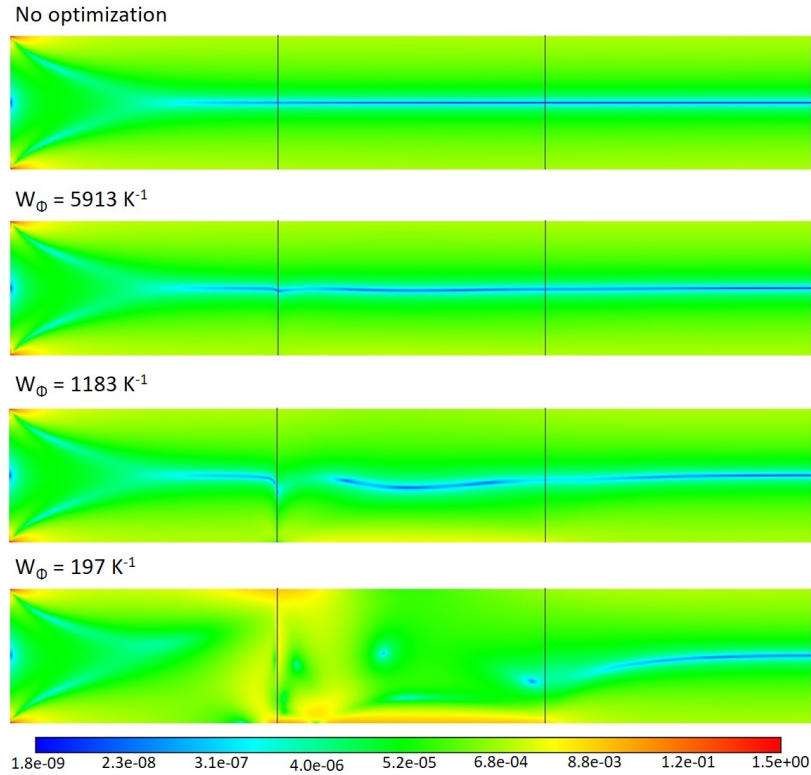


Figure 3.18: Local entropy generation rate by viscous friction in $[W.K^{-1}.m^{-3}]$ for $W_\phi = 5913 \text{ K}^{-1}$, 1183 K^{-1} , 197 K^{-1} and when no optimization is applied. Color scale is logarithmic.

Key physical quantities

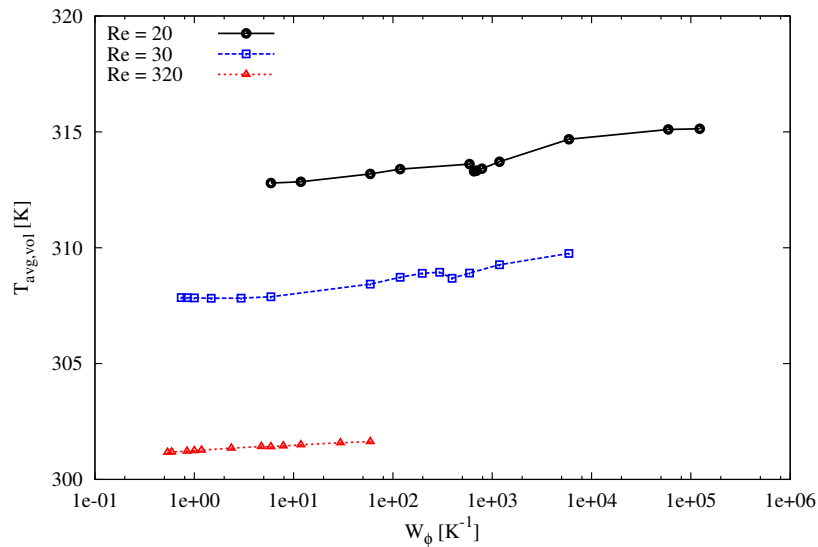


Figure 3.19: Average temperature in the Channel $[\text{K}]$.

The volume average of the temperature in the channel (Fig. 3.19) is an increasing function of W_ϕ , while staying in a narrow interval: as an example, when $Re = 30$,

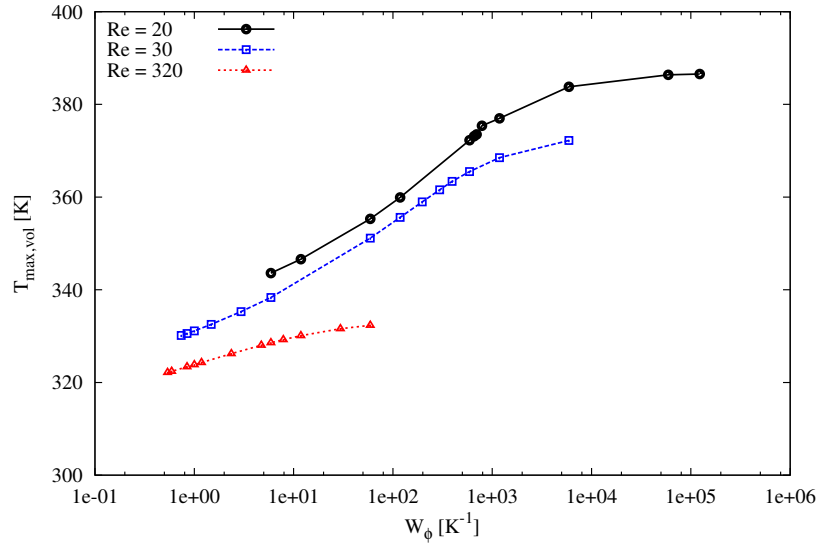


Figure 3.20: Maximum temperature in the Channel [K].

the mean temperature is located between 309.8 K and 307.9 K while W_ϕ decreases from 5914 K^{-1} to 6 K^{-1} . The maximum temperature inside the channel (Fig. 3.20) also decreases as W_ϕ gets smaller and it is the same for the standard deviation of the temperature that drops from 15.54 K to 8.06 K over the same range of W_ϕ , in accordance with a better thermal mixing due to the applied force field. Higher Reynolds numbers lead to lower maximal and average temperatures: the total injected thermal power is a constant and an increase of the inlet velocity leads to a higher exchange coefficient that induces lower temperature gaps.

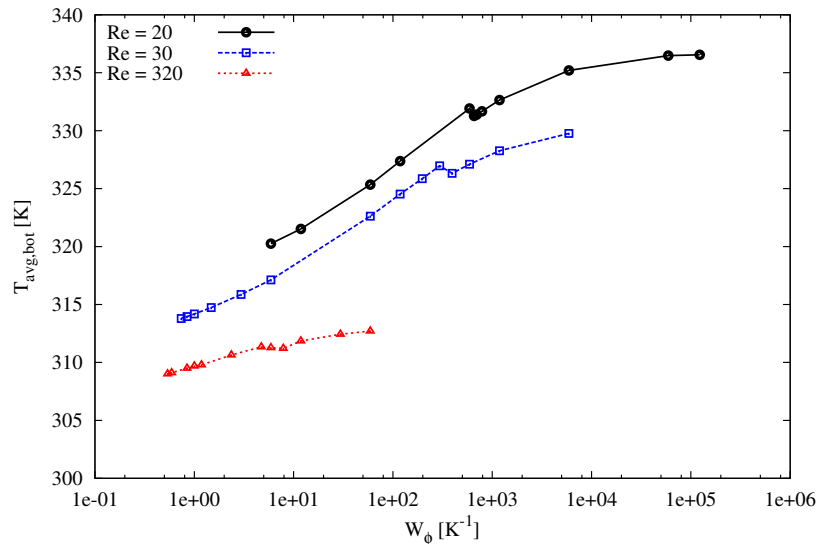


Figure 3.21: Average temperature on the bottom plate [K].

The average temperature of the heated wall is also lower as W_ϕ decreases (Fig. 3.21) and the same behavior can be observed for the maximum temperature at the same wall (Fig. 3.22): Using the example of simulations where $Re = 30$, the maximum temperature of the lower wall is 373.5 K when no optimization is applied. For a high

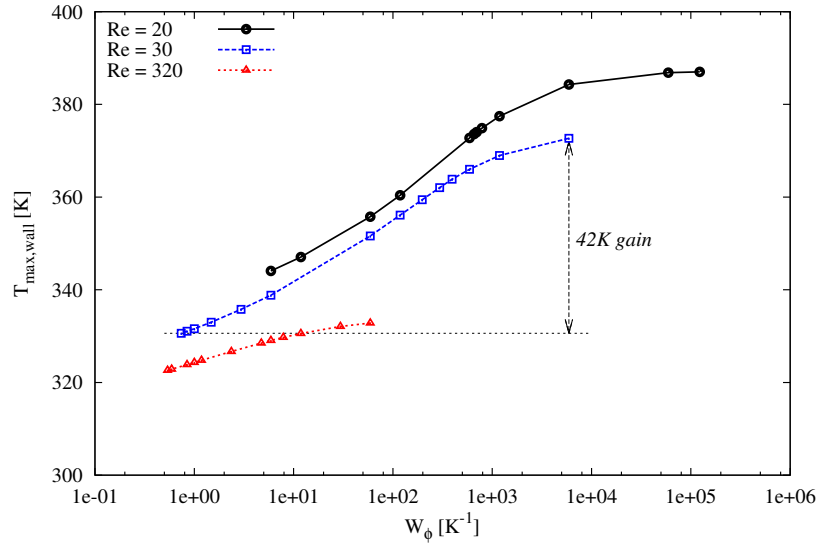


Figure 3.22: Maximum temperature on the bottom plate [K].

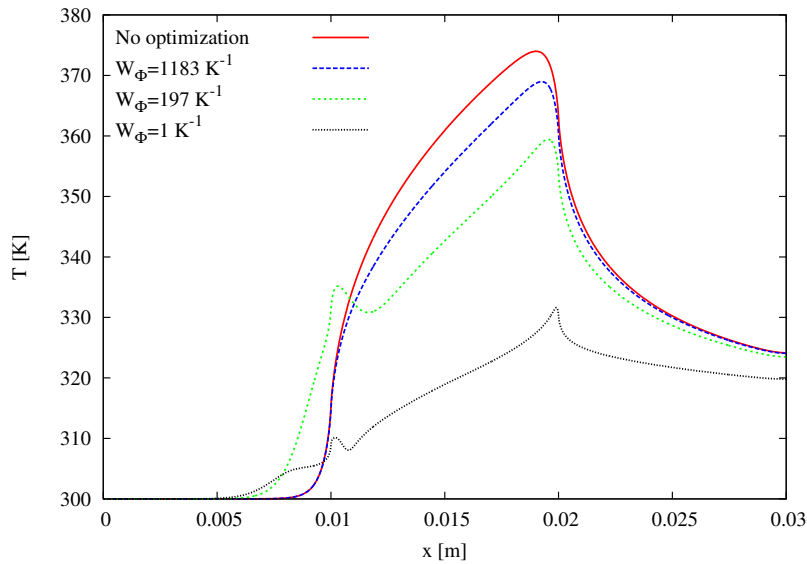


Figure 3.23: Temperature along the bottom plate [K].

value of W_{Φ} like 5914 K^{-1} , this temperature is 372.2 K , a value very close to the non-optimized situation. On the other hand, for a smaller weighting factor, such as $W_{\Phi} = 0.74 \text{ K}^{-1}$, the heated plate peak temperature is only 330.1 K , corresponding to a gain of 42 K . The temperature profiles of the bottom plate as a function of the abscissa are shown in Fig. 3.23 for several values of W_{Φ} and demonstrate the narrowing of the temperature range at the heated plate as W_{Φ} decreases. The reduction of the maximum temperature and the better thermal homogeneity of the heated plate are an advantage in applications like concentrate solar power where materials are subjected to high temperature stress that can be the cause of damage or accelerate aging due to thermo-mechanical [135] [162] or chemical [198] [194] constraints (oxidation for example [85]).

The average temperature at the outlet of the channel is practically independent on

the value of W_{Φ} (Fig. 3.24). On the other hand, the smaller the value of W_{Φ} , the more homogeneous the temperature at the outlet of the channel as demonstrated in Fig. 3.25.

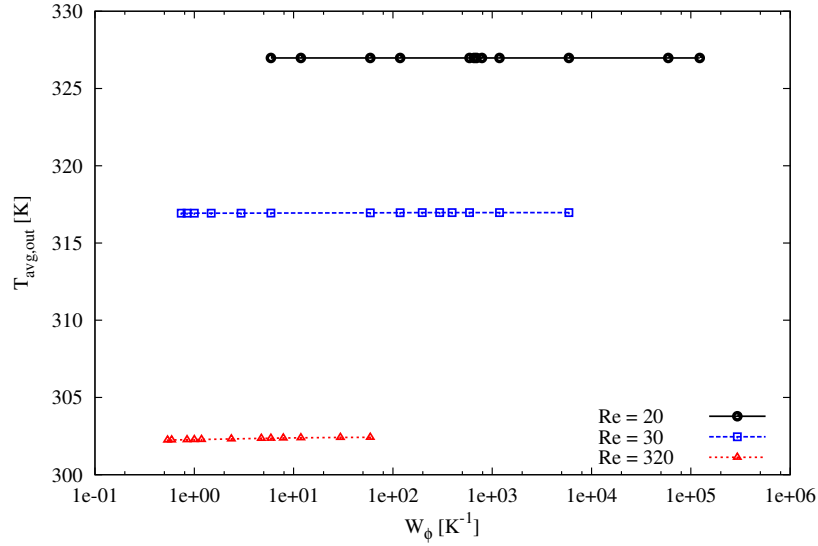


Figure 3.24: Average temperature at outlet [K].

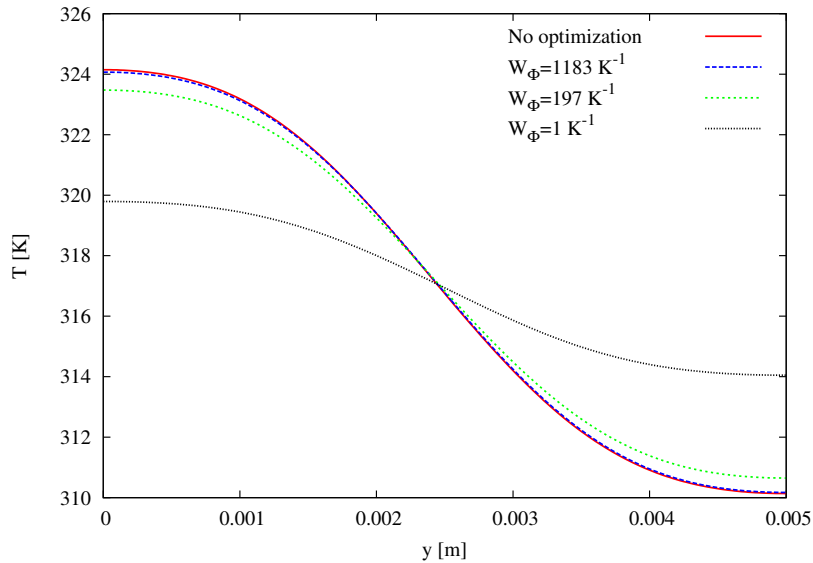


Figure 3.25: Temperature profile at outlet [K].

The different temperature profiles and fields presented above show that the velocity field pattern obtained by variational optimization leads to a better homogeneity of the thermal field, compatible with a reduction in the entropy generation rate in the channel. This improvement is achieved at the cost of an increase in entropy generation by viscous dissipation, which is linked to velocity gradients: the maximum velocity magnitude observed in the channel increases when W_{Φ} gets smaller (Fig. 3.26). Its profile is similar in appearance to that of the total viscous dissipation (Fig. 3.6) or the rate of entropy generation by viscous dissipation (Fig. 3.5): for large values of W_{Φ} ,

the maximum velocity magnitude is practically stable (and close to that which would be observed without optimization). From the transition to disturbed flow regimes, the maximum velocity magnitude in the channel increases rapidly as W_ϕ decreases, the slope being higher as the Reynolds number gets higher.

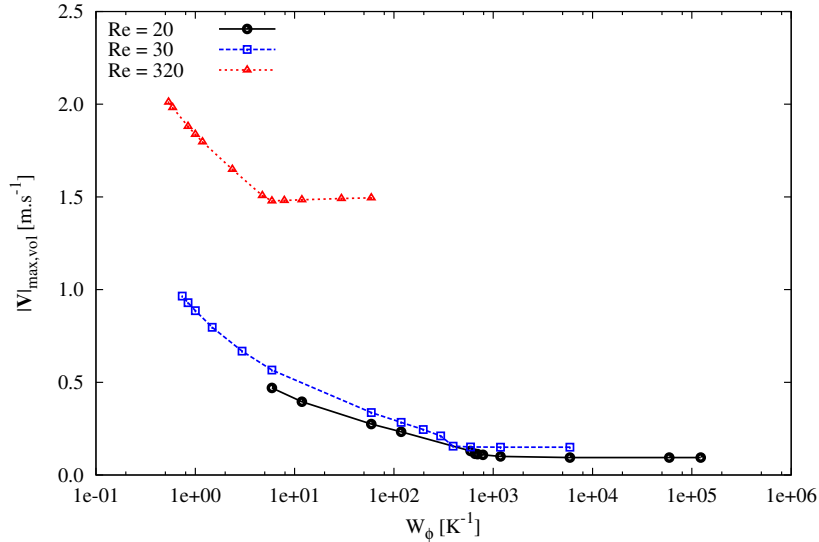


Figure 3.26: Maximum velocity magnitude in the Channel [$m.s^{-1}$].

3.1.7 Conclusion

In section 3.1, convective heat transfer optimization in a channel flow is addressed using variational methods applied to an objective functional built as a linear combination of the entropy generation rate by heat conduction (which is largely dominant in the cases studied) and the viscous dissipation function, a coefficient that acts as a weighting factor being assigned to the latter. Optimal velocity field patterns are induced by a volume force field that is a solution of the variational problem. Several simulations have been performed, at different Reynolds numbers and for a wide range of weighting factor values, in order to assess the improvement in terms of entropy reduction. The resulting velocity, temperature and local entropy generation rate fields are described, as well as the influence of the viscous dissipation function weighting factor on the flow and on the key physical quantities like the average and maximum temperatures in the channel, at the heated plate and at the outlet.

Depending on the value of the weighting factor, the optimized velocity and temperature fields are more or less perturbed by comparison to the case where no optimization is applied and a critical value of this factor determines the transition from low to high-disruption solutions. The higher the Reynolds number, the lower the critical value of the weighting factor. Small values of the weighting factor lead to highly perturbed velocity patterns exhibiting one or more vortexes and a tightening of the flow closer to the heated area. The corresponding thermal field is influenced by this mixing and the temperatures are lower and more homogeneous in the channel, at the heated plate and at the outlet. This improvement is reflected in the total entropy generation rate that is significantly reduced (the lower the weighting factor, the lower the entropy generation rate in the channel). The reduction in entropy generation rate is done at the

expense of an increase of the total viscous dissipation, the velocity magnitudes being higher in the channel and the velocity field being more complex. The entropy generation rate by viscous friction increases alongside but has no effect on the improvement in total entropy generation rate, due to its small relative order of magnitude. From the application point of view, it is found that a significant wall temperature reduction can be obtained, while maintaining the same power transferred to the fluid. This result shows an increase of heat transfer efficiency at the wall. The optimal suggested velocity fields provide a target to be approached using, for example, passive physical means like porous media [141] or modifications of the geometry inside the channel [108]. They also provide a better understanding of how flow structures are related to the minimums of entropy generated and the values of the total viscous dissipation.

3.2 Application to different advection-diffusion situations

To assess the general interest and investigate the behavior of the variational approach used above in the case of air flow heat transfer, the same method is applied to different situations. First, the case of convective heat transfer is performed with a different fluid (water, whose physical properties are quite distinct from those of air) and the influence of the boundary conditions is analyzed. Secondly, mass transfer is studied with the diffusion of a chemical minor species in water and a comparison is done between heat and mass transfer at the same Reynolds number in order to identify similarities.

3.2.1 Introduction

This study also addresses the application of variational methods to improve transfers in convective flows, by looking for optimal velocity fields. The main objective is to apply the method described in section 3.1 to another fluid and to broaden the range of situations by varying boundary conditions and examining not only the case of thermal diffusion, but also the case of mass diffusion.

In many industries and engineering applications, it is necessary to optimize heat or mass transfers in order to improve the technical or economic efficiency of machines, plants or processes. The intensification of heat transfer is sought in thermal power plants like concentrated solar [1, 82, 216], nuclear [147] or geothermal [242] ones, but also in the process, automotive or aerospace industries and for cooling systems. As detailed in section 3.1.1, heat transfer enhancement is an innovative field of research [205] using many techniques whether active (requiring an external energy input) such as the use of oscillating walls, or passive such as the addition of mixing promoters in the flow channel [63] [58] or the search for optimized transfer fluids. Convective mass transfer enhancement is also an area of particular interest for chemical processes [44] and biotechnology [129, 222] that take advantage of passive [5, 3] or active methods [207, 73]. In both heat transfer and mass diffusion, the use of suspended fine particles [128] or nanofluids [6, 34] is also being studied to increase exchanges. The intensification of heat or mass transfers is often produced by the passive promotion or the active realization of mixing [164] whose performance is dependent on the fluid flow pattern [241, 7, 175]. Therefore, searching for optimal flow patterns can be useful to improve heat or mass transfer in convective flows.

One way to address this issue is applying thermodynamic optimization by using the entropy generation rate as a criterion [23, 171]. In convective flow heat and mass transfer, the total generated entropic power is generally a sum of several terms. In the absence of radiative heat transfer [149], chemical reaction [40, 35], cross effects such as Dufour or Soret ones [197] and dissipation related to electric or magnetic fields [39, 154], the entropy generation rate originates from viscous friction, on the one hand, and from the diffusion of heat or mass through finite temperature or mass concentration differences, on the other hand. Acting on one of the two terms, for example by reducing the rate of heat conduction entropy generation, can lead to an increase in viscous friction entropy generation and it is necessary to seek the right compromise between two opposing effects. The total generated entropy rate can be minimized in order to find this optimal trade-off [24, 26, 107]. It is also possible to

look for a minimum of entropy generation while fixing a constraint on the total viscous dissipation in the flow [141, 108], the latter being related to the pressure drop, which is a quantity to be controlled in industrial applications.

In the present study, the calculus of variations is used to minimize a functional objective constructed as a linear combination of the entropy generation rate main contributor (which is the heat conduction or the mass diffusion, depending on the type of advection-diffusion process) on the one hand and the viscous dissipation on the other hand [47, 46, 109, 10]. A weighting coefficient allowing to give more or less importance to the viscous dissipation is used during the optimization process. For each value of this weighting factor, the optimal velocity and temperature fields are obtained by varying a volume force field source term and the improvement in terms of generated entropic power is calculated. The method is applied to heat transfer and mass diffusion cases in order to identify common behaviors or differences and the influence of the following boundary conditions is analyzed: the inlet velocity, the intensity of the incoming heat flow or minor chemical species injection and the inlet mass fraction of the minor species. Depending on the value of the total viscous dissipation weighting coefficient, two different flow patterns appear and the robustness of the transition between these two regimes is analyzed.

3.2.2 Governing equations

Two types of advection-diffusion processes in a convective flow are analyzed: heat transfer on the one hand and mass diffusion of a chemical minor species on the other hand. The corresponding equations are presented below (the ones concerning heat transfer are identical to those already indicated in sections 3.1.2 and 3.1.3: they are recalled here in order to show the similarities and differences between the heat transfer case on the one hand and the mass diffusion case on the other hand).

We consider the two-dimensional steady-state incompressible forced flow of a Newtonian fluid with constant properties, the effects of gravity being neglected. The corresponding mass and momentum conservation equations are the following:

$$\nabla \cdot \mathbf{V} = 0 \quad (3.14)$$

$$\rho \mathbf{V} \cdot \nabla \mathbf{V} = -\nabla P + \mu \nabla^2 \mathbf{V} + \mathbf{F} \quad (3.15)$$

In this set of equations, \mathbf{V} is the velocity vector of the fluid, ρ its density, P its pressure, μ its dynamic viscosity and \mathbf{F} is a volume force field that will be used in the optimization process described below.

Depending on the diffusion process, the transported scalar is respectively the temperature (for heat transfer) or the mass fraction of the minor species (for mass transfer).

In the case of heat transfer, viscous heating is neglected and there is no source term in the energy equation nor any radiative exchange. The energy equation writes:

$$\mathbf{V} \cdot \nabla T = \frac{k}{\rho C_p} \nabla^2 T \quad (3.16)$$

where T is the fluid temperature, k its thermal conductivity and C_p its thermal capacity at constant pressure.

In the case of mass diffusion, a two species high dilution ideal solution is considered and the diffusion equation writes:

$$\mathbf{V} \cdot \nabla w_1 = D \nabla^2 w_1 \quad (3.17)$$

where w_1 is the mass fraction of the minor species and D is the diffusion coefficient. Eqs. 3.16 and 3.17 have similar mathematical form and differ in the diffusivity coefficient physical meaning and magnitude.

In the case of heat transfer, the local entropy generation rate (by unit of volume) can be calculated using the following expression, where Φ is the viscous dissipation function [26] and u and v are the longitudinal and normal (to the heated wall) components of the velocity respectively:

$$\dot{S}_{gen}''' = \frac{k}{T^2} (\nabla T)^2 + \frac{\Phi}{T} \quad (3.18)$$

$$\Phi = \mu \left\{ 2 \left[\left(\frac{\partial u}{\partial x} \right)^2 + \left(\frac{\partial v}{\partial y} \right)^2 \right] + \left(\frac{\partial u}{\partial y} + \frac{\partial v}{\partial x} \right)^2 \right\} \quad (3.19)$$

In the case of mass diffusion, the expression of the local entropy generation rate is more complex [48] and takes into account the existence of two species in the fluid:

$$\dot{S}_{gen}''' = \frac{\rho^2 \bar{R} D}{\bar{M}_1 \bar{M}_2 w_1 (1 - w_1) \bar{c}} (\nabla w_1)^2 + \frac{\Phi}{T} \quad (3.20)$$

In Eq. 3.20, \bar{R} is the (molar) ideal gas constant, \bar{M}_1 and \bar{M}_2 are the molar masses of the minor species and of the solvent respectively and \bar{c} is the total molar concentration in [$mol \cdot m^{-3}$], which is assumed to be constant for the high dilution ideal solution.

3.2.3 Variational problem

Since the aim is to minimize the entropy generation rate due to the diffusion phenomenon while taking into account the total viscous dissipation, it is reasonable to consider a linear combination of these two terms, formalized in Eqs. 3.21 and 3.22 corresponding to the case of heat transfer and mass diffusion respectively (Ω being the control volume domain):

$$J = \iiint_{\Omega} \left(\frac{k}{T^2} (\nabla T)^2 + W_{\Phi} \Phi \right) d\Omega \quad (3.21)$$

$$J = \iiint_{\Omega} \left(\frac{\rho^2 \bar{R} D}{\bar{M}_1 \bar{M}_2 w_1 (1 - w_1) \bar{c}} (\nabla w_1)^2 + W_{\Phi} \Phi \right) d\Omega \quad (3.22)$$

In order to take into account the constraints expressed by Eqs. 3.14 and 3.16 or 3.17, Lagrange multipliers λ_1 and λ_2 (depending on the position) are introduced. Finally, the Lagrangian criteria to minimize are Eq. 3.23 for heat transfer and Eq. 3.24 for mass diffusion.

$$J^* = \iiint_{\Omega} \left\{ \frac{k}{T^2} (\nabla T)^2 + W_{\Phi} \Phi + \lambda_2 \left[\frac{k}{\rho C_p} \nabla^2 T - \mathbf{V} \cdot \nabla T \right] + \lambda_1 \nabla \cdot \mathbf{V} \right\} d\Omega \quad (3.23)$$

$$J^* = \iiint_{\Omega} \left\{ \frac{\rho^2 \bar{R} D}{\bar{M}_1 \bar{M}_2 w_1 (1 - w_1) \bar{c}} (\nabla w_1)^2 + W_{\Phi} \Phi + \lambda_2 \left[D \nabla^2 w_1 - \mathbf{V} \cdot \nabla w_1 \right] + \lambda_1 \nabla \cdot \mathbf{V} \right\} d\Omega \quad (3.24)$$

Making the first variation of J^* with respect to u and v vanish and taking into account the momentum conservation equation Eq. 3.2 gives the formula for the volume force field \mathbf{F} in Eq. 3.25 and Eq. 3.26 for heat transfer and mass diffusion respectively.

$$\mathbf{F} = \frac{\lambda_2}{2W_{\Phi}} \nabla T + \rho \mathbf{V} \cdot \nabla \mathbf{V} \quad (3.25)$$

$$\mathbf{F} = \frac{\lambda_2}{2W_{\Phi}} \nabla w_1 + \rho \mathbf{V} \cdot \nabla \mathbf{V} \quad (3.26)$$

In addition, equaling to zero the first variation of J^* with respect to T leads to the transport equation of the λ_2 Lagrange multiplier in Eq. 3.27 for the heat transfer case and in Eq. 3.28 for the mass diffusion case.

$$\nabla \cdot \left(\rho \mathbf{V} \lambda_2 - \frac{-k}{C_p} \nabla \lambda_2 \right) = \frac{2k\rho}{T} \nabla \cdot \left(\frac{\nabla T}{T} \right) \quad (3.27)$$

$$\nabla \cdot [\rho \mathbf{V} \lambda_2 - (-\rho D) \nabla \lambda_2] = \frac{\rho^3 \bar{R} D}{\bar{M}_1 \bar{M}_2 w_1 (1 - w_1) \bar{c}} \left[\nabla \cdot \left(\frac{\nabla w_1}{w_1 (1 - w_1)} \right) + \frac{\nabla \cdot (\nabla w_1)}{w_1 (1 - w_1)} \right] \quad (3.28)$$

The boundary conditions to be applied to Eqs. 3.27 or 3.28 depend on those defined for the transported scalar (the temperature or the mass fraction of the minor species): if the scalar function is set at a boundary (Dirichlet condition), Eq. 3.29 applies. On the other hand, if the flux density of the scalar function is set at the boundary (Von Neumann condition), Eq. 3.30 or Eq. 3.31 are used for heat transfer and mass diffusion respectively.

$$\lambda_2 = 0 \quad (3.29)$$

$$\frac{\partial \lambda_2}{\partial n} = \frac{2\rho C_p}{T^2} \frac{\partial T}{\partial n} \quad (3.30)$$

$$\frac{\partial \lambda_2}{\partial n} = \frac{\rho^2 \bar{R}}{\bar{M}_1 \bar{M}_2 \bar{c}} \frac{2}{w_1 (1 - w_1)} \frac{\partial w_1}{\partial n} \quad (3.31)$$

In these equations, $\partial/\partial n$ is the normal derivative to the boundary.

Finally, in the case of heat transfer, for each selected value of the W_{Φ} weighting coefficient, Eqs. 3.14, 3.15, 3.16, 3.25 and 3.27 are solved with the boundary conditions 3.29 or 3.30 complemented by the dynamical and thermal boundary conditions. In the case of mass diffusion, the solved equations are Eqs. 3.14, 3.15, 3.17, 3.26 and 3.28 and the boundary conditions are Eqs. 3.29 or 3.31 complemented by the dynamical and mass fraction boundary conditions.

3.2.4 Physical and numerical setup

The fluid is water (a pure substance when the heat transfer case is considered and a highly dilute solution where water is the solvent when the mass diffusion case is studied). The domain dimensions are $30\text{ mm} \times 5\text{ mm}$ and a 1200×200 uniform mesh is used (Fig. 3.27). Mesh independence checks have been performed with 2400×400 and 3600×600 meshes and are described in section 3.2.7. The top and bottom plates are impermeable and the no-slip boundary condition is applied. The inlet velocity V_{in} is uniform and constant and the gage pressure is set to zero at the outlet. In the case of heat transfer, the inlet temperature is set to $T_{in} = 300\text{ K}$ and the walls are adiabatic except for the central third of the lower plate where a uniform and constant heat flux density q'' is set to 15000 W.m^{-2} unless otherwise indicated. In the case of mass diffusion, the inlet mass fraction of the minor species is set to a fixed value $w_{1,in} = 0.01$ unless otherwise stated and the central third of the lower wall is subjected to a fixed production rate per unit area of the minor species \dot{m}_1 set to $0.01\text{ kg.m}^{-2}.s^{-1}$ unless otherwise indicated.

The CFD code is ANSYS Fluent 15.0 using the SIMPLE velocity-pressure coupling algorithm. UDF scripts are used to solve the additional transport equation (3.27 or 3.28) and to define the source terms (in particular the \mathbf{F} volume force field that is applied in the central region of the domain).

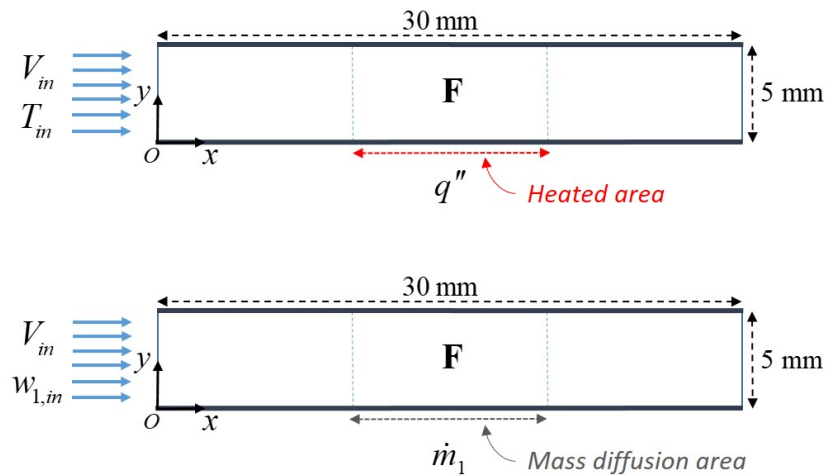


Figure 3.27: Domain characteristics.

Second-order discretization schemes are used for pressure and energy. Momentum and λ_2 equations are solved with a QUICK scheme.

About a hundred simulations were performed to simulate heat transfer or mass diffusion situations, with different values of the W_{ϕ} weighting coefficient that spans across four orders of magnitudes. Moreover, several parameters have been varied in order to analyze their influence: the inlet velocity, the heat flux density (in the heat transfer case), the mass flux density and the inlet mass fraction of the minor species (in the mass diffusion case).

3.2.5 Heat transfer

In this section, we consider the heat transfer case where the channel is heated from the central third of its bottom plate with a constant and uniform heat flux density q'' . The mass diffusion case will be examined later in section 3.2.6. The study is conducted for a fluid with thermo-physical properties very different from those of air and allows to assess the robustness of the behaviors already observed (cf. section 3.2.7, in particular).

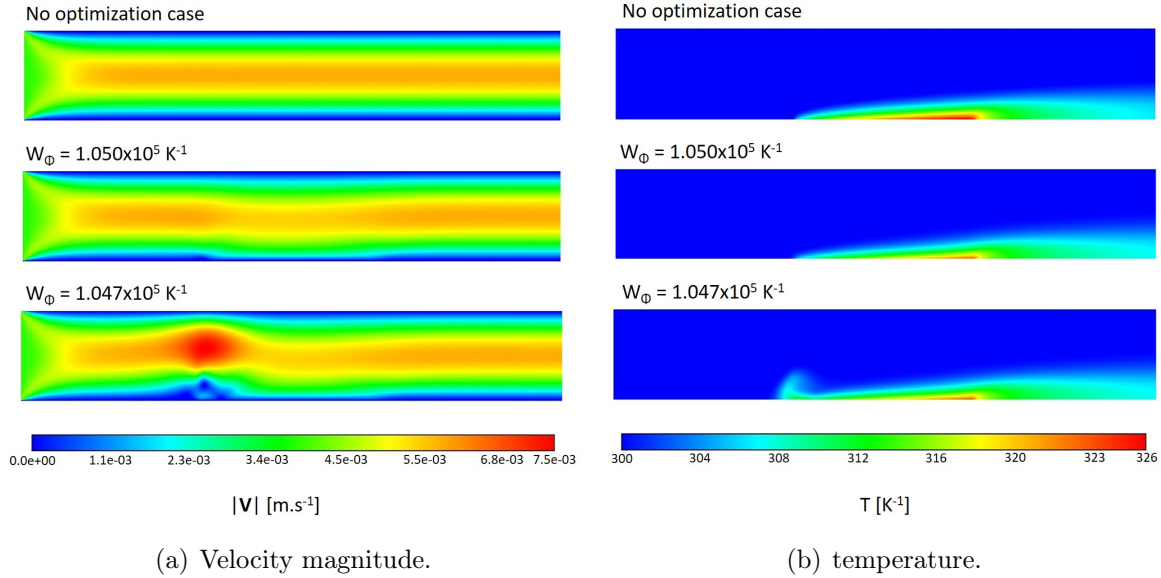


Figure 3.28: Velocity magnitude and temperature fields with no optimization and with slightly and highly perturbed profiles ($Re = 20$)

Depending on the importance of the weighting factor W_{Φ} , the velocity (Fig. 3.28(a)) and temperature (Fig. 3.28(b)) fields exhibit different shapes corresponding to flow regimes more or less perturbed when compared to a reference simulation for which no optimization is activated (i.e. when the applied volume force field \mathbf{F} is zero) [10]. For very large values of W_{Φ} (for example, when $W_{\Phi} = 10^7 \text{ K}^{-1}$) these fields are very close to those obtained without optimization. For smaller W_{Φ} values, like $W_{\Phi} = 1.05 \times 10^5 \text{ K}^{-1}$, the fields are modified without being disrupted: in particular, the flow is slightly pressed against the heated area. For even smaller W_{Φ} values, for example $W_{\Phi} = 1.047 \times 10^5 \text{ K}^{-1}$, the temperature and velocity profiles are clearly perturbed compared to the situation without optimization: the fluid is still pushed towards the heated zone but a clockwise vortex also appears (Fig. 3.29) that tends to capture the heated fluid at the beginning of the heat exchange zone near the lower plate to move it up in the channel and then accelerate it, before pushing it towards the lower plate. This velocity field results in a thermal plume shape at the beginning of the heated zone. The presence of a vortex in the velocity field resulting from variational optimization is also observed in other physical situations, such as the improvement of chemical reaction [46] or diffusion [108] processes and the optimization of heat transfer in a turbulent gas flow [141]. Vortex generation is also a subject of numerical simulation [58] and experimental [63] work aimed, for example, at associating and optimizing actuators and riblets to produce vortexes.

The transition from a low to a highly perturbed regime occurs around a critical

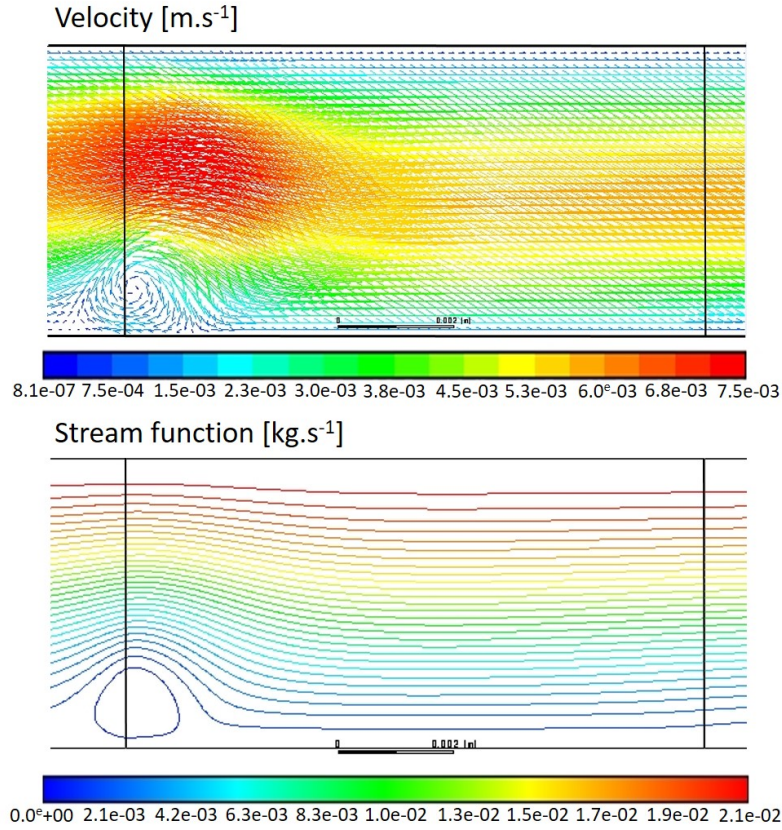


Figure 3.29: Zoom of velocity vector and stream function fields when $W_{\Phi} = 1.047 \times 10^5 K^{-1}$. The vertical lines materialize the abscissa $x = 10 \text{ mm}$ and $x = 20 \text{ mm}$ of the heated region. $Re = 20$.

value of W_{Φ} that depends in particular on the Reynolds number. When $Re = 10$, the transition takes place around $W_{\Phi} = 2.53 \times 10^5 K^{-1}$ while for $Re = 20$ it occurs around $W_{\Phi} = 1.05 \times 10^5 K^{-1}$. As can be seen in Figs. 3.28(a) and 3.28(b), a small change in the W_{Φ} value can lead to a significant change in flow: when $Re = 20$, reducing W_{Φ} by about 0.3 % is enough to induce the transition. Due to this relatively abrupt change, the evolution of the key variables in the channel (such as the total entropy generated) as a function of W_{Φ} shows a disruption.

When the optimization is applied (i.e. the force field \mathbf{F} is computed and used in the momentum equation), the total entropy generated in the channel is smaller than the case with no optimization (see Fig. 3.30(a) where the two vertical bars materialize the critical W_{Φ} values triggering the transition between the slightly to the highly perturbed velocity and temperature profiles). The reduction in entropy generated is all the more important as W_{Φ} is small and the gain obtained compared to the case without optimization can be estimated using an improvement factor I_s defined in Eq. 3.13 and presented in Fig. 3.30(b). When $Re = 20$ and $W_{\Phi} = 2.3 \times 10^4 K^{-1}$, $I_s \approx 30\%$ and the total entropy generation rate in the channel is about 70% of the case with no optimization. For high values of W_{Φ} , decreasing this factor by one order of magnitude leads to a small (or even zero) marginal gain in entropy rate reduction. On the other hand, when W_{Φ} approaches its critical value and below this point, the slope of the marginal gain is higher (around 8 mW.K^{-1} by order of magnitude of W_{Φ}).

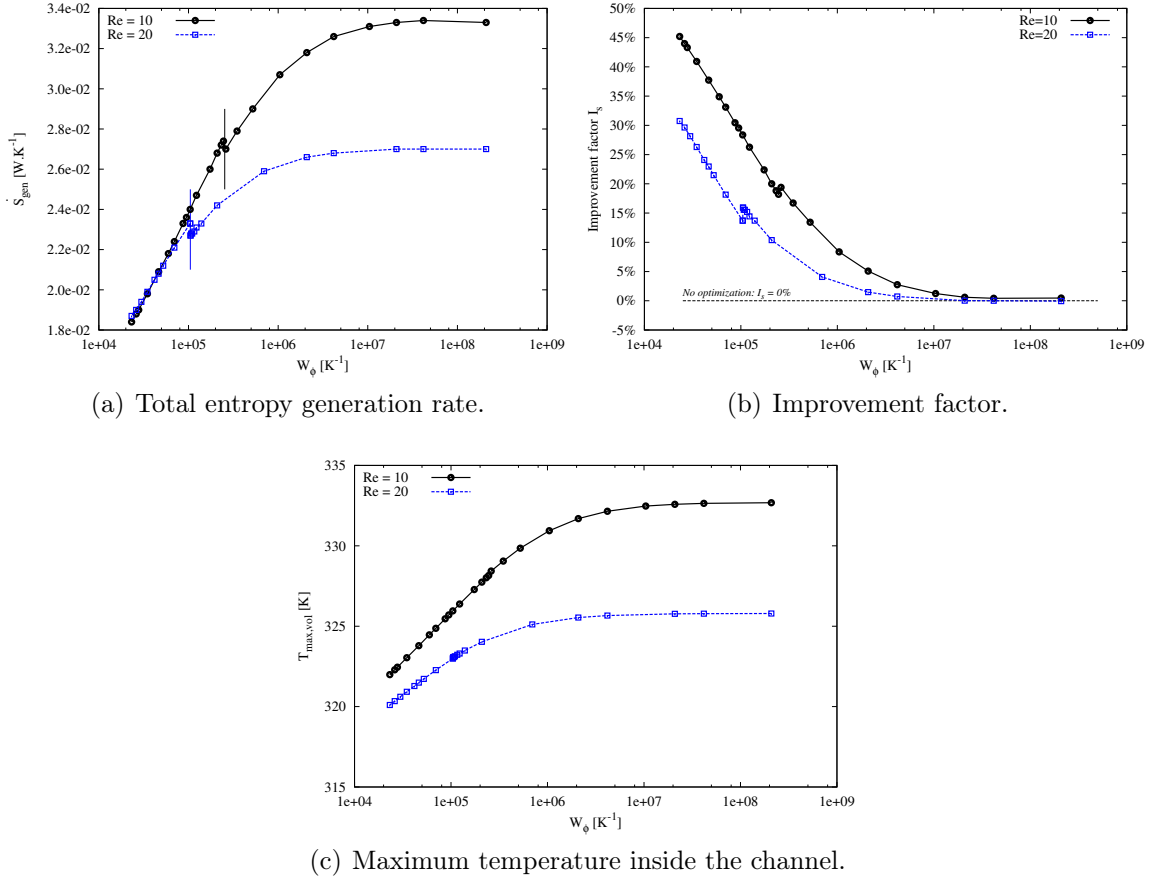


Figure 3.30: Total entropy generation rate, improvement factor and maximum temperature inside the channel.

As can be seen in Fig. 3.30(c), the maximum temperature inside the channel significantly decreases as W_ϕ declines and for medium values of W_ϕ the curve slope increases when the Reynolds number decreases. The velocity fields resulting from the optimization increase the homogeneity of the temperature field: the standard deviation of the temperature is reduced from 3.74 K to 3.32 K when W_ϕ changes from $2.09 \times 10^8 \text{ K}^{-1}$ to $1.047 \times 10^5 \text{ K}^{-1}$ at $Re = 20$.

The entropy generation rate by viscous friction increases as W_ϕ decreases (Fig. 3.31(a)) and so does the total viscous dissipation Φ_{tot} (Fig. 3.31(b)) and the maximum velocity within the flow (Fig. 3.31(c)). The order of magnitude of the viscous friction entropy generation rate $\dot{S}_{gen,f}$ (between 1 nW.K^{-1} and 10 nW.K^{-1} , depending on the Reynolds number) is much lower than that of the heat conduction entropy generation rate $\dot{S}_{gen,c}$ (10 mW.K^{-1}), which is by far the main contributor to the total entropy generation rate $\dot{S}_{gen} = \dot{S}_{gen,c} + \dot{S}_{gen,f}$. The smaller W_ϕ , the higher the velocities in the channel, leading to increased velocity gradients, viscous dissipation and generation of entropy of viscous origin. At the same time, the better thermal mixing obtained with the optimized velocity fields results in a reduction in entropy generation by thermal conduction through finite temperature differences. The two components of the entropy generation rate evolve in opposite directions. However, since heat conduction entropy generation is the overwhelming majority, decreasing W_ϕ ultimately results in a decrease in the total entropy generation rate.

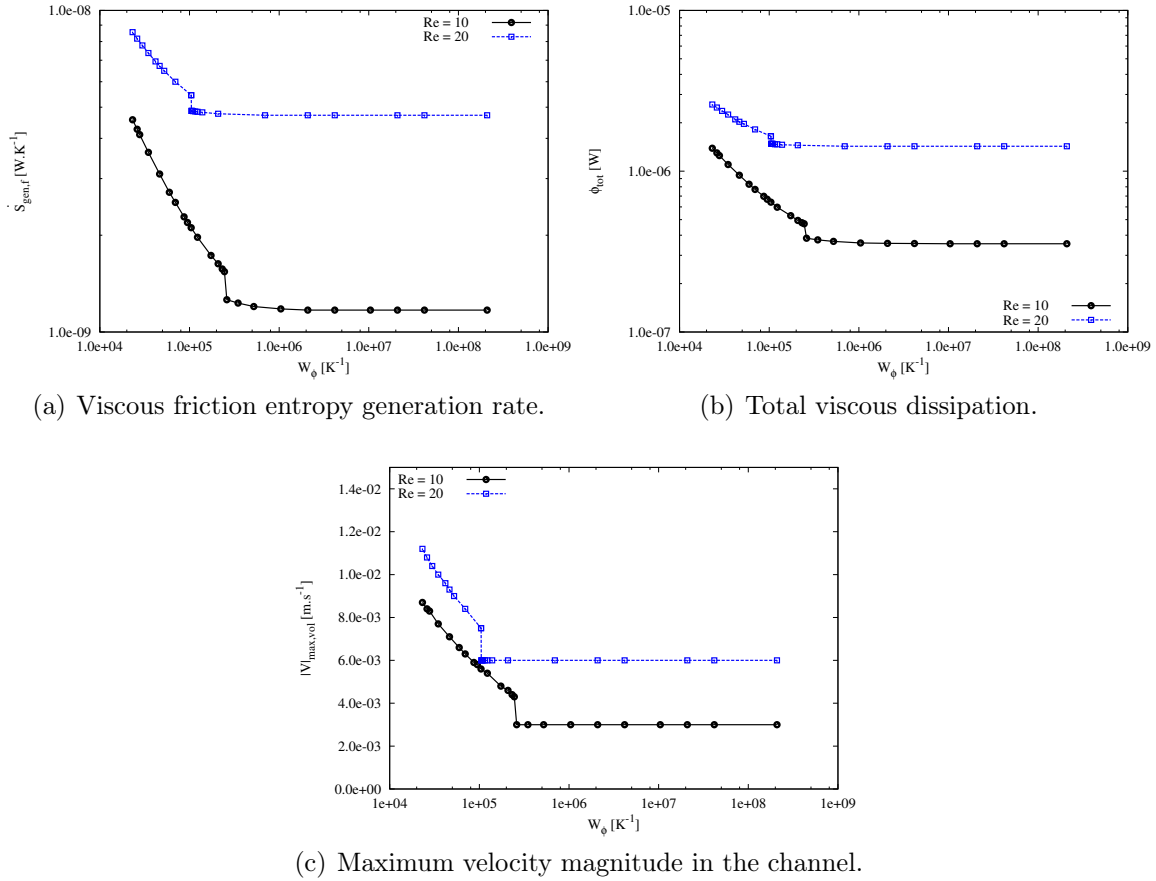


Figure 3.31: Viscous friction entropy generation rate, total viscous dissipation and maximum velocity in the channel.

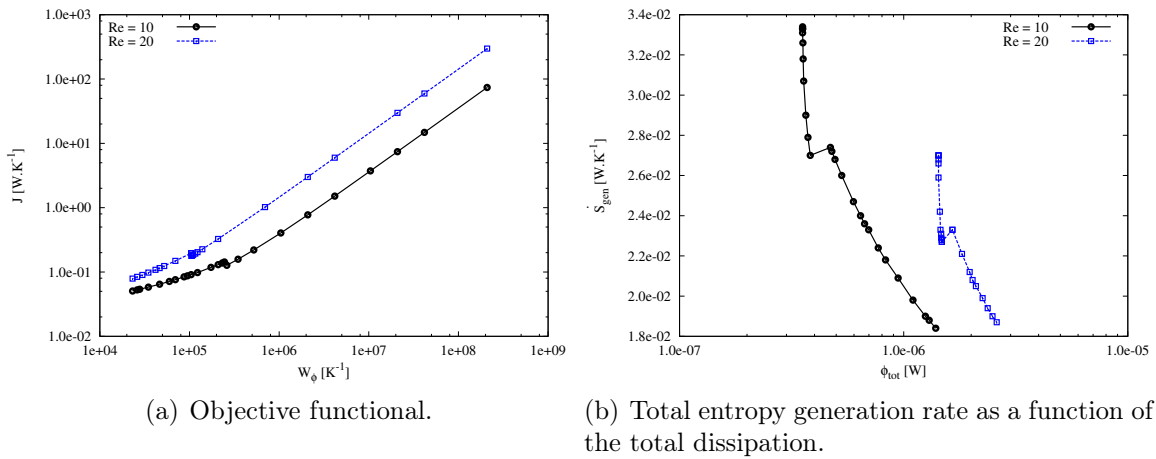


Figure 3.32: Objective functional and relationship between total entropy generation rate and total viscous dissipation

The objective functional defined in Eq. 3.21 decreases as W_{Φ} gets smaller (Fig. 3.32(a)). It is a linear combination of two terms, $\dot{S}_{gen,c} \approx \dot{S}_{gen}$ and Φ_{tot} that evolve in opposite ways when W_{Φ} varies (Fig. 3.32(b)). Taking the case $Re = 20$ as an example, when W_{Φ} falls by approximatively four orders of magnitude from $2.1 \times 10^8 K^{-1}$ to $2.3 \times$

$10^4 K^{-1}$, the entropy generation rate by heat conduction decreases from $27 mW.K^{-1}$ to $19 mW.K^{-1}$ and the total viscous dissipation raises from $1.43 \mu W$ to $2.60 \mu W$. Since the entropy generation by heat conduction and the total dissipation do not change their order of magnitude, the evolution of $W_{\mathcal{D}}$ has the decisive effect and leads to a decrease of the objective functional.

The boundary conditions have an effect on the optimized solutions. the influence of the heat flux density q'' and of the inlet velocity V_{in} are discussed below.

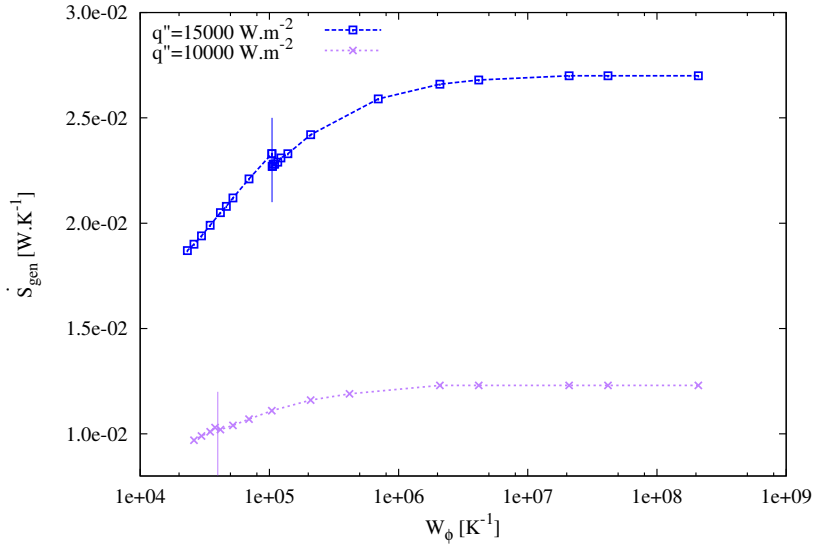


Figure 3.33: Total entropy generation rates for two values of the input heat flux. $Re = 20$.

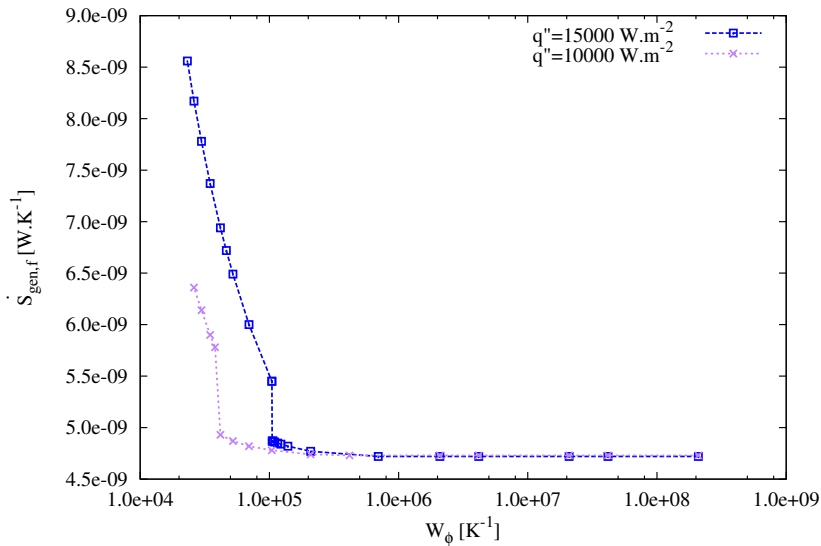


Figure 3.34: Viscous friction entropy generation rate for two values of the input heat flux.

The higher the heat flux density, the higher the entropy generation rate by heat conduction and the higher the total entropy generation rate in the channel (Fig. 3.33). The critical value of $W_{\mathcal{D}}$ is lower for a reduced heat flux density: when $Re = 20$,

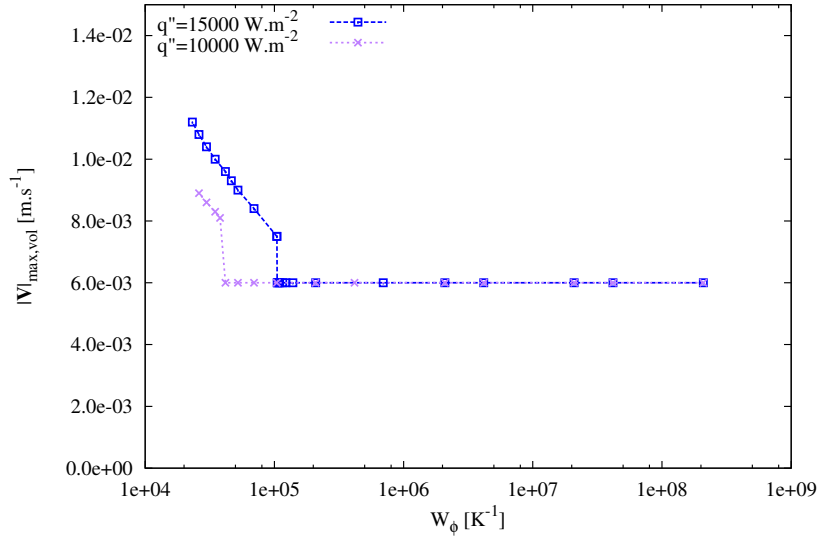


Figure 3.35: Maximum velocity magnitude in the channel as a function of W_Φ for two values of the input heat flux.

changing the heat flux boundary condition from 15000 W.m^{-2} to 10000 W.m^{-2} leads to a fall of the critical W_Φ from about $1 \times 10^5 \text{ K}^{-1}$ to $4 \times 10^4 \text{ K}^{-1}$. This change in the critical W_Φ values directly affects the behavior of the entropy generation rate by viscous friction (Fig. 3.34) as well as the maximum velocity in the channel (Fig. 3.35): as long as W_Φ is large enough, these two quantities are almost independent of the value of the flow density applied to the heated wall. On the other hand, as soon as W_Φ falls below the highest critical value (here, the one corresponding to 15000 W.m^{-2}), the curves are dissociated and the rate of generation of viscous entropy is higher in the case where $q'' = 15000 \text{ W.m}^{-2}$ compared to that where $q'' = 10000 \text{ W.m}^{-2}$.

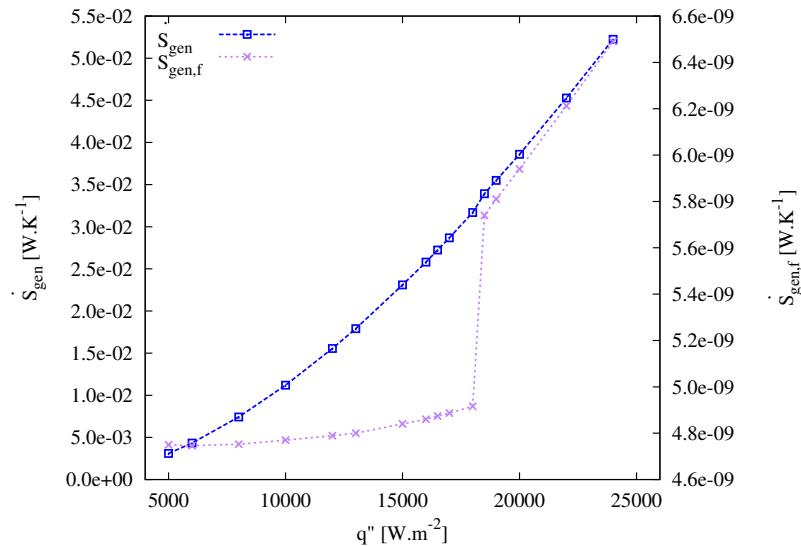


Figure 3.36: Total and viscous entropy generation rates as functions of the heat flux input from the bottom of the channel ($Re = 20$ and $W_\Phi = 1.23 \times 10^5 \text{ K}^{-1}$).

For a fixed W_Φ value, a reduction in the heat flux density applied to the wall results

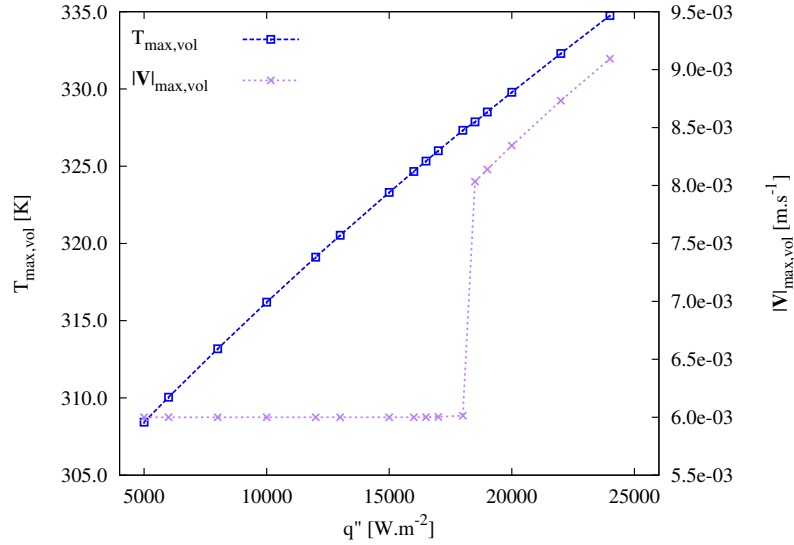


Figure 3.37: Maximum temperature and maximum velocity magnitude in the channel ($Re = 20$ and $W_{\Phi} = 1.23 \times 10^5 K^{-1}$).

in a reduction in the rate of entropy generation by heat conduction and therefore in the rate of total entropy generation (Fig. 3.36), the conductive component still remaining largely dominant in the entropy generation mix when compared to the viscous component. Similarly, the maximum temperature reached inside the channel decreases with the imposed heat flow density (Fig. 3.37). The maximum velocity reached in the channel as well as the rate of viscous entropy generation also decrease as the imposed heat flux density is reduced (while keeping Re and W_{Φ} fixed). For high values of q'' , the flow regime is of the highly perturbed type when compared to the case without optimization, whereas for a small applied heat flux density, the flow regime is of the slightly or very slightly perturbed type. The transition between the two regimes, visible in Figs. 3.36 and 3.37 takes place for a critical value $q''_{critical}$, which is about $18000 W.m^{-2}$ for $Re = 20$ and $W_{\Phi} = 1.23 \times 10^5 K^{-1}$. Indeed, as observed during the examination of Figs. 3.33 to 3.35, a reduction in the heat flux density applied to the heated wall leads to a reduction in the critical value of W_{Φ} . As a result, W_{Φ} being set to a given value $W_{\Phi,0}$ ($= 1.25 \times 10^5 K^{-1}$ for example), reducing q'' from a value corresponding to a highly perturbed ($24000 W.m^{-2}$) regime ends up making $W_{\Phi,critical}(q'')$ coincide with $W_{\Phi,0}$, which induces the transition to a low perturbed flow regime where viscous entropy generation rates and maximum velocities are lower and stabler.

If now W_{Φ} is fixed (at $1.23 \times 10^5 K^{-1}$) and q'' is also fixed (at $15000 W.m^{-2}$) while varying the inlet velocity V_{in} between $6 mm.s^{-1}$ ($Re \approx 30$) and $1 mm.s^{-1}$ ($Re \approx 5$), one can observe that the entropy generation rate of viscous origin as well as the maximum speed in the flow decrease with V_{in} (Figs. 3.38 and 3.39). A transition also appears very clearly for a critical value $V_{in,critical}$ approximately equal to $3.2 mm.s^{-1}$ ($Re = 15.8$) between highly perturbed flow regimes (when the inlet velocity is lower than $V_{in,critical}$) and slightly perturbed ones. Indeed, as already observed in Fig. 3.30(a), a reduction in the Reynolds number leads to an increase of the critical W_{Φ} . If one sets W_{Φ} to a fixed value $W_{\Phi,0}$ and reduces the inlet velocity, there is a point where the increasing critical weighting parameter $W_{\Phi,critical}(V_{in})$ reaches the value $W_{\Phi,0}$ and triggers the transition from slightly to highly perturbed profiles.

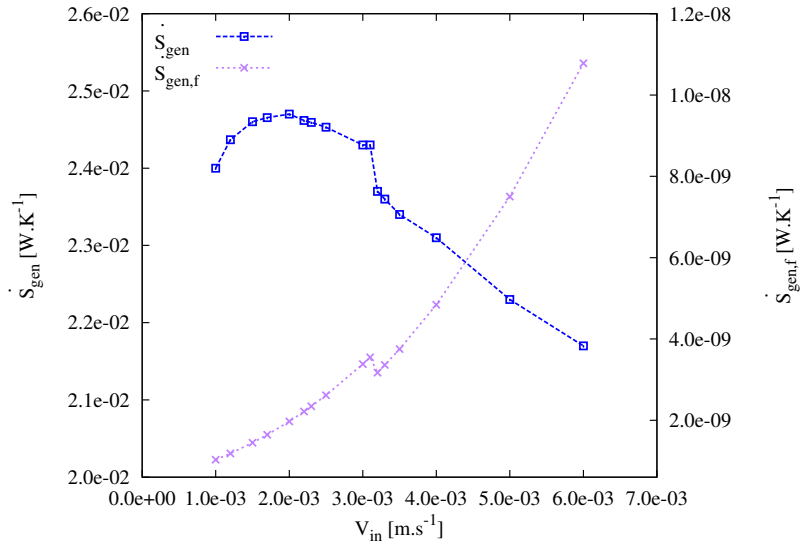


Figure 3.38: Total and viscous entropy generation rates as functions of V_{in} ($W_{\Phi} = 1.23 \times 10^5 K^{-1}$).

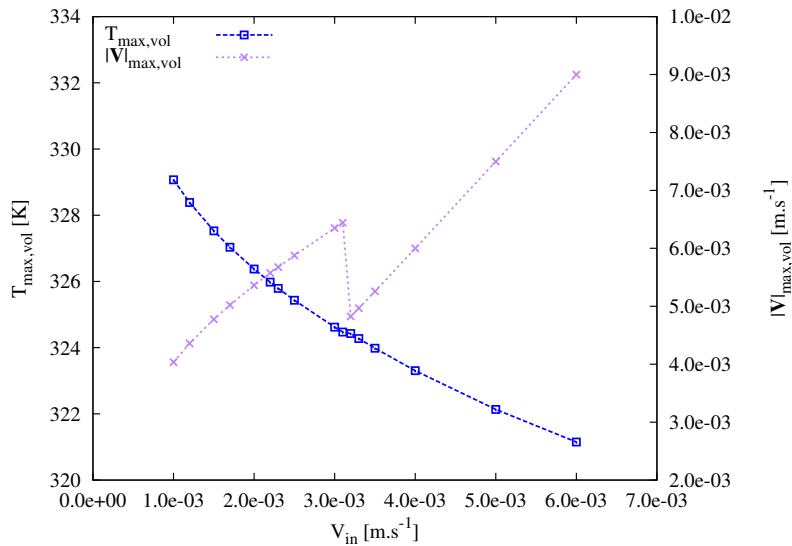


Figure 3.39: Maximum velocity magnitude and maximum scalar value in the channel as functions of V_{in} ($W_{\Phi} = 1.23 \times 10^5 K^{-1}$).

At fixed W_{Φ} and q'' , lowering the inlet velocity leads to an increase of the maximum temperature in the channel (Fig. 3.39). The total entropy generation rate also grows as V_{in} decreases with the exception of a behavior change for very small inlet velocities (when $V_{in} \leq 2 \text{ mm.s}^{-1}$) as exhibited in Fig. 3.38. This non-monotonous behavior could result from the higher complexity of the optimized velocity field obtained for very small values of the input velocity: the number of vortexes increases and leads to increased mixing effects.

3.2.6 Mass transfer

In this section, we consider the mass transfer case where at the central third of the bottom plate a minor species diffuses at a constant and uniform mass production time rate by unit of surface \dot{m}_1 . The objective is to verify if the behaviors described in section 3.2.5 are similar in a different advection-diffusion phenomenon but with close mathematical model. The comparison between heat and mass transfer simulations is done at the same Reynolds number $Re = 10$.

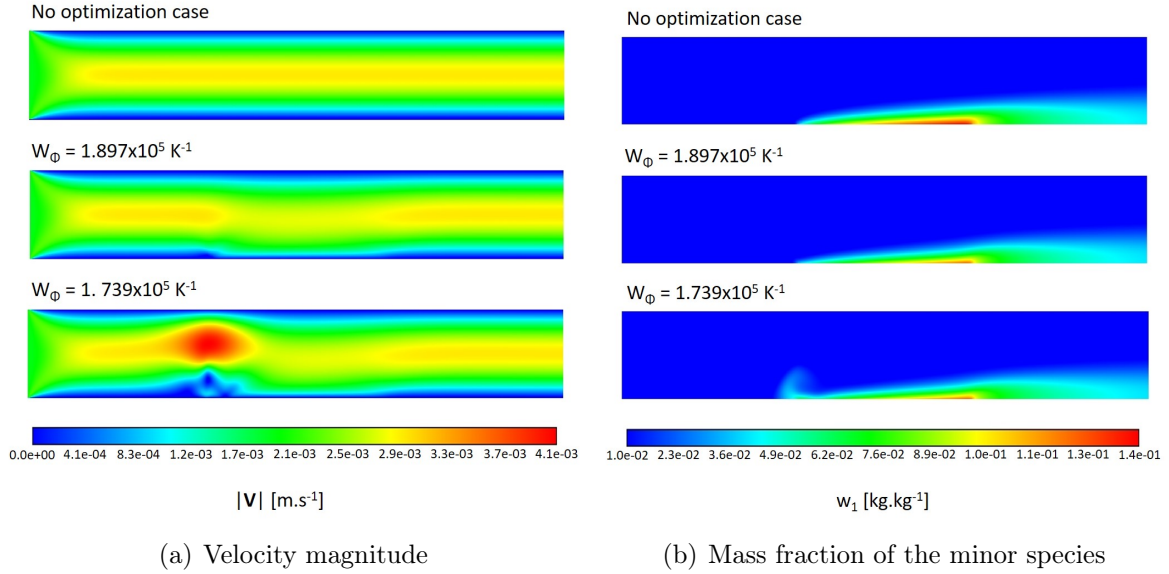
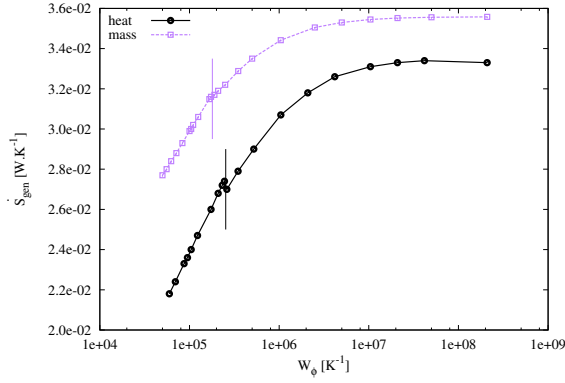


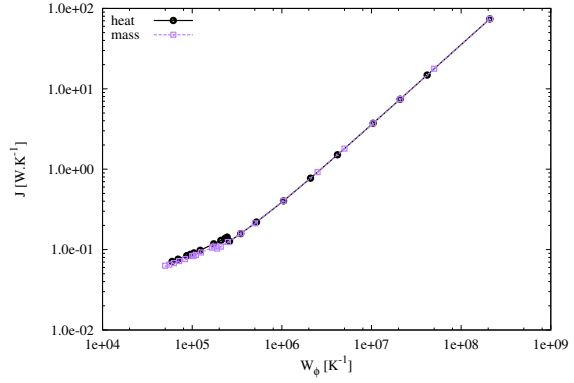
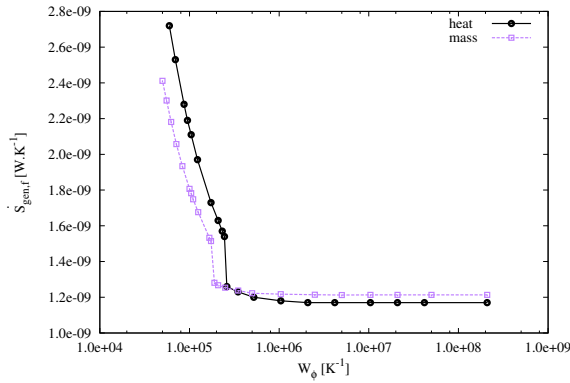
Figure 3.40: Velocity magnitude and minor species mass fraction fields with no optimization and with slightly and highly perturbed profiles ($Re = 10$)

First, one finds again the presence of slightly and highly perturbed flow regimes (Figs 3.40(a) and 3.40(b)) when compared to the non-optimized case, whose shapes are very similar to that of the velocity and transported scalar profiles of the heat transfer case (Figs. 3.28(a) and 3.28(b)), the key scalar quantity being here the mass fraction of the chemical minor species whereas this was previously the temperature.

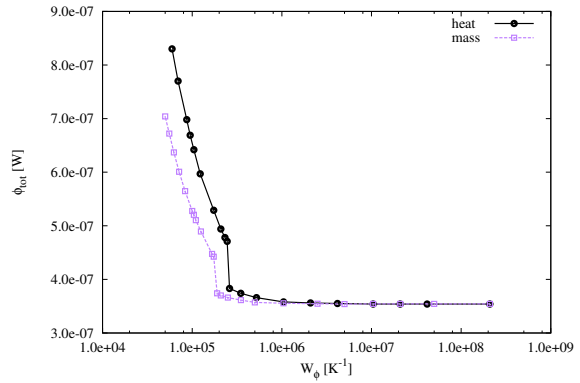
The evolution of entropy generation and viscous dissipation quantities as a function of the weighting parameter W_{Φ} are presented in Figures 3.41(a) to 3.41(f) by comparing the case of heat transfer with that of mass diffusion at $Re = 10$. A decrease in W_{Φ} leads to a reduction in the total entropy generation rate (Fig. 3.41(a)) and in the objective functional (Fig. 3.41(b)), unlike the entropy generation rate by viscous dissipation (Fig. 3.41(c)) and the total viscous dissipation (Fig. 3.41(d)) that increase as W_{Φ} decreases. These behaviors are quite similar to those observed previously in the case of heat transfer and it is the same for the relationship between the total entropy generation rate and the total viscous dissipation (Fig. 3.41(e)). The entropic improvement factor Is defined in Eq. 3.13 becomes higher as W_{Φ} gets lower (Fig. 3.41(f)). Whether it is a heat transfer case or a mass diffusion case, there is a critical W_{Φ} value that triggers the transition from the slightly perturbed regime (when W_{Φ} is large) to the highly perturbed regime (for W_{Φ} smaller than $W_{\Phi,critical}$). The critical value of W_{Φ} is about $2.5 \times 10^5 K^{-1}$ for the heat transfer case and around $1.8 \times 10^5 K^{-1}$ for the mass diffusion case. As a conclusion, without being strictly identical, the optimization of heat transfer and mass diffusion exhibit very similar behaviors.



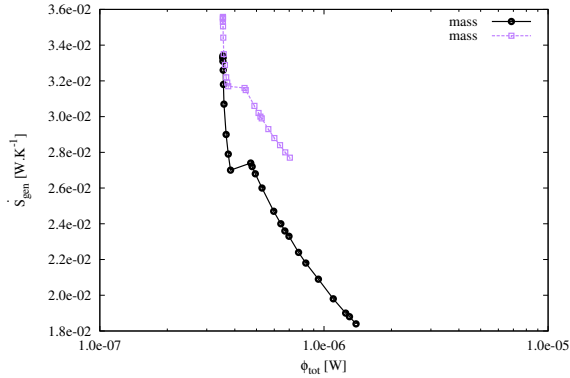
(a) Total entropy generation rate.

(b) Objective functional J .

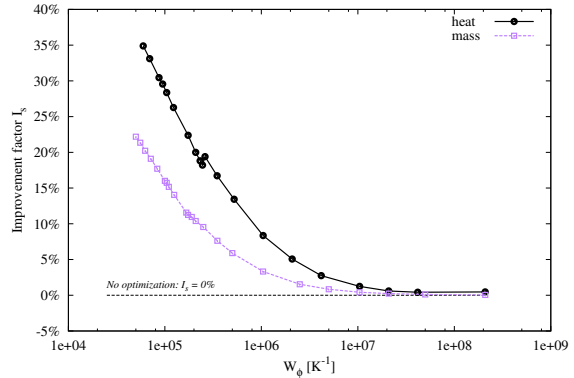
(c) Viscous friction entropy generation rate.



(d) Total viscous dissipation.



(e) Total entropy generation rate as a function of the total dissipation.



(f) Improvement factor.

Figure 3.41: Heat vs. mass transfer entropy generation rate and viscous dissipation quantities ($Re = 10$)

If the value of W_{ϕ} is set to $1.67 \times 10^5 \text{ K}^{-1}$ at a fixed Reynolds number ($Re = 10$) and the mass production rate at the exchange section of the bottom part of the channel is varied, the total and viscous entropy generation rates have profiles similar to those of heat transfer: all entropy generation rates decrease as the input flux density decreases (Fig. 3.42). In addition, a critical value of \dot{m}_1 exists for which the transition takes place between the very disturbed flow regime (for large values of \dot{m}_1) and the slightly disturbed regime (below $\dot{m}_{1,critical} \approx 9 \times 10^{-3} \text{ kg.m}^{-2}.\text{s}^{-1}$). As \dot{m}_1 gets lower,

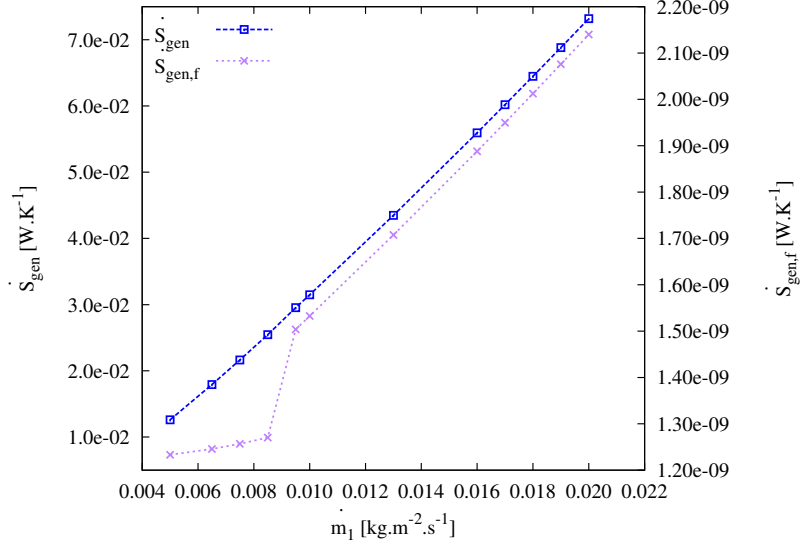


Figure 3.42: Total and viscous entropy generation rates as functions of the diffusion intensity from the bottom plate ($W_{\Phi} = 1.67 \times 10^5 K^{-1}$ and $Re = 10$).

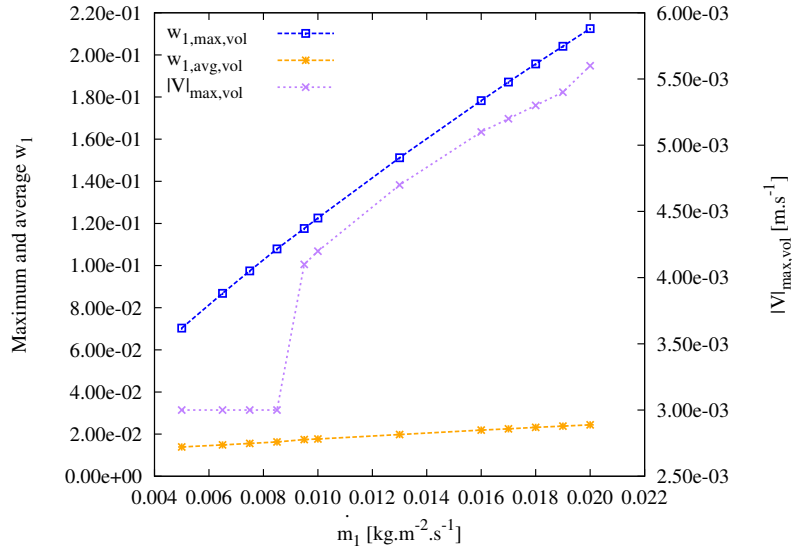


Figure 3.43: Maximum and average mass fraction of the minor species and maximum velocity as functions of the diffusion intensity from the bottom plate ($W_{\Phi} = 1.67 \times 10^5 K^{-1}$ and $Re = 10$).

the maximum and average mass fraction of the minor species decrease as does the maximum velocity in the channel (3.43), which exhibits the disruption at the critical value $\dot{m}_{1,critical}$.

If now, for a fixed value of the weighting factor ($W_{\Phi} = 1.67 \times 10^5 K^{-1}$), the Reynolds number ($Re = 10$) and the bottom plate mass flux density are fixed ($0.01 kg.m^{-2}.s^{-1}$), while varying the minor mass fraction $w_{1,in}$ at the inlet from 10^{-5} to 0.03 , all velocity and mass fraction fields stay in the highly perturbed flow regime and there is no observed critical value of $w_{1,in}$ in the tested value range. A decrease in the inlet mass fraction of the minor species leads to an increase in all entropy generation rates whether

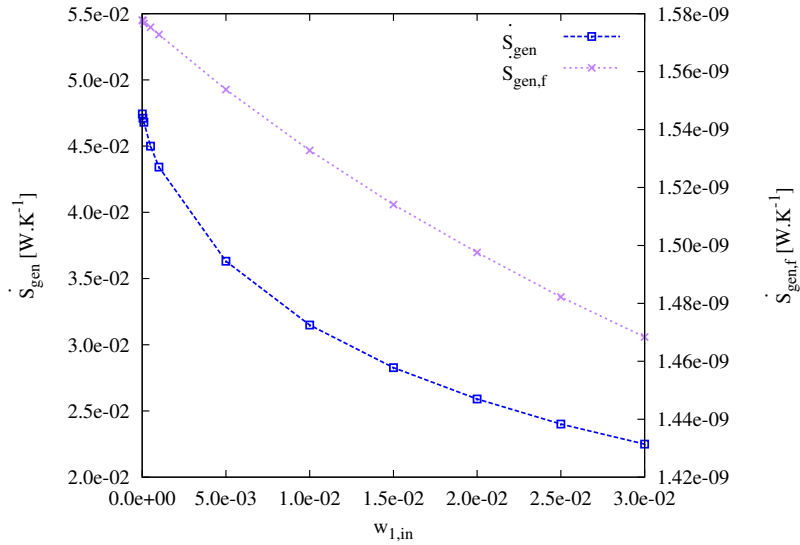


Figure 3.44: Total and viscous entropy generation rates in the channel as functions the inlet mass fraction of the minor species ($W_{\Phi} = 1.67 \times 10^5 K^{-1}$ and $Re = 10$).

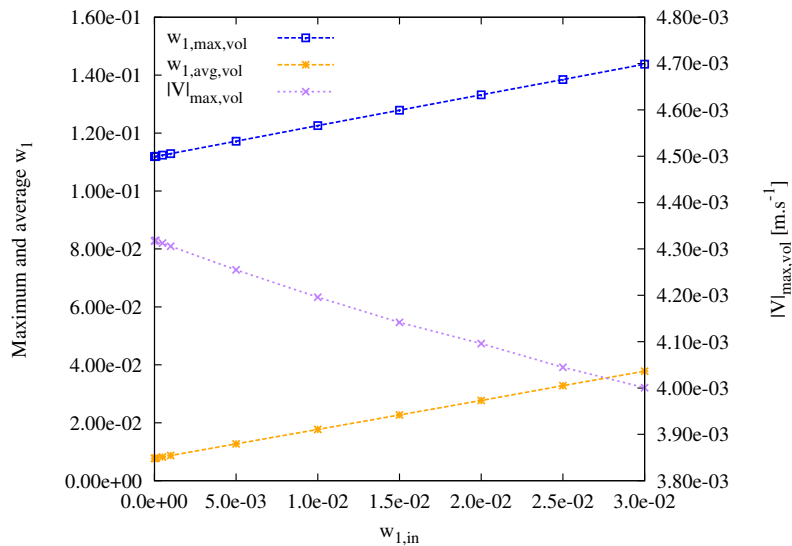


Figure 3.45: Maximum velocity magnitude in the channel as functions the inlet mass fraction of the minor species ($W_{\Phi} = 1.67 \times 10^5 K^{-1}$ and $Re = 10$).

it comes from mass diffusion or from viscous friction (Fig. 3.44). Correlatively, a lower value of $w_{1,in}$ corresponds to a reduction in the maximum and the average mass fraction of the minor species in the channel and to an increase of the maximum velocity (Fig. 3.45).

3.2.7 Robustness of the flow regime transition

In sections 3.2.5 and 3.2.6, the presence of a regime transition between slightly and highly perturbed velocity and scalar fields has been pointed out, as the existence of critical values of the W_{Φ} weighting parameter in the functional objective that trigger this transition. This has been observed for different Reynolds numbers, different values

of the physical diffusivity coefficients and different boundary conditions. It is also useful to examine the mesh independence of this regime transition, whether it depends on initial conditions and what could be its underlying cause.

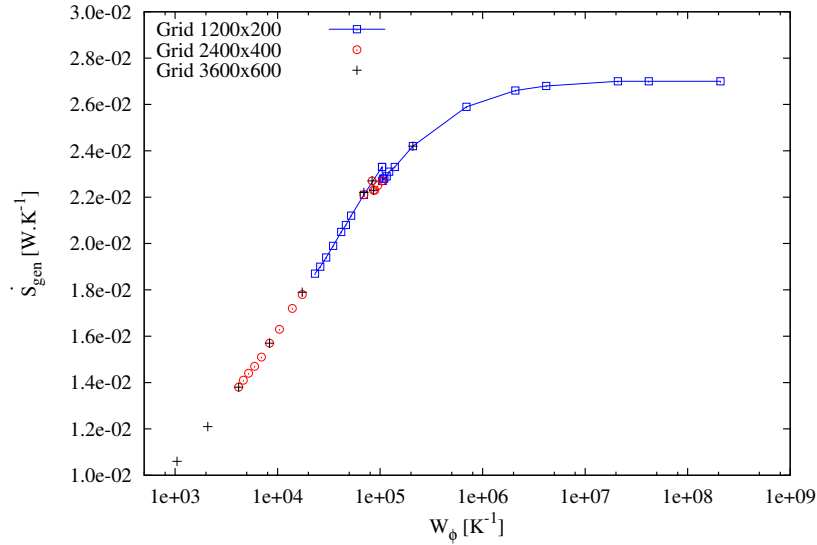


Figure 3.46: Total entropy generation rate as a function of W_{Φ} , complemented by finer mesh simulations. $Re = 20$.

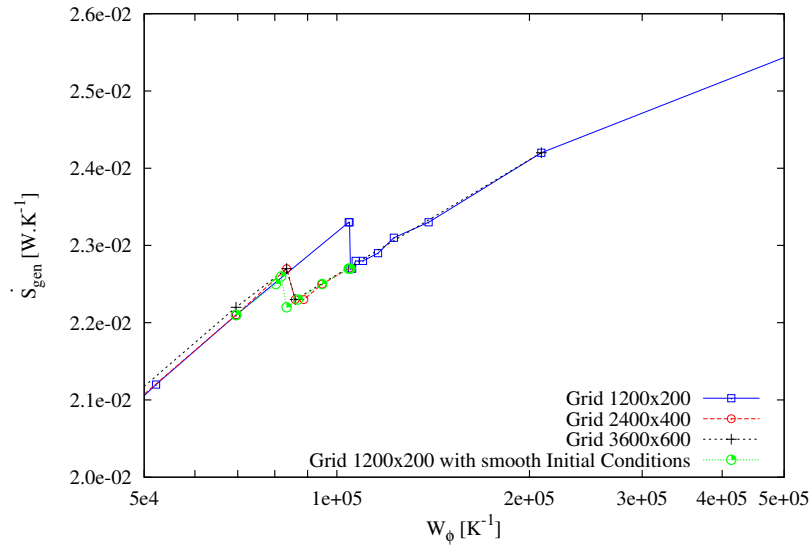


Figure 3.47: Total entropy generation rate as a function of W_{Φ} - zoom on transition zone showing the influence of the grid resolution and the initial conditions. $Re = 20$.

Keeping the same physical domain size, two finer meshes have been tested for the heat transfer case when $Re = 20$ and $q'' = 15 \text{ kW.m}^{-2}$: in addition to the base 1200×200 mesh, 2400×400 and 3600×600 meshes have been used and the corresponding results for the total entropy generation rate as a function of W_{Φ} are presented in Fig. 3.46. The \dot{S}_{gen} curve has been extended to smaller values of W_{Φ} (down to 10^3 K^{-1}) and the corresponding extended part of the graph is consistent with the above results: the total entropy generation rate keeps declining as W_{Φ} decreases.

A zoom around the critical W_{Φ} value is provided in Fig. 3.47. In the case of finer grids, the critical W_{Φ} still exists but at a lower value while keeping the same order of magnitude ($\approx 8.5 \times 10^4 K^{-1}$ in place of $\approx 1 \times 10^5 K^{-1}$). Furthermore, tests have been performed with the 1200×200 mesh by approaching the critical value of W_{Φ} step by step in a smooth manner, each simulation starting from the results of the converged previous one with a value of W_{Φ} slightly lower (while all the simulations presented above are started from the homogeneous initial conditions where the temperature of the channel is set to T_{in} and the longitudinal velocity is set to V_{in} , the normal velocity being zero at the initial time of the simulation). The corresponding results are presented in Fig. 3.47: the existence of the critical W_{Φ} is still confirmed at a value close to the one obtained with the finer grids ($\approx 8.4 \times 10^4 K^{-1}$). So, the existence and the approximate critical W_{Φ} value are quite robust.

For the high values of W_{Φ} , the product ΦW_{Φ} is much higher than the diffusion entropy generation rate (by heat conduction or mass diffusion, depending on the type of simulation performed) and the second term of the objective functional is predominant. Conversely, for small values of W_{Φ} , the first term of J in Eq. 3.21 or 3.22 is the majority. In the critical value area of W_{Φ} , in which the change in flow regime takes place, the two terms composing the objective functional have close orders of magnitude: the difference in orders of magnitude, estimated by $\text{Log}_{10}(\Phi_{tot} W_{\Phi} / \dot{S}_{gen,d})$, where $\dot{S}_{gen,d}$ is the entropy generation rate by diffusion of heat or mass, lies between 0.37 and 0.85 depending on the Reynolds number and the transfer type. The flow regime transition could therefore be related to the fact that the optimization program focuses on viscous dissipation when W_{Φ} is large and on entropy generation by heat conduction or mass diffusion when W_{Φ} is small. In the second case, the optimized solution can rely on a more complex and intense velocity field to produce a thermal mixture, at the expense of an increase in viscous dissipation which effect on the objective criterion is negligible due to the small size of the W_{Φ} factor. The transition from one regime to another would then be linked at least in part to the shift from an optimization focused on viscous dissipation to an optimization focused on entropy generation by diffusion.

3.2.8 Conclusion

In section 3.2, convective flow transfer is submitted to variational methods in order to find optimized velocity and scalar fields (temperature or mass fraction of a minor species, depending on the type of diffusion process) that minimize the entropy generation rate in a channel while keeping control on the total viscous dissipation via a weighting factor in the objective functional, allowing to give a varying importance to the viscous dissipation in the optimization process. Heat transfer and mass diffusion cases are studied and the influence of the weighting factor on the resulting fields and the key physical quantities is analyzed.

At identical Reynolds number, the optimization of mass diffusion and heat transfer exhibit similar behaviors. The velocity patterns suggested by the optimization program lead to a reduced total entropy generation rate in the channel, the relative improvement being larger as the weighting factor or the Reynolds number are lower. These patterns can be a reference for the design of enhanced exchangers. Improved scalar homogeneity (of the temperature or the minor species mass fraction, depending on the type of transfer) is observed as the scalar maximum value and standard deviation are lower while the weighting factor is reduced. This enhancement is achieved at the expense of an

increase in the entropy generation rate by viscous friction, which stays nevertheless at a negligible level. The maximum velocity and the total viscous dissipation also increase when the weighting factor decreases. Two main flow regimes are observed, depending on the level of perturbation of the velocity and scalar fields. In highly perturbed regimes, a more complex flow is observed with a vortex and a displacement of the flow towards the diffusion entry area (the heated segment or the mass diffusion entry zone, depending on the transfer process). The transition from a slightly to a highly perturbed flow is triggered by a critical value of the weighting factor, the highest perturbation level corresponding to the lowest weighting factors. This critical value depends on the Reynolds number, the heat or mass transfer intensity at the exchange plate and on the inlet velocity. The existence of the transition between two perturbation flow regimes and the corresponding critical value of the viscous dissipation weighting factor are confirmed with finer meshes and smoother initial conditions.

3.3 Conclusion and perspectives

In chapter 3, the same general optimization technique is applied to different situations in order to study its behavior. The variational approach is used for several boundary conditions (Reynolds numbers and injected flux density intensities), two fluids (with different properties) and two advection-diffusion processes (with different characteristic diffusion coefficients): the results are qualitatively similar. The optimized velocity fields lead to a reduction in the total entropy generation rate and their complexity depends on the viscous dissipation function weighting factor in the objective functional. Moreover, in the convective heat transfer case, the maximum temperature at the heated wall is reduced and thermal fields are homogenized. This method can be used as a heuristic to suggest velocity fields for the design of heat exchangers. It now remains to look for practical ways to generate these fields, by passive (like a modification of channel shape) and/or active (like a rotating device or a field applied to sensitive particles) means, while assessing and minimizing any required additional energy consumption or induced viscous dissipation. Before the flow regime transition, i.e. as long as the velocity fields are of the slightly disturbed type compared to the non-optimized case, the practical generation of these velocity fields seems simpler (but the entropy generation rate reduction is less). In addition, the variational model can be enhanced by integrating the compressibility and thermo-dependence of the fluid and different turbulence models could be used to compare the resulting fields with the laminar cases that have been presented above. Before acting on the velocity fields, it is useful to know the behavior of the entropy generation rates in a turbulent channel flow by approaching the operating conditions of the solar receivers (in particular, the presence of strong thermal gradients with asymmetric boundary conditions). This is the subject of the next chapter.

Chapter 4

Entropy generation rates in the turbulent flow

In this chapter, several characteristics of actual solar receivers are taken into account: a turbulent flow is considered and the properties of the fluid depend on temperature. In addition, a significant temperature gradient is imposed and thermal boundary conditions are asymmetric. A first published work [11], presented in section 4.1, consists in producing Direct Numerical Simulations (DNS) for a fully-developed low Mach turbulent flow of an ideal gas with thermo-dependent viscosity and thermal conductivity in a flat channel at mean friction Reynolds number $Re_\tau = 180$ submitted to asymmetric heating with a wall temperature ratio $T_2/T_1 = 2$. Mean and turbulent statistics of the flow are presented and compared for two different thermal boundary conditions: fixed temperatures on the one hand and fixed heat flux densities on the other hand. The influence of the boundary condition type is studied. Temperature variance is particularly impacted by this choice and exhibits asymmetric profiles with different behavior depending on the boundary condition. The simulations described in section 4.1 are then used as a reference and initial conditions, after adaptation of the thermo-hydraulic software, to calculate new quantities related to the entropy generation within the channel. The results are presented in section 4.2. In these two sections, the velocity component magnitudes are in capital letters for instantaneous quantities, the average of which is symbolized by the $\langle . \rangle$ symbol and lowercase letters with a "prime" are used to write fluctuating quantities. Thus, the Reynolds decomposition of the longitudinal velocity is written: $U = \langle U \rangle + u'$. Similarly, the Reynolds decomposition of the temperature writes: $T = \langle T \rangle + \theta'$, where θ' has been chosen for the fluctuation of the temperature in order to avoid a confusion with the time.

4.1 Reference simulations and influence of the thermal boundary condition type

4.1.1 Introduction

Since the seminal works of Orzag [182], Kim [123] and Moser [168], Direct Numerical Simulations (DNS) have proved to be a reference tool to study wall-bounded turbulent flows and have lead to numerous publications. Vreman [237] made a comparison of several of the resulting databases at $Re_\tau = 180$, a popular turbulent Reynolds number

(Eq. 4.10), and assessed their accuracy and reproducibility. Among the research works presenting a thermal analysis and in particular the profiles of temperature fluctuations, some are dealing with incompressible flows and assume the temperature to be a passive scalar [166], which can be an appropriate approximation when temperature gradients are small. However, in a large number of industrial applications and thermal exchangers, the gradient of temperature can be high and temperature dependent material properties must be considered. This is the case, for example, in solar receivers [211] [8] [9] [68] [69] [230], a key device in concentrated solar power plants which is worth optimizing [63]. The coupling between turbulence and significant thermal fluxes is studied thoroughly in the case of high-speed compressible flows [217] [57] [101] [165] [223] [212] but more rarely when the flow is subsonic and the fluid properties vary with the temperature [179] [230].

Moreover, the type of thermal boundary condition at the walls has an impact on the turbulent flow and on temperature fluctuations in particular. Many studies impose constant and uniform wall temperatures. For example, Dhamarathne [65] performed DNS of an incompressible channel flow with temperature treated as a passive scalar at $Re_\tau = 395$ and $Pr = 0.71$ while setting dimensionless wall temperatures to -1 and 1 respectively. He shows that the temperature fluctuation standard deviation vanishes at the walls, reaches a local maximum near the wall and then decreases to a local minimum before growing again up to the central zone of the channel. Staying in the case of incompressible flow and of passive scalar temperature, other research works deal with constant and uniform heat flux density at the walls. Different geometries have been addressed, some by Large Eddy Simulations, among which flows in tubes [186] [200], in annuli [185] [183], in rotating cylinders [184] [41] and in flat plate channels [118] [119] [31].

A part of these studies set a strong constraint on temperature fluctuations by forcing them to be zero at the walls (e.g.: [200], [184]), while other leave temperature fluctuation free (e.g. [185], [183]).

Estimating temperature variance at the walls is necessary when thermal fatigue and long-term aging of materials are at stake. Several authors compare the influence of thermal boundary condition type on the flow statistics, by analyzing fluid-solid conjugation. Flageul et al. [80] compared several thermal boundary condition types (Dirichlet isothermal, Neumann isoflux, Robin and 3D fluid-solid conjugate heat transfer) and confirmed the strong impact of the boundary condition on turbulent thermal correlation coefficients and on the variance of temperature. Tiselj et al. [227] [228] [229] also compared fluid-solid conjugation and idealized thermal boundary conditions and showed that wall temperature fluctuations depend on the fluid versus wall effusivity ratio (at the limit, when this ratio tends towards zero, the fluctuations of temperature are zero at the wall).

Nevertheless, these studies focus on incompressible and passive scalar flows. Recently, Bellec et al. [29] performed a comparison between fixed temperature vs. imposed heat flux boundary condition based upon Large Eddy Simulations for a subsonic turbulent flow in an open channel and a fluid with variable properties. To the best of our knowledge, there is no Direct Numerical Simulation equivalent comparison for a fully-developed turbulent low Mach channel flow in the presence of high temperature gradient from non-symmetric heating with thermo-dependent fluid properties. This is the scope of the present work. It can be applied, for example, to the solar receivers of concentrated solar power plants where low Mach flow turbulent temperature fluctua-

tions contribute to the thermal stress of stretched materials.

4.1.2 The governing equations of the low Mach flow

We focus on low Mach number flows for which the characteristic fluid velocity is small against the speed of sound. In a (strictly) incompressible flow, the density of each fluid particle stays unchanged (the material derivative $D\rho/Dt$ is zero, which implies that the velocity vector is divergence free). A particular situation where the flow is incompressible is when the fluid has a uniform and constant density. In a large number of flows of practical interest, the density variations of a fluid particle are negligibly small and the simplified governing equations of the incompressible flow can be applied without losing excessive precision, one necessary condition being a small Mach number: $Ma \ll 1$ [20]. This is the case in aerodynamics when the $Ma < 1/3$ criteria is used [189]. Nevertheless, even if the Mach number is small, significant density variations can come from high temperature gradients and the incompressible flow model is no longer suitable. To address this specific situation, a low Mach approximation can be defined by filtering acoustic waves [190] while keeping density variations due to the temperature. This low Mach approximation allows better numerical solving efficiency in comparison with compressible models because the Courant-Friedrichs-Lewy (CFL) stability conditions on the time step are less severe [179]. In this study we consider situations where $Ma \approx 10^{-2}$ and a hot to cold wall temperature ratio $T_2/T_1 \approx 2$ over a short distance, leading to corresponding high density variation as the study fluid is an ideal gas: this makes the low-Mach approximation a reasonable approach. In our study simulations, the density varies with the temperature and buoyancy forces are necessarily present, although their effect is not significant. The relative importance of inertial and buoyancy effects has to be assessed in order to decide whether buoyancy may be neglected or not. The Richardson number $Ri = Gr/Re^2$, where Gr is the Grashof number reflects this relative importance [33]. When $Ri < 0.1$ the flow is generally considered as being dominated by forced convection [15] [111]. For $Ri > 10$, natural convection is the main phenomena and the case where $0.1 \leq Ri \leq 10$ corresponds to mixed convection situations, where natural and forced convection have to be taken in consideration together. For the simulations presented in our manuscript, the Richardson number is small ($Ri \approx 0.01$) and the forced convection flow regime can be considered [139] [179]. Moreover, the fluid flows between two horizontal plates (Fig. 4.1), the channel height is small and the hot plate is the upper one. For all these reasons, gravity effects and buoyancy force terms are neglected in the set of governing equations. We assume there is no heat source in the volume and no radiative thermal transfer inside the channel. In the case of an ideal gas, this set of hypothesis leads to a simplified form of the Navier-Stokes equations which now read [190]:

$$\frac{\partial \rho}{\partial t} + \frac{\partial(\rho U_j)}{\partial x_j} = 0 \quad (4.1)$$

$$\begin{aligned} \frac{\partial(\rho U_i)}{\partial t} + \frac{\partial(\rho U_i U_j)}{\partial x_j} &= -\frac{\partial P_{dyn}}{\partial x_i} \\ + \frac{\partial}{\partial x_j} \left[\mu \left(\frac{\partial U_i}{\partial x_j} + \frac{\partial U_j}{\partial x_i} \right) \right] &- \frac{2}{3} \frac{\partial}{\partial x_j} \left(\mu \frac{\partial U_k}{\partial x_k} \right) \end{aligned} \quad (4.2)$$

$$\rho C_p \left(\frac{\partial T}{\partial t} + U_j \frac{\partial T}{\partial x_j} \right) = \frac{\partial P_{th}}{\partial t} + \frac{\partial}{\partial x_j} \left(k \frac{\partial T}{\partial x_j} \right) \quad (4.3)$$

$$\frac{\partial P_{th}}{\partial x_i} = 0 \quad (4.4)$$

In this system of equations the subscripts i and j obey the summation convention and ρ is the density of the fluid, U_i are the components of its velocity, μ is its dynamic viscosity, $C_p = 1005 \text{ J.kg}^{-1}\text{K}^{-1}$ is its heat capacity, k is its thermal conductivity and T is its temperature. x_i are the Cartesian coordinates and t is the time. Pressure is composed of two terms: $P = P_{dyn} + P_{th}$ where P_{dyn} accounts for the variations of pressure due the velocity and P_{th} is a uniform pressure related to density and temperature through the equation of state of the fluid:

$$P_{th} = \rho r T \quad (4.5)$$

where $r = 287 \text{ J.kg}^{-1}\text{K}^{-1}$ is the ideal gas constant.

Moreover, dynamic viscosity depends on the temperature and follows the Sutherland law, which is valid in the working temperature range of our study [221]:

$$\mu = 1.461 \times 10^{-6} \frac{T^{1.5}}{T + 111} \quad (4.6)$$

The thermal conductivity is also dependent on the temperature and is derived from the dynamic viscosity and from the constant Prandtl number $Pr = 0.76$:

$$k = \frac{\mu C_p}{Pr} \quad (4.7)$$

4.1.3 Physical and numerical model

The flow occurs between two parallel flat plates and Lx and Lz dimensions are periodic (Fig. 4.1). The domain lengths are $2\pi h \times 2h \times (\frac{4}{3})\pi h$ where $h = 0.014923 \text{ m}$.

The mesh consists of $192 \times 190 \times 128$ cells. It is uniform in the x and z directions. Mesh size follows a hyperbolic tangential law in the y direction in order to be finer close to the walls:

$$y_k = h \left\{ 1 + \frac{1}{a} \tanh \left[\left(-1 + \frac{k-1}{N-1} \right) \text{artanh}(a) \right] \right\}, \quad k \in [1, N] \quad (4.8)$$

where N is the number of nodes over h (the half-height of the channel) and a is a mesh dilatation parameter. Mesh sizes in wall units are provided in table 4.1 in the "Main" domain column. The averaging time (normalized by $h/U_{\tau m}$, where $U_{\tau m}$ is the mean friction velocity $U_{\tau m} = (U_{\tau hot} + U_{\tau cold})/2$), is $\Delta t^+ \approx 322$. These mesh sharpness and integration time are well positioned with regard to simulations that have shown a good convergence [237], [230]. After $\Delta t^+ \approx 200$, heat fluxes at the walls had stabilized and stayed within a range of $\pm 0.1\%$ of their mean values. Moreover a mesh independence check has been performed with a finer mesh ($384 \times 266 \times 384$) when temperature are imposed at the walls, whose mesh sizes in wall units are given in table 4.1 in the "Check" domain column. The resulting friction values and wall heat fluxes are respectively less than 0.6% and 0.4% different from the main mesh

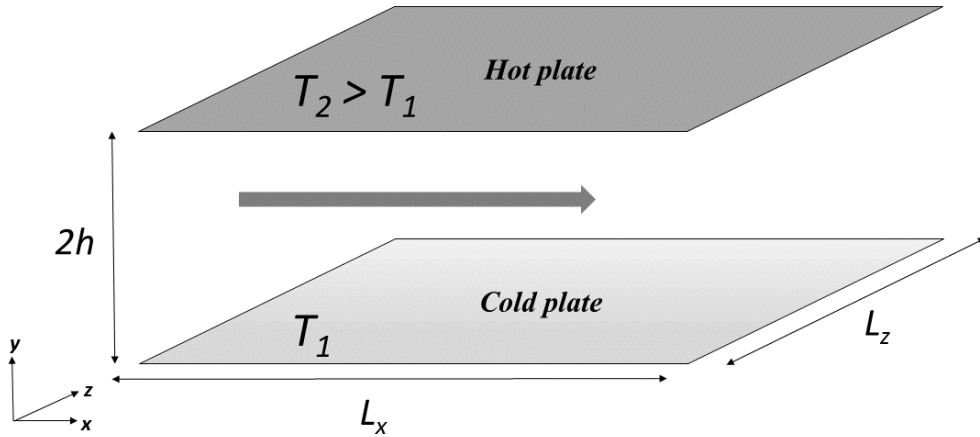


Figure 4.1: Bi-periodic flat plate channel

case. The comparison of velocity and temperature means and root-mean-square of velocity fluctuations between the main domain and the check domain exhibits very similar results (Fig. 4.2). The check domain is also larger than the main one (twice as long in the flow direction and 1.5 times larger transversely) and the proximity of the resulting flows (Fig. 4.2) indicates that the study domain is large enough so that no large scale structures are affecting the results. This confirms the observations of a previous study [230] also carried out with a $4\pi h \times 2h \times 2\pi h$ domain size, in which the two-point streamwise and spanwise velocity and temperature correlations fall near zero when the midpoints of the longitudinal and transverse dimensions of the domain are reached respectively.

Table 4.1: Domain characteristics

	Main	Check
Domain size	$2\pi h \times 2h \times \frac{4}{3}\pi h$	$4\pi h \times 2h \times 2\pi h$
Number of cells	$192 \times 190 \times 128$	$384 \times 266 \times 384$
Δx^+	4.64	4.64
Δy_{cold}^+	0.48	0.25
Δy_{center}^+	2.95	2.30
Δy_{hot}^+	0.20	0.10
Δz^+	4.64	2.32
Δt^+	322	202

The DNS were carried out with the TrioCFD thermo-hydraulic code [45] created at the French Atomic and Alternative Energies Agency (CEA) and ran on a HPC server provided by the French National Computing Center for Higher Education (CINES).

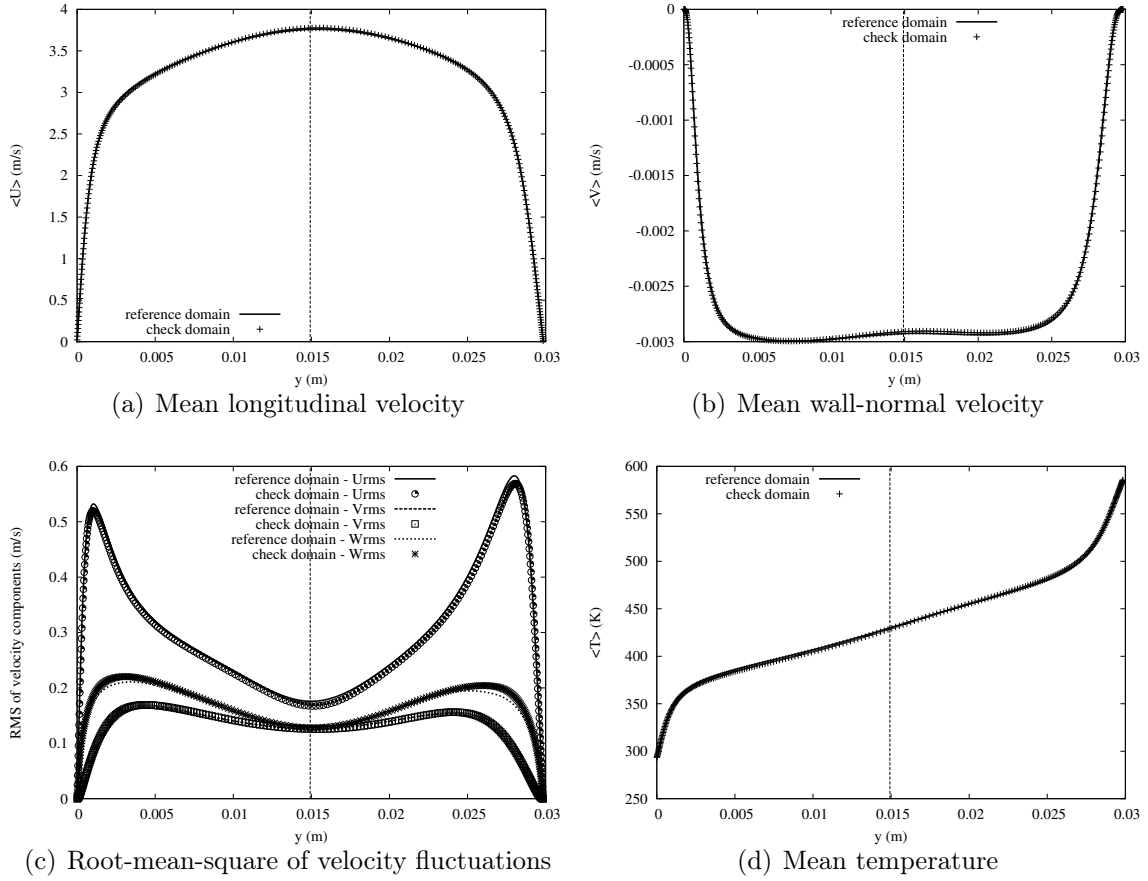


Figure 4.2: Grid and domain volume independence check

Velocity convection and diffusion are handled by a second order centered scheme. It is the same for temperature diffusion. A third order upstream QUICK scheme (Quadratic Upstream Interpolation for Convective Kinetics) is used for temperature convection. Time integration is handled by a third-order Runge-Kutta numerical scheme. As an order of magnitude in terms of computing time, the "Check" simulation in Table 4.1 corresponds to 277 runs of 24 hours on 128 processors.

A couple of comparable simulations with a wall temperature ratio $T_2/T_1 = 2$ is created. First a wall fixed temperature simulation is performed with $T_1 = 293$ K and $T_2 = 586$ K, that leads to steady mean heat flux densities at the walls which value is about 1708 W/m². These fluxes are then applied as boundary conditions to the wall fixed heat flux simulation.

4.1.4 Results

Statistics are computed by averaging results over the two periodic directions and over time. This averaging is noted by using brackets $\langle . \rangle$. The mean friction Reynolds number is set to $Re_{\tau m} = 180$, where $Re_{\tau m}$ is the mean value between the turbulent Reynolds numbers taken at the cold and the hot walls:

$$Re_{\tau m} = (Re_{\tau, cold} + Re_{\tau, hot})/2 \quad (4.9)$$

Each Reynolds number is based on the friction velocity at the corresponding wall:

$$Re_\tau = \frac{U_\tau h}{\nu_w} \quad (4.10)$$

$$U_\tau = \sqrt{\left. \frac{\langle \mu_w \rangle}{\langle \rho_w \rangle} \frac{\partial \langle U \rangle}{\partial y} \right|_w} \quad (4.11)$$

Results are normalized using the classical scaling based on the friction velocity and the friction temperature of the nearest wall:

$$y^+ = \frac{yU_\tau}{\nu_w}, \quad \langle U \rangle^+ = \frac{\langle U \rangle}{U_\tau}, \quad U_{rms}^+ = \frac{U_{rms}}{U_\tau} \quad (4.12)$$

$$\langle T \rangle^+ = \frac{|\langle T \rangle - \langle T_w \rangle|}{T_\tau}, \quad T_{rms}^+ = \frac{T_{rms}}{T_\tau}, \quad T_\tau = \frac{\langle k_w \rangle \left. \frac{\partial \langle T \rangle}{\partial y} \right|_w}{\langle \rho_w \rangle C_p U_\tau} \quad (4.13)$$

Table 4.2: Mean friction variables

Variable	Fixed temperature	Fixed heat flux
$U_{\tau, cold}$	0.175	0.173
$U_{\tau, hot}$	0.234	0.235
$Re_{\tau, cold}$	258	258
$Re_{\tau, hot}$	106	106
$T_{\tau, cold}$	5.4	5.5
$T_{\tau, hot}$	8.1	8.2

Friction variables are presented in table 4.2. The small differences between fixed temperature and fixed flux simulation friction quantities are not significant enough, when put in balance with the variability due to the grid resolution and the convergence of wall fluxes, to conclude that one of these two simulations is weaker or stronger than the other. In this study, grid and domain size independence have been assessed. Mesh resolutions and simulation times have been set in order to be well positioned when compared to previous studies [230] and the literature [179] [237]. A systematic and detailed estimation of the uncertainties coming from the discretization of the governing equations and the statistical sampling of the data, which is an active and challenging research area [181], has not been performed.

There is a slight relaminarization at the hot wall (suggested by the slight asymmetry of the profile of the mean longitudinal velocity visible in Fig. 4.2(a), the hot side exhibiting more parabolicity than the cold side). Nevertheless, turbulence is not suppressed as the root-mean-squares of all velocity component fluctuations are almost symmetrical with no serious damping at the hot side (Fig. 4.2(c)). The U_{rms} local maximum at the hot-side of the channel is even greater although slightly further from the wall. Relaminarization would be significant for higher temperature gradients [139] and hot to cold wall temperature ratios like $T_2/T_1 = 5$, for which higher friction

Reynold number like $Re_{\tau m} = 395$ would be necessary to avoid turbulence suppression as demonstrated in [211].

As shown in Fig. 4.3(a), the mean longitudinal velocity is almost unaffected by the boundary condition type. The difference is even smaller for the root-mean-squares of all velocity components and for the covariance of the longitudinal and the normal velocities presented in Fig. 4.3(c), 4.3(d), 4.3(e), and 4.3(f) respectively. The relative gap is greater for the wall-normal velocity, in particular in the central zone of the channel (fig. 4.3(b)).

The mean wall-normal velocity is different from zero as can be seen in Fig. 4.2(b) and Fig. 4.3(b), except at the walls where it is forced to zero by the boundary condition. From the equation of energy (Eq. 4.3), using Eqs. 4.4 and 4.5 that formulate the properties of the pressure P_{th} , the following expression can be derived for the divergence of the velocity field:

$$\frac{\partial U_j}{\partial x_j} = \frac{\gamma - 1}{\gamma P_{th}} \frac{\partial}{\partial x_j} \left(k \frac{\partial T}{\partial x_j} \right) - \frac{1}{\gamma P_{th}} \frac{dP_{th}}{dt} \quad (4.14)$$

In the case of fixed heat flux densities at the walls, averaging and integrating the above eq. 4.14 leads to the following dependence of the mean wall-normal velocity on the ordinate y [179]:

$$\langle V \rangle = \frac{\gamma - 1}{\gamma P_{th}} \left(\left\langle k \frac{\partial T}{\partial x_j} \right\rangle - \left\langle k \frac{\partial T}{\partial x_j} \right\rangle \Big|_{\text{cold wall}} \right) \quad (4.15)$$

The mean-normal velocity is directly linked with the conservation of energy and with the conductive heat flux crossing each horizontal plane in the channel. It is non-zero except at the walls. The total mean heat flux is constant across the channel and the vertical convective heat flux due to the average wall-normal velocity balances the variation of the mean conductive heat flux. When temperatures are fixed at the walls, eq. 4.15 is still valid when neglecting the term $\langle P'_{th} \partial_j u'_j \rangle / \langle P_{th} \rangle$. The mean wall-normal velocity is negative and pushes the flow from the hot side towards the cold side of the channel, which is also the denser area [70].

The dimensionless temperature as defined in eq. 4.13 shows very close profiles, almost independent on the thermal boundary condition type (Fig. 4.4(a)). The same stands for the turbulent wall-normal heat flux (Fig. 4.4(d)). A larger gap can be observed for the turbulent longitudinal heat flux with higher values when the heat flux is fixed (Fig. 4.4(c)), except in the central zone where the gap vanishes. The dimensionless coefficients $U_\tau T_\tau$ of the two kinds of boundary conditions are very close and this gap reflects the real values with a slight attenuation.

The boundary condition type has a major influence on the fluctuations of temperature as shown in Fig. 4.4(b). When the wall temperatures are fixed, the root-mean-square of temperature fluctuations approaches zero when getting close to the walls. This is not the case when the heat fluxes are fixed: they are about 2.5 at the hot wall and slightly below 3.0 at the cold wall. These values are compatible with previous studies when taking into account that the wall temperature fluctuations increase when the Reynolds or the Prandtl number increase [185], [80], [227]. The local maximum near the wall is higher and closer to the wall when the heat flux is fixed. The asymmetry of the thermal boundary condition leads to the corresponding asymmetric profiles of the temperature fluctuations. Real T_{rms} are higher at the hot wall than at the cold one.

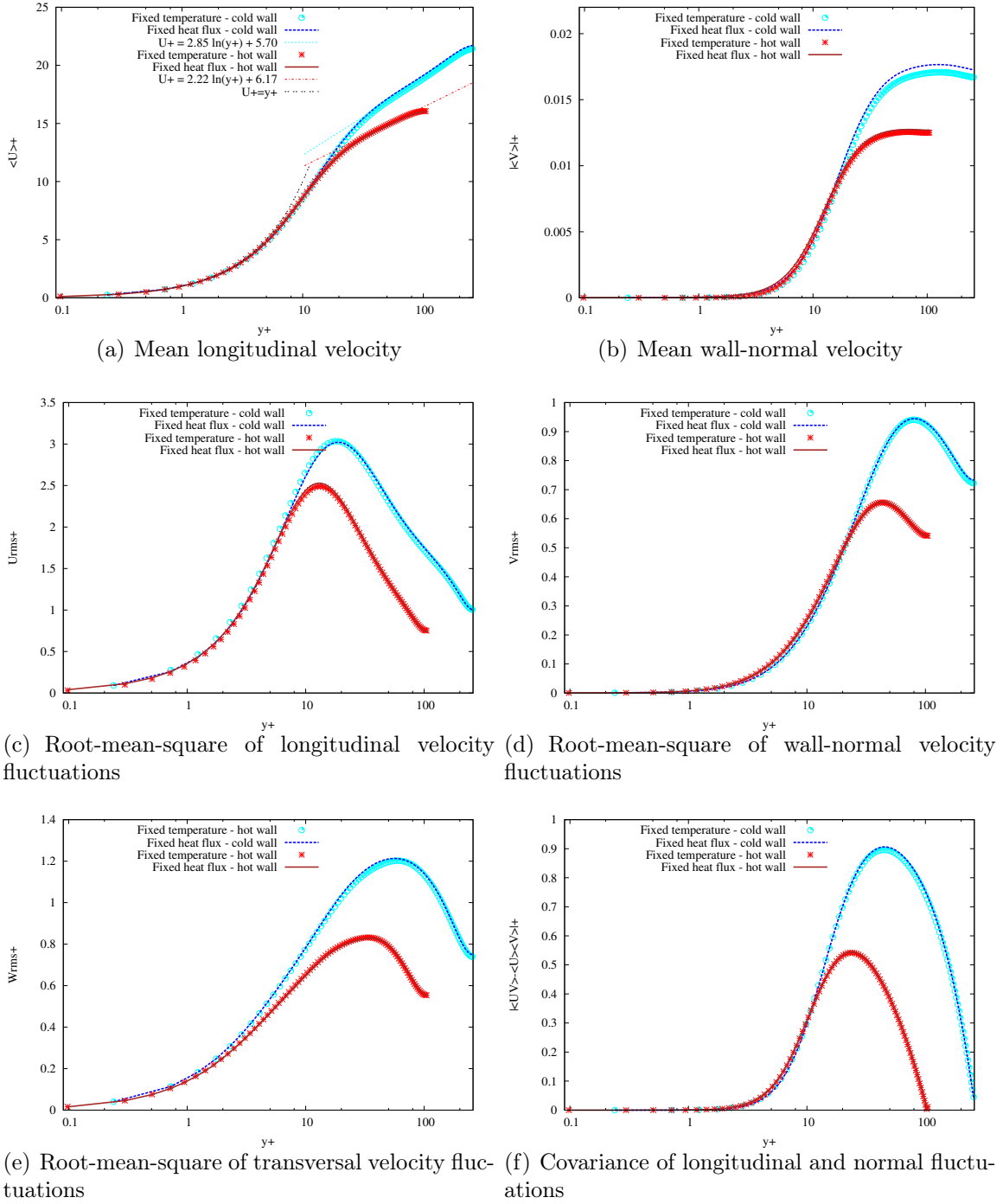


Figure 4.3: Dynamic statistics

The dimensionless coefficient T_τ is also higher at the hot wall and the net effect leads to a lower dimensionless standard deviation of temperature fluctuations at the hot wall. In the central area of the channel, the temperature fluctuations become independent on the boundary condition type. Unlike results from symmetric heating [80] or from a developing flow in an open channel [29], temperature fluctuations do not collapse in the central area: they keep the same order of magnitude across the section.

$$R_{UT} = \frac{\langle UT \rangle - \langle U \rangle \langle T \rangle}{U_{rms} T_{rms}} \quad (4.16)$$

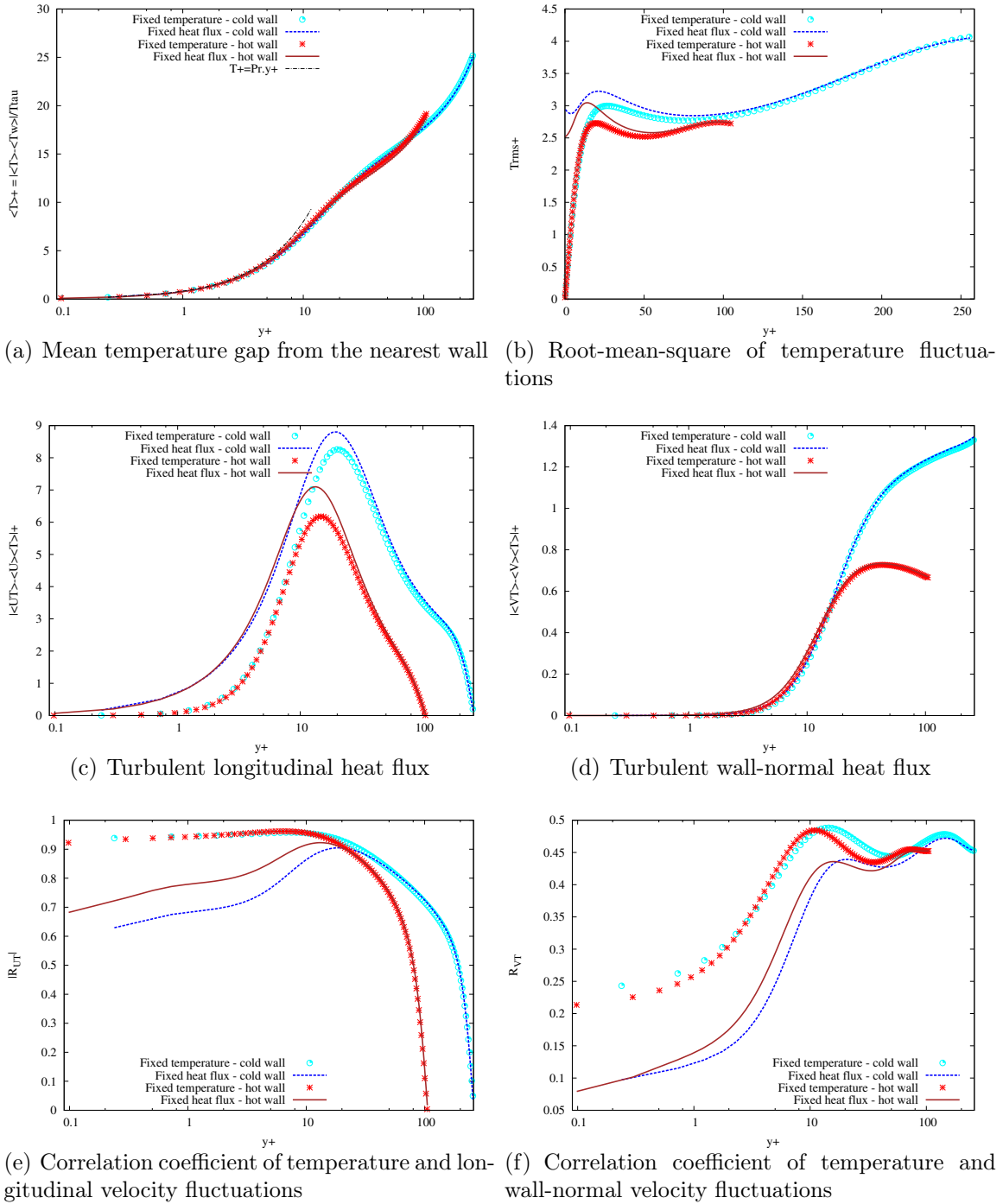


Figure 4.4: Statistics involving temperature

$$R_{VT} = \frac{\langle VT \rangle - \langle V \rangle \langle T \rangle}{V_{rms} T_{rms}} \quad (4.17)$$

The correlation coefficients R_{UT} (eq. 4.16) and R_{VT} (eq. 4.17) combine the behaviors of the turbulent heat fluxes and the standard deviations of temperature and velocities.

In the central area of the channel R_{UT} approaches zero and is the same whatever the boundary condition type (Fig. 4.4(e)). Indeed, the longitudinal turbulent heat flux vanishes near the centerline while the fluctuations of the temperature and the

longitudinal velocity stay finite. Near the walls, the correlation coefficient is higher when wall temperatures are fixed and about 0.9 (in good agreement with value cited by Huang et al. [101]). If the heat flux is imposed, the correlation splits into asymmetric profiles from the hot and the cold wall respectively. The correlation coefficient is higher at the hot wall side of the channel: near the walls (for $y^+ < 10$), the longitudinal turbulent heat flux and the U_{rms} are almost identical whatever the wall side but the T_{rms} are lower at the hot wall and this leads to a greater correlation coefficient.

The correlation coefficient of the temperature and the wall-normal velocity (Fig. 4.4(f)) is lower near the walls when heat fluxes are imposed, because the temperature is free to fluctuate and leads to higher and non-zero T_{rms} while the V_{rms} and the wall-normal heat fluxes are almost independent on the boundary condition type. In the central area of the channel, R_{VT} are closer for the two kinds of boundary conditions as the temperature fluctuations share the same order of magnitude.

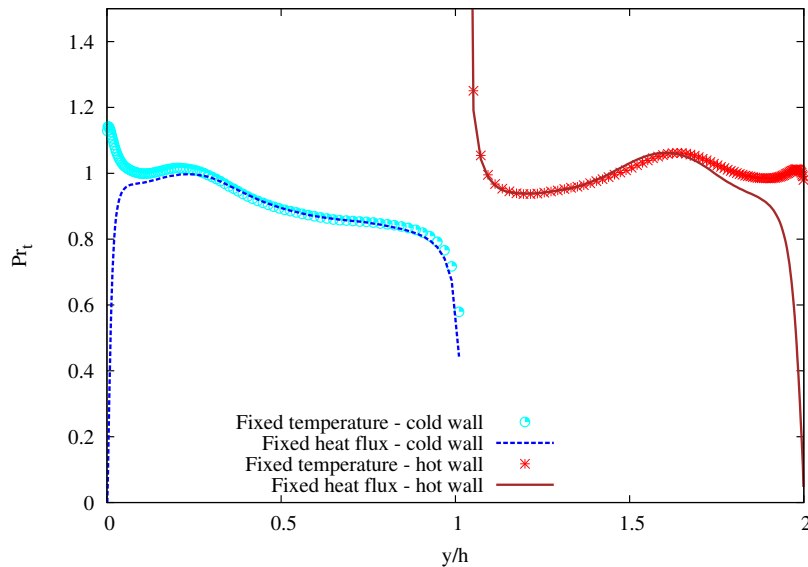


Figure 4.5: Turbulent Prandtl number Pr_t

$$Pr_t = \frac{(\langle UV \rangle - \langle U \rangle \langle V \rangle) \frac{\partial \langle T \rangle}{\partial y}}{(\langle VT \rangle - \langle V \rangle \langle T \rangle) \frac{\partial \langle U \rangle}{\partial y}} \quad (4.18)$$

When the temperature is fixed at the walls, the turbulent Prandtl number (eq. 4.18 and Fig. 4.5) takes values between 0.8 and 1.07 except near the centerline (when $0.95 < y/h < 1.05$) and close to the cold wall (when $y/h < 0.02$). With fixed wall temperatures, Pr_t is about 1.13 at the cold wall and 0.98 at the hot wall. Near the centerline of the channel, the covariance of the longitudinal and wall-normal velocity fluctuations $\langle UV \rangle - \langle U \rangle \langle V \rangle$ vanishes. It is the same for the normal derivative of the mean longitudinal velocity $\partial \langle U \rangle / \partial y$. These two zero points do not coincide exactly and their dimensionless distance is around 8×10^{-3} . The Reynolds shear stress zero point happens before the maximum of $\langle U \rangle$ and this gap leads to a discontinuity and a divergent behavior of the turbulent Prandtl number with a vertical asymptote. This observation is in agreement with a previous study done with a finer grid [230]. The discontinuity point is located slightly after the centerline in the hot side of the

channel, because of the asymmetry of the boundary conditions. Non-coincidence of the positions of zero shear stress and maximum mean longitudinal velocity have also been observed in other cases where boundary conditions are asymmetric: in turbulent annular concentric pipe flows with asymmetrical curvature effects ([201] [202]) and in fully-developed asymmetric flow in plane channels with different roughening of the planes ([97]).

If heat flux is imposed, the turbulent Prandtl number is hardly changed except near the walls where it vanishes. Both the wall-normal heat flux and the covariance of the longitudinal and normal velocities approach zero when getting close to the walls, but the latter vanishes faster and rules the behavior of the turbulent Prandtl number at the walls.

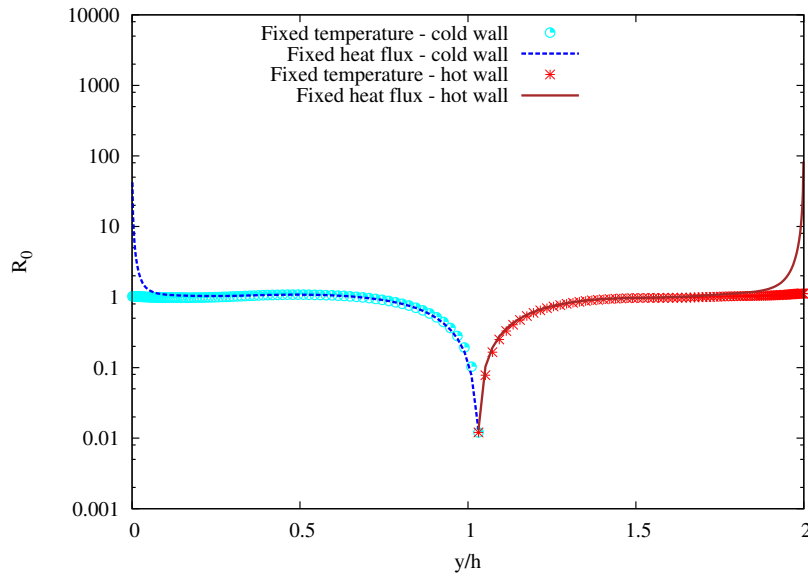


Figure 4.6: R_0 coefficient (eq. 4.19) with logarithmic y -scale

$$R_0 = \frac{T_{rms} \left| \frac{\partial \langle U \rangle}{\partial y} \right|}{U_{rms} \left| \frac{\partial \langle T \rangle}{\partial y} \right|} \quad (4.19)$$

The R_0 coefficient [230] is defined in eq. 4.19. For fixed temperature walls, R_0 takes values between 0.95 and 1.13 except in the central area (when $0.73 < y/h < 1.44$) where the normal derivative of the mean longitudinal velocity approaches zero (Fig. 4.6). The assumption $Pr_t \approx \frac{1}{R_0}$ made by Gaviglio [89] is verified with a $\pm 15\%$ relative error with respect to Pr_t except in the centerline vicinity (when $0.67 < y/h < 1.37$) where $\frac{1}{R_0}$ grows or decreases faster than Pr_t . If heat fluxes are imposed at the walls, R_0 diverges when approaching the cold or the hot wall because U_{rms} vanishes while T_{rms} stays finite.

The Nusselt numbers for the hot and cold walls are presented in Table 4.3, as well as the values obtained using three correlations (Dittus & Boelter [66] in eq. 4.20, Battista & Perkins [21] in eq. 4.21 and Jo [112] in eq. 4.22). All computations are based on the channel height $2h$, on the bulk Reynolds number and on the properties of the fluid at the walls. The temperature of the fluid T_f is taken at the center of the channel.

Table 4.3: Nusselt numbers ($L_c = 2h$)

	Cold wall	Hot wall
<i>Present simulations</i>	15	8.5
<i>Dittus – Boelter</i>	31	12
<i>Battista – Perkins</i>	38	15
<i>Jo</i>	28	9

$$Nu = 0.023Re^{0.8}Pr^{0.4} \quad (4.20)$$

$$Nu = 0.021Re^{0.8}Pr^{0.4} \left(\frac{T_w}{T_f} \right)^{-0.7} \quad (4.21)$$

$$Nu = 0.0058Re^{0.9383}Pr^{0.4} \quad (4.22)$$

The Nusselt number at the hot wall is lower than the one at the cold wall, the thermal conductivity being around 1.6 larger at the hot wall because of its dependency on the temperature. This is also accounted by the three correlations used as a comparison in Table 4.3. All correlations provide estimates that are significantly larger than the simulation results, the gap being more important at the cold wall. Nevertheless, the aspect ratio of the flat plate bi-periodic channel is very particular and far from the tubular or square geometries at the origin of the correlations. The correlation developed in [112] provides almost exactly the Nusselt value at the hot wall, the gap being still high at the cold wall, although a bit reduced. It is interesting to notice that this last correlation has been developed to fit narrow rectangular channels.

4.1.5 Conclusion and perspectives

In this section, we have studied the influence of thermal boundary conditions at the walls (fixed temperatures versus imposed heat flux) on a fully developed turbulent channel flow at friction Reynolds number 180 and with a wall temperature ratio of 2. The fluid is an ideal gas and its viscosity and thermal conductivity depend on the temperature. Results show that the longitudinal velocity and the velocity fluctuations are little modified. It is the same for the covariance of the longitudinal velocity and the wall-normal velocity and for the turbulent wall-normal heat flux. Mean temperature also stays almost unchanged. Whatever the boundary condition type, positions of zero shear stress and maximum mean longitudinal velocity are non-coincident and slightly shifted to the hot side of the channel. This leads to a divergent behavior of the turbulent Prandtl number in the central area of the channel.

Other statistics are more impacted by the thermal boundary condition type. This impact appears mainly near the walls, the central area of the channel being almost independent on the boundary condition. The turbulent longitudinal heat flux is higher when the wall heat flux is fixed. The opposite stands for the related correlation coefficient. The correlation coefficient of the temperature and the wall-normal velocity

is lower when the heat flux is imposed. The turbulent Prandtl number is also lower and vanishes at the walls when heat fluxes are fixed. The temperature fluctuations are strongly impacted. They keep the same order of magnitude all across the channel and do not vanish at the walls when heat fluxes are fixed. Dimensionless temperature variance is asymmetric and reaches about 2.5 at the hot wall and 3.0 at the cold wall.

4.2 Analysis of the entropy generation rate in the turbulent flow

4.2.1 Introduction

The reference simulations described in section 4.1 have been continued after a modification of the thermo-hydraulic calculation code to compute the instantaneous and average magnitudes of additional quantities such as the entropy generation rate. In addition, new simulations have been launched to examine the influence of several flow parameters (such as the mean friction Reynolds number and the hot to cold wall temperature ratio) on the entropy generation rate profiles. The characteristics of these different simulations are detailed in appendix B. Their progress in terms of dimensionless averaging simulation time are varied: the reference simulations ($T_2/T_1 = 2$ and $Re_{\tau m} = 180$ with the "main" mesh resolution defined in table 4.1) have been continued up to $\Delta t^+ \geq 350$ for the base quantities like the velocity components and the temperature and $\Delta t_{additional}^+ \geq 74$ for the additional ones, like the entropy generation rate. The new simulations, used for the parametric study (with different friction Reynolds numbers or temperature ratios), have been calculated on smaller integration times. Mesh independence has been successfully verified (see section 4.2.8).

The statistics (means, root-mean-squares and correlations) are computed by averaging on horizontal (xz) planes and on time. They are presented as functions of the height from the bottom wall (y) or the dimensionless distance to the closest wall (y^+). Unless otherwise specified, the default characteristics of the simulations are: a hot to cold wall temperature ratio $T_2/T_1 = 2$, a mean friction Reynolds number $Re_{\tau m} = 180$, fixed wall temperatures and the "main" mesh definition. The local entropy generation rates in the flow are computed by applying the usual formulas:

$$\dot{S}_{gen}''' = \frac{k}{T^2} \left[\left(\frac{\partial T}{\partial x} \right)^2 + \left(\frac{\partial T}{\partial y} \right)^2 + \left(\frac{\partial T}{\partial z} \right)^2 \right] + \frac{\Phi}{T} \quad (4.23)$$

$$\Phi = \mu \left\{ 2 \left[\left(\frac{\partial U}{\partial x} \right)^2 + \left(\frac{\partial V}{\partial y} \right)^2 + \left(\frac{\partial W}{\partial z} \right)^2 \right] + \left(\frac{\partial U}{\partial y} + \frac{\partial V}{\partial x} \right)^2 + \left(\frac{\partial U}{\partial z} + \frac{\partial W}{\partial x} \right)^2 + \left(\frac{\partial V}{\partial z} + \frac{\partial W}{\partial y} \right)^2 - \frac{2}{3} \left(\frac{\partial U}{\partial x} + \frac{\partial V}{\partial y} + \frac{\partial W}{\partial z} \right)^2 \right\} \quad (4.24)$$

4.2.2 Mean and turbulent entropy production rates

The mean local entropy generation rate $\langle \dot{S}_{gen}''' \rangle$ as a function of the ordinate y is presented in Fig. 4.7 when the hot to cold wall fixed temperature ratio is $T_2/T_1 = 2$ and the mean friction Reynolds number is $Re_{\tau} = 180$. The main entropy generation rates are located in the vicinity of the walls, where the temperature gradients are the highest and the ratios between the wall entropy generation rates and the one observed at the center of the channel are about 51 and 8 for the cold and hot walls respectively. The profile is asymmetrical and the entropy generation rate is higher at the cold wall. The temperature gradient at the hot wall is smaller than at the cold wall and the temperature is obviously higher: these two effects contribute to reducing the entropy

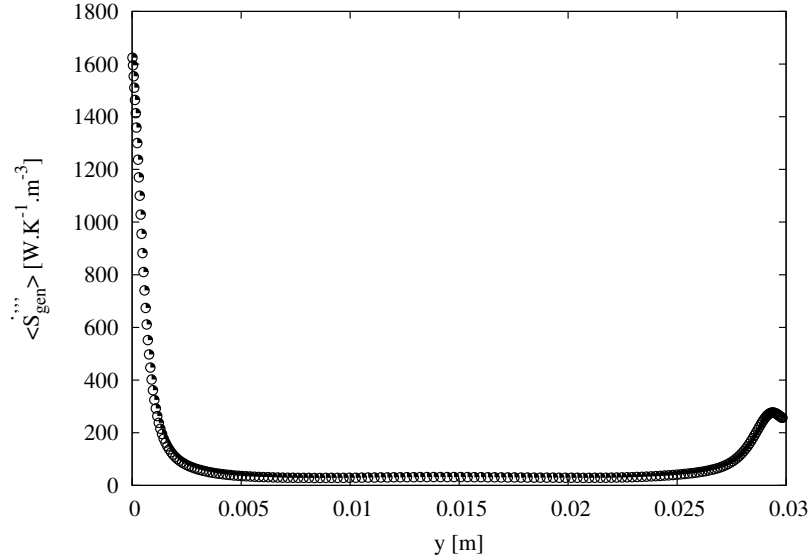


Figure 4.7: Mean local entropy generation rate.

generation rate on the hot side of the channel, although the effect is somewhat offset by a higher thermal conductivity on the hot side. Finally, the ratio between the entropy generation rate at the cold wall compared to the hot one is approximately 6. The entropy generation rate presents a local maximum near the hot wall whereas this is not the case for the cold one, where it is only decreasing. On the cold side, the temperature increases and its gradient drops with the distance to the wall: both effects contribute to a rapid decrease in the entropy generation rate (again, the increasing thermal conductivity away from the cold wall only slightly dampens the decrease of the mean local entropy generation rate without reversing the trend). Near the hot wall, the temperature gradient is almost constant while the temperature decreases, hence the increase in the entropy production rate very close to the wall. A little further from the hot wall, the temperature gradient drops rapidly while the temperature declines at a slower rate and the combination of these effects results in a decrease in the entropy generation rate. The position of the maximum entropy production rate at the hot side of the channel is located at $y^+ = 3.4$, i.e. a little below the usual value taken for the end of the viscous sublayer ($y^+ \approx 5$). Nevertheless, a close look at the $\langle U \rangle^+(y^+)$ curves shows that in the case of asymmetrically heated channel, the separation between the $\langle U \rangle^+ = y^+$ law and the actual curves occurs a little earlier when compared to symmetrical heating situations [120], which also start separating from the theoretical law between $y^+ = 3$ and $y^+ = 4$. The existence of a local maximum of the entropy generation rate due to the competition of the decreasing of the temperature and its vertical gradient had also been found in section 2 in the case of a laminar boundary layer. Near-wall entropy generation rate local maximums are also reported in [125] [126] for high Prandtl numbers ($Pr = 5$).

As previously practiced, the entropy generation rate can be divided into two sub-parts: the one resulting from heat conduction and that due to viscous friction (Eq. 4.25).

Table 4.4: Relative importance of heat conduction and viscous friction in the mean local entropy generation rate [$W.K^{-1}.m^{-3}$]. Be is the Bejan thermodynamic number.

	Cold wall	Channel center	Hot wall
Heat conduction $\langle \dot{S}_{gen,c}''' \rangle$	1623.3	31.6	255.1
Viscous friction $\langle \dot{S}_{gen,f}''' \rangle$	0.84	1.7×10^{-3}	1.79
Ratio $\langle \dot{S}_{gen,f}''' \rangle / \langle \dot{S}_{gen,c}''' \rangle$	5.2×10^{-4}	5.3×10^{-5}	7.1×10^{-3}
Be ($\langle \dot{S}_{gen,c}''' \rangle / \langle \dot{S}_{gen}''' \rangle$)	0.999	≈ 1.000	0.993

$$\dot{S}_{gen,c}''' = \frac{k}{T^2} \left[\left(\frac{\partial T}{\partial x} \right)^2 + \left(\frac{\partial T}{\partial y} \right)^2 + \left(\frac{\partial T}{\partial z} \right)^2 \right] \quad (4.25)$$

$$\dot{S}_{gen,f}''' = \frac{\Phi}{T}$$

The heat conduction part is by far the largest part in the mean local entropy generation rate (see Table 4.4), the Bejan number being almost equal to unity: in the studied configuration where temperature gradients are significant while the Reynolds number is moderate, the viscous part of the entropy generation rate can be neglected. The relative importance of the entropy generation rate due to viscous friction is a little higher at the hot wall: this viscous part has the same order of magnitude on both walls (around $1 W.K^{-1}.m^{-3}$), but the heat conduction entropy generation rate is lower at the hot wall as explained above. The ratio between the viscous part and the heat conduction part is about 15 times higher at the hot wall when compared to the cold wall: this is due in particular to the higher temperature and the lower average square of the vertical temperature gradient $\langle (\partial T / \partial y)^2 \rangle$ at the hot side.

The entropy generation rate due to heat conduction consists in three contributors, depending on the derivative direction of the temperature (Eqs. 4.26 and 4.27):

$$\dot{S}_{gen,c}''' = \dot{S}_{gen,c,T_x}''' + \dot{S}_{gen,c,T_y}''' + \dot{S}_{gen,c,T_z}''' \quad (4.26)$$

$$\dot{S}_{gen,c,T_x}''' = \frac{k}{T^2} \left(\frac{\partial T}{\partial x} \right)^2 \quad \dot{S}_{gen,c,T_y}''' = \frac{k}{T^2} \left(\frac{\partial T}{\partial y} \right)^2 \quad \dot{S}_{gen,c,T_z}''' = \frac{k}{T^2} \left(\frac{\partial T}{\partial z} \right)^2 \quad (4.27)$$

At the wall vicinities, the main contributor to the mean local heat conduction entropy generation rate (Fig. 4.8) is the vertical gradient of the temperature (due to the fixed temperature boundary condition, the x and z derivatives of the temperature are zero at the walls). In the center of the channel, the orders of magnitudes of the three direction components are similar and around $10 W.K^{-1}.m^{-3}$. Neglecting the horizontal and transversal heat conduction parts in the entropy generation rate due to heat conduction leads to about 20% underestimation of the total channel entropy generation rate in $W.K^{-1}$.

The composition of the mean local entropy generation rate due to viscous friction (see Eqs. 4.28 to 4.31) demonstrates that the main contributor is the vertical

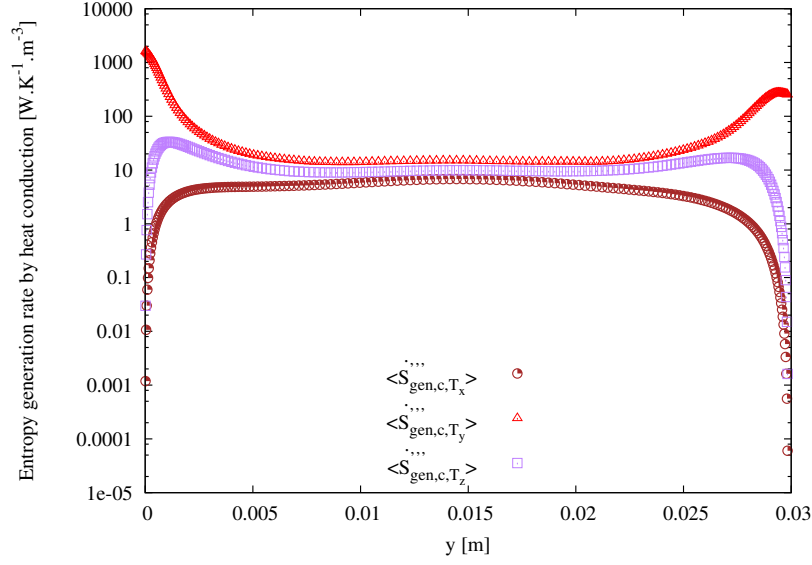


Figure 4.8: Mean local entropy generation rate by heat conduction components (Eqs. 4.26 and 4.27).

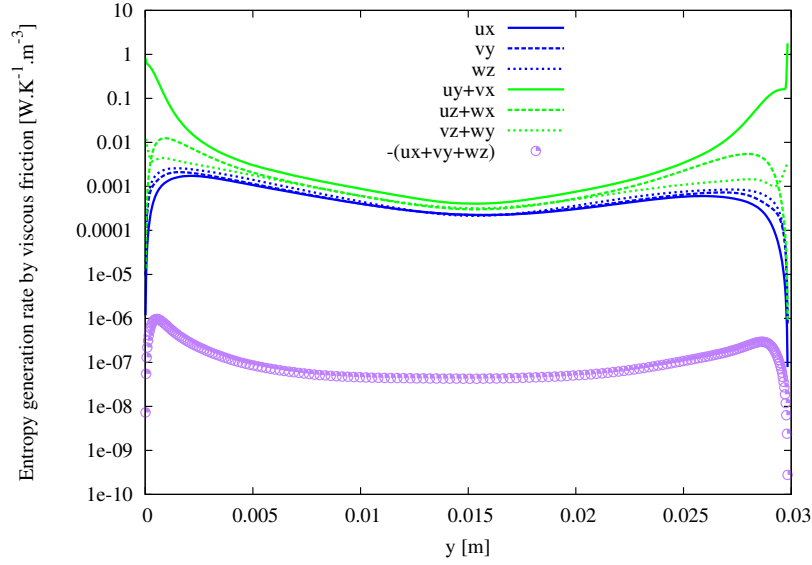


Figure 4.9: Mean local entropy generation rate by viscous friction components - Eqs. 4.28 and 4.29; e.g. $uy+vx$ stands for $\langle \dot{S}_{gen,f,u_y+v_x}^{'''}$.

derivative of the velocity longitudinal component (Figs. 4.9 and 4.10). The velocity divergence term is negligible and would disappear for an incompressible flow. All terms depending on longitudinal or transversal derivatives vanish at the walls because of the no-slip boundary condition. After the main term $\dot{S}_{gen,f,u_y+v_x}^{'''}$, the second contributor is $\dot{S}_{gen,f,v_z+w_y}^{'''}$, which order of magnitude at the walls is nevertheless 10^2 less.

$$\begin{aligned} \dot{S}_{gen,f}^{'''} = & \dot{S}_{gen,f,u_x}^{'''} + \dot{S}_{gen,f,v_y}^{'''} + \dot{S}_{gen,f,w_z}^{'''} + \dot{S}_{gen,f,u_y+v_x}^{'''} \\ & + \dot{S}_{gen,f,u_z+w_x}^{'''} + \dot{S}_{gen,f,v_z+w_y}^{'''} + \dot{S}_{gen,f,u_x+v_y+w_z}^{'''} \end{aligned} \quad (4.28)$$

$$\begin{aligned}
\dot{S}_{gen,f,u_x}''' &= \frac{2\mu}{T} \left(\frac{\partial U}{\partial x} \right)^2 & \dot{S}_{gen,f,v_y}''' &= \frac{2\mu}{T} \left(\frac{\partial V}{\partial y} \right)^2 & \dot{S}_{gen,f,w_z}''' &= \frac{2\mu}{T} \left(\frac{\partial W}{\partial z} \right)^2 \\
\dot{S}_{gen,f,u_y+v_x}''' &= \frac{\mu}{T} \left(\frac{\partial U}{\partial y} + \frac{\partial V}{\partial x} \right)^2 & \dot{S}_{gen,f,u_z+w_x}''' &= \frac{\mu}{T} \left(\frac{\partial U}{\partial z} + \frac{\partial W}{\partial x} \right)^2 \\
\dot{S}_{gen,f,v_z+w_y}''' &= \frac{\mu}{T} \left(\frac{\partial V}{\partial z} + \frac{\partial W}{\partial y} \right)^2 & \dot{S}_{gen,f,u_x+v_y+w_z}''' &= -\frac{2}{3} \frac{\mu}{T} (\nabla \cdot \mathbf{V})^2
\end{aligned} \tag{4.29}$$

$$\dot{S}_{gen,f,u_y+v_x}''' = \dot{S}_{gen,f,u_y}''' + \dot{S}_{gen,f,v_x}''' + \dot{S}_{gen,f,u_y.v_x}''' \tag{4.30}$$

$$\dot{S}_{gen,f,u_y}''' = \frac{\mu}{T} \left(\frac{\partial U}{\partial y} \right)^2 \quad \dot{S}_{gen,f,v_x}''' = \frac{\mu}{T} \left(\frac{\partial V}{\partial x} \right)^2 \quad \dot{S}_{gen,f,u_y.v_x}''' = \frac{2\mu}{T} \frac{\partial U}{\partial y} \frac{\partial V}{\partial x} \tag{4.31}$$

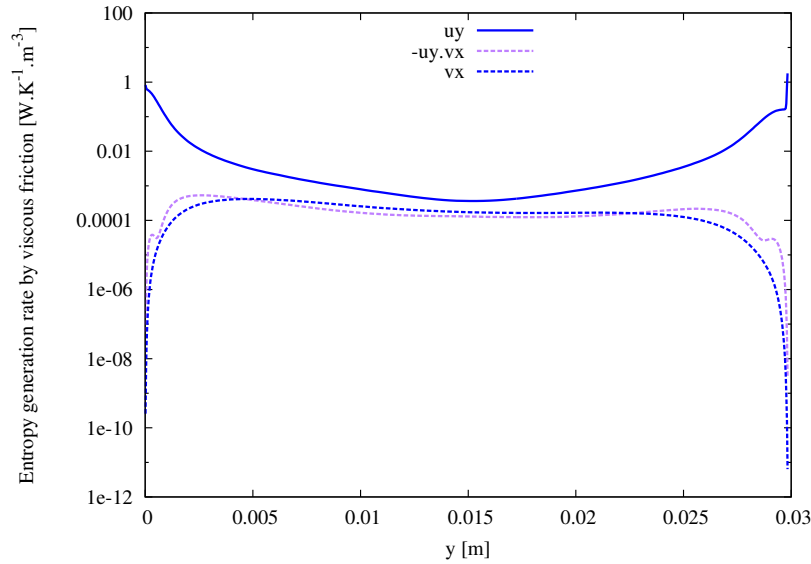


Figure 4.10: Decomposition of the $\langle \dot{S}_{gen,f,u_y+v_x}''' \rangle$ term in the viscous friction mean local entropy generation rate - Eqs. 4.30 and 4.31.

Apart from neglecting the smallest contributors in the mean local entropy generation rate (such as the viscous part and possibly the heat conduction parts in horizontal or transverse directions), another type of simplifying approximation consists in using the average fields of the quantities involved in the expression of the generated entropy. This type of simplification is appreciated in practice because it allows to estimate the entropy generation rates from the fields already calculated (such as mean velocity or temperature) by post-processing the averages. The effect of progressive simplifications in the expression of the vertical conduction entropy generation rate $\langle (k/T^2)(\partial T/\partial y)^2 \rangle$ (the majority term in the total entropy generation rate) is presented in Fig. 4.11. Using the average fields of thermal conductivity and temperature in the k/T^2 factor has no visible impact on the rate of entropy generation by vertical heat conduction. In contrast, the average square of the vertical temperature gradient

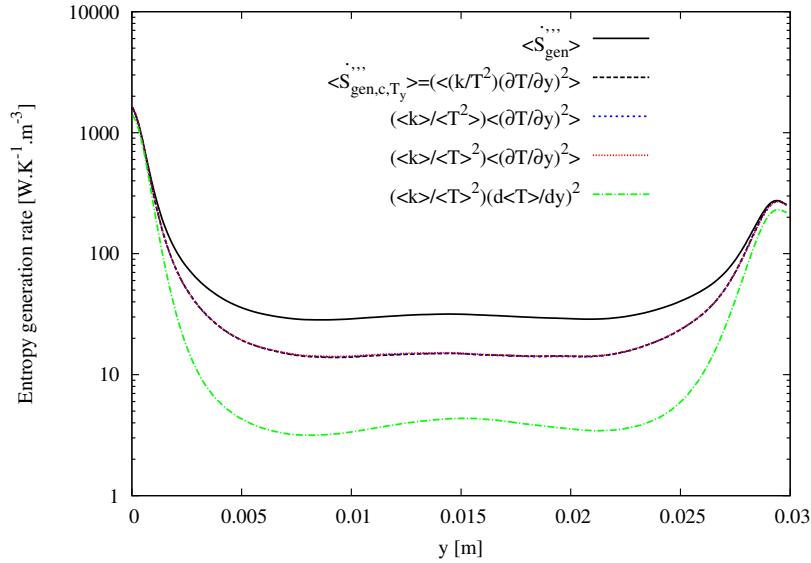


Figure 4.11: Successive approximations of the mean local entropy generation rate \dot{S}_{gen}''' .

cannot be replaced by the square of the average temperature vertical gradient without making a significant error.

In Table 4.5, the total entropy generation rate in the channel is indicated, along with the results of the successive approximations: first, the viscous entropy generation is discarded, which has a negligible effect on the result. Then, the vertical heat conduction part is kept alone and the entropy production rate is underestimated by about 20%. Finally, the average fields are used in the calculation, first by using the averages of the temperature and the thermal conductivity while keeping the $\langle (\frac{\partial T}{\partial y})^2 \rangle$ term, which has very little effect, then by neglecting the fluctuations of the latter term and by using $(\frac{d\langle T \rangle}{dy})^2$, which ultimately leads to a global underestimation of the entropy generation rate by almost 45%.

Table 4.5: Successive approximations of the mean total entropy generation rate in the channel

	[W.K ⁻¹]	%
Total entropy generation rate $\langle \dot{S}_{gen} \rangle$	0.015	100%
Entropy generation rate by heat conduction $\langle \dot{S}_{gen,c} \rangle$	0.015	100%
Vertical heat conduction contribution $\langle \dot{S}_{gen,c,T_y} \rangle$	0.012	80%
Mean fields approximation I $\frac{\langle k \rangle}{\langle T^2 \rangle} \langle (\frac{\partial T}{\partial y})^2 \rangle$	0.012	80%
Mean fields approximation II $\frac{\langle k \rangle}{\langle T^2 \rangle} (\frac{d\langle T \rangle}{dy})^2$	0.008	56%

Thus, the average fields are not sufficient to correctly explain the local entropy generation rate and it is necessary to take into account the correlations and variances of the quantities from which it derives. This echoes other work that highlights the essential effect of turbulence on entropy generation rates [4]. The decomposition (Eqs. 4.32) of the vertical conduction of heat mean local entropy generation rate \dot{S}_{gen,c,T_y}''' into

its share $\dot{S}_{gen,c,T_y,MEAN}'''$ from the mean fields of temperature and thermal conductivity, on the one hand, and its share $\dot{S}_{gen,c,T_y,FLUCT}'''$ from fluctuations, on the other hand, is presented in Fig. 4.12 in dimensional form and in Figs. 4.13 in dimensionless quantities. The reference magnitude used to normalize the local entropy generation rates due to the vertical conduction of heat (Eq.4.33) is defined at each wall as a function of the mean wall heat flow density $\langle q_w'' \rangle$, the mean wall temperature $\langle T_w \rangle$ and the corresponding mean thermal conductivity $\langle k_w \rangle$.

$$\dot{S}_{gen,c,T_y,MEAN}''' = \frac{\langle k \rangle}{\langle T \rangle^2} \left(\frac{d \langle T \rangle}{dy} \right)^2 \quad (4.32)$$

$$\dot{S}_{gen,c,T_y,FLUCT}''' = \langle \dot{S}_{gen,c,T_y}''' \rangle - \dot{S}_{gen,c,T_y,MEAN}'''$$

$$\langle \dot{S}_{gen,c}''' \rangle^+ = \frac{\langle \dot{S}_{gen,c}''' \rangle}{\langle q_w'' \rangle^2 / (k_w \langle T_w \rangle^2)} \quad (4.33)$$

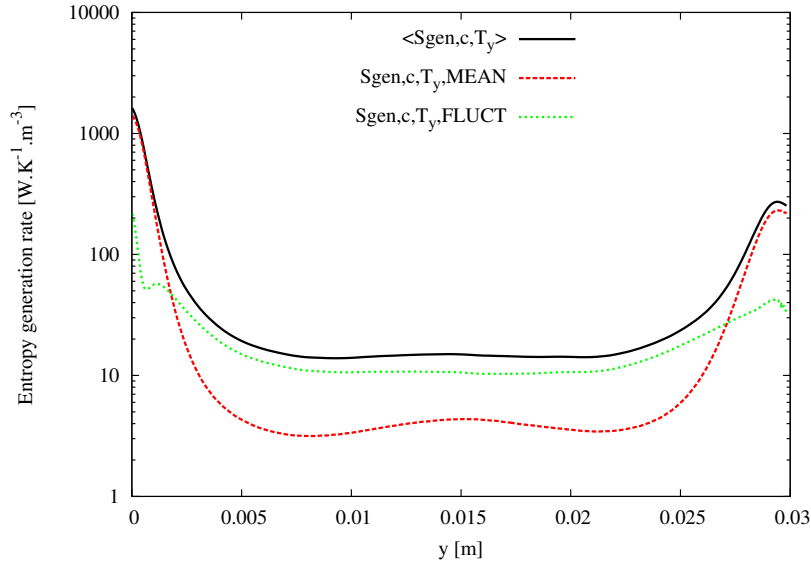


Figure 4.12: Decomposition of the mean local entropy generation rate by vertical heat conduction (cf. Eqs. 4.32).

The highest entropy generation rates are located near the walls (Fig. 4.12) and more precisely in the viscous sublayer ($y^+ \leq 5$), which confirms it is the region where thermal irreversibilities are the most important. The rates keep the same order of magnitude in this region (Figs. 4.13). The part coming from mean fields (Fig.4.13(a)) is in good accordance with the $T^+ = Pr.y^+$ law at the walls. It decreases rapidly in the buffer zone ($5 \leq y^+ \leq 30$) before reaching a local minimum and rising slightly in the central zone of the channel, an asymmetry being visible between the hot and cold sides. Indeed, as can be seen in Fig. 4.3(a), the logarithmic zones end at different values for the hot side ($y^+ \approx 70$) and the cold side ($y^+ \approx 100$), which is reflected in the entropy generation rate profile. The fluctuation part of the entropy generation rate by vertical conduction of heat (Fig.4.13(b)) equals approximatively 20% of the mean part at the walls [125] [126] and exhibits changes located at sublayer transitions: the highest rates concentrate in the viscous sublayer. Then, the behavior changes

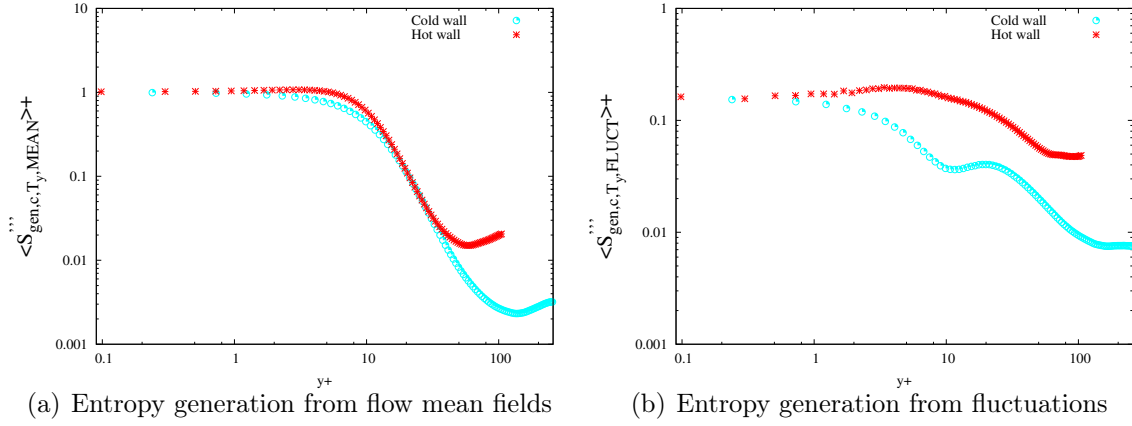


Figure 4.13: Decomposition of the dimensionless mean local entropy generation rate by vertical heat conduction (cf. Eqs. 4.32 and 4.33)

according to the side of the channel: on the hot side, the generation rate reaches a local maximum at $y^+ \approx 5$ and decreases in the buffer and logarithmic zones before stabilizing. On the cold side, the entropy generation rate decreases over the first third of the buffer zone, reaches a local minimum in $y^+ \approx 10$ and a local maximum in $y^+ \approx 30$ before decreasing in the logarithmic zone and stabilizing beyond. The presence of an oscillation in the rate of entropy generation by heat conduction in the area near the wall ($y^+ \leq 30$) is also visible in the results presented by [125] [126] and based on simulations at $Pr = 0.71$ $Re_{\tau m} = 395$ and $Pr = 5$ $Re_{\tau m} = 180$ [120] [119]. However, this result is not easy to interpret physically since it takes place within the buffer zone and not at a sublayer transition or near it: this oscillation will have to be studied further later because it is numerically sensitive to the calculation methods of the derivatives (in the buffer zone, the second derivative of the temperature is the highest).

The same kind of decomposition (Eqs. 4.34) between the local entropy generation rate from mean and fluctuating fields can also be performed for the viscous entropy generation rate contributor due to the longitudinal velocity gradient vertical component. The corresponding entropy generation rates are presented in Fig. 4.14 in dimensional quantities and Figs. 4.15 in dimensionless form, the reference value being defined in as a function of the wall friction velocity, the wall mean temperature and the wall mean dynamic and kinematic viscosities (Eq. 4.35).

$$\dot{S}_{gen,f,u_y,MEAN}^{\prime\prime\prime} = \frac{\langle \mu \rangle}{\langle T \rangle} \left(\frac{d \langle U \rangle}{dy} \right)^2 \quad (4.34)$$

$$\dot{S}_{gen,f,u_y,FLUCT}^{\prime\prime\prime} = \langle \dot{S}_{gen,f,u_y}^{\prime\prime\prime} \rangle - \dot{S}_{gen,f,u_y,MEAN}^{\prime\prime\prime}$$

$$\langle \dot{S}_{gen,f}^{\prime\prime\prime} \rangle^+ = \frac{\langle \dot{S}_{gen,f}^{\prime\prime\prime} \rangle}{\langle \mu_w \rangle U_\tau^4 / (\langle \nu_w \rangle^2 \langle T_w \rangle)} \quad (4.35)$$

The part of the mean local viscous entropy generation rate due to the mean longitudinal velocity vertical gradient $\dot{S}_{gen,f,u_y,MEAN}^{\prime\prime\prime}$ (Fig. 4.14) is maximum at the walls. Its minimum value is located near the center of the channel and slightly on the hot side: this comes from the asymmetry of the mean longitudinal velocity that reaches its maximum at this position (see Fig. 4.2(a)). Viscous entropy generation rates from

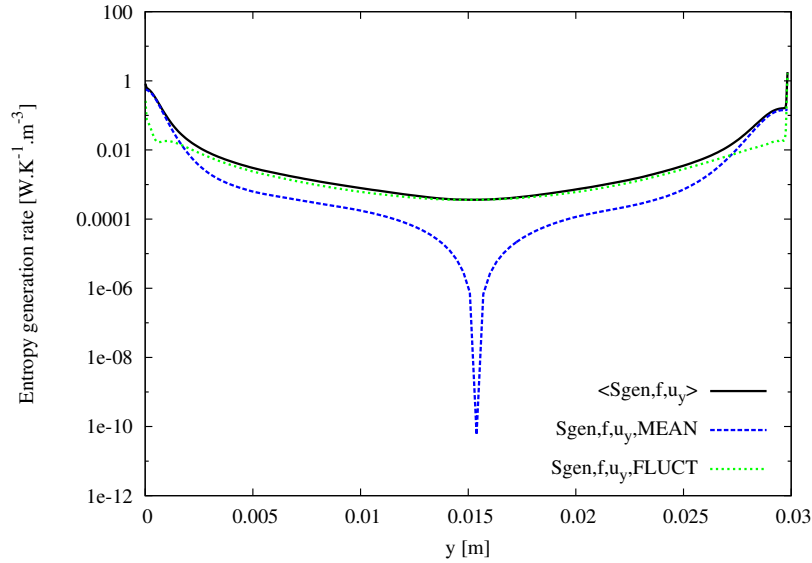
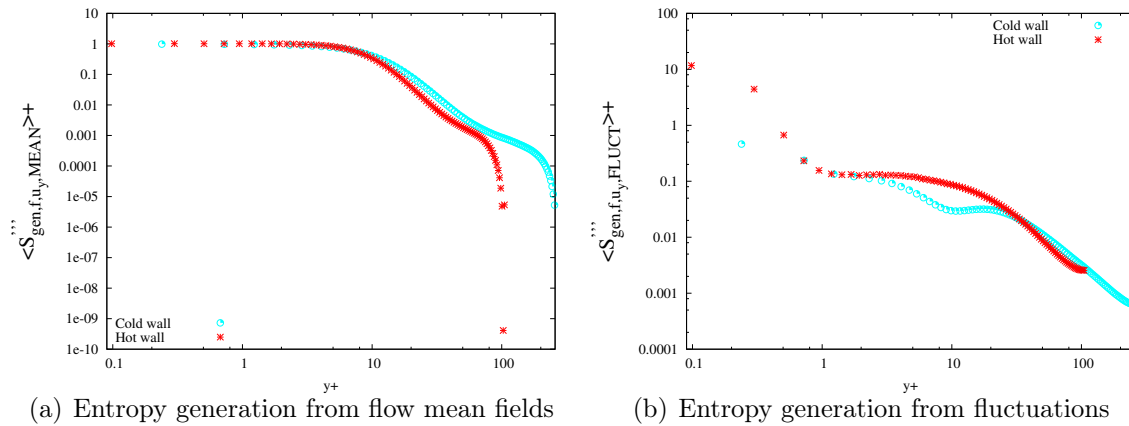


Figure 4.14: Decomposition of the mean local viscous entropy generation rate due to the vertical component of the gradient of the longitudinal velocity (cf. Eqs. 4.34) ($T_2/T_1 = 2$ and $Re_{\tau m} = 180$).



(a) Entropy generation from flow mean fields

(b) Entropy generation from fluctuations

Figure 4.15: Decomposition of the mean local viscous entropy generation due to the vertical component of the gradient of the longitudinal velocity (cf. Eqs. 4.34)

the mean fields are the highest in the viscous sublayer (Fig. 4.15(a)) and keep the same order of magnitude in this region. In the buffer and logarithmic zones, the rates are decreasing. The drop is stronger in the outer zone: unlike rates from heat conduction, they collapse in the central channel zone because the average longitudinal velocity reaches its maximum there (while temperature gradients are strictly positive in the center of the channel as can be seen in Fig. 4.4(a), which would not be the case in a symmetrical heating configuration). The fluctuation part of the viscous entropy generation rate is decreasing in the viscous sublayer: this was not the case for contribution of heat conduction. Turbulent viscous entropy generation rate concentrated in the viscous sub-layer and maximum at the walls (fig. 4.34(b)) is also attested in other works [157]. However, at the hot wall the fluctuation part is ten times the mean one, which may not be physical and needs to be cross-checked (this should not alter the results on the total entropy generation rate as the viscous contribution is very low).

4.2.3 Influence of the hot to cold wall temperature ratio

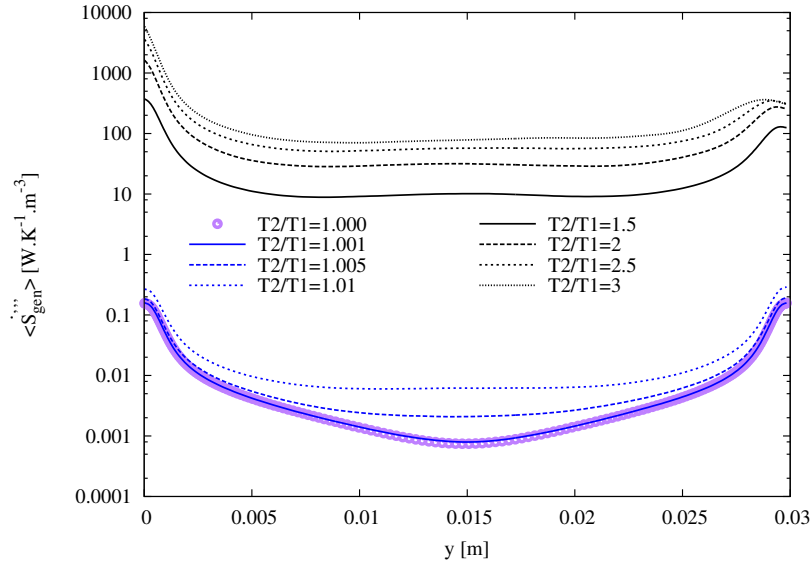


Figure 4.16: Mean local entropy generation rate for various hot to cold wall temperature ratios ($Re_{\tau m} = 180$).

The hot to cold wall temperature ratio ($Re_{\tau m}$ being maintained at 180) has an influence on the mean local and global entropy generation rates that increase with T_2/T_1 (Fig. 4.16). Moreover, the higher the temperature gap, the more asymmetric the profile of the local entropy generation rate and at the $T_2/T_1 = 1$ limit, the entropy generation rates at the walls are equivalent. In the center of the channel, the profile of the local entropy generation rate is flatter as soon as non isothermal boundary conditions are fixed and $T_2/T_1 \geq 1.005$.

4.2.4 Influence of the mean friction Reynolds number

When the mean friction Reynolds number is increased from 150 to 210 (T_2/T_1 being maintained at 2), the mean local entropy generation rates are raised near the walls (Fig. 4.17). On the one hand, provided that the imposed temperatures are not changed, the wall rate of entropy generation by viscous friction changes approximately in proportion to the mean friction Reynolds number at power four. On the other hand, the rate of entropy generation from heat conduction varies according to the square of the friction Reynolds number, resulting in an increase of the relative part of entropy generation from viscous origin in the total entropy generation rate. These evolution ratios are consistent with those expected from entropy generation rates related to vertical temperature and longitudinal velocity gradients from the mean fields ($\dot{S}_{gen,c,T_y,MEAN}'''$ and $\dot{S}_{gen,f,u_y,MEAN}'''$).

4.2.5 RMS and correlations

$$[\dot{S}_{gen}''']_{rms} = \sqrt{\langle (\dot{S}_{gen}''')^2 \rangle - \langle \dot{S}_{gen}''' \rangle^2} \quad (4.36)$$

The root-mean-square of the local entropy generation rate fluctuations (Eq. 4.36) is presented in Fig. 4.18. Its profile is similar to that of the entropy generation

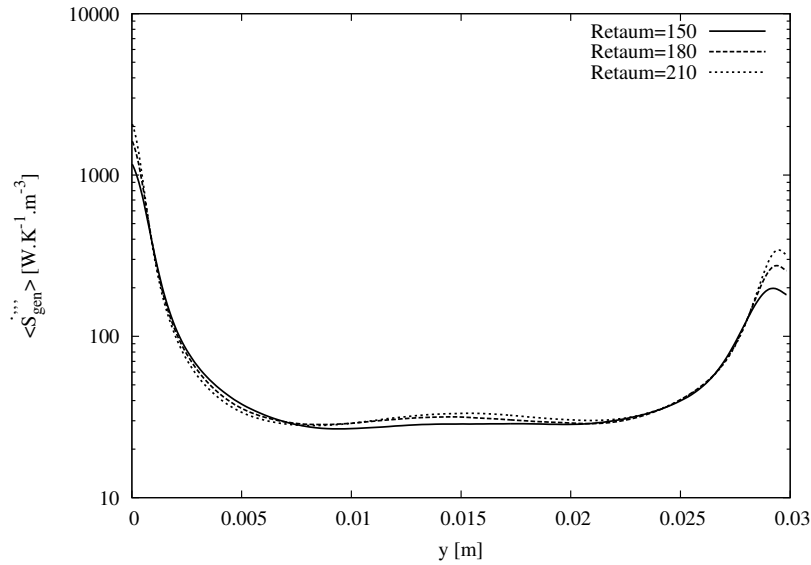


Figure 4.17: Mean local entropy generation rate for various mean friction Reynolds number ($T_2/T_1 = 2$).

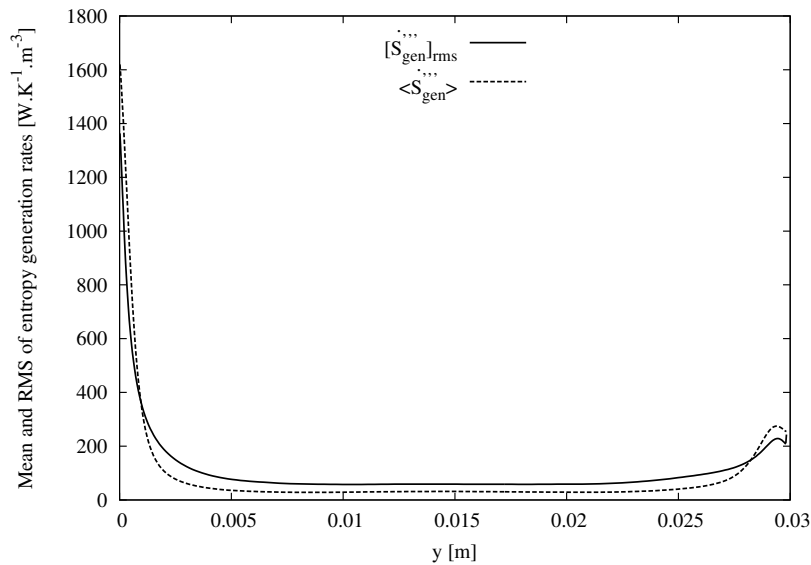


Figure 4.18: Root-mean-square of the local entropy generation rate fluctuations compared to the mean value $\langle \dot{S}_{gen}''' \rangle$.

rate $\langle \dot{S}_{gen}''' \rangle$ itself and the orders of magnitude are close: the statistical dispersion of the entropy generation rate is not negligible and the relative standard deviation $[\dot{S}_{gen}''']_{rms} / \langle \dot{S}_{gen}''' \rangle$ lies between ≈ 0.8 and ≈ 2.2 , the largest values being located in the center of the channel. Since temperatures are fixed at the walls (and so is the thermal conductivity), T_{rms} is zero and the source of the fluctuations in the entropy generation rate is to be sought in particular in the fluctuations of the vertical gradient of the temperature, which effectively presents significant relative values at the walls (larger at the cold one) and which magnitude is higher than the mean in the central part of the channel (Fig. 4.19).

The correlation coefficients of the local entropy generation rate with the temper-

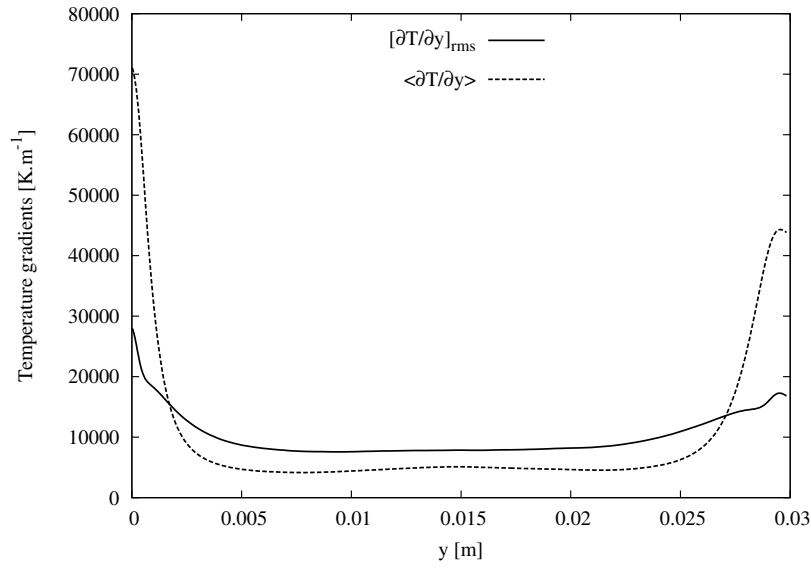


Figure 4.19: Root-mean-square of the temperature gradient vertical component fluctuations compared to the mean value $\langle \frac{\partial T}{\partial y} \rangle$.

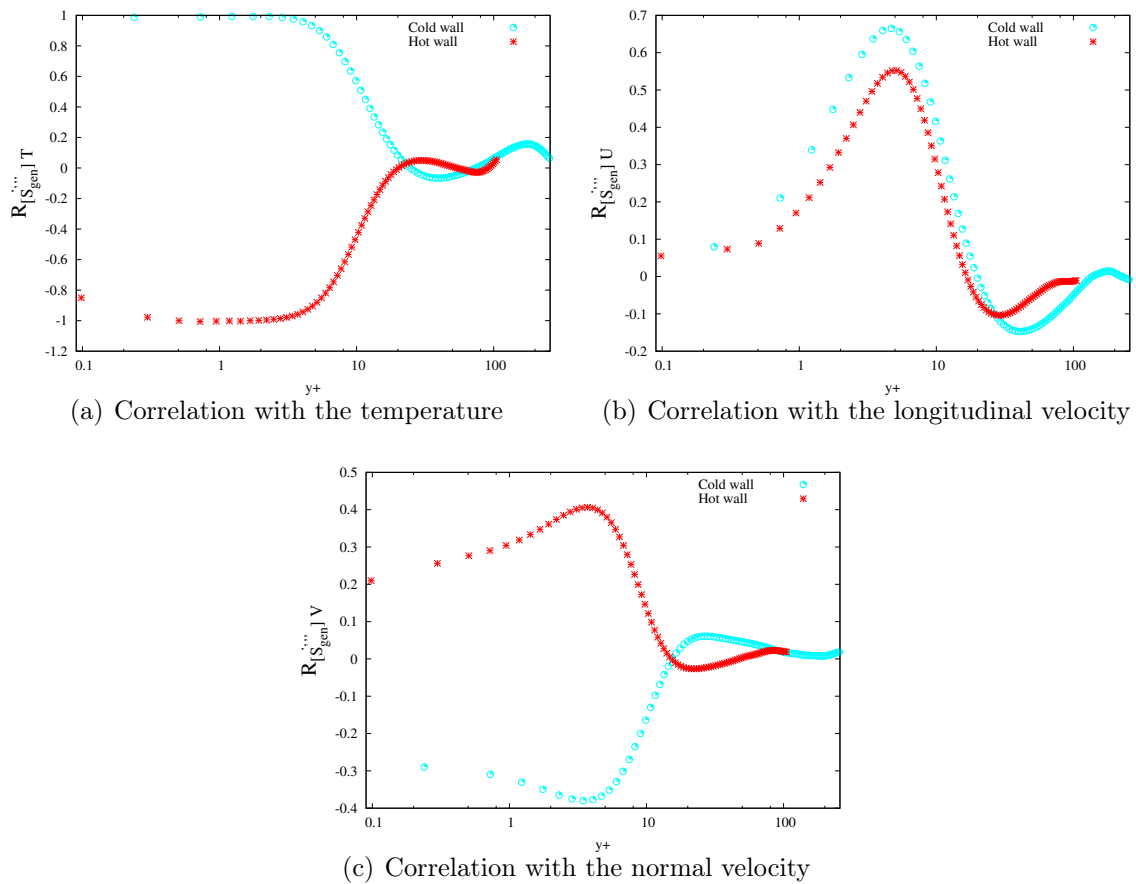
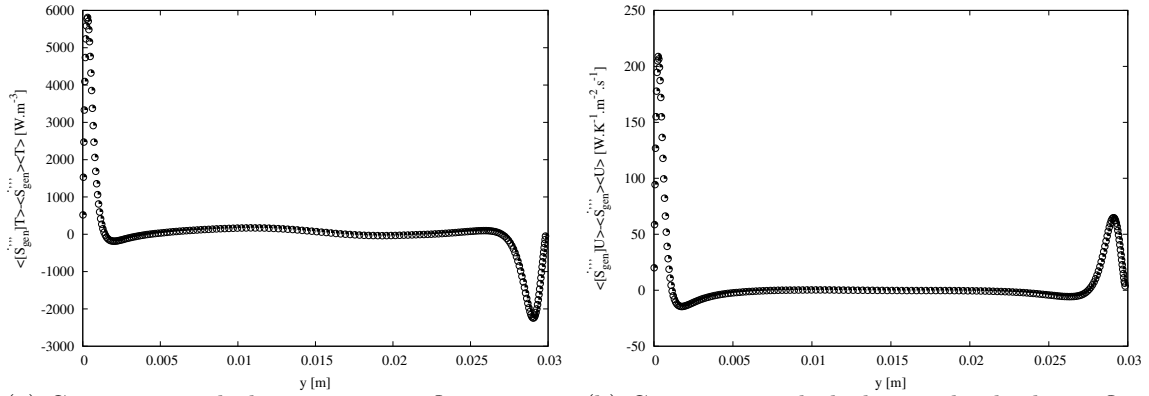
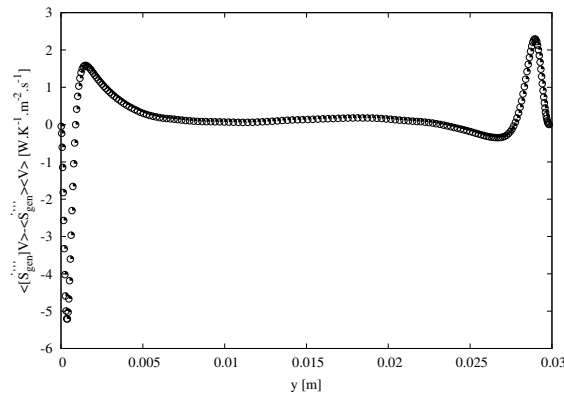


Figure 4.20: Correlations of the local entropy generation rate fluctuations

ature and the longitudinal and normal components of the velocity are presented in Figs. 4.20. The local entropy generation rate exhibits a high linear correlation to the



(a) Covariance with the temperature fluctuations. (b) Covariance with the longitudinal velocity fluctuations.



(c) Covariance with the normal velocity fluctuations

Figure 4.21: Covariances of the local entropy generation rates

temperature near the walls where the correlation coefficient has an absolute value close to 1 (Fig. 4.20(a)). On the other hand, at the center of the channel, the covariance of the temperature and the local entropy generation rate is close to zero, for non-zero values of the standard deviations of these two quantities and the fluctuations of the temperature and the local entropy generation rate behave almost like linearly uncorrelated random variables. On the cold side of the channel, the temperature vs. entropy generation rate correlation is positive: a positive temperature fluctuation $\theta' > 0$ leads to a positive fluctuation of the local entropy generation rate $\langle \dot{S}_{gen}''' \rangle$ (linked to an increase of the fluctuation of the vertical gradient of the temperature $\partial\theta'/\partial y$). Conversely, an equivalent $\theta' > 0$ on the hot side, reduces the temperature gap with the hot wall and the correlation is there negative. The correlations of the local entropy generation rate and the longitudinal velocity fluctuations exhibit similar profiles on the hot and cold sides of the channel and a positive peak value at $y^+ \approx 5$. The correlation coefficients with the wall-normal velocity have a lower magnitude (less than ± 0.4) and are negative near the cold wall and positive near the hot one.

Covariances of the local entropy generation rate with the temperature and the longitudinal and normal velocity are provided in Figs. 4.21. All covariances are near zero in a large central region of the channel. They also vanish at the walls, where the fluctuations of the temperature and the velocity components are set to zero due to the isothermal and no-slip boundary conditions respectively.

4.2.6 Influence of the thermal boundary condition type

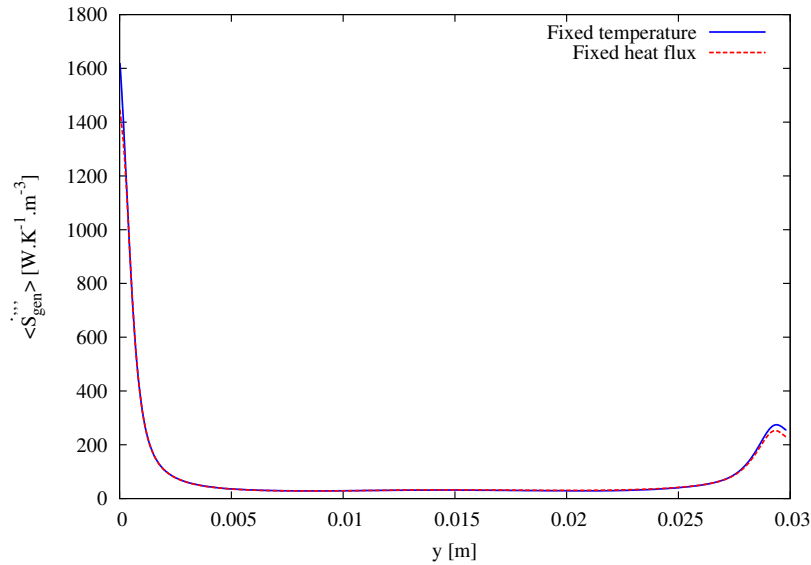


Figure 4.22: Mean local entropy generation rate for two types of boundary conditions ($T_2/T_1 \approx 2$ and $Re_{\tau m} = 180$).

The type of thermal boundary condition (fixed temperatures vs. fixed heat flux density at the walls), the hot to cold wall temperature ratio and the mean friction Reynolds number remaining essentially identical, does not drastically modify the mean local entropy generation rates (Fig. 4.22), except very close to the walls where it is about 10% lower when the wall heat flux density is imposed (the total entropy generation rate within the channel is only reduced by about 2%). In the wall-imposed heat flux density simulation, the composition of the entropy generation rate is quite similar to that observed in the wall-imposed temperatures case: the viscous part is negligible and most of the diffusive part comes from the vertical conduction of heat (the parts related to longitudinal and transverse conductions representing about 20%). However, these two latter contributions are no longer zero at the walls since the temperature is free to fluctuate. In terms of approximations, also neglecting the fluctuations in the vertical gradient of heat by calculating this entropy generation rate based on average temperature fields results in an underestimation of the total entropy generation rate by about 45%.

In the mean local rate of entropy generation by vertical heat conduction within the channel, the turbulent fluctuation part (corresponding to the decomposition described in Eq. 4.32) is slightly less important when the heat flux density is imposed (29% instead of 31%). However, this share is very low in the local rate of entropy generation at the walls (less than 0.5%) whereas this was not the case at imposed temperatures (about 13%). There is therefore a differentiated phenomenon linked to the thermal boundary condition type: indeed, when the heat flux density is imposed at the walls, only fluctuations in temperature (Fig. 4.4(b)) have an effect on the fluctuations in the entropy generation rate. However, the standard deviation of the temperature fluctuations at the walls represents only 5.4% and 3.4% of the mean wall temperature (at the cold and hot wall respectively). On the other hand, if the temperatures are imposed at the walls, it is the parietal fluctuations of the temperature gradient that play the main

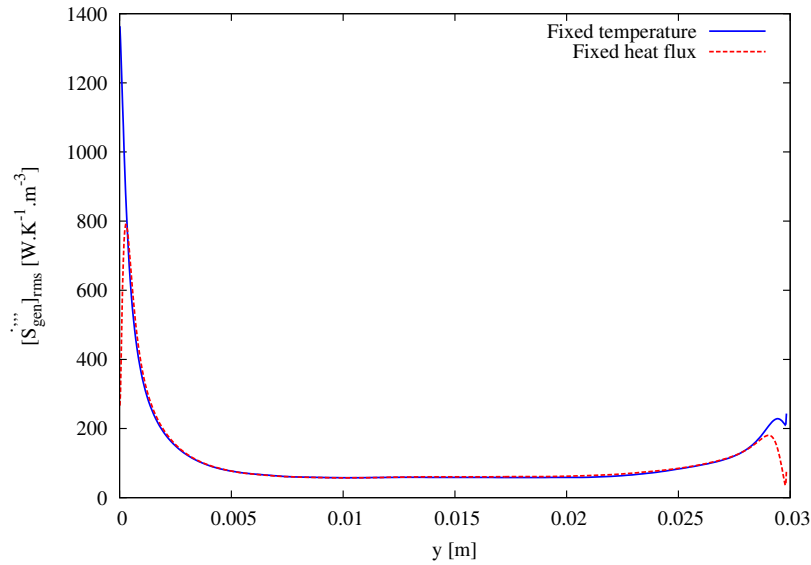


Figure 4.23: Standard deviation of the local entropy generation rate for two types of boundary conditions ($T_2/T_1 \approx 2$ and $Re_{\tau m} = 180$).

role and they can be high as indicated above. In the case of imposed heat flux density, the standard deviation of the entropy generation rate exhibits a sudden drop in the near wall area, a phenomenon that is absent in the case of fixed wall temperatures.

4.2.7 Instantaneous local entropy generation rates

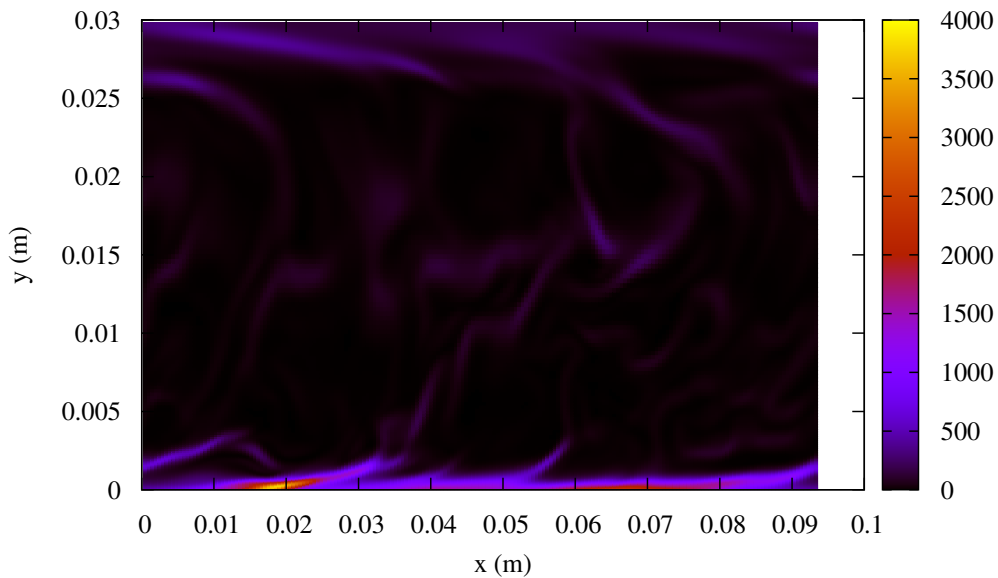


Figure 4.24: Front-face view of the instantaneous local entropy generation rate at (xy) plane with $z = z_{min}$ [$W.K^{-1}.m^{-3}$].

The instantaneous local entropy generation rates for the fixed wall temperature case are presented at the cold (Figs. 4.25) and hot (Fig. 4.26) plates with xz plane views and one-dimensional projection views on x and z axes separately. A front-face view is also provided (Fig. 4.24), i.e. on the (xy) plane at $z = z_{min}$.

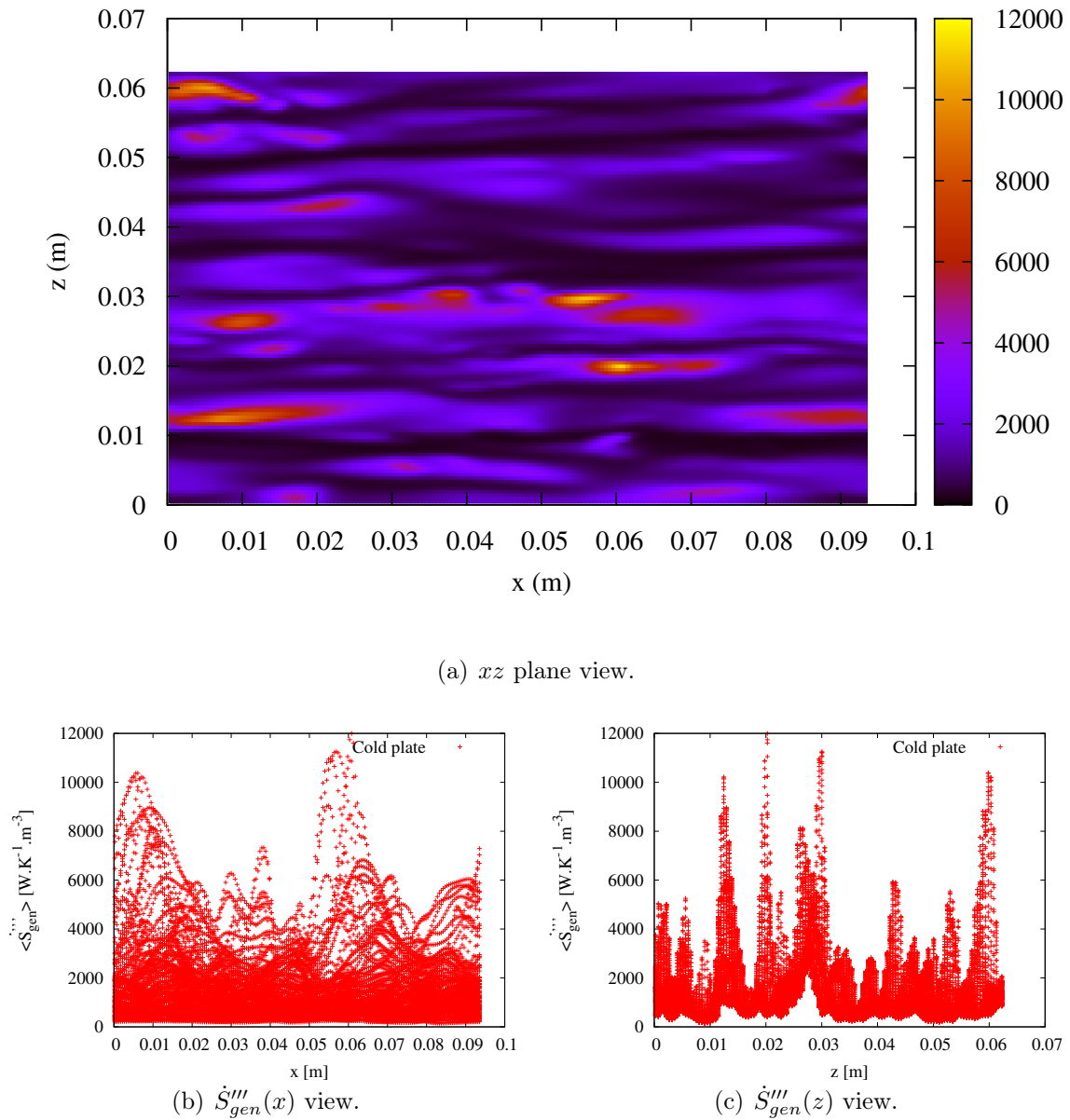


Figure 4.25: Instantaneous local entropy generation rate at the cold plate [$W.K^{-1}.m^{-3}$]

At the top and bottom walls, the local entropy generation rate field exhibits elongated structures in the direction of the flow: the areas of the plates concentrating the highest levels of local entropy generation rate have a larger length (Figs. 4.25(b) and 4.26(b)) than width (Figs. 4.25(c) and 4.26(c)). The front face view (Fig. 4.24) seems to show that puffiness appears on the walls and is carried in the direction of the flow as it leaves the walls. The central area of the channel exhibits filament shaped structures.

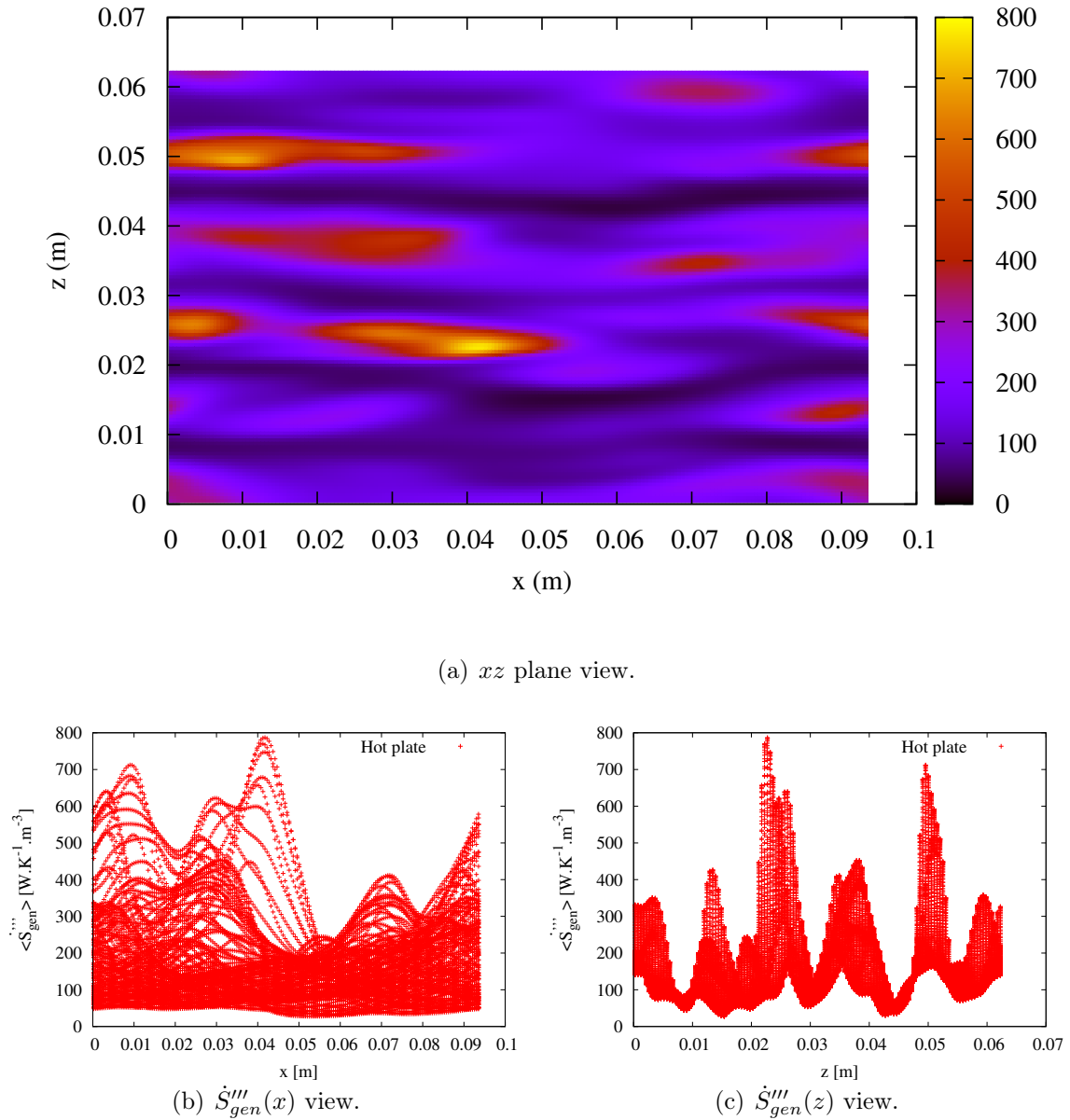


Figure 4.26: Instantaneous local entropy generation rate at the hot plate [$W.K^{-1}.m^{-3}$]

the range of values of the local entropy generation rate is wider at the cold wall (up to $12000 W.K^{-1}.m^{-3}$) than the hot one (up to $800 W.K^{-1}.m^{-3}$). These pick values can be compared to the mean local entropy generation rates at the cold and hot walls ($1620 W.K^{-1}.m^{-3}$ and $255 W.K^{-1}.m^{-3}$ respectively), which is a demonstration of the high dispersion of the local entropy generation rate that exhibits strong spatial fluctuations. Moreover, a large range of values is densely populated (from $200 W.K^{-1}.m^{-3}$ to $2000 W.K^{-1}.m^{-3}$ at the cold wall and from $50 W.K^{-1}.m^{-3}$ to $200 W.K^{-1}.m^{-3}$ at the hot wall). This great spatial (and probably temporal) variability encourages the continuation of simulations in order to improve their convergence and make the results more robust.

The instantaneous local entropy generation along the vertical line defined by $x = x_{min}$ and $z = z_{min}$ is presented in Figs. 4.27. The entropy generation rate is higher at the walls and presents irregularities along the height of the channel (Fig. 4.27(a)). The relative importance of spatial fluctuations with respect to the mean value is important at the center of the channel (Fig. 4.27(b)). Spatial fluctuations represent a smaller relative share very close to the walls.

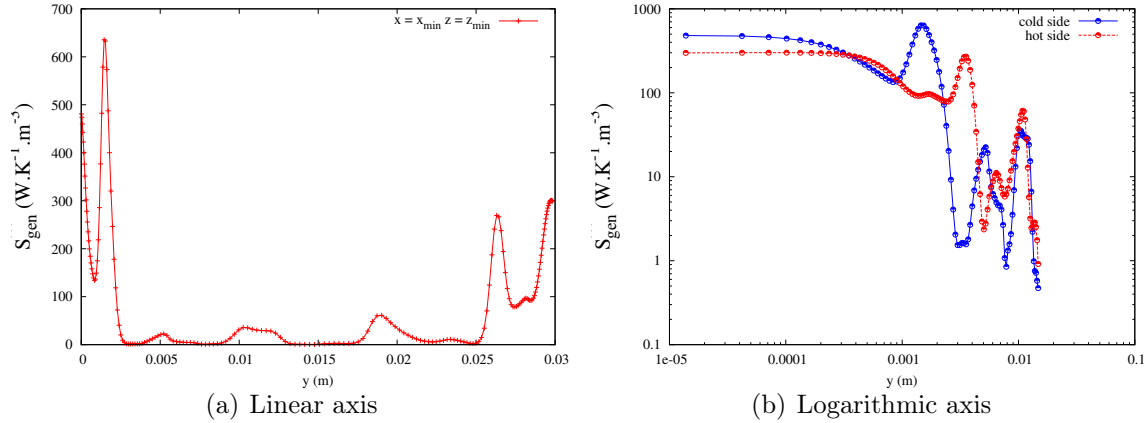


Figure 4.27: Instantaneous local entropy generation rate at $x = x_{min}$ and $z = z_{min}$.

4.2.8 Influence of mesh definition

Simulations with a finer mesh (see description in table 4.1 for the "check" mesh) have been used as a control tool to check mesh independence. The comparison for the local entropy generation rate and its root-mean-square (at fixed hot to cold wall temperature ratio $T_2/T_1 = 2$ and mean friction Reynolds number $Re_{\tau m} = 180$) are presented in Figs. 4.28 and are in good agreement with the results presented above.

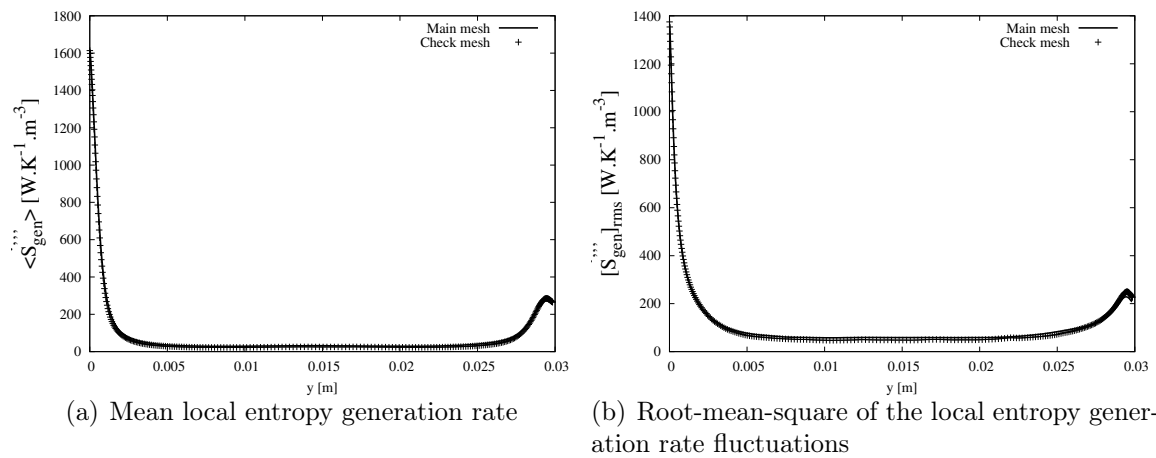


Figure 4.28: Comparison of local entropy generation rate and its root-mean-square for two domain definitions (see table 4.1)

4.2.9 Conclusion

In this section, the local entropy generation rates have been computed for a bi-periodic flat-plate channel turbulent flow of a fluid with thermo-dependent properties. The hot to cold wall temperature ratio is 2 and the mean friction Reynolds number is set to 180. Moreover, these two flow characteristics are varied in order to identify their influence on the local entropy generation rate profiles. A comparison is also made between two types of thermal boundary conditions: fixed wall temperatures on the one hand and fixed heat flux density on the other hand. The mean local entropy generation rates are mainly located near the walls (particularly in the viscous sublayer) and exhibit an asymmetric profile, the highest rates being on the cold side. This confirms the interest of acting in the near wall region by texturing and in particular on the cold wall. The viscous part is negligible compared to the heat conduction part, which major contributor is due to the vertical conduction of heat (the longitudinal and transversal heat conductions, due to fluctuations of the temperature field, still account for about one fifth of the total conductive entropy generation rate in the channel). Indeed, turbulent fluctuations are not negligible: their terms (coming from variances and covariances of fluctuations) induce about 45% of the total entropy generation rate and the root-mean-square of the local entropy generation rate is of the same order of magnitude as its mean. Instantaneous local entropy generation rates exhibit elongated structures in the direction of the flow, their mean size being larger at the hot wall and future work will focus on the analysis of these structures in relation to the thermal and dynamic structures of the turbulent flow. Increasing the hot to cold wall temperature ratio leads to higher entropy generation rates and to a higher hot to cold wall asymmetry. It will thus be interesting to study, in future work, configurations corresponding to higher heat flow densities (which also require greater computing resources). If the Reynolds number is increased, the thermal gap being kept constant, the entropy generation rates at the walls increase. The boundary condition type has an influence on the local entropy generation rates at the walls: they are lower in the case of fixed heat flux compared to the wall fixed temperature case because of the drop of the vertical temperature gradient fluctuations.

General conclusion

The aims of the present study are to compute the local entropy generation rate, to analyze its distribution in the flow space and its composition, to study how it is influenced by boundary conditions (in particular the thermal ones) and to search how the total entropy generation rate can be minimized. Due to the high complexity of actual solar receivers, the present work has investigated three simplified situations that provide complementary insights into the entropy generation rates in forced convective flows submitted to temperature gradients and to asymmetric thermal boundary conditions.

In the first situation, the canonical case of the developing laminar boundary layer over a heating flat plate is used as a sandbox to study the influence of the thermal boundary condition type while allowing to vary key parameters. The magnitude and composition of local and total entropy generation rates in the boundary layer have been computed and analyzed for two main thermal boundary conditions: isothermal vs. isoflux plate. In addition to local Reynolds, Prandtl and Eckert numbers, the entropy generation rates depend on the thermal dimensionless number τ (defined as the temperature of the wall divided by the temperature gap between the wall and the free stream at a reference position). If the total thermal power transferred between the plate and the fluid is fixed, the total entropy generation rate between two longitudinal positions along the plate (the starting position being fixed), exhibits a critical value of τ which minimizes entropy generation. The value of the optimum τ depends on the thermal boundary condition. In the isoflux plate case, τ_{opt} depends on the total fixed heat power exchanged and on the starting integration point along the plate. This is not the case for an isothermal plate where τ_{opt} is invariable. In this study, the temperature gap is not neglected when compared to the wall temperature, horizontal conduction of heat is not neglected in the calculation of entropy generation rates and the behavior of the model has also been studied near the leading edge in order to know its asymptotic trend. For small values of τ (corresponding to high temperature gaps compared to the wall temperature) and at a fixed thermal power exchanged between the plate and the fluid, the total entropy generation rate is sensitive to changes in the value of τ . For solar receivers, this means that there is a significant potential for gains by better controlling temperature differences between the walls and the fluid, even if the operating point is far from optimal.

In a second work, the calculus of variation has been applied to the optimization of high Bejan number internal convective heat transfer in a flat-plate channel by minimizing a linear combination of the entropy generation rate by heat conduction on the one hand and the viscous dissipation on the other hand. The central third of one of the plates is heated with a fixed and uniform heat flux density. Two fluids and several Reynolds numbers have been taken into account. For each value of the viscous dissipation in the channel, a volume force is computed that leads to optimized velocity and

temperature fields. The viscous dissipation relative importance in the optimization process can be adjusted through a weighting factor W_{ϕ} in the objective functional. As a general trend in the optimized solutions, lowering this weighting factor leads to lower entropy generation by heat transfer and to a better homogenization of the temperature field. At the same time, the viscous dissipation, the entropy generated by viscous friction and the maximum velocity show an increasing trend. All in all, the total entropy generation rate is reduced and the improvement factor is increased (defined as the relative reduction of the total entropy generation rate with regard to the reference entropy generation rate when no optimization is applied). There is a critical value of the weighting factor at which a flow regime transition occurs, making velocity and temperature fields change from profiles that are slightly different from the non-optimized case to highly perturbed profiles. This critical value depends on the boundary conditions, like the inlet velocity or the heat flux density. The optimization approach allows to suggest velocity fields that reduce the entropy generation rate in the channel, homogenize the temperature field and reduce the maximum temperature reached by the heating plate, which is an advantage in solar receivers. The same method can be applied to other advection-diffusion processes like the diffusion of a minor species in a convective flow: the comparison shows that mass diffusion and heat diffusion share the same qualitative behaviors, the actual magnitudes of the physical fields and the critical values of the W_{ϕ} weighting coefficient being different.

In the third situation, Direct Numerical Simulations (DNS) have been carried out for a quasi-compressible flow in a bi-periodic flat-plate channel with a fluid which properties depend on the temperature at a mean friction Reynolds number $Re_{\tau} = 180$ and for a hot to cold wall temperature ratio $T_2/T_1 = 2$. The average local entropy generation rates have been computed and exhibit a visible hot vs. cold wall asymmetry, the highest entropy generation rates being located at the cold wall, which encourages us to focus on the latter to implement textures, vortex generators or any other device to improve heat exchange. However, the hot plate should not be neglected because entropy generation, although lower, is spread over a greater thickness. The standard deviation of the local entropy generation rate and its correlations with the temperature and the longitudinal and normal components of the velocity have also been computed and show that the turbulent fluctuations of the physical fields (in particular of the temperature and its vertical gradient) play a significant role in the entropy generation rate. In the studied configuration, the entropy generation rate due to viscous friction is very small compared to the heat conduction part: it is therefore quite possible to disturb the velocity field (by taking inspiration from the results of variational optimization, for example) in order to improve heat exchange at the cost of an increase in viscous dissipation. This would reduce temperature differences and improve receiver efficiency (as suggested by work on the boundary layer). The influence of the mean friction Reynolds number and of the wall hot to cold temperature ratio have been explored: both induce an increase of the entropy generation rate, in particular at the walls. The higher the temperature ratio, the higher the asymmetry of the entropy generation rate and the need to concentrate on the cold wall. The effect of the thermal boundary condition type on the flow statistics and on the entropy generation rate has also been investigated and shows that the entropy generation rate in the case of fixed wall heat flux is a little lower at the walls when compared to fixed wall temperature plates.

Appendices

Appendix A

Derivation of the equations of the second Lagrange multiplier and the volume force field

In this appendix, the transport equation for the λ_2 Lagrange multiplier (Eq. 3.9) and the volume force field \mathbf{F} (Eq. 3.8) are found by applying the calculus of variations.

The Lagrangian criterion to minimize writes (cf. Eq. 3.7):

$$J^\star = \iiint_{\Omega} \left\{ \frac{k}{T^2} (\nabla T)^2 + W_{\Phi} \Phi \right. \\ \left. + \lambda_2 \left[\frac{k}{\rho C_p} \nabla^2 T - \mathbf{V} \cdot \nabla T \right] + \lambda_1 \nabla \cdot \mathbf{V} \right\} d\Omega = \iiint_{\Omega} F_{J^\star} d\Omega \quad (\text{A.1})$$

In this equation, Φ is the dissipation function and λ_1 and λ_2 are two Lagrangian multipliers depending on the position. The term to be integrated has been named F_{J^\star} and a compact notation is used in the following calculations: the subscript $(\cdot)_{,X}$ stands for the derivative with respect to X and $(\cdot)_{,XX}$ stands for the second derivative. So, F_{J^\star} can be rewritten:

$$F_{J^\star} = \frac{k}{T^2} (T_{,x}^2 + T_{,y}^2) + W_{\Phi} \mu \left[2(u_{,x}^2 + v_{,y}^2) + (u_{,y} + v_{,x})^2 \right] \\ + \lambda_2 \left[\frac{k}{\rho C_p} (T_{,xx} + T_{,yy}) - (uT_{,x} + vT_{,y}) \right] + \lambda_1 (u_{,x} + v_{,y}) \quad (\text{A.2})$$

Making the first variation of J^\star with respect to the temperature vanish implies the following equation:

$$\frac{\partial F_{J^\star}}{\partial T} - \frac{\partial}{\partial x} \frac{\partial F_{J^\star}}{\partial T_{,x}} - \frac{\partial}{\partial y} \frac{\partial F_{J^\star}}{\partial T_{,y}} + \frac{\partial^2}{\partial x^2} \frac{\partial F_{J^\star}}{\partial T_{,xx}} + \frac{\partial^2}{\partial y^2} \frac{\partial F_{J^\star}}{\partial T_{,yy}} = 0 \quad (\text{A.3})$$

Each term of Eq. A.3 writes:

$$\begin{aligned}
\frac{\partial F_{J^*}}{\partial T} &= \frac{-2k}{T^3}(T_{,x}^2 + T_{,y}^2) \\
\frac{\partial}{\partial x} \frac{\partial F_{J^*}}{\partial T_{,x}} &= \frac{2k}{T^2}T_{,xx} - \frac{4k}{T^3}T_{,x}^2 - \lambda_2 u_{,x} - u \lambda_{2, ,x} \\
\frac{\partial}{\partial y} \frac{\partial F_{J^*}}{\partial T_{,y}} &= \frac{2k}{T^2}T_{,yy} - \frac{4k}{T^3}T_{,y}^2 - \lambda_2 v_{,y} - v \lambda_{2, ,y} \\
\frac{\partial^2}{\partial x^2} \frac{\partial F_{J^*}}{\partial T_{,xx}} &= \frac{k}{\rho C_p} \lambda_{2, ,xx} \\
\frac{\partial^2}{\partial y^2} \frac{\partial F_{J^*}}{\partial T_{,yy}} &= \frac{k}{\rho C_p} \lambda_{2, ,yy}
\end{aligned} \tag{A.4}$$

Injecting the above expressions into Eq. A.3 and taking into account the continuity equation $u_x + v_y = 0$ leads to Eq. A.5 that can be written in the form of a transport equation for the λ_2 scalar (Eq. A.6).

$$\frac{2k}{T^3}(T_{,x}^2 + T_{,y}^2) - \frac{2k}{T^2}(T_{,xx} + T_{,yy}) + u \lambda_{2, ,x} + v \lambda_{2, ,y} + \frac{k}{\rho C_p}(\lambda_{2, ,xx} + \lambda_{2, ,yy}) = 0 \tag{A.5}$$

$$\nabla \cdot \left(\rho \mathbf{V} \lambda_2 - \frac{-k}{C_p} \nabla \lambda_2 \right) = \frac{2k\rho}{T} \nabla \cdot \left(\frac{\nabla T}{T} \right) \tag{A.6}$$

The same method can be used to find the expression of the volume force field \mathbf{F} by making the first variation of J^* vanish with respect to the longitudinal and wall-normal components of the velocity (u and v respectively) and by using the continuity equation, which leads to:

$$\begin{aligned}
\lambda_2 T_{,x} + \lambda_{1, ,x} + 2W_{\Phi} \mu (u_{,xx} + u_{,yy}) &= 0 \\
\lambda_2 T_{,y} + \lambda_{1, ,y} + 2W_{\Phi} \mu (v_{,xx} + v_{,yy}) &= 0
\end{aligned} \tag{A.7}$$

These two equations can be combined into a more compact vector equation (Eq. A.8) that can be compared with the momentum equation (Eq. A.9), which leads to identify ∇P (Eq. A.10) and \mathbf{F} , the expression searched for the volume force.

$$-\frac{\lambda_2}{2W_{\Phi}} \nabla T - \frac{1}{2W_{\Phi}} \nabla \lambda_1 = \mu \nabla^2 \mathbf{V} \tag{A.8}$$

$$\rho \mathbf{V} \cdot \nabla \mathbf{V} + \nabla P - \mathbf{F} = \mu \nabla^2 \mathbf{V} \tag{A.9}$$

$$\nabla P = -\frac{1}{2W_{\Phi}} \nabla \lambda_1 \tag{A.10}$$

$$\mathbf{F} = \frac{\lambda_2}{2W_{\Phi}} \nabla T + \rho \mathbf{V} \cdot \nabla \mathbf{V} \tag{A.11}$$

Appendix B

DNS characteristics

The main characteristics of the DNS discussed in section 4.2 are presented in the following two tables. The names of these simulations are coded as follows: Field1Field2-Field3-Field4, where the four fields are defined hereunder. As an example, T180-2-main corresponds to a fixed wall temperature simulation at mean friction Reynolds number 180 with a hot to cold wall temperature ratio of 2 in the "main" volume and mesh domain. DNS name coding is:

1. Field 1: thermal wall boundary condition type: F=Fixed heat flux density, T=Fixed temperatures.
2. Field 2: mean friction Reynolds number $Re_{\tau m}$.
3. Field 3: hot to cold wall temperature ratio T_2/T_1 .
4. Field 4: domain and mesh definition: Main=reference domain, Check=domain used for mesh and volume independence tests (see table 4.1).

Mesh definitions are given in wall units by reference to ν_w/U_τ , where U_τ and ν_w are the friction velocity and the kinematic viscosity at the wall. For the mesh definition at the center of the channel and along the longitudinal and transversal axis, the mean friction velocity and kinematic viscosity are used. Dimensionless averaging times are given by reference to h/U_τ , where h is the channel half-height. Two averaging times are provided: the first one Δt^+ is about the usual quantities like the velocity components and the temperature and the second one $\Delta t_{additional}^+$ deals with the additional quantities like the entropy generation rate and other derived magnitudes (its root-mean-square or its correlations, for example).

Table B.1: DNS characteristics I: mesh definitions and averaging times in wall units.

	Δ_x^+	$\Delta_{y,cold}^+$	$\Delta_{y,center}^+$	$\Delta_{y,hot}^+$	Δ_z^+	Δt^+	$\Delta t_{additional}^+$
T180-2-main	4.64	0.48	2.95	0.20	4.64	400	80
F180-2-main	4.67	0.47	2.97	0.20	4.67	356	74
T180-1-main	5.89	0.33	3.75	0.33	5.89	261	136
T180-1.001-main	5.89	0.33	3.75	0.33	5.89	44	44
T180-1.005-main	5.89	0.33	3.75	0.33	5.89	25	25
T180-1.01-main	5.88	0.34	3.74	0.33	5.88	49	49
T180-1.5-main	5.37	0.42	3.42	0.25	5.37	96	90
T180-2.5-main	3.92	0.51	2.50	0.16	3.92	46	44
T180-3-main	3.29	0.53	2.09	0.13	3.29	26	25
T150-2-main	3.85	0.40	2.45	0.16	3.85	90	68
T210-2-main	5.35	0.55	3.40	0.23	5.35	113	89
T180-2-check	4.64	0.25	2.31	0.10	2.32	207	3
F180-2-check	4.66	0.25	2.31	0.10	2.33	100	3

Table B.2: DNS characteristics II: friction quantities.

	$U_{\tau,cold} [m.s^{-1}]$	$T_{\tau,cold} [K]$	$Re_{\tau,cold}$	$U_{\tau,hot} [m.s^{-1}]$	$T_{\tau,hot} [K]$	$Re_{\tau,hot}$
T180-2-main	0.175	5.4	258	0.234	8.1	106
F180-2-main	0.174	5.4	256	0.235	8.0	108
T180-1-main	0.123	0.0	180	0.123	0.0	180
T180-1.001-main	0.123	0.0	180	0.123	0.0	180
T180-1.005-main	0.123	0.0	180	0.123	0.0	179
T180-1.01-main	0.123	0.0	181	0.123	0.1	178
T180-1.5-main	0.154	3.0	226	0.183	3.7	133
T180-2.5-main	0.187	7.6	276	0.274	12.8	86
T180-3-main	0.195	9.4	288	0.301	17.6	71
T150-2-main	0.145	5.6	214	0.195	8.3	88
T210-2-main	0.201	5.3	297	0.270	7.9	122
T180-2-check	0.176	5.4	259	0.235	8.1	106
F180-2-check	0.175	5.4	256	0.236	8.0	107

Nomenclature

Acronyms

CRS	Central Receiver System
CSP	Concentrated (or Concentrating) Solar Power
CV	Control volume
DNS	Direct Numerical Simulation
DSG	Direct Steam Generation
EU	European Union
HTF	Heat Transfer Fluid
LCOE	Levelized Cost of Electricity (or of Energy)
LHS	Left Hand Side of an equation
OM	Order of Magnitude
ORC	Organic Rankine Cycle
PV	Photovoltaic
RHS	Right Hand Side of an equation
USD	US dollar

Roman symbols

\bar{c}	Total molar concentration (molarity)	$[mol.m^{-3}]$
\bar{M}_i	Molar mass of chemical species number i	$[kg.mol^{-1}]$
\bar{R}	Ideal gas constant (molar)	$[J.K^{-1}.mol^{-1}]$
\mathbf{F}	Volume force vector by unit of volume	$[N.m^{-3}]$
\mathbf{V}	Velocity vector	$[m.s^{-1}]$
\dot{m}	Mass flow rate	$[kg.s^{-1}]$
\dot{Q}	Heat flow rate	$[W]$
\dot{S}_{gen}'''	Local entropy generation rate	$[W.K^{-1}.m^{-3}]$
\dot{S}_{gen}''	Surface entropy generation rate	$[W.K^{-1}.m^{-2}]$
\dot{S}_{gen}'	Total entropy generation rate between two positions along a plate	$[W.K^{-1}.m^{-1}]$
\dot{S}_{gen}	Entropy generation rate	$[W.K^{-1}]$

\dot{W}	Power	[W]
\dot{W}^+	Power accounted positively when a system delivers work ($\dot{W}^+ = -\dot{W}$)	[W]
Be	Bejan thermodynamic number	
Br	Brinkman number	
C_p	Thermal capacity at constant pressure (by unit of mass)	[J.kg ⁻¹ .K ⁻¹]
D	Diffusion coefficient	[m ² .s ⁻¹]
e_I	Specific internal energy	[J.kg ⁻¹]
e_K	Specific kinetic energy	[J.kg ⁻¹]
e_M	Specific total energy	[J.kg ⁻¹]
Ec	Eckert number	
Ec_w	$U_\infty^2/(C_p T_w)$	
f	Dimensionless Blasius velocity function (Eq. (2.20))	
f_i	i th component of the specific volume force vector	[N.kg ⁻¹]
g	Gravitational acceleration	[m.s ⁻²]
Gr	Grashof number	
h	Channel half-height (in chapter 4)	[m]
h	Specific enthalpy	[J.kg ⁻¹]
h^t	Specific total enthalpy	[J.kg ⁻¹]
I_s	Improvement factor	
J, J^*	Objective criterion and objective functional respectively	[W.K ⁻¹]
k	Thermal conductivity	[W.m ⁻¹ .K ⁻¹]
Kn	Knudsen number	
L, L_c	Characteristic length	[m]
Ma	Mach number	
Nu	Nusselt number	
P	Pressure	[Pa]
P_{dyn}	Dynamic pressure (in chapter 4)	[Pa]
P_{th}	Thermodynamic pressure (in chapter 4)	[Pa]
Pr	Prandtl number	
q''	Heat flux density at the plate	[W.m ⁻²]
q_1	Dimensionless heat flux density at the plate (Eq. (2.61))	
q_i	i th component of the heat flux vector	[W.m ⁻²]
r_{disc}	discount rate	
Re	Reynolds number	
Re_a, Re_b	Boundaries of a local Reynold number interval	
Re_x	Local Reynolds number	

$Re_{\tau m}$	Mean friction Reynolds number	
Ri	Richardson number	
s	Specific entropy	$[J.K^{-1}.kg^{-1}]$
S_1	Dimensionless total entropy generation rate between two positions along the plate	
S_2	Dimensionless surface entropy generation rate	
S_3	Dimensionless local entropy generation rate	
S_{ij}	Component (i,j) of the strain rate tensor	$[s^{-1}]$
T	Temperature	$[K]$
t	Time	$[s]$
T^+	Dimensionless temperature gap to the wall	
T_w	Wall temperature	$[K]$
T_∞	Free stream temperature	$[K]$
U	Instantaneous longitudinal velocity (in chapter 4)	$[m.s^{-1}]$
u, v	Longitudinal and normal components of the velocity	$[m.s^{-1}]$
U_i	Ith component of the instantaneous velocity vector (in chapter 4)	$[m.s^{-1}]$
u_i	ith component of the velocity vector	$[m.s^{-1}]$
U_∞	Free stream longitudinal velocity	$[m.s^{-1}]$
$U_{\tau m}$	Mean friction velocity	$[m.s^{-1}]$
V	Instantaneous wall-normal velocity (in chapter 4)	$[m.s^{-1}]$
$V, \mathbf{V} $	Velocity magnitude	$[m.s^{-1}]$
W	Instantaneous transversal velocity (in chapter 4)	$[m.s^{-1}]$
w_i	Mass fraction of chemical species number i	$[kg.kg^{-1}]$
W_Φ	Weighting factor in objective criterion or functional	$[K^{-1}]$
x, y	Longitudinal and normal coordinates	$[m]$
x_i	ith component of the position vector	$[m]$
y^+	Dimensionless distance from the closest wall in wall units (in chapter 4)	
z	Transversal coordinate; elevation in Eq. 1.3	$[m]$

Greek symbols

α	Thermal diffusivity	$[m^2.s^{-1}]$
$\bar{\tau}$	viscous stress tensor	$[Pa]$
β	volumetric coefficient of thermal expansion	$[K^{-1}]$
ΔT	Temperature gap ($T_w - T_\infty$)	$[K]$
Δt^+	Dimensionless averaging time	
δ	Dynamic boundary layer thickness	$[m]$

δ_T	Thermal boundary layer thickness	[m]
δ_{ij}	Kronecker delta	
η	Dimensionless coordinate (Eq. (2.19))	
η_c	Carnot efficiency ($1 - \frac{T_{cold}}{T_{hot}}$)	
η_{col}	Efficiency of solar collectors and concentrators	
η_{csp}	Efficiency of the CSP plant $\eta_{csp} = \eta_{col}\eta_{rec}\eta_{pb}$	
η_{pb}	Efficiency of the thermodynamic cycle / the power block	
η_{rec}	Efficiency of solar receptors	
γ	Heat capacity ratio	
λ_i	Lagrange coefficient	
μ	Dynamic viscosity	[Pa.s]
μ'	Second viscosity coefficient	[Pa.s]
ν	Kinematic viscosity	[m ² .s ⁻¹]
Φ	Viscous dissipation function (Eq. (1.18))	[W.m ⁻³]
ψ	Stream function (Eq. (2.21))	[m ² .s ⁻¹]
ρ	Density	[kg.m ⁻³]
Σ	A thermodynamic system	
σ_{ij}	Component (i,j) of the stress tensor	[Pa]
τ	Dimensionless thermal parameter ($T_w/\Delta T$)	
τ_{ij}	Component (i,j) of the viscous stress tensor	[Pa]
θ	Dimensionless temperature gap (Eq. (2.22))	
θ'	Fluctuation of the temperature (in chapter 4)	[K]

Superscripts

- (.)⁺ Dimensionless quantity in relation to friction velocity and temperature (in chapter 4)
- (.)['] Fluctuation of a quantity in the Reynolds decomposition (in chapter 4)
- (.)['] Superscript related to the derivative with respect to η (in chapter 2)
- (.)[×] Superscript related to a dimensionless quantity

Subscripts

- (.)_{,XX} Second order partial derivative with respect variable X (i.e. ∂_{XX}^2)
- (.)_{,X} Partial derivative with respect variable X (i.e. ∂_X)
- (.) _{τ} Friction quantity
- (.)_{amb} Ambient (e.g. T_{amb})
- (.)_{ch} Subscript related to the horizontal conduction of heat

- (.)_{cold} Subscript related to the channel cold plate
- (.)_{cv} Subscript related to the vertical conduction of heat
- (.)_c Subscript related to the conduction of the heat (e.g. $\dot{S}_{gen,c}$: entropy generation (time) rate by heat conduction)
- (.)_{f,marg} Subscript related to marginal viscous friction terms (Eqs. (2.53), (2.54) (2.55))
- (.)_{FLUCT} Part of a quantity coming from the variances and correlations of its component turbulent fluctuations
- (.)_f Subscript related to the entropy generation due to viscous friction
- (.)_f Subscript related to the main viscous friction term (in chapter 2)
- (.)_{hot} Subscript related to the channel hot plate
- (.)_{in} Entering in a system
- (.)_{lost} Lost part of a quantity
- (.)_{max} Maximum of a quantity
- (.)_{MEAN} Part of a quantity coming from mean fields of its components
- (.)_{out} Leaving a system
- (.)_{ref} Subscript related to the value at the reference position x_{ref}
- (.)_{rms} Root-mean-square of a quantity
- (.)_w Subscript related to a value at a wall
- $\langle . \rangle$ Statistical average over (xz) planes and time

List of figures

1	Couche limite au dessus d'une plaque plane	v
2	Puissance entropique adimensionnelle générée localement (S_3). Plaque isotherme (à gauche) et isoflux (à droite). La courbe de S_3 pour le cas isotherme est également affichée pour servir de comparaison sur le graphique du cas isoflux (ligne noire en traits pleins).	viii
3	Plaque isotherme (à gauche) et isoflux (à droite) : puissance entropique surfacique adimensionnelle pour $\tau_{ref} = 10$ et Re_x de 100 à 1000000	ix
4	Puissance entropique totale générée à partir de $Re_a = 1000$ avec $q_1 = 26.67$ (τ_{ref} allant de 5 à 190.)	x
5	Caractéristiques du domaine.	xi
6	Puissance entropique totale générée dans le canal \dot{S}_{gen} en fonction de W_{Φ}	xiii
7	Puissance entropique générée dans le canal du fait des frottements visqueux $\dot{S}_{gen,f}$ en fonction de W_{Φ}	xiv
8	Norme du vecteur vitesse pour $W_{\Phi} = 394 K^{-1}$, $296 K^{-1}$ et $197 K^{-1}$. $Re = 30$	xiv
9	Température maximale de la paroi chauffante [K].	xv
10	Puissance entropique totale générée \dot{S}_{gen} ainsi que sa composante provenant du frottement visqueux $\dot{S}_{gen,f}$ en fonction de la densité de flux thermique à la paroi chauffante ($Re = 20$ et $W_{\Phi} = 1.23 \times 10^5 K^{-1}$).	xvi
11	Canal plan bi-périodique : les axes x et z sont des directions d'homogénéité	xviii
12	Ecart-type des fluctuations de la température (adimensionnées par la température de frottement T_{τ}) en fonction de la distance addimensionnelle à la paroi la plus proche $y^+ = (y/h)Re_{\tau}$	xx
13	Moyenne de la puissance entropique générée localement.	xxi
14	Approximations successives la puissance entropique générée localement. Le terme noté \dot{S}_{gen,c,T_y}''' correspond à la part provenant de la conduction verticale de la chaleur.	xxi
15	Decomposition de la puissance entropique locale due à la conduction verticale de la chaleur (cf. Eqs. 50 and 51)	xxii
16	Moyenne de la puissance entropique générée localement pour plusieurs ratios de températures T_2/T_1 entre le mur chaud et le mur froid ($Re_{\tau m} = 180$).	xxiii
17	valeur instantanée de la puissance entropique générée localement au mur froid $W.K^{-1}.m^{-3}$	xxiv
1.1	Cost reduction of solar thermal electricity [169]	5
1.2	THEMIS Solar Power Plant [191]	6
1.3	PEGASE Project [133]	6

1.4	Influence of concentration ratio (CR) and the receiver surface temperature on the theoretical performance of a CSP plant	9
1.5	Gemasolar Thermosolar Plant [226]	10
1.6	Solar One central receiver [219]	11
1.7	Open system Σ to illustrate the Gouy-Stodola theorem	12
1.8	Elementary control volume CV to illustrate Eq. 1.30 demonstration	20
2.1	Boundary layer over a flat plate	25
2.2	Functions f , f' and f'' cross-checked with Ganapol [87]	33
2.3	$\theta'(0)$ cross-checked with Churchill and Ozoe [53, 54]	33
2.4	Variation of τ as a function of Re_x	34
2.5	θ and θ' functions for an isothermal and an isoflux plate	34
2.6	Local entropy generation rate. Isothermal (left) and Isoflux (right). The isothermal curve S_3 is also plotted as a reference on the corresponding isoflux chart (black plain line).	35
2.7	Local entropy generation rate. Isothermal (left) and Isoflux (right), showing all marginal viscous friction contributors.	37
2.8	Isothermal plate surface entropy generation rates for two values of τ_{ref} and Re_x from 100 to 1000000	38
2.9	Isoflux plate surface entropy generation rates for two values of τ_{ref} and Re_x from 100 to 1000000	38
2.10	Isoflux plate total entropy generation rate between two positions Re_a and Re_b	40
2.11	Total entropy generation rate starting at $Re_a = 1000$ with $q_1 = 26.67$ (τ_{ref} spreads from 5 to 190.)	41
2.12	Isothermal plate ($Re_a = 1000$, $q_1 = 26.67$, $2 \leq \tau_{ref} \leq 30$): Comparison with a model where $\Delta T \ll T_w$	41
2.13	τ_{opt} as a function of q_1	42
2.14	τ_{opt} as a function of Re_a	42
2.15	Simulation1 and Simulation2 boundary conditions	44
2.16	Temperature as a function of the distance to the wall	46
2.17	Temperature gap between Simulation1 and Simulation2 as a function of the distance to the wall	46
2.18	Internal energy (convective) fluxes as functions of the energy equation residual	48
2.19	Entropy (convective) fluxes as functions of the energy equation residual	49
2.20	Internal energy and entropy balance relative deviation as functions of the energy equation residual	49
2.21	Comparison between Blasius and Navier-Stokes longitudinal velocity ($\tau = 2$ and $Re_x = 20850$)	51
2.22	Comparison between Blasius and Navier-Stokes temperature at $Re_x = 20850$ when $\tau = 2$ and the temperature of the plate is fixed	51
2.23	Comparison between Blasius and Navier-Stokes temperature at $Re_x = 20850$ when $\tau = 2$ and the heat flux density of the plate is fixed	52
3.1	Domain characteristics.	57
3.2	Improvement factor I_S (Eq. 3.13) as a function of W_{Φ} . $Re = 30$	58
3.3	Total entropy generation rate \dot{S}_{gen} as a function of W_{Φ}	58

3.4	Entropy generation rate due to heat conduction $\dot{S}_{gen,c}$ as a function of W_{Φ}	59
3.5	Entropy generation rate due to viscous friction $\dot{S}_{gen,f}$ as a function of W_{Φ}	59
3.6	Total viscous dissipation Φ_{tot} as a function of W_{Φ}	60
3.7	Total entropy generation rate \dot{S}_{gen} as a function of the total viscous dissipation Φ_{tot}	60
3.8	J objective functional as a function of W_{Φ}	61
3.9	Temperature field with no optimization and when $W_{\Phi} = 5914 K^{-1}$. $Re = 30$)	61
3.10	Velocity magnitude field with no optimization and when $W_{\Phi} = 5914 K^{-1}$. $Re = 30$)	62
3.11	Temperature field for $W_{\Phi} = 394 K^{-1}$, $296 K^{-1}$ and $197 K^{-1}$. $Re = 30$.	62
3.12	Velocity magnitude field for $W_{\Phi} = 394 K^{-1}$, $296 K^{-1}$ and $197 K^{-1}$. $Re = 30$	63
3.13	Stream function [$kg.s^{-1}$]. $Re = 30$	64
3.14	Velocity vector (zoom) with an indication of the main flow directions and of the rotational direction of vortexes: " + " means clockwise. $Re = 30$.	64
3.15	λ_2 Lagrange multiplier [$J.m^{-3}.K^{-2}$] field ($Re = 30$).	65
3.16	Force field \mathbf{F} applied above the heated segment area [$N.m^{-3}$] ($Re = 30$).	65
3.17	Local entropy generation rate by heat conduction in [$W.K^{-1}.m^{-3}$] for $W_{\Phi} = 5913 K^{-1}$, $1183 K^{-1}$, $197 K^{-1}$ and when no optimization is applied.	66
3.18	Local entropy generation rate by viscous friction in [$W.K^{-1}.m^{-3}$] for $W_{\Phi} = 5913 K^{-1}$, $1183 K^{-1}$, $197 K^{-1}$ and when no optimization is applied. Color scale is logarithmic.	67
3.19	Average temperature in the Channel [K].	67
3.20	Maximum temperature in the Channel [K].	68
3.21	Average temperature on the bottom plate [K].	68
3.22	Maximum temperature on the bottom plate [K].	69
3.23	Temperature along the bottom plate [K].	69
3.24	Average temperature at outlet [K].	70
3.25	Temperature profile at outlet [K].	70
3.26	Maximum velocity magnitude in the Channel [$m.s^{-1}$].	71
3.27	Domain characteristics.	77
3.28	Velocity magnitude and temperature fields with no optimization and with slightly and highly perturbed profiles ($Re = 20$)	78
3.29	Zoom of velocity vector and stream function fields when $W_{\Phi} = 1.047 \times$ $10^5 K^{-1}$. The vertical lines materialize the abscissa $x = 10 mm$ and $x = 20 mm$ of the heated region. $Re = 20$	79
3.30	Total entropy generation rate, improvement factor and maximum tem- perature inside the channel.	80
3.31	Viscous friction entropy generation rate, total viscous dissipation and maximum velocity in the channel.	81
3.32	Objective functional and relationship between total entropy generation rate and total viscous dissipation	81
3.33	Total entropy generation rates for two values of the input heat flux. $Re = 20$	82
3.34	Viscous friction entropy generation rate for two values of the input heat flux.	82

3.35	Maximum velocity magnitude in the channel as a function of W_{Φ} for two values of the input heat flux.	83
3.36	Total and viscous entropy generation rates as functions of the heat flux input from the bottom of the channel ($Re = 20$ and $W_{\Phi} = 1.23 \times 10^5 K^{-1}$).	83
3.37	Maximum temperature and maximum velocity magnitude in the channel ($Re = 20$ and $W_{\Phi} = 1.23 \times 10^5 K^{-1}$).	84
3.38	Total and viscous entropy generation rates as functions of V_{in} ($W_{\Phi} = 1.23 \times 10^5 K^{-1}$).	85
3.39	Maximum velocity magnitude and maximum scalar value in the channel as functions of V_{in} ($W_{\Phi} = 1.23 \times 10^5 K^{-1}$).	85
3.40	Velocity magnitude and minor species mass fraction fields with no optimization and with slightly and highly perturbed profiles ($Re = 10$)	86
3.41	Heat vs. mass transfer entropy generation rate and viscous dissipation quantities ($Re = 10$)	87
3.42	Total and viscous entropy generation rates as functions of the diffusion intensity from the bottom plate ($W_{\Phi} = 1.67 \times 10^5 K^{-1}$ and $Re = 10$).	88
3.43	Maximum and average mass fraction of the minor species and maximum velocity as functions of the diffusion intensity from the bottom plate ($W_{\Phi} = 1.67 \times 10^5 K^{-1}$ and $Re = 10$).	88
3.44	Total and viscous entropy generation rates in the channel as functions the inlet mass fraction of the minor species ($W_{\Phi} = 1.67 \times 10^5 K^{-1}$ and $Re = 10$).	89
3.45	Maximum velocity magnitude in the channel as functions the inlet mass fraction of the minor species ($W_{\Phi} = 1.67 \times 10^5 K^{-1}$ and $Re = 10$).	89
3.46	Total entropy generation rate as a function of W_{Φ} , complemented by finer mesh simulations. $Re = 20$	90
3.47	Total entropy generation rate as a function of W_{Φ} - zoom on transition zone showing the influence of the grid resolution and the initial conditions. $Re = 20$	90
4.1	Bi-periodic flat plate channel	97
4.2	Grid and domain volume independence check	98
4.3	Dynamic statistics	101
4.4	Statistics involving temperature	102
4.5	Turbulent Prandtl number Pr_t	103
4.6	R_0 coefficient (eq. 4.19) with logarithmic y-scale	104
4.7	Mean local entropy generation rate.	108
4.8	Mean local entropy generation rate by heat conduction components (Eqs. 4.26 and 4.27).	110
4.9	Mean local entropy generation rate by viscous friction components - Eqs. 4.28 and 4.29; e.g. u_y+v_x stands for $\langle \dot{S}_{gen,f,u_y+v_x}''' \rangle$	110
4.10	Decomposition of the $\langle \dot{S}_{gen,f,u_y+v_x}''' \rangle$ term in the viscous friction mean local entropy generation rate - Eqs. 4.30 and 4.31.	111
4.11	Successive approximations of the mean local entropy generation rate \dot{S}_{gen}'''	112
4.12	Decomposition of the mean local entropy generation rate by vertical heat conduction (cf. Eqs. 4.32).	113
4.13	Decomposition of the dimensionless mean local entropy generation rate by vertical heat conduction (cf. Eqs. 4.32 and 4.33)	114

4.14	Decomposition of the mean local viscous entropy generation rate due to the vertical component of the gradient of the longitudinal velocity (cf. Eqs. 4.34) ($T_2/T_1 = 2$ and $Re_{\tau m} = 180$).	115
4.15	Decomposition of the mean local viscous entropy generation due to the vertical component of the gradient of the longitudinal velocity (cf. Eqs. 4.34)	115
4.16	Mean local entropy generation rate for various hot to cold wall temperature ratios ($Re_{\tau m} = 180$).	116
4.17	Mean local entropy generation rate for various mean friction Reynolds number ($T_2/T_1 = 2$).	117
4.18	Root-mean-square of the local entropy generation rate fluctuations compared to the mean value $\langle \dot{S}_{gen}''' \rangle$	117
4.19	Root-mean-square of the temperature gradient vertical component fluctuations compared to the mean value $\langle \frac{\partial T}{\partial y} \rangle$	118
4.20	Correlations of the local entropy generation rate fluctuations	118
4.21	Covariances of the local entropy generation rates	119
4.22	Mean local entropy generation rate for two types of boundary conditions ($T_2/T_1 \approx 2$ and $Re_{\tau m} = 180$).	120
4.23	Standard deviation of the local entropy generation rate for two types of boundary conditions ($T_2/T_1 \approx 2$ and $Re_{\tau m} = 180$).	121
4.24	Front-face view of the instantaneous local entropy generation rate at (xy) plane with $z = z_{min}$ [$W.K^{-1}.m^{-3}$].	121
4.25	Instantaneous local entropy generation rate at the cold plate [$W.K^{-1}.m^{-3}$]122	
4.26	Instantaneous local entropy generation rate at the hot plate [$W.K^{-1}.m^{-3}$]123	
4.27	Instantaneous local entropy generation rate at $x = x_{min}$ and $z = z_{min}$	124
4.28	Comparison of local entropy generation rate and its root-mean-square for two domain definitions (see table 4.1)	124

List of tables

2.1	Entropy generation rate by unit of transversal length [$W.K^{-1}.m^{-1}$] . . .	45
2.2	Internal energy balance by unit of transversal length [$W.m^{-1}$]	47
2.3	Entropy balance by unit of transversal length [$W.K^{-1}.m^{-1}$]	48
2.4	Entropy generation rate by heat conduction and by viscous friction, by unit of transversal length [$W.K^{-1}.m^{-1}$]	50
4.1	Domain characteristics	97
4.2	Mean friction variables	99
4.3	Nusselt numbers ($L_c = 2h$)	105
4.4	Relative importance of heat conduction and viscous friction in the mean local entropy generation rate [$W.K^{-1}.m^{-3}$]. Be is the Bejan thermodynamic number.	109
4.5	Successive approximations of the mean total entropy generation rate in the channel	112
B.1	DNS characteristics I: mesh definitions and averaging times in wall units.	134
B.2	DNS characteristics II: friction quantities.	134

Bibliography

- [1] S. Akbarzadeh and M. S. Valipour. Heat transfer enhancement in parabolic trough collectors: A comprehensive review. *Renewable and Sustainable Energy Reviews*, 92:198–218, 2018. doi: 10.1016/j.rser.2018.04.093.
- [2] E. F. Akyürek, K. Gelis, B. Sahin, and M. Eyüphan. Experimental analysis for heat transfer of nanofluid with wire coil turbulators in a concentric tube heat exchanger. *Results in Physics*, 9:376–389, 2018. doi: 10.1016/j.rinp.2018.02.067.
- [3] A. Al Mers, A. Azzabakh, A. Mimet, and H. El Kalkha. Optimal design study of cylindrical finned reactor for solar adsorption cooling machine working with activated carbon–ammonia pair. *Applied Thermal Engineering*, 26:1866–1875, 2006. doi: 10.1016/j.applthermaleng.2006.01.021.
- [4] K. Alabi, F. Ladeinde, M. vonSpakovsky, D. Moorhouse, and J Camberos. Assessing CFD modeling of entropy generation for the air frame subsystem in an integrated aircraft design/synthesis procedure. In *44th AIAA Aerospace Sciences Meeting and Exhibit, Reno, Nevada, 9-12 January, 2006*. doi: 10.2514/6.2006-587.
- [5] G. P. Aravind and M. Deepu. Numerical study on convective mass transfer enhancement by lateral sweep vortex generators. *International Journal of Heat and Mass Transfer*, 115:809–825, 2017. doi: 10.1016/j.ijheatmasstransfer.2017.07.104.
- [6] S.-S. Ashrafmansouri and M. N. Esfahany. Mass transfer in nanofluids: A review. *International Journal of Thermal Sciences*, 82:84–99, 2014. doi: 10.1016/j.ijthermalsci.2014.03.017.
- [7] J. Aubin, M. Ferrando, and V. Jiricny. Current methods for characterising mixing and flow in microchannels. *Chemical Engineering Science*, 65(6):2065–2093, 2010. doi: 10.1016/j.ces.2009.12.001.
- [8] F. Aulery, A. Toutant, F. Bataille, and Y. Zhou. Energy transfer process of anisothermal wall-bounded flows. *Physics Letters A*, 379(24-25):1520–1526, 2015. doi: 10.1016/j.physleta.2015.03.022.
- [9] F. Aulery, D. Dupuy, A. Toutant, F. Bataille, and Y. Zhou. Spectral analysis of turbulence in anisothermal channel flows. *Computers & Fluids*, 151:115–131, 2017. doi: 10.1016/j.compfluid.2016.06.011.
- [10] J. M. Avellaneda, S. Jia, P. Neveu, F. Bataille, X. Yuan, and G. Flamant. Similarities between heat and mass transfer enhancement in convective flow,

- using variational optimization technique. *International Heat Transfer Conference 16, 2018, 10-15 August, Beijing, China*, pages 2715–2722, 2018. doi: 10.1615/IHTC16.cov.021341.
- [11] J. M. Avellaneda, F. Bataille, and A. Toutant. DNS of turbulent low mach channel flow under asymmetric high temperature gradient: Effect of thermal boundary condition on turbulence statistics. *International Journal of Heat and Fluid Flow*, pages 40–47, 2019. doi: 10.1016/j.ijheatfluidflow.2019.03.002.
- [12] J. M. Avellaneda, A. Toutant, G. Flamant, P. Neveu, and F. Bataille. Entropy generation in nonisothermal flows: Influence of boundary condition type and intensity. *Journal of Thermophysics and Heat Transfer*, July 2019. doi: 10.2514/1.T5748.
- [13] A.L. Avila-Marin. Volumetric receivers in solar thermal power plants with central receiver system technology - a review. *Solar Energy*, 85(5):891–910, 2011. doi: 10.1016/j.solener.2011.02.002.
- [14] M. M. Awad. The science and the history of the two Bejan numbers. *International Journal of Heat and Mass Transfer*, 94:101–103, 2016. doi: 10.1016/j.ijheatmasstransfer.2015.11.073.
- [15] O. Aydin and W-J. Yang. Mixed convection in cavities with locally heated lower wall and moving sidewalls. *Numerical Heat Transfer, Part A: Applications: An International Journal of Computation and Methodology*, 37(7):695–710, 2000. doi: 10.1080/104077800274037.
- [16] A. Aziz. A similarity solution for laminar thermal boundary layer over a flat plate with convective surface boundary condition. *Communications in Nonlinear Science and Numerical Simulation*, 14(4):1064–1068, 2009. doi: 10.1016/j.cnsns.2008.05.003.
- [17] M. S. Baba, A. V. Sita Rama Raju, and M. Baghvant Rao. Heat transfer enhancement and pressure drop of Fe_3O_4 -water nanofluid in a double tube counter flow heat exchanger with internal longitudinal fins. *Case Studies in Thermal Engineering*, 12:600–607, 2018. doi: 10.1016/j.csite.2018.08.001.
- [18] L. H. Back and R. F. Cuffel. Compressible laminar boundary layers with large acceleration and cooling. *AIAA Journal*, 14(7):968–971, 1976. doi: 10.2514/3.7170.
- [19] B. Banks, M. A. Frederick, R. R. Tracy, J. R. Matischeck, and N.D. Vanecek. In-flight boundary layer transition on a large flat plate at supersonic speeds. *NASA Technical Memorandum*, NASA/TM-2012-216021, 2012.
- [20] G. K. Batchelor. *An introduction to fluid dynamics*. Cambridge University Press, 2000.
- [21] E. Battista and H. C. Perkins. Turbulent heat and momentum transfer in a square duct with moderate property variations. *International Journal of Heat and Mass Transfer*, 13:1063–1065, 1970. doi: 10.1016/0017-9310(70)90172-9.

- [22] N. Beck, T. Landa, A. Seitz, L. Boermans, Y. Liu, and R. Radespiel. Drag reduction by laminar flow control. *Energies*, 11(1), 252, 2018. doi: 10.3390/en11010252.
- [23] A. Bejan. A study of entropy generation in fundamental convective heat transfer. *Journal of Heat Transfer*, 101(4):718–725, 1979. doi: 10.1115/1.3451063.
- [24] A. Bejan. Entropy generation minimization: the new thermodynamics of finite-sized devices and finite-time processes. *Journal of Applied Physics*, 79(3):1191–1218, 1996. doi: 10.1063/1.362674.
- [25] A. Bejan. Fundamentals of exergy analysis, entropy generation minimization, and the generation of flow architecture. *International Journal of Energy Research*, 26:545–565, 2002. doi: 10.1002/er.804.
- [26] A. Bejan. *Entropy generation minimization*. CRC Press, 2013. ISBN 0-8493-9651-4. doi: 10.1201/9781482239171. ISBN: 9781482239171.
- [27] A. Bejan. *Convection Heat Transfer*, page 84. John Wiley & sons, 4th edition, 2013. ISBN 978-0-470-90037-6. doi: 10.1002/9781118671627. ISBN: 978-0-470-90037-6.
- [28] A. Bejan and D. L. Siems. The need for exergy analysis and thermodynamic optimization in aircraft development. *Exergy, An International Journal*, 1(1): 12–24, 2001. doi: 10.1016/S1164-0235(01)00005-X.
- [29] M. Bellec, A. Toutant, and G. Olalde. Large eddy simulations of thermal boundary layer developments in a turbulent channel flow under asymmetrical heating. *Computers and fluids*, 151:159–176, 2017. doi: 10.1016/j.compfluid.2016.07.001.
- [30] A. Benabderrahmane, A. Miloud, L. Samir, B. Abdelylah, and J. P. Solano. Heat transfer enhancement in a parabolic trough solar receiver using longitudinal fins and nanofluids. *Journal of Thermal Science*, 25(5):410–417, 2016. doi: 10.1007/s11630-016-0878-3.
- [31] R. Bergant and I. Tiselj. Near-wall passive scalar transport at high Prandtl numbers. *Physics of Fluids*, 19:065105, 2007. doi: 10.1063/1.2739402.
- [32] A. E. Bergles. The implications and challenges of enhanced heat transfer for the chemical process industries. *Chemical Engineering Research and Design*, 79(4): 437–444, 2001. doi: 10.1205/026387601750282562.
- [33] T. L. Bergman, A. S. Lavine, F. P. Incropera, and D. P. Dewitt. *Fundamentals of heat and mass transfer*. John Wiley & Sons, 2011.
- [34] V. Bianco, O. Manca, S. Nardini, and K. Vafai. *Heat Transfer Enhancement with Nanofluids*. Taylor & Francis Group, Boca Raton, FL, 2015. ISBN 978-1-4822-5402-0. ISBN:978-1-4822-5402-0.
- [35] M. Bidi, M. R. H. Nobari, and M. S. Avval. A numerical evaluation of combustion in porous media by EGM (Entropy Generation Minimization). *Energy*, 35(8): 3483–3500, 2010. doi: 10.1016/j.energy.2010.04.053.

- [36] R. B. Bird, W. E. Stewart, and E. N. Lightfoot. *Transport Phenomena*. Wiley, 2006. ISBN: 978-0-470-11539-8.
- [37] H. Blasius. Grenzsichten in Flüssigkeiten mit kleiner Reibung. *Zeitschrift für Mathematik und Physik*, 56:1–37, 1908.
- [38] L. Borel and D. Favrat. *Thermodynamique et énergétique*. Presses Polytechniques et Universitaires Romandes, 2011. ISBN: 978-2-88074-545-5.
- [39] M. Bouabid, N. Hidouri, M. Magherbi, and A. Ben Brahim. Heat and mass transfer for Hartmann and Dufour’s effects on irreversibilities at double-diffusive natural convection in a square cavity. *Journal of Advanced Chemical Engineering*, 7:2, 2017. doi: 10.4172/2090-4568.1000180.
- [40] F. Bouras, M. E. H. Attia, and F. Khaldi. Entropy generation optimization in internal combustion engine. *Environmental Processes*, 2(Suppl 1):233:233–242, 2015. doi: 10.1007/s40710-015-0102-6.
- [41] M. Bousbai, M. Ould-Rouiss, A. Mazouz, and A. Mataoui. Turbulent heat transfer characteristics of water flow in a rotating pipe. *Heat Mass Transfer*, 49:469–484, 2013. doi: 10.1007/s00231-012-1094-7.
- [42] O. Bulliard-Sauret, S. Ferrouillat, L. Vignal, and A. Mempoiteil. Heat transfer enhancement using 2 MHz ultrasound. *Ultrasonics - Sonochemistry*, 39:232–271, 2017. doi: 10.1016/j.ultsonch.2017.04.021.
- [43] C. Cai. Near continuum boundary layer flows at a flat plate. *Theoretical and Applied Mechanics Letters*, 5:134–139, 2015. doi: 10.1016/j.taml.2015.03.005.
- [44] W. Cai, J. Zhang, X. Zhang, Y. Wang, and X. Qi. Enhancement of CO₂ absorption under Taylor flow in the presence of fine particles. *Fluid Dynamics and Transport Phenomena, Chinese Journal of Chemical Engineering*, 21(2):135–143, 2013. doi: 10.1016/S1004-9541(13)60451-6.
- [45] C. Calvin, O. Cueto, and P. Emonot. An object-oriented approach to the design of fluid mechanics software. *ESAIM: Mathematical Modeling and Numerical Analysis*, 36(05):907–921, 2002. doi: 10.1051/m2an:2002038.
- [46] X. Cao, S. Jia, J.-M. Avellaneda, Y. Luo, X. Yuan, G. Flamant, and K.-T. Yu. An optimization method to find the thermodynamic limit on enhancement of solar thermal decomposition of methane. *International Journal of Hydrogen Energy*, 44(31):16164–16175, 2019. doi: 10.1016/j.ijhydene.2019.04.261.
- [47] X. Cao, S. Jia, Y. Luo, X. Yuan, Z. Qi, and K.-T. Yu. Multi-objective optimization method for enhancing chemical reaction process. *Chemical Engineering Science*, 195:494–506, 2019. doi: 10.1016/j.ces.2018.09.048.
- [48] C. G. Carrington and Z. F. Sun. Second law analysis of combined heat and mass transfer phenomena. *International Journal of Heat and Mass Transfer*, 34(11):2767–2773, 1991. doi: 10.1016/0017-9310(91)90235-7.

- [49] P. Chakraborty, T. Ma, L. Cao, and Y. Wang. Significantly enhanced convective heat transfer through surface modification in nanochannels. *International Journal of Heat and Mass Transfer*, 136:702–708, 2019. doi: 10.1016/j.ijheatmasstransfer.2019.03.053.
- [50] C. Chang, C. Xu, Z. Y. Wu, X. Li, Q. Q. Zhang, and Z. F. Wang. Heat transfer enhancement and performance of solar thermal absorber tubes with circumferentially non-uniform heat flux. *Energy Procedia - International Conference on Concentrating Solar Power and Chemical Energy Systems, SolarPACES 2014*, 69:320–327, 2015. doi: 10.1016/j.egypro.2015.03.036.
- [51] S. W. Chang, T.-M. Liu, K. F. Chiang, and G. F. Hong. Heat transfer and pressure drop in rectangular channel with compound roughness of v-shaped ribs and deepened scales. *International Journal of Heat and Mass Transfer*, 51(3-4): 457–468, 2008. doi: 10.1016/j.ijheatmasstransfer.2007.05.010.
- [52] S. L. Chernyshev, M. D. Gamirullin, V. Y. Khomich, A. P. Kuryachii, V. M. Litvinov, S. V. Manuilovich, S. I. Moshkunov, I. E. Rebrov, D. A. Rusyanov, and V. A. Yamshchikov. Electrogasdynamic laminar flow control on a swept wing. *Aerospace science and technology*, 59:155–161, 2016. doi: 10.1016/j.ast.2016.10.019.
- [53] S. W. Churchill and H. Ozoe. Correlations for laminar forced convection in flow over an isothermal flat plate and in developing and fully developed flow in an isothermal tube. *Journal of Heat Transfer*, 95(3):416–419, 1973. doi: 10.1115/1.3450078.
- [54] S. W. Churchill and H. Ozoe. Correlations for laminar forced convection with uniform heating in flow over a plate and in developing and fully developed flow in a tube. *Journal of Heat Transfer*, 95(1):78–84, 1973. doi: 10.1115/1.3450009.
- [55] M. E. Cilgin and O. Turan. Entropy generation calculation of a turbofan engine: A case of CFM56-7B 2017. *International Journal of Turbo & Jet-Engines*, 35(3): 217–228, 2017. doi: 10.1515/tjj-2017-0053.
- [56] R. Cipollone, A. Cinocca, and A. Gualtieri. Gases as working fluid in parabolic trough CSP plants. *Procedia Computer Science - SEIT 2013*, 19:702–711, 2013. doi: 10.1016/j.procs.2013.06.093.
- [57] G. Coleman, J. M. Kim, and R. D. Moser. A numerical study of turbulent supersonic isothermal-wall channel flow. *Journal of Fluid Mechanics*, 305:159–183, 1995. doi: 10.1017/S0022112095004587.
- [58] A. Colleoni, A. Toutant, G. Olalde, and J.-M. Foucaut. Optimization of winglet vortex generators combined with riblets for wall/fluid heat exchange enhancement. *Applied Thermal Engineering*, 50:1092–1100, 2013. doi: 10.1016/j.applthermaleng.2012.08.036.
- [59] F. G. Collins. Boundary-layer control on wings using sound and leading-edge serrations. *AIAA Journal*, 19(2):129–130, 1981. doi: 10.2514/3.50930.

- [60] Cornellsimulation. *Overshoot in velocity profile: Explanation*, 2019 (accessed June 13, 2019). URL <https://www.youtube.com/watch?v=LnIsw07iuew>.
- [61] G. Crabtree, J. Misewich, R. Ambrosio, K. Clay, P. DeMartini, R. James, M. Lauby, V. Mohta, J. Moura, P. W. Sauer, F. Slakey, and J. Lieberman. Integrating renewable electricity on the grid. In *AIP Conference Proceedings*. 1401., 2011. doi: 10.1063/1.3653865.
- [62] G. da Silva, O. Silvaes, and E Zerbini. Boundary-layers integral analysis - heated airfoils in icing conditions. In *46th AIAA Aerospace Sciences Meeting and Exhibit, 7-10 January, Reno, Nevada*, 2008. doi: 10.2514/6.2008-475.
- [63] X. Daguene-Frick, J. M. Foucaut, S. Couderc, A. Toutant, and G. Olalde. Experimental analysis of the turbulent flow behavior of a textured surface proposed for asymmetric heat exchangers. *Flow Turbulence and Combustion*, 89(1):149–169, 2012. doi: 10.1007/s10494-012-9387-y.
- [64] S. Dey and D. Chakraborty. Enhancement of convective cooling using oscillating fins. *International Communications in Heat and Mass Transfer*, 36:508–212, 2009. doi: 10.1016/j.icheatmasstransfer.2009.01.018.
- [65] S. Dharmarathne, M. Tutkun, G. Araya, and L. Castillo. Structures of scalar transport in a turbulent channel. *European Journal of Mechanics B/Fluids*, 55: 259–271, 2016. doi: 10.1016/j.euromechflu.2015.06.010.
- [66] F. W. Dittus and L. M. K. Boelter. Heat transfer in automobile radiators of the tubular type. *International Communications in Heat and Mass Transfer*, 12: 3–22, 1985.
- [67] M. T. Dunham and B. Iverson. High-efficiency thermodynamic power cycles for concentrated solar power systems. *Renewable and Sustainable Energy Reviews*, 30:758–770, 2014. doi: 10.1016/j.rser.2013.11.010.
- [68] D. Dupuy, A. Toutant, and F. Bataille. Turbulence kinetic energy exchanges in flows with highly variable fluid properties. *Journal of Fluid Mechanics*, 834:5–54, 2018. doi: 10.1017/jfm.2017.729.
- [69] D. Dupuy, A. Toutant, and F. Bataille. Equations of energy exchanges in variable density turbulent flows. *Physics Letters A*, 382(5):327–333, 2018. doi: 10.1016/j.physleta.2017.11.026.
- [70] I. Eames and J. C. R. Hunt. Inviscid flow around bodies moving in weak density gradients without buoyancy effects. *Journal of Fluid Mechanics*, 353:331–355, 1997. doi: 10.1017/S002211209700760X.
- [71] O. Edenhofer, R. Pichs-Madruga, Y. Sokona, K. Seyboth, S. Kadner, T. Zwickel, and P. (Eds.) . . . Matschoss. *Renewable Energy Sources and Climate Change Mitigation: Special Report of the Intergovernmental Panel on Climate Change*. Cambridge University Pres, 2011. doi: 10.1017/CBO9781139151153.
- [72] EIA. Cost and performance characteristics of new generating technologies, Annual Energy Outlook 2019. Technical report, EIA, 2019. U.S. Energy Information Administration.

- [73] T. Elperin and A. Fominykh. Mass transfer during solute extraction from a fluid sphere with internal circulation in the presence of alternating electric field. *Chemical Engineering and Processing*, 45:578–585, 2006. doi: 10.1016/j.cep.2006.01.002.
- [74] J. A. Esfahani and P. B. Shahabi. Effect of non-uniform heating on entropy generation for the laminar developing pipe flow of high Prandtl number fluid. *Energy Conversion and Management*, 51(11):2087–2097, 2010. doi: 10.1016/j.enconman.2010.02.022.
- [75] EUROSTAT. Renewable energy in the EU - Share of renewable energy in the EU up to 17.5% in 2017. Technical report, EUROSTAT, 2019. Eurostat Newsrelease 27/2019 - 12 February 2019.
- [76] M. Everts, S. R. Ayres, F. A. M. Houwer, C. P. Vanderwagen, N. M. Kotze, and J. P. Meyer. The influence of surface roughness on heat transfer in the transitional flow regime. *Proceedings of the 15th International Heat Transfer Conference, IHTC-15, August 10-15, 2014, Kyoto, Japan*, pages 1626–1637, 2014. doi: 10.1615/IHTC15.cnv.008338.
- [77] A. V. Fedorov. Prediction and control of laminar-turbulent transition in high-speed boundary-layer flows. *Procedia IUTAM*, 14:3–14, 2015. doi: 10.1016/j.piutam.2015.03.017.
- [78] D. Feldman and R. Margolis. Q1/Q2 2018 Solar Industry Update. *Golden, CO: National Renewable Energy Laboratory.*, NREL/PR-6A20-72036, 2018. (accessed on October 13, 2019). URL <https://www.nrel.gov/docs/fy18osti/72036.pdf>.
- [79] R. S. Figliola, R. Tipton, and H. Li. Exergy approach to decision-based design of integrated aircraft thermal systems. *Journal of Aircraft*, 40(1):49–55, 2003. doi: 10.2514/2.3056.
- [80] C. Flageul, S. Benhamadouche, E. Lamballais, and D. Laurence. DNS of turbulent channel flow with conjugate heat transfer: Effect of thermal boundary conditions on the second moments and budgets. *International Journal of Heat and Fluid Flow*, 55:34–44, 2015. doi: 10.1016/j.ijheatfluidflow.2015.07.009.
- [81] G. Flamant, D. Gauthier, H. Benoit, J. L. Sans, R. Garcia, B. Boissière, R. Ansart, and M. Hemati. Dense suspension of solid particles as a new heat transfer fluid for concentrated solar thermal plants: On-sun proof of concept. *Chemical Engineering Science*, 102:567–576, 2013. doi: 10.1016/j.ces.2013.08.051.
- [82] G. Flamant, D. Gauthier, H. Benoit, J.-L. Sans, B. Boissière, R. Ansart, and M. Hemati. A new heat transfer fluid for concentrating solar systems: Particle flow in tubes. *Energy Procedia, SolarPACES 2013*, 49:617–626, 2014. doi: 10.1016/j.egypro.2014.03.067.
- [83] G. I. Font. Boundary-layer control with atmospheric plasma discharges. *AIAA Journal*, 44(7):1572–1578, 2006. doi: 10.2514/1.18542.

- [84] M. Gad-el Hak. The fluid mechanics of microdevices - the Freeman scholar lecture. ASME. *Journal of Fluids Engineering*, 121(1):5–33, 1999. doi: 10.1115/1.2822013.
- [85] T. Galiullin, B. Gobereit, D. Naumenko, R. Buck, L. Amsbeck, M. Neises-von Puttkamer, and W. J. Quadakkers. High temperature oxidation and erosion of candidate materials for particle receivers of concentrated solar power tower systems. *Solar Energy*, 188:883–889, 2019. doi: 10.1016/j.solener.2019.06.057.
- [86] A. Gallo, J. Spelling, M. Romero, and J. Gonzalez-Aguilar. Preliminary design and performance analysis of a multi-megawatt scale dense particle suspension receiver. *Energy Procedia - International Conference on Concentrating Solar Power and Chemical Energy Systems SolarPACES 2014*, 69:388–397, 2015. doi: 10.1016/j.egypro.2015.03.045.
- [87] B. Ganapol. Highly accurate solutions of the blasius and Falkner-Skan boundary layer equations via convergence acceleration. *eprint arXiv:1006.3888*, 2010.
- [88] P. Garcia, A. Ferrière, S. Plays, and J. J. Beziau. Modélisation de centrales thermodynamiques - cas du projet PEGASE à THEMIS. In *Congrès Français de Thermique, SFT 2007, Île des Embiez, 29 mai - 1 juin 2007*, 2007.
- [89] J. Gaviglio. Reynolds analogies and experimental study of heat transfer in supersonic boundary layer. *International Journal of Heat and Mass Transfer*, 30(05):911–926, 1987. doi: 10.1016/0017-9310(87)90010-X.
- [90] I. M. Gelfand and S. V. Fomin. *Calculus of variations*. Prentice-Hall, Englewood Cliffs, New Jersey, 1963. ISBN 978-0-486-41448-5. ISBN: 978-0-486-41448-5.
- [91] P. Good, G. Zanganeh, G. Ambrosetti, M. C. Barbato, A. Pedretti, and A. Steinfeld. Towards a commercial parabolic trough CSP system using air as heat transfer fluid. *Energy Procedia - SolarPACES 2013*, 49:381–385, 2014. doi: 10.1016/j.egypro.2014.03.041.
- [92] S. Gordeyev and T. J. Juliano. Optical measurements of transitional events in a Mach-6 laminar boundary layer. *AIAA Journal*, 55(11):3629–3639, 2017. doi: 10.2514/1.J055759.
- [93] G. Gouy. Sur les transformations et l'équilibre en thermodynamique. *Comptes-rendus de l'Académie des Sciences, Paris*, 108(10):507–509, 1889.
- [94] G. Gouy. Sur l'énergie utilisable et le potentiel thermodynamique. note de M. Gouy. *Comptes-rendus de l'Académie des Sciences, Paris*, 108(10):794, 1889.
- [95] G. Gouy. Sur l'énergie utilisable. *Journal de Physique*, 8:501–518, 1889.
- [96] M. Gupta, N. Arora, R. Kumar, S. Kumar, and N. Dilbaghi. A comprehensive review of experimental investigations of forced convective heat transfer characteristics for various nanofluids. *International Journal of Mechanical and Materials Engineering*, 9:11, 2014. doi: 10.1186/s40712-014-0011-x.

- [97] K. Hanjalic and B. E. Launder. Fully developed asymmetric flow in a plane channel. *Journal of Fluid Mechanics*, 51(2):301–335, 1972. doi: 10.1017/S0022112072001211.
- [98] L. Heller. Literature review on heat transfer fluids and thermal energy storage systems in CSP plants. In *STERG Report*, 2013.
- [99] C.K. Ho. A review of high-temperature particle receivers for concentrating solar power. *Applied Thermal Engineering*, 109:958–969, 2016. doi: 10.1016/j.applthermaleng.2016.04.103.
- [100] B. Horacek, K. T. Kiger, and J. Kim. Single nozzle spray cooling heat transfer mechanisms. *International Journal of Heat and Mass Transfer*, 48:1425–1438, 2005. doi: 10.1016/j.ijheatmasstransfer.2004.10.026.
- [101] P. G. Huang, G. N. Coleman, and P. Bradshaw. Compressible turbulent channel flows: DNS results and modeling. *Journal of Fluid Mechanics*, 305:185–218, 1995. doi: 10.1017/S0022112095004599.
- [102] A. M. Hussein, R. A. Bakar, and K. Kadirgama. Study of forced convection nanofluid heat transfer in the automotive cooling system. *Case Studies in Thermal Engineering*, 2:50–61, 2014. doi: 10.1016/j.csite.2013.12.001.
- [103] IEA. Global energy & CO₂ status report. Technical report, International Energy Agency, 2018.
- [104] IEA/NEA. Projected costs of generating electricity - Executive summary. Technical report, IEA/NEA, 2015. International Energy Agency and Nuclear Energy Agency.
- [105] IPCC. Climate Change 2014: Synthesis Report. contribution of working groups i, ii and iii to the Fifth Assessment Report of the Intergovernmental Panel on Climate Change. Technical report, PCC, 2014. IPCC, Geneva, Switzerland, 151pp.
- [106] IRENA. Renewable energy technologies: cost analysis series, Volume 1: power sector, Issue 2/5: concentrating solar power. Technical report, IRENA, 2012. International Renewable Energy Agency.
- [107] T. A. Jankowski. Minimizing entropy generation in internal flows by adjusting the shape of the cross-section. *International Journal of Heat and Mass Transfer*, 52(15-16):3439–3445, 2009. doi: 10.1016/j.ijheatmasstransfer.2009.03.016.
- [108] S. Jia, C. Zhang, X. Yuan, and K.-T. Yu. An optimization approach to find the thermodynamic limit on convective mass transfer enhancement for a given viscous dissipation. *Chemical Engineering Science*, 146:26–34, 2016. doi: 10.1016/j.ces.2016.01.059.
- [109] S. Jia, X. Qian, Y. Luo, X. Yuan, and K.-T. Yu. A criterion beyond conservation equations for complex transport process modeling – a case of Rayleigh-Bénard convection. *Chemical Engineering Science*, 128:44–55, 2018. doi: 10.1016/j.ces.2018.02.017.

- [110] L. M. Jiji. *Heat convection*. Springer, 2nd edition, 2009. ISBN 978-3-662-52917-1. doi: 10.1007/978-3-642-02971-4. ISBN: 978-3-642-02970-7.
- [111] W. Jing, T. Tao, L. Xiyuan, and P. Yifei. Analysis on influence of gravity on convection heat transfer in manned spacecraft during terrestrial test. *International Journal of Aerospace and Mechanical Engineering*, 6(9):1908–1913, 2012.
- [112] D. Jo, R. M. Al-yahia, R. M. Altamini, J. Park, and H. Chae. Experimental investigation of convective heat transfer in narrow rectangular channel for upward and downward flows. *Nuclear Engineering and Technology*, 46(2):195–206, 2014. doi: 10.5516/NET.02.2013.057.
- [113] R. D. Joslin. Aircraft laminar flow control. *Annual review of fluid mechanics*, 30:1–29, 1998. doi: 10.1146/annurev.fluid.30.1.1.
- [114] D. Jou, J. Casas-Vazquez, and G. Lebon. *Extended irreversible thermodynamics*. Springer, 2010. doi: 10.1007/978-90-481-3074-0. ISBN: 978-90-481-3073-3.
- [115] S. Kakaç and A. Pramuanjaroenkij. Review of convective heat transfer enhancement with nanofluids. 52(13-14):3187–3196, 2009. doi: 10.1016/j.ijheatmasstransfer.2009.02.006.
- [116] S. Kakaç, Y. Yener, and A. Pramuanjaroenkij. *Convective heat transfer*. CRC Press, 3rd edition, 2013. ISBN 9781466583474. doi: 10.1201/b16194. ISBN: 9781466583474.
- [117] S. Karathanasis. *Linear Fresnel Reflector Systems for Solar Radiation Concentration*. Springer Nature Switzerland AG, 2019. doi: 10.1007/978-3-030-05279-9.
- [118] N. Kasagi, A. Kuroda, and Y. Tomita. Direct numerical simulations of passive scalar field in a turbulent channel flow. *Transaction of the ASME*, 114:598–606, 1992. doi: 10.1115/1.2911323.
- [119] H. Kawamura, K. Ohsaka, H. Abe, and K. Yamamoto. DNS of turbulent heat transfer in channel flow with low to medium-high Prandtl number fluid. *International Journal of Heat and Fluid Flow*, 19:482–491, 1998. doi: 10.1016/S0142-727X(98)10026-7.
- [120] H. Kawamura, H. Abe, and Y. Matsuo. DNS of turbulent heat transfer in channel flow with respect to Reynolds and Prandtl number effects. *International Journal of Heat and Fluid Flow*, 20:196–207, 1999. doi: 10.1016/s0142-727x(99)00014-4.
- [121] J. Kierzenka and L. F. Shampine. A BVP solver based on residual control and the Matlab PSE. *ACM Transactions on Mathematical Software*, 27-3:299–316, 2006. doi: 10.1145/502800.502801.
- [122] J. Kim. Spray cooling heat transfer: The state of the art. *International Journal of Heat and Fluid Flow*, 28:753–767, 2007. doi: 10.1016/j.ijheatfluidflow.2006.09.003.
- [123] J. Kim, P. Moin, and R. Moser. Turbulence statistics in fully developed channel flow at low reynolds number. *Journal of Fluid Mechanics*, 177:133–166, 1987. doi: 10.1017/S0022112087000892.

- [124] J. Kim, Z. Rusak, and N. Korathar. Small-scale airfoil aerodynamic efficiency improvement by surface temperature and heat transfer. *AIAA Journal*, 41(11): 2105–2113, 2003. doi: 10.2514/2.6829.
- [125] F. Kock and H. Herwig. Local entropy production in turbulent shear flows: a high-Reynolds number model with wall functions. *International Journal of Heat and Mass Transfer*, 47:2205–2215, 2004. doi: 10.1016/j.ijheatmasstransfer.2003.11.025.
- [126] F. Kock and H. Herwig. Entropy production calculation for turbulent shear flows and their implementation in cfd codes. *International Journal of Heat and Fluid Flow*, 26:672–680, 2005. doi: 10.1016/j.ijheatfluidflow.2005.03.005.
- [127] G. J. Kolb, C. K. Ho, T. R. Macini, and J. A. Gary. Power tower technology roadmap and cost reduction. Technical report, SANDIA, 2011. Sandia National Laboratories, SAND2011-2419.
- [128] M. Kordac and V. Linek. Mechanism of enhanced gas absorption in presence of fine solid particles. effect of molecular diffusivity on mass transfer coefficient in stirred cell. *Chemical Engineering Science*, 61:7125–7132, 2006. doi: 10.1016/j.ces.2006.06.025.
- [129] N. J. R. Kraakman, J. Rocha-Rios, and M. C. M. van Loosdrecht. Review of mass transfer aspects for biological gas treatment. *Applied Microbiology Biotechnology*, 91:873–886, 2011. doi: 10.1007/s00253-011-3365-5.
- [130] A. Kribus. Concentrated solar power: Components and materials. *EPJ Web Conferences*, 148, 2017. doi: 10.1051/epjconf/201714800009.
- [131] B. Kumar, G. P. Srivastava, M. Kumar, and A. K. Patil. A review of heat transfer and fluid flow mechanism in heat exchanger tube with inserts. *Chemical Engineering and Processing - Process Intensification*, 123:126–137, 2018. doi: 10.1016/j.cep.2017.11.007.
- [132] P. Kumar, K. Schmidmayer, F. Topin, and M. Miscevic. Heat transfer enhancement by dynamic corrugated heat exchanger wall: Numerical study. *Journal of Physics: Conference Series, 7th European Thermal-Sciences Conference (Eurotherm2016)*, 032061, 2016. doi: 10.1088/1742-6596/745/3/032061.
- [133] PROMES Laboratory. *PEGASE Project*, 2019 (accessed May 1, 2019). URL <https://www.promes.cnrs.fr/index.php?page=pegase-accueil>.
- [134] L. Léal, M. Miscevic, P. Lavieille, M. Amokrane, F. Pigache, F. Topin, B. Nogarède, and L. Tadrist. An overview of heat transfer enhancement methods and new perspectives: Focus on active methods using electroactive materials. *International Journal of Heat and Mass Transfer*, 61:505–524, 2013. doi: 10.1016/j.ijheatmasstransfer.2013.01.083.
- [135] Y. Lalau, O. Faugeroux, B. Claudet, E. Guillot, D. Andre, M. Huger, A. Proust, and T. Chotard. A method for experimental thermo-mechanical aging of materials submitted to concentrated solar irradiation. *Solar Energy Materials and Solar Cells*, 192:161–169, 2019. doi: 10.1016/j.solmat.2018.12.017.

- [136] A. Lanjewar, B. Bhanvase, D. Barai, S. Chawhan, and S. Sonawane. Intensified thermal conductivity and convective heat transfer of ultrasonically prepared CuO-Polyaniline nanocomposite based nanofluids in helical coil heat exchanger. *Periodica Polytechnica Chemical Engineering*, 2019. doi: 10.3311/PPch.13285.
- [137] S. Laohalertdecha, P. Naphon, and S. Wongwises. A review of electrohydrodynamic enhancement of heat transfer. *Renewable and Sustainable Energy Reviews*, 11:858–876, 2007. doi: 10.1016/j.rser.2005.07.002.
- [138] LAZARD. Lazard’s Levelized Cost of energy Analysis — Version 11.0. Technical report, LAZARD, 2017.
- [139] B. Lessani and M. V. Papalexandris. Time-accurate calculation of variable density flows with strong temperature gradients and combustion. *Journal of Computational Physics*, 212:218–246, 2006. doi: 10.1016/j.jcp.2005.07.001.
- [140] C. J. Li, P. Li, K. Wang, and E. E. Molina. Survey of properties of key single and mixture halide salts for potential application as high temperature heat transfer fluids for concentrated solar thermal power systems. *AIMS Energy*, 2(2):133–157, 2014. doi: 10.3934/energy.2014.1.133.
- [141] Q. Li, X. Yuan, P. Neveu, G. Flamant, and L. Luo. A novel optimization approach to convective heat transfer enhancement for solar receiver. *Chemical Engineering Science*, 116:806–816, 2014. doi: 10.1016/j.ces.2014.05.051.
- [142] R. Li. Numerical simulation on forced convection cooling of horizontal ionic wind with multi-electrodes. *16th International Refrigeration and Air Conditioning Conference, July 11-14, 2016 - Paper 1696*, 2016. URL <http://docs.lib.purdue.edu/iracc/1696>.
- [143] S. Li, W. Kong, H. Zhang, F. Sabatier, R. Ansart, G. Flamant, and J. Baeyens. The fluidized bed air heat exchanger in a hybrid Brayton-cycle solar power plant. *AIP Conference Proceedings*, 2126, 140002 (2019). doi: 10.1063/1.5117650.
- [144] L. Liebenberg and J. P. Meyer. In-tube passive heat transfer enhancement in the process industry. *Applied Thermal Engineering*, 27:2713–2726, 2007. doi: 10.1016/j.applthermaleng.2007.06.003.
- [145] T. C. Lin. Influence of laminar boundary-layer transition on entry vehicle designs. *Journal of Spacecraft and Rockets*, 45(2):165–175, 2008. doi: 10.2514/1.30047.
- [146] C. Liu and W. Cao. Study of predicting aerodynamic heating for hypersonic boundary layer over a flat plate. *International Journal of Heat and Mass Transfer*, 111:1079–1086, 2017. doi: 10.1016/j.ijheatmasstransfer.2017.04.001.
- [147] K. Liu, C. P. Titan, L. A. Carrilho, and J. A. Khan. Enhancement of heat transfer performance in nuclear fuel rod using nanofluids and surface roughness technique. *ASME International Mechanical Engineering Congress and Exposition, Volume 8B: Heat Transfer and Thermal Engineering: V08BT10A011.*, 2015. doi: 0.1115/IMECE2015-51476.

- [148] S. Liu and M. Sakr. A comprehensive review on passive heat transfer enhancements in pipe exchangers. *Renewable and Sustainable Energy Reviews*, 19:64–81, 2013. doi: 10.1016/j.rser.2012.11.021.
- [149] C. Lou and Z. Zhang. Experimental and numerical analysis of radiative entropy generation in industrial and boiler furnaces. *Journal of Quantitative Spectroscopy & Radiative Transfer*, 232:27–34, 2019. doi: 10.1016/j.jqsrt.2019.04.039.
- [150] K. Lovegrove and J. Pye. *Fundamental principles of concentrating solar power (CSP) systems - in concentrating solar power technology*. Woodhead Publishing Limited, 2012. ISBN: 978-1-84569-769-3.
- [151] S. Ölz, R. Sims, and N. Kirchner. Contribution of renewables to energy security. Technical report, IEA, 2007. International Energy Agency.
- [152] L. Maestrello, F.F. Badavi, and K. W. Noonan. Control of the boundary layer separation about an airfoil by active surface heating. In *1st National Fluid Dynamics Conference, Cincinnati, Ohio*, pages 830–838, 1988. doi: 10.2514/6.1988-3545.
- [153] E. Magyari, I. Pop, and B. Keller. Mixed convection boundary-layer flow past a horizontal permeable flat plate. *Fluid Dynamics Research*, 31(3):215–225, 2002. doi: 10.1016/S0169-5983(02)00116-8.
- [154] S. Mahmud, S. H. Tasnim, and M. A. H. Mamun. Thermodynamic analysis of mixed convection in a channel with transverse hydromagnetic effect. *International Journal of Thermal Sciences*, 42:731–740, 2003. doi: 10.1016/S1290-0729(03)00040-1.
- [155] A. Malvandi, F. Hedayati, and D. D. Ganji. Thermodynamic optimization of fluid flow over an isothermal moving plate. *Alexandria Engineering Journal*, 52(3):277–283, 2013. doi: 10.1016/j.aej.2013.06.006.
- [156] F. Martín, R. Wiesenberg, and D. Santana. Solar thermal power & gas turbine hybrid design with molten salt storage tank. In *AIP Conference Proceedings. 1850*, 2017. doi: 10.1063/1.4984551.
- [157] M. McEligot, J. Walsh, and E. Laurien. Entropy generation in the viscous layer of a turbulent channel flow. *ICHMT Digital Library*, 5th International Symposium on Turbulence, Heat and Mass Transfer (THMT-5):167–170, 2006. doi: 10.1615/ICHMT.2006.TurbulHeatMassTransf.240.
- [158] M. Mehos, C. Turchi, J. Jorgenson, P. Denholm, C. Ho, and K. Armijo. On the path to SunShot: Advancing concentrating solar power technology, performance, and dispatchability. *Golden, CO: National Renewable Energy Laboratory.*, NREL/TP-5500-65688, 2016. (accessed on October 13, 2019). URL <http://www.nrel.gov/docs/fy16osti/65688.pdf>.
- [159] H. Müller-Steinhagen and H. Trieb. Concentrating solar power - a review of the technology. *Ingenia*, 18:43–50, 2004.
- [160] V. J. Modi, J. L. C. Sun, T. Akutsu, P. Lake, K. McMillan, P. G. Swinton, and D. Mullins. Moving-surface boundary-layer control for aircraft operation at high incidence. *Journal of Aircraft*, 18(11):963–968, 1981. doi: 10.2514/3.57587.

- [161] V. J. Modi, M. S. U. K. Fernando, and T. Yokomizo. Moving surface boundary-layer control: studies with bluff bodies and application. *AIAA Journal*, 29(9): 1400–1406, 1991. doi: 10.2514/3.10753.
- [162] A. Montoya, M. R. Rodriguez-Sanchez, J. Lopez-Puente, and D. Santana. Thermal and mechanical stresses in a solar central receiver. *Renewable Energy and Power Quality Journal*, International Conference on Renewable Energies and Power Quality (ICREPQ18), 2018. doi: 10.24084/repqj16.376.
- [163] S-K. Moon, J. Kim, S. Cho, B. J. Kim, J. K. Park, Youn Y-J., and C-H. Song. Single-phase convective heat transfer enhancement by spacer grids in a rod bundle. *Journal of Nuclear Science and Technology*, 51:4:543–557, 2014. doi: 10.1080/00223131.2014.881726.
- [164] H. V. Moradi and J. M. Floryan. On the mixing enhancement in annular flows. *Physics of Fluids*, 29, 024106, 2017. doi: 10.1063/1.4976325.
- [165] Y. Morinishi, S. Tamano, and K. Nakabayashi. Direct numerical simulation of compressible turbulent channel flow between adiabatic and isothermal walls. *Journal of Fluid Mechanics*, 502:273–308, 2004. doi: 10.1017/S0022112003007705.
- [166] Y. Morinishi, S. Tamano, and E. Nakamura. New scaling of turbulence statistics for incompressible thermal channel flow with different total heat flux gradients. *International Journal of Heat and Mass Transfer*, 50 (9-10):1781–1789, 2007. doi: 10.1016/j.ijheatmasstransfer.2006.10.012.
- [167] S. C. Morris, E. Perez, J. T. Schmitz, J. D. Cameron, and J. P. Clark. Fundamental research on boundary layer separation and entropy generation using a transonic research turbine. In *50th AIAA Aerospace Sciences Meeting including the New Horizons Forum and Aerospace Exposition, 9-12 January, Nashville, Tennessee*, 2012. doi: 10.2514/6.2012-735.
- [168] R. D. Moser, J. Kim, and N. N. Mansour. Direct numerical simulation of turbulent channel flow up to $Re_\tau = 590$. *Physics of Fluids*, 11(4):943–945, 1999. doi: 10.1063/1.869966.
- [169] C. Murphy, Y. Sun, W. Cole, G. Maclaurin, C. Turchi, and M. Mehos. The potential role of concentrating solar power within the context of DOE’s 2030 solar cost targets. *National Renewable Energy Laboratory*, NREL/ TP-6A20-71912, 2019. (accessed on October 13, 2019). URL <https://www.nrel.gov/docs/fy19osti/71912.pdf>.
- [170] NACA. The boundary layers in fluids with little friction by H. Blasius - english translation. *National Advisory Committee for Aeronautics*, Technical memorandum 1256 - NACA TM 1256, 1950.
- [171] G. P. Narayan, J. H. V. Lienhard, and S. M. Zubair. Entropy generation minimization of combined heat and mass transfer devices. *International Journal of Thermal Sciences*, 49:2057–2066, 2010.

- [172] I. Nastase and F. Bode. Impinging jets – a short review on strategies for heat transfer enhancement. *E3S Web of Conferences*, 32, 01013, 2018. doi: 10.1051/e3sconf/20183201013.
- [173] G. F. Naterer and J. A. Camberos. Entropy and the second law fluid flow and heat transfer simulation. *Journal of Thermophysics and Heat Transfer*, 17(3): 360–371, 2003. doi: 10.2514/2.6777.
- [174] G. F. Naterer and J. A. Camberos. *Entropy based design and analysis of fluids engineering systems*. CRC Press, 2008. ISBN 978-0-8493-7262-9. doi: 10.1201/9781420006919. ISBN: 978-0-8493-7262-9.
- [175] G. J. Nathan, J. Mi, Z. T. Alwahabi, G. J. R. Newbold, and D. S. Nobes. Impacts of a jet’s exit flow pattern on mixing and combustion performance. *Progress in Energy and Combustion Science*, 32:496–538, 2006. doi: 10.1016/j.pecs.2006.07.002.
- [176] P. A. Nelson, M. C. M. Wright, and J. L. Rioual. Automatic control of laminar boundary-layer transition. *AIAA Journal*, 35(1):85–90, 1991. doi: 10.2514/2.66.
- [177] T. Neuenhahn and H. Olivier. Influence of the wall temperature and the entropy layer effects on double wedge shock boundary layer interactions. In *14th AIAA/AHI Space Planes and Hypersonic Systems and Technologies Conference*, 2006. doi: 10.2514/6.2006-8136.
- [178] I. Newton. *Philosophiae Naturalis Principia Mathematica*. Londini, July 5, 1687. (accessed October 13, 2019). URL <https://gallica.bnf.fr/ark:/12148/bpt6k3363w/f3.image>.
- [179] F. Nicoud. Conservative high-order finite-difference schemes for low Mach number flows. *Journal of Computational Physics*, 158:71–97, 2000. doi: 10.1006/jcph.1999.6408.
- [180] H. Olia, M. Torabi, M. Bahiraei, M. H. Ahmadi, M. Goodarzi, and M. R. Safaei. Application of nanofluids in thermal performance enhancement of parabolic trough solar collector: State of the art. *Applied Sciences*, 9(3)463, 2019. doi: 10.3390/app9030463.
- [181] T. A. Oliver, M. Malaya, R. Ulerich, and R. D. Moser. Estimating uncertainties in statistics computed from direct numerical simulation. *Physics of Fluids*, 26, 035101, 2014. doi: 10.1063/1.4866813.
- [182] S. A. Orzag. Analytical theories of turbulence. *Journal of Fluid Mechanics*, 41(02):363–386, 1970. doi: 10.1017/S0022112070000642.
- [183] M. Ould-Rouiss, L. Redjem-Saad, and G. Lauriat. Direct numerical simulation of turbulent heat transfer in annuli: Effect of heat flux ratio. *International Journal of Heat and Fluid Flow*, 30:579–589, 2009. doi: 10.1016/j.ijheatfluidflow.2009.02.018.
- [184] M. Ould-Rouiss, A. Dries, and A. Mazouz. Numerical predictions of turbulent heat transfer for air flow in rotating pipe. *International Journal of Heat and Fluid Flow*, 31:507–517, 2010. doi: 10.1016/j.ijheatfluidflow.2010.02.015.

- [185] M. Ould-Rouiss, L. Redjem-Saad, G. Lauriat, and A. Mazouz. Effect of Prandtl number on the turbulent thermal field in annular pipe flow. *International Communications in Heat and Mass Transfer*, 37:958–963, 2010. doi: 10.1016/j.icheatmasstransfer.2010.06.027.
- [186] M. Ould-Rouiss, M. Bousbai, and A. Mazouz. Large eddy simulation of turbulent heat transfer in pipe flows with respect to Reynolds and Prandtl number effects. *Acta Mech.*, 224:1133–1155, 2013. doi: 10.1007/s00707-012-0796-8.
- [187] K. Oyakawa, A. Umdea, M. D. Islam, N. Saji, and S. Matsuda. Flow structure and heat transfer of impingement jet. *Heat Mass Transfer*, 46(1):53–61, 2009. doi: 10.1007/s00231-009-0543-4.
- [188] O. Pade, A. Postan, D. Anshelovitz, and M. Wolfshein. The influence of acceleration on laminar similar boundary layers. *AIAA Journal*, 23(10):1469–1475, 1985. doi: 10.2514/3.9112.
- [189] R. L. Panton. *Incompressible Flow*. Wiley, 2013. doi: 10.1002/9781118713075. ISBN: 9781118013434.
- [190] S. Paolucci. On the filtering of sound from the Navier-Stokes equations. *Tech. Rep. SAND82-8257, Livermore: Scandia National Laboratories*, 1982.
- [191] Thémis Solaire Innovation Travail personnel. *Centrale Solaire Thémis*, 2019 (accessed May 29, 2019). URL <https://commons.wikimedia.org/w/index.php?curid=6825524>.
- [192] British Petroleum. BP statistical review of world energy 2018. Technical report, British Petroleum, 2018.
- [193] L. G. Pheng, R. Affandi, M. R. Ab Ghani, C. K. Gan, Z. Jano, and T. Sutikno. A review of parabolic Dish-Sterling engine system based on concentrating solar power. *TELKOMNIKA*, 12(4):1142–1152, 2014. doi: 10.12928/TELKOMNIKA.v12i4.1132.
- [194] B. Pierrat, M. Balat-Pichelin, L. Silvestroni, and D. Sciti. High temperature oxidation of $\text{ZrC}-20\%\text{MoSi}_2$ in air for future solar receivers. *Solar Energy Materials & Solar Cells*, 95:2228–2237, 2011. doi: 10.1016/j.solmat.2011.03.028.
- [195] L. Prandtl. Über Flüssigkeitsbewegungen bei sehr kleiner Reibung. *Verhandlungen des III. Internationalen Mathematiker Kongresses, Heidelberg*, 8-13 August 1904:484–491, 1904.
- [196] I. Pérez-Grande and T. J. Leo. Optimization of a commercial aircraft environmental control system. *Applied Thermal Energy*, 22(17):1885–1904, 2002. doi: 10.1016/S1359-4311(02)00130-8.
- [197] S. Qayyum, T. Hayat, M. I. Khan, M.I. Khan, and A. Alsaedi. Optimization of entropy generation and dissipative nonlinear radiative von karman’s swirling flow with solet and dufour effects. *Journal of Molecular Liquids*, 262:261–274, 2018. doi: 10.1016/j.molliq.2018.04.010.

- [198] O. Raccurt, F. Matino, A. Disdier, J. Braillon, A. Stollo, D. Bourdon, and A. Maccari. In air durability study of solar selective coating for parabolic trough technology. *AIP Conference Proceedings*, 1850, 130010 (2017). doi: 10.1063/1.4984504.
- [199] S. S. Rao. *Engineering Optimization*. John Wiley & Sons, Hoboken, New Jersey, 2009. ISBN 978-0-470-18352-6. ISBN: 978-0-470-18352-6.
- [200] L. Redjem-Saad, M. Ould-Rouiss, and G. Lauriat. Direct numerical simulation of turbulent heat transfer in pipe flows: Effect of Prandtl number. *International Journal of Heat and Fluid Flow*, 28:847–861, 2007. doi: 10.1016/j.ijheatfluidflow.2007.02.003.
- [201] K. Rehme. Turbulent flow in smooth concentric annuli with small radius ratios. *Journal of Fluid Mechanics*, 64(2):263–287, 1974. doi: 10.1017/S0022112074002394.
- [202] K. Rehme. Turbulence measurements in smooth concentric annuli with small radius ratios. *Journal of Fluid Mechanics*, 72(1):189–206, 1975. doi: 10.1017/S0022112075003023.
- [203] REN21. Renewable 2018 global status report. Technical report, REN21, 2018. Renewable Energy Policy Network for the 21st Century.
- [204] K. Risse, F. Schuelcke, E. Stumpf, and G. H. Schrauf. Conceptual wing design methodology for aircraft with hybrid laminar flow control. In *52nd Aerospace Sciences Meeting, AIAA SciTech Forum, 13-17 January, National Harbor, Maryland, (AIAA 2014-0023)*, 2014. doi: 10.2514/6.2014-0023.
- [205] S. K. Saha, M. Tiwari, B. Sundén, and Z. Wu. *Advances in Heat Transfer Enhancement*. Springer, 2016. ISBN 978-3-319-29478-0. ISBN:978-3-319-29478-0.
- [206] A. Z. Sahin and R. Ben-Mansour. Entropy generation in laminar fluid flow through a circular pipe. *Entropy*, 5(5):404–416, 2003. doi: 10.3390/e5050404.
- [207] J. Saien, H. Bamdadi, and S. Daliri. Liquid–liquid extraction intensification with magnetite nanofluid single drops under oscillating magnetic field. *Journal of Industrial and Engineering Chemistry*, 21:1152–1159, 2015. doi: 10.1016/j.jiec.2014.05.028.
- [208] H. Schlichting. *Boundary layer theory*. Springer, 9th edition, 2017. ISBN 978-3-662-52917-1. doi: 10.1007/978-3-662-52919-5. ISBN: 978-3-662-52917-1.
- [209] J. W. Schmelzer, E. D. Zanutto, and V. M Fokin. Pressure dependence of viscosity. *The Journal of Chemical Physics*, 122, 2005, 074511. doi: 0.1063/1.1851510.
- [210] A. Selamet and V. S. Arpaci. Entropy production in boundary layers. *Journal of Thermophysics and Heat Transfer*, 4(3):404–407, 1990. doi: 10.2514/3.197.
- [211] S. Serra, A. Toutant, F. Bataille, and Y. Zhou. Turbulent kinetic energy spectrum in very anisothermal flows. *Physics Letters A*, 376(45):3177–3184, 2012. doi: 10.1016/j.physleta.2012.08.005.

- [212] M. S. Shadloo, A. Hadjadj, and Hussain F. Statistical behavior of supersonic turbulent boundary layers with heat transfer at $M_\infty = 2$. *International Journal of Heat and Fluid Flow*, 53:113–134, 2015. doi: 10.1016/j.ijheatfluidflow.2015.02.004.
- [213] H. Shahmohamadi and M. M. Rashidi. Experimental investigation and a novel analytical solution of turbulent boundary layer flow over a flat plate in a wind tunnel. *International Journal of Mechanics Sciences*, 133:121–128, 2017. doi: 10.1016/j.ijmecsci.2017.08.043.
- [214] W. Short, D. J. Packey, and T. Holt. *A manual for the economic evaluation of energy efficiency and renewable energy technologies*. National Renewable Energy Laboratory (NREL), 1995. NREL/TP-462-5173.
- [215] S. Sieniutycz. *Thermodynamic Approaches in Engineering Systems*. Elsevier, 2016. ISBN: 978-0-12-805462-8.
- [216] Y. C. Soo Too and R. Benito. Enhancing heat transfer in air tubular absorbers for concentrated solar thermal applications. *Applied Thermal Engineering*, 50:1076–1083, 2013. doi: 10.1016/j.applthermaleng.2012.06.025.
- [217] E. F. Spina, A. J. Smits, and Robinson S. K. The physics of supersonic turbulent boundary layers. *Annu. Rev. Fluid Mech.*, 26:287–319, 1994. doi: 10.1146/annurev.fluid.26.1.287.
- [218] W. D. Steinmann. Thermal energy storage systems for concentrating solar power (CSP) technology. In Woodhead Publishing Series in Energy Louisa F. Cabeza, editor, *Advances in Thermal Energy Storage Systems*, chapter 21, pages 511–531. Woodhead Publishing, 2015. doi: 10.1533/9781782420965.4.511.
- [219] W. Stine and R. W. Harrigan. *Power from the sun, published on-line*, 2019 (accessed May 29, 2019). URL <https://www.powerfromthesun.net/Book/chapter10/chapter10.html>.
- [220] A. S. Sunden, Z. Wu, and D. Huang. Comparison of heat transfer characteristics of aviation kerosene flowing in smooth and enhanced mini tubes at supercritical pressures. *International Journal of Numerical Methods for Heat & Fluid Flow*, 24(3/4):1289–1308, 2016. doi: 10.1108/HFF-12-2015-0538.
- [221] W. Sutherland. The viscosity of gases and molecular force. *Philosophical Magazine Series 5*, 36:223:507–531, 1893. doi: 10.1080/14786449308620508.
- [222] D. Taherdazeh, C. Picioreanu, and H. van Harald. Mass transfer enhancement in moving biofilm structures. *Biophysical Journal*, 102:1483–1492, 2012. doi: 10.1016/j.bpj.2012.02.033.
- [223] S. Tamano and Y. Morinishi. Effect of different wall boundary conditions on compressible turbulent channel flow at $M = 1.5$. *Journal of Fluid Mechanics*, 548:361–373, 2006. doi: 10.1017/S0022112005007639.
- [224] E. Terrado, M. Mendis, and K. Fitzgerald. Impact of lower oil prices on renewable energy technologies. Technical report, The World Bank, 1989. The World Bank.

- [225] A. S. W. Thomas. Active wave control of boundary-layer transition. *in: Viscous drag reduction in boundary layers, AIAA, Washington*, pages 179–199, 1990. doi: 10.2514/4.865978.
- [226] Ion Tichy. *Thermo-solar power station Gemasolar near Seville/Spain. The bright light is visible over a long distance (own experience: about 30km)*, 2019 (accessed May 29, 2019). URL <https://commons.wikimedia.org/wiki/File:Gemasolar2012.JPG>.
- [227] I. Tiselj. Tracking of large-scale structures in turbulent channel with direct numerical simulation of low prandtl number passive scalar. *Physics of Fluids*, 26:125111, 2014. doi: 10.1063/1.4905018.
- [228] I. Tiselj and Cizelj L. DNS of turbulent channel flow with conjugate heat transfer at Prandtl number 0.01. *Nuclear Engineering and Design*, 253:153–160, 2012. doi: 10.1016/j.nucengdes.2012.08.008.
- [229] I. Tiselj, R. Bergant, B. Mavko, I. Bajsic, and G. Hetsroni. DNS of turbulent heat transfer in channel flow with heat conduction in the solid wall. *Journal of Heat Transfer*, 123:849–847, 2001. doi: 10.1115/1.1389060.
- [230] A. Toutant and F. Bataille. Turbulence statistics in a fully developed channel flow submitted to a high temperature gradient. *International Journal of Thermal Sciences*, 74:104–118, 2013. doi: 10.1016/j.ijthermalsci.2013.06.003.
- [231] J. L. Troutman. *Variational calculus and optimal control*. Springer, 1996. ISBN 978-1-4612-6887-1. doi: 10.1007/978-1-4612-0737-5. ISBN: 978-1-4612-6887-1.
- [232] C. S. Turchi and Z. Ma. Gas turbine/solar parabolic trough hybrid design using molten salt heat transfer fluid. Technical report, NREL, 2011. NREL - National Renewable Energy Laboratory.
- [233] T. Ukai, K. Kontis, and L. Yang. Flow structure generated by laser-induced blast wave through the boundary layer of a flat plate. *Aerospace science and technology*, 78:569–573, 2018. doi: 10.1016/j.ast.2018.05.012.
- [234] European Union. EU energy in figures, statistical pocketbook 2017. Technical report, European Union, 2017.
- [235] A. Verbruggen, E. Laes, and S. Lemmens. Assessment of the actual sustainability of nuclear fission power. *Renewable and Sustainable Energy Reviews*, 32:16–28, 2014. doi: 10.1016/j.rser.2014.01.008.
- [236] K. Vignarooban, X. Xu, A. Arvay, K. Hsu, and A.M. Kannan. Heat transfer fluids for concentrating solar power systems - A review. *Applied Energy*, 146:383–396, 2015. doi: 10.1016/j.apenergy.2015.01.125.
- [237] A. W. Vreman and J. G. M. Kuerten. Comparison of direct numerical simulation databases of turbulent channel flow at $Re_\tau = 180$. *Physics of Fluids*, 26:015102, 2014. doi: 10.1063/1.4861064.

- [238] D. P. Wall and S. K. Wilson. The linear stability of flat-plate boundary layer flow of fluid with temperature-dependent viscosity. *Physics of fluids*, 9:2885–2898, 1997. doi: 10.1063/1.869401.
- [239] X. Wang, E. Bibeau, and G. F. Naterer. Experimental correlation of forced convection heat transfer from a NACA airfoil. *Experimental Thermal and Fluid Science*, 31(8):1073–1082, 2007. doi: 10.1016/j.expthermflusci.2006.11.008.
- [240] B. M. Wheaton and S. P. Schneider. Roughness-induced instability in a hypersonic laminar boundary layer. *AIAA Journal*, 50(6):1245–1256, 2012. doi: 10.2514/1.J051199.
- [241] T. Winnemöller, M. Meinke, and W. Schröder. Comparison of the mixing efficiency of different injector configurations. *Computers & Fluids*, 117:262–272, 2015. doi: 10.1016/j.compfluid.2015.05.017.
- [242] R. Xu, L. Zhang, Fuzhen. Zhang, and P. Jiang. A review on heat transfer and energy conversion in the enhanced geothermal systems with water/CO₂ as working fluid. *International Journal of Energy Research*, 39:1722–1741, 2015. doi: 10.1002/er.3352.
- [243] S-J. Yang. A numerical investigation of heat transfer enhancement for electronic devices using an oscillating vortex generator. *Numerical Heat Transfer - Part A: Applications*, 42:3:269–284, 2017. doi: 10.1080/10407780290059549.
- [244] K. Yousefi and A. Razeghi. Determination of the critical Reynolds number for flow over symmetric NACA airfoils. In *AIAA Aerospace Sciences Meeting, Kissimmee Florida, 8-12 January*, 2018. doi: 10.2514/6.2018-0818.
- [245] H. L. Zhang, J. Baeyens, J. Degrève, and G. Cacères. Concentrated solar power pants: Review and design methodology. *Renwable and Sustainable Energy Reviews*, 22:466–481, 2013. doi: 10.1016/j.rser.2013.01.032.

Thermodynamic optimization of solar receivers: analysis of entropy generation rates in anisothermal flows subjected to asymmetric thermal boundary conditions

Abstract This thesis work is part of research aimed at improving the performance of concentrated solar power plant receivers with large temperature gradients and asymmetric thermal boundary conditions. It is necessary to analyze the power lost due to thermal and viscous irreversibility. This is achieved by studying the entropy generation rate within the flow and by adopting three different axis of analysis that provide complementary insights: (1) the detailed study of the entropy generation rate in a laminar boundary layer by examining in particular the effect of the thermal boundary condition type (imposed temperature vs. fixed heat flux density) (2) the use of the calculus of variations to determine which velocity fields optimize an objective functional related to the entropy generation rate in a flat plate channel flow, one-third of one of the walls being at imposed heat flux density (3) the study of the entropy generation rate in a flat plate channel flow, turbulent, quasi-compressible and for a fluid which thermo-physical properties depend on temperature.

Keywords Solar receivers, Thermodynamic optimization, Entropy generation rates, Anisothermal flows, Asymmetric thermal boundary conditions

Optimisation thermodynamique des récepteurs solaires : analyse de la puissance entropique générée dans des écoulements anisothermes soumis à des conditions aux limites thermiques asymétriques

Résumé Ce travail de thèse s'inscrit dans le cadre des recherches visant à améliorer la performance des récepteurs de centrales solaires à concentration qui présentent des gradients de température importants et des conditions aux limites thermiques asymétriques. Il est nécessaire d'analyser les puissances utiles perdues du fait des irréversibilités thermiques et visqueuses. Ceci est réalisé par l'étude de la puissance entropique générée au sein de l'écoulement en adoptant trois axes d'analyse différents qui apportent des éclairages complémentaires : (1) l'étude détaillée de la puissance entropique générée dans une couche limite laminaire en examinant en particulier l'effet du type de condition aux limites (température imposée vs densité de flux thermique imposée) (2) l'utilisation du calcul variationnel afin de déterminer quels champs de vitesse optimisent une fonctionnelle objectif reliée à la puissance entropique générée dans un écoulement en canal plan dont le tiers d'une des parois est à densité de flux imposée (3) l'étude de la puissance entropique générée dans un écoulement en canal plan, turbulent, quasi-compressible et pour un fluide dont les propriétés thermophysiques dépendent de la température.

Mots-clés Récepteurs solaires, Optimisation thermodynamique, Puissance entropique générée, Ecoulements anisothermes, Conditions aux limites thermiques asymétriques